Alma Mater Studiorum – Università di Bologna

DOTTORATO DI RICERCA IN

INGEGNERIA CIVILE, CHIMICA, AMBIENTALE E DEI MATERIALI

Ciclo XXIX

Settore Concorsuale di afferenza: 08/B2

Settore Scientifico disciplinare: ICAR/08

Elastic waves in periodic and locally resonant metamaterials: algorithms for fast dispersion computation and applications for seismic wave isolation

Presentata da: **Antonio Palermo**

Coordinatore Dottorato

Prof. Luca Vittuari

Relatore

Prof. Alessandro Marzani

Correlatore

Prof. Chiara Daraio

Esame finale anno 2017

To my family and my fiancée.

ACKNOWLEDGMENTS

I would like to express my sincere gratitude to my advisor, Prof. Alessandro Marzani. He gave me the right guidance, he supported my research, he always listened to my ideas and gave me great freedom to pursue my interests. I greatly appreciated this all.

I would like to extend my special appreciation and thanks to my co-advisor, Prof. Chiara Daraio. She gave me the chance to join a fantastic research group and did everything to make me feel an important part of it.

I would also like to thank Prof. Eleni Chatzi and Dr. Vasileios Ntertimanis for their help and support on the metabarrier experimental setup and the fruitful discussions about it.

I extend my gratitude to all my officemates in Bologna: Federica, Lisa, Andrea, Andrea, Luca, Mattia, Mattia, Antonio, Carlotta. Thanks for creating such a relaxed and congenial work environment.

I thank all the master students from Bologna and ETH which contributed to the analysis of the metabarrier: Isotta, Rachele, Matteo and Erick. It has been a great pleasure to share ideas and look for different design solutions with you.

I thank all my colleagues at ETH and Caltech: Luca, Vincenzo, Sebastian, Jinwoong, Katie, Wei-Hsun, Miguel, Marc, Anton, Jan, Osama, Raffaele, Andre', Eleftheria, Bastian. I greatly appreciate you support, our interesting discussions at the meetings and the lively atmosphere of the group. Sebastian, I really enjoyed our collaboration, and I am grateful for the opportunity you gave me to improve my skills as an "experimentalist". Luca, Vinnie I am happy I found such good friends in Zürich, and I am so glad we will spend more time together in LA.

Finally, I would like to express my deepest gratitude to my parents for their unconditional support and love and my brother Michele, who is and always will be my best guidance and mentor.

Last but not least, I thank my fiancée Susanna for her support, love, patience, and infinite care. Thank you for pushing me to go after my dreams and not letting me fail. I am forever indebted to you.

ABSTRACT

Periodic and locally resonant materials, also referred as metamaterials, provide unique opportunities for elastic wave control across different length scales, ranging from thermal insulation at the nanoscale to meter-size devices for seismic attenuation. The properties of periodic/locally resonant media can be investigated at the unit cell level, which describes the full dynamics of the material. Unit cell modeling requires fast computational approaches which can capture the filtering properties of these materials. Additionally, when large scale applications for seismic wave attenuation are envisioned, the extra challenge is to design unit cells of feasible dimensions and practical implementation.

Starting from these considerations, in this dissertation, two primary objectives are pursued within two distinct Parts of the thesis. In Part I, fast numerical approaches to extract the dispersive properties of periodic/locally resonant materials are investigated. In Part II, an innovative isolation device for seismic wave attenuation, named seismic metabarrier, is presented. In more detail, Part I presents two Finite Element based model reduction techniques: (i) the first one combines a Component Mode Synthesis (CMS) reduction and a Wave Finite Element approach to accurately extract the material complex dispersion with reduced computational time; (ii) the second one relies on a Wave-based model reduction technique applied on the CMS reduced model to further ease the band structure computational effort.

Part II presents the seismic metabarrier, which consists of an array of local resonators buried at the soil surface to convert Rayleigh waves into shear bulk waves. Analytical, numerical and scaled experimental studies performed on the metabarrier show promising results for the attenuation of surface waves in the low-frequency regime. The required barrier dimensions to achieve a significant ground motion attenuation are evaluated with different parametric studies. Finally, the metabarrier design is optimized using multi-mass resonators which minimize the barrier dimensions for its practical implementation.

CONTENTS

1 INTRODUCTION 1
  1.1 Background and motivation 1
    1.1.1 Phononic crystals and periodic structures 1
    1.1.2 Locally resonant media: acoustic/elastic materials 3
    1.1.3 Applications and open challenges 5
  1.2 Thesis objectives 6
  1.3 Organization of the thesis 6

I PERIODIC AND LOCALLY RESONANT MEDIA: DISPERSION CURVE FROM FINITE ELEMENT APPROACHES 9

2 DISPERSION ANALYSIS OF PERIODIC AND LOCALLY RESONANT MEDIA 11
  2.1 Introduction 11
  2.2 Bloch theorem and band structure 11
  2.3 Elastic Band structure: real $\omega(k)$ vs. complex $k(\omega)$ approach 14
  2.4 Computational method for elastic band structure calculation 15
    2.4.1 Plane-Wave Expansion Method 16
    2.4.2 Finite Element based techniques 17
  2.5 Review of Bloch operator transformation approach 17
    2.5.1 Strong formulation of the elastic Bloch eigenvalue problem 18
  2.6 Review of Wave Finite Element Method 19
    2.6.1 Wave Finite Element Method for 1D periodic waveguides 20
    2.6.2 Wave Finite Element Method for 2D periodic waveguides 22
  2.7 Conclusion 26

3 A CMS REDUCTION TECHNIQUE FOR COMPLEX BAND STRUCTURES 29
  3.1 Introduction 29
  3.2 CMS WFEM for one-dimensional periodic waveguide 31
    3.2.1 Numerical applications 33
  3.3 CMS-WFEM for two-dimensional periodic waveguides: the EBMS method 40
    3.3.1 Numerical application 42
  3.4 Conclusions 49

4 A COMBINED CMS-WAVE REDUCTION FOR COMPLEX BAND STRUCTURES 51
  4.1 Introduction 51
  4.2 A wave-based model reduction for $k(\omega)$ WFE approach 52
    4.2.1 Extraction of waveguide rigid body motions 53
    4.2.2 Definition of the cut-on frequency subset $\tilde{\omega}$ 54
    4.2.3 Extraction of the wave shapes Φ and construction of the reduced basis 54

4.3 Numerical applications 55
    4.3.1 A.R.E.M.A. rail steel section 56
    4.3.2 Periodic stubbed beam 60
    4.3.3 Conclusions 62

II PERIODIC AND LOCALLY RESONANT MEDIA FOR SEISMIC WAVE ATTENUATION: A SEISMIC METABARRIER 65

5 PERIODIC AND LOCALLY RESONANT MEDIA FOR SEISMIC WAVE ATTENUATION 67
  5.1 Introduction: A short historical perspective on Earthquake Engineering 67
  5.2 Strategies for earthquake resistant structures 68
  5.3 New devices and strategies towards the control of seismic waves 70
    5.3.1 Periodic structures for seismic wave attenuation 71
    5.3.2 Resonant structures for seismic wave attenuation 75
    5.3.3 Further strategies to control seismic waves: Lensing, cloaking, and clamped metamaterials 78
  5.4 Conclusions 79
6 AN ENGINEERED METABARRIER FOR SEISMIC SURFACE WAVE ATTENUATION 81
  6.1 Introduction 81
  6.2 Concept 82
  6.3 Analytical model 83
    6.3.1 Single-dof surface resonators: Behavior at vertical and horizontal resonance 84
    6.3.2 Horizontal-Vertical coupling and full 3-DOFs metabarrier 90
  6.4 Numerical Model 93
    6.4.1 Numerical dispersion relation 93
    6.4.2 FE simulations on a finite length metabarrier 94
  6.5 Experimental test on a small scale metabarrier 97
  6.6 Conclusions 102
7 METABARRIER OPTIMIZATION WITH MULTI-MASS RESONATORS 105
  7.1 Introduction 105
  7.2 Single mass seismic metabarrier: Performance and Limitations 106
    7.2.1 Attenuation vs resonators mass and metabarrier length 107
    7.2.2 Results and Limitations 111
  7.3 Multi-mass seismic metabarrier 111
    7.3.1 Analytical model 111
    7.3.2 A double-mass (DM) resonator 113
    7.3.3 DM metabarrrier vs. Equivalent SDOF metabarrier 113
    7.3.4 DM metawedge barrier vs. 2SDOF equivalent one 115
  7.4 Multi-mass metabarrier: Optimization with GAs 117
    7.4.1 Metabarrier Transfer Function and Frame response 119
    7.4.2 A case study: a multi-mass metabarrier for two concrete frames 119

- 7.5 Conclusion 122

8 CONCLUSIONS, ONGOING RESEARCH AND FUTURE OUTLOOK 125
- 8.1 Main Conclusions of Part I 125
- 8.2 Main Conclusions of Part II 126
- 8.3 Ongoing research 127
  - 8.3.1 Model reduction technique for the FE Bloch operator transformation approach 127
  - 8.3.2 Metabarriers in inhomogeneous soil profile 128
- 8.4 Future outlook 129

III APPENDIX 131
- .1 Appendix A 133
- .2 Appendix B 135

BIBLIOGRAPHY 137

LIST OF FIGURES

Figure 1 a) 1D, 2D and 3D periodic media (phononic crystals) made of two different elastic materials arranged periodically. b) An example of a band diagram $\omega = \omega(k)$ for a two-dimensional phononic crystal, calculated along the high symmetry unit cell directions $\Gamma - X - M - \Gamma$. The range of forbidden frequencies, phononic band gap PBG, is shown in orange. (Adapted from Ref. [3]). 3

Figure 2 a) Ordinary material with positive stiffness $K > 0$ and positive density $\rho > 0$. b) Metamaterial with negative stiffness $K < 0$ and positive density $\rho > 0$. (c) Metamaterial with positive stiffness $K > 0$ and negative density $\rho < 0$. (c) Double negative $K < 0$, $\rho < 0$ metamaterial. (From Ref. [26]). 5

Figure 3 a) Generic 3D periodic media. b) Unit Cell geometry. c) Reciprocal lattice space. 12

Figure 4 a) First Brillouin zone of cubic lattice unit cell. b) First Brillouin zone of an orthorhombic lattice unit cell. In red the boundaries of the Irreducible Brillouin Zone. (From Ref. [51]). 13

Figure 5 a) Discrete mass-spring chain. b) Mass-spring unit cell. 14

Figure 6 a) Complex band structure curves of a LE, a KV and a SLS mass-spring chain. 15

Figure 7 Generic 1D waveguide unit cell. 20

Figure 8 a) Unit cell geometry and b) Unit cell Brillouin Zone. 23

Figure 9 Unit cell node numbering. 24

Figure 10 a) Schematic of the generic 1D waveguide unit cell. b).1) Unit cell node partition .2) Modal reduced unit cell description. c) Schematic of boundary and constrained modes. 32

Figure 11 a) Mesh of the finite length portion of the octagonal waveguide built in COMSOL. b) Cross-section mesh used in the SAFE formulation. c) Phase velocity and d) attenuation dispersion curves. 35

Figure 12 a) Error real wavenumber prediction k_r vs. number of fixed-interface mode n_{fi}. b) Error imaginary wavenumber prediction k_i vs. number of fixed-interface mode n_{fi}. 36

Figure 13 Unit cell of the phononic stubbed beam. Dimension and FE mesh 37

Figure 14 a) Dispersion and b) attenuation curve for a linear elastic and a viscoelastic (hysteretic) stubbed beam. 39

Figure 15 a) Dispersion and b) attenuation curve for the hysteretic stubbed beam. Full vs. CB reduced results. 40
Figure 16 a) Error real wavenumber prediction k_r vs. number of fixed-interface mode n_{fi}. b) Error imaginary wavenumber prediction k_i vs. number of fixed-interface mode n_{fi}. 40
Figure 17 Unit cell of the considered aluminum stubbed plate. 42
Figure 18 Complex band structures of the aluminum stubbed plate:full 3D representation (ω, k_r, k_i). 43
Figure 19 Complex band structures of the aluminum stubbed plate:a) ω vs. k_r and b) k_i vs. k_r. 44
Figure 20 Band structures and selected mode shapes of the stubbed plate along Γ-X direction obtained with a refined mesh of 14559 dofs. 45
Figure 21 Full vs. reduced complex band structures along the Γ-X direction. Dots represent solutions of the full-dof model (7341 dofs) whereas crosses denote solutions of the reduced model with 100 interface modes (700 dofs). 47
Figure 22 a) Propagative modes along the Γ-X direction computed considering 30 (green), 100 (magenta) and 500 (blue) interface modes as well as considering the full model (black); b) the inset shows the modal dependency. 47
Figure 23 Propagative modes: a) error e_{k_r} versus number of fixed-interface modes n_{fi}. b) error e_{k_r} versus the computational time fraction T_{fr}. 48
Figure 24 Evanescent X-edge modes calculated for $n_{fi} = 30$ (green triangle), 100 (magenta star) and 500 (blu cross) fixed-interface modes ϕ_i vs the evanescent X-edge modes calculated using the full model (black dot). 49
Figure 25 a) Error e_{k_i} versus the number of fixed-interface modes n_{fi} for the evanescent X-edge modes at four considered frequencies. b) Error e_{k_i} versus the computational time fraction T_{fr} (in percentage) for the evanescent X-edge modes at four considered frequencies. 49
Figure 26 Geometry and FE mesh of the finite length portion of the A.R.E.M.A waveguide built in COMSOL®.® 56
Figure 27 Dispersion k_r vs. f and attenuation k_i vs. f curve for the Full Model, CMS reduced model and CMS-Wave reduced model. 57
Figure 28 Errors in the real and imaginary wavenumber predictions for the first 4 propagative modes for the CMS-Wave reduced model vs. Full model. 59
Figure 29 Relative errors in the real and imaginary wavenumber predictions for the first 4 propagative modes for the CMS-Wave reduced model vs. CMS reduced model. 59

Figure 30 Errors in real and imaginary wavenumber predictions vs. number of fixed-interface mode. In black lines are shown the errors for the CMS models, while in red lines the errors for the related CMS-Wave models. 60
Figure 31 Complex dispersion curve of an hysteretic periodic stubbed beam. Full model vs. CMS-Wave reduced models. 61
Figure 32 Performance objectives for buildings (Adapted from SEAOC 1995). 69
Figure 33 Schematic of the investigated soil trench. (From Ref. [95]). 72
Figure 34 a) The test zone located in the alpine city of Grenoble (France). (Adapted from Ref. [45]). 73
Figure 35 Test setup for specimens A (with a periodic foundation) and B (without a periodic foundation). (From Ref. [108]). 74
Figure 36 Schematic of the Helmotz resonators for seismic attenuation. (From Ref. [109]). 75
Figure 37 a) Schematic diagram showing vulnerable buildings (white structures) that are endangered by incoming seismic waves. The red ring around the buildings represents the area with buried local resonators. b) Components in a resonator, consisting of a cylindrical hollow tube (left), containing a heavy bulk cylinder (right, shown separately) suspended by polymeric springs (black). (From Ref. [46]). 76
Figure 38 Surface-to-shear waves conversion of a forest. (From Ref. [114]). 77
Figure 39 Composite soil lenses. (From Ref. [120]). 78
Figure 40 Examples of uncloaked (a,c) and cloaked objects (a,c). (From Ref. [121]). 79
Figure 41 a) The seismic metabarrier. b) The resonant unit. 83
Figure 42 Schematic of the analytical model. a) Dynamic of 3DOFS resonators excited by Rayleigh waves. b) Rotational and coupled horizontal-rotational stiffness of the resonator. 84
Figure 43 Simplified analytical models. a) SDOF vertical resonators excited by Rayleigh waves. b) SDOF horizontal resonators excited by Rayleigh waves. c) 2DOFs vertical-horizontal resonators excited by Rayleigh waves. 86
Figure 44 Simplified analytical models. a) SDOF vertical resonators excited by Rayleigh waves. b) 2DOFs vertical-horizontal resonators excited by Rayleigh waves. 88
Figure 45 Dispersion relation for the 3DOFs metabarrier. 92
Figure 46 Normalized bandwidth for varying soils vs. resonator design. 92
Figure 47 Metabarrier unit cell. a) Planar view. b) 3D view. 93
Figure 48 Numerical dispersion relation. 94

Figure 49 Numerical simulation of the wave conversion mechanism. a) 3D stripe finite element model of soil engineered with 12 lines of resonators. b) Harmonic response at 5 Hz with and without the resonators. c) Horizontal surface ground motion. d) Horizontal ground motion attenuation as a function of the number of resonators in the array (5.0 Hz), averaged over a distance of 20 m at 30 m away from the resonator barrier. 96

Figure 50 Tabletop experimental setup. a) Resin block with embedded 30 resonators in a triangular lattice. (b) The resonator consists of rigid aluminum shell, a heavy steel mass and soft spring. c) Experimental setup to measure the surface out-of-plane velocity wave field using a laser doppler vibrometer. 98

Figure 51 Resonator response. a) Typical transient response of the scaled resonator and b) the corresponding frequency spectrum. 99

Figure 52 1D seismographs and frequency transmission. a) Experimental seismograph of free propagation. b) Transient response at 5 cm and at 35 cm distance from the source. c) Normalized spectrum of the far field response compared to the spectrum of the adopted Ricker's wavelet pulse. d) Experimental seismograph of propagation with resonators. e) Transient response at 5 cm and at 35 cm (after the resonators) distance from the source. f) Normalized spectrum of the far field response. 100

Figure 53 Experimental dispersion and surface velocity field. a) Experimental dispersion diagram of free propagation of Rayleigh waves. b) Experimental dispersion diagram of the propagation of Rayleigh through the metabarrier. c) Full velocity field of experimental Rayleigh wave propagation at 3 sequential time instants ($t_1 = 0.26$ ms, $t_2 = 0.38$ ms and $t_3 = 0.5$ ms) on the free surface. Numerical comparison for time instant t_3. d) Full velocity field of experimental Rayleigh wave propagation at 3 sequential time instants ($t_1 = 0.26$ ms, $t_2 = 0.38$ ms and $t_3 = 0.5$ ms) on the surface with the metabarrier. Numerical comparison for time instant t_3. 101

Figure 54 FE Dispersion law. a) FE model geometry. b) Dispersion law - SDOF resonators. 107

Figure 55 FE 2D Numerical Model. a) Schematic of the model geometry. b) Displacement field at the attenuation peak. 108

Figure 56 SDOF Parametric study. a) Normalized average vertical acceleration vs. resonator mass m. b) Normalized average vertical acceleration vs. metabarrier lenght L_{res}. 109

Figure 57 Rayleigh, Rayleigh-Bloch, and Shear wave shapes. The frequency-wavenumber values where the wave shapes are calculated are represented with colored dots in Fig. 54. 110
Figure 58 Schematic of the MDOF system 112
Figure 59 Dispersion law - DM resonator. 113
Figure 60 Equivalent 2SDOFi. 115
Figure 61 Attenuation vs barrier length - DM vs Equivalent 2SDOF. 115
Figure 62 Attenuation - DM metawedge vs. equivalent 2SDOF metawedge 116
Figure 63 GA Optimization strategy 118
Figure 64 Concrete-frame structures. In red the main frames along the x direction. 120
Figure 65 Concrete frame base shear transfer function T_h. 121
Figure 66 Attenuation function hybrid FM metabarrier 122
Figure 67 Frames base shear response. a) ChiChi (TCU045 Station) ground motion. b) Trinidad (CDMG090 Station) ground motion 122
Figure 68 a) 3D Lattice structure. b) Real dispersion curve: Full $\omega(k)$ solution vs. Reduced $k(\omega)$ Bloch transformation approach. 127
Figure 69 a) Small scale experimental setup. b) Granular medium velocity profile. c) Embedded scaled metabbarier. 128
Figure 70 a) Numerical and b) Experimental velocity seismographs of surface waves traveling through the metabarrier in the granular medium. c) Wave conversion of a metabarrier in a homogeneous soil. d) Wave conversion and back reflection in the inhomogeneous soil. 129

LIST OF TABLES

Table 1 Mechanical parameters of the octagonal steel bar. 34
Table 2 Octagonal beam: Computational time vs. accuracy. 37
Table 3 Stubbed beam: Computational time vs. accuracy. 40
Table 4 A.R.E.M.A. rail steel section mechanical parameters. 56
Table 5 A.R.E.M.A: Computational time vs. accuracy. 60
Table 6 Stubbed Beam: Error analysis for propagative low damped solutions and complex/edge modes. 62
Table 7 Dimensions and mechanical parameters of resonators and sedimentary soil 90
Table 8 SDOF-Resonator for numerical evaluations 107
Table 9 Soil class C, in accordance with EC8 [**EC8**] 107
Table 10 DM-Resonator for numerical evaluations 114

Table 11 Mechanical and geometrical properties of the equivalent SDOFi resonators. 114
Table 12 Genetic Algorithm settings. 119
Table 13 First natural frequencies and modal participating masses of two 2D frames. 120
Table 14 FM-Resonators for the metabarrier. 121
Table 15 Stiffness scaling factors for the DM metawedge 135
Table 16 2SDOF resonators properties for equivalent metawedge 136

1

INTRODUCTION

1.1 BACKGROUND AND MOTIVATION

Light propagation through crystals, sound propagation through fluids, and mechanical vibrations in solids share a common feature: the interaction of waves with a medium. When the medium has a peculiar structure, interesting phenomena arise like the rainbow generated by reflection-refraction of light in water droplets or the diffraction of water waves in a harbor. Attempts to intentionally manipulate the propagation of waves have been made from ages as demonstrated by the lenses used by the ancient Greeks to focus sunlight and start fires on enemy ships. However, it is only in the last two decades that significant progress has been made in the wave propagation control with the design of appropriate artificial composite media, referred as metamaterials. The word 'meta', which means 'beyond' in Greek, refers to the ability of such materials to achieve properties that go beyond what is possible with conventional materials [1].

The field of metamaterials owes much to the optic/electromagnetic community which first introduced the idea of using periodic crystals, also referred as photonic crystals, to achieve wave filtering and directionality effects [2]. Using these artificial periodic media, waves operating at length scales comparable to the material periodicity can be controlled; later on, the possibility of controlling light at the sub-wavelength regime was achieved employing metamaterials. Both the photonic and the metamaterial concepts were then translated to the acoustic and elastic domain leading to the developments of phononic and acoustic/elastic metamaterials. Phononic and acoustic/elastic metamaterials can be applied at different lengths scale to control material vibration properties at various frequencies: in the hypersound regime for thermal isolation, in the ultrasound range for imaging and medical applications and in the infrasound region for vibrations isolation and earthquake protection [3].

In what follows, a short historical perspective on the major contributions in the field of phononic materials and elastic metamaterials is provided to discuss both the state-of-the-art and the open challenges for achieving the full control of their vibrational properties.

1.1.1 *Phononic crystals and periodic structures*

A periodic medium is a material or structural system characterized by some form of spatial periodicity, either in the arrangement of the different material phases or in its geometry [4] (see Fig. 1a). Material periodicity interacts with various forms of waves, including electromagnetic and acoustic waves, crystal vibrations at the atomic scale and mechanical vibrations [5, 6]. For all these systems, the interaction occurs when propagating waves have wavelengths in the order of the periodicity length of the material, giving rise to wave dispersion effects. Dispersion is the dependence of the wave velocity (both phase and group velocity) from the wave frequency (or equally from its wavelength). In periodic materials, strong dispersion effects are caused by destructive interference between transmitted and reflected waves, scattered by the periodicity of the media. Such phenomenon, referred as Bragg scattering, creates band gaps (BGs), frequency ranges within the dispersion relation where waves cannot propagate [5]. The control and full exploitation of such dispersive effects have attracted the attention of several researchers during the last decades, interested in designing innovative materials able to control the propagation of elastic waves at will.

The first systematic study on the dispersive properties of periodic elastic media can be found in the work by Brillouin [5], who analyzed the propagation of elastic waves in periodic strings in parallel with electromagnetic waves in electrical circuits, and electrons in crystals. In his study, Brillouin introduced the concepts of unit cell, Brillouin zone, and frequency band gaps, already used in the context of electron band structures, to the field of elastic waves. The unit cell of a periodic medium corresponds to the smallest portion of the material that constitutes the repeating pattern of the periodic structure. Conversely, the Brillouin zone is the representation of the unit cell in the wave vector space, also referred as reciprocal space. Within the reciprocal space, the first Brillouin zone identifies the full range of wave vectors spanned by the dispersion relation, which in turn relates frequency and wave vector of elastic waves propagating in the medium (see Fig. 1b for an example of the dispersion relation of a 2D-periodic material). After Brillouin, in the early nineties, a great research effort was devoted to the analysis and design of materials with periodic modulation of refractive index, named photonic crystals, able to control the motion of photons [2]. Later on, the parallel concept of phononic crystals was conceived, namely materials designed to control the propagation of mechanical vibrations thanks to a periodic modulation of elastic properties and mass density.

In this regards, it is fundamental to mention the pioneering studies of Sigalas and Economou [7, 8] that described for the first time the band structures of in-plane longitudinal and transversal waves in 2D solid and fluid phononic crystal. Later on, Kushwaha et al. [9, 10] analyzed the propagation of out-of-plane waves in a periodic array of nickel alloy cylinders in an aluminum alloy matrix, and the same Economou and Sigalas [11] the elastic band structure of a 3D phononic crystal. Similarly, phononic crystals in 2D semi-infinite domain as well as in plate-like structures were investigated to assess the effect of periodicity on Rayleigh and Lamb waves [12–16]. The reader may refer to Ref. [4] for a more exhaustive review of further contributions in the field of phononic crystal.

In parallel to the field of phononic crystals, several studies on the propagation of elastic waves in periodic structures have been conducted in the area of structural

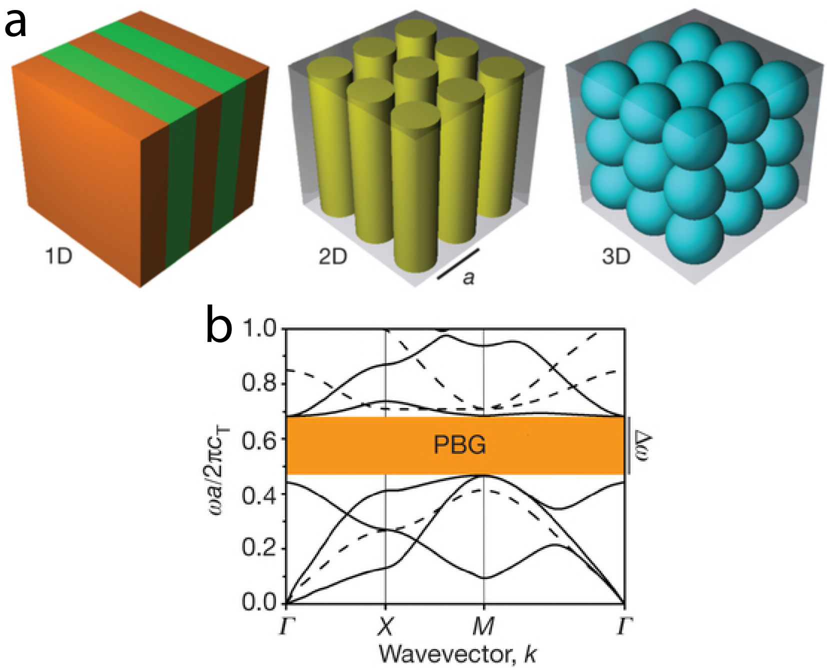

Figure 1: a) 1D, 2D and 3D periodic media (phononic crystals) made of two different elastic materials arranged periodically. b) An example of a band diagram $\omega = \omega(k)$ for a two-dimensional phononic crystal, calculated along the high symmetry unit cell directions $\Gamma - X - M - \Gamma$. The range of forbidden frequencies, phononic band gap PBG, is shown in orange. (Adapted from Ref. [3]).

and aeronautical engineering. Among the others, it is worth citing the works from the research group lead by Mead at the University of Southampton, which studied the propagation of flexural waves in periodic beams and rib-skin structures and whose main contributions are summarized in his review work [17].
Waves in periodic structures have also been the focus of different numerical studies based on Finite Elements approaches. Among the others, it is worth mentioning the seminal work of Orris et al. [18], on the propagation of flexural waves in periodically supported infinite beams and the works by Mace et al. [19, 20] on the Wave Finite Element Method for one-dimensional and two-dimensional periodic structures. Further details on this approach are given in Chapt. 2. Finally, different researchers have analyzed the directional properties of periodic materials, with the aim of identifying and engineering wave beaming phenomena and directional band gaps or exploiting anisotropic wave propagation patterns [21–25].

1.1.2 *Locally resonant media: acoustic/elastic materials*

The term 'metamaterial' has not a unique definition in literature and refers to a broad class of engineered materials, usually composites, characterized by an internal structure able to induce effective properties which substantially differ from those found in its components [26]. Although phononic crystals and periodic media are sometimes classified as metamaterials, in the field of acoustic and elastic wave propagation it is more common to restrict the class of acoustic/elastic metamaterials to composites with local resonance particles/structures in a hosting medium [4]. These resonances provide peculiar dynamic properties to such materials as the possibility of opening subwavelength band gaps, to control the propagation of low-frequency vibrations, or the ability to obtain negative refraction index and resolve acoustic and elastic waves beyond the diffraction limit [27]. These features differentiate metamaterials from phononic crystals, which operate at wavelengths comparable to the unit cell dimensions. Nonetheless, the subwavelength nature of metamaterials allows analyzing their dynamic behavior in terms of effective properties (typically effective bulk-material or effective density for an elastic medium) which can be estimated from simulations or measurements of very small samples.

The first realization of a local resonant acoustic metamaterial is from Liu et al. [28], who experimentally proved the possibility of obtaining subwavelength band gaps as well as effective negative stiffness using lead spheres coated with silicone rubber, hosted in an epoxy matrix. Subwavelength band gaps were later obtained using materials with soft inclusions [29], resonant masses attached to beams or plates [30, 31], plates or surfaces with pillars [32–34], inertial amplifications [35, 36], and architected lattices with internal resonators [37]. As for the phononic crystal section, a more detailed review on locally resonant elastic metamaterials can be found in Ref. [4].

In addition to that, different exotic effective properties have been achieved by means of locally resonant metamaterials. For example, metamaterials with negative effective stiffness and positive density have been obtained with open and closed cavity resonators [38], able to create monopolar resonances. Conversely, metamaterials with positive stiffness and negative effective density have been designed exploiting dipolar resonances, generated for example by membranes or coated-spheres structures [28, 39]. Double negative stiffness and density materials resulting from the coupling of monopolar and dipolar resonances, and characterized by a negative refractive index material [40], have been realized by means of space-coiling metamaterials. A graphical summary of the possible effective properties achievable with acoustic/elastic metamaterials is reported in Fig. 2, reproduced from Ref. [26]. Building on these concepts, more exotic effective properties can be achieved, like effective anisotropic density or hybrid elastic solids, able to behave as a fluid or solid material at will in selected frequency ranges [41, 42]. It is worth noting that although a period arrangement of such local resonances is not strictly required to obtain the desired dynamic behavior [28], periodicity allows studying the material with a unit-cell based description, resulting in a periodic locally resonant material.

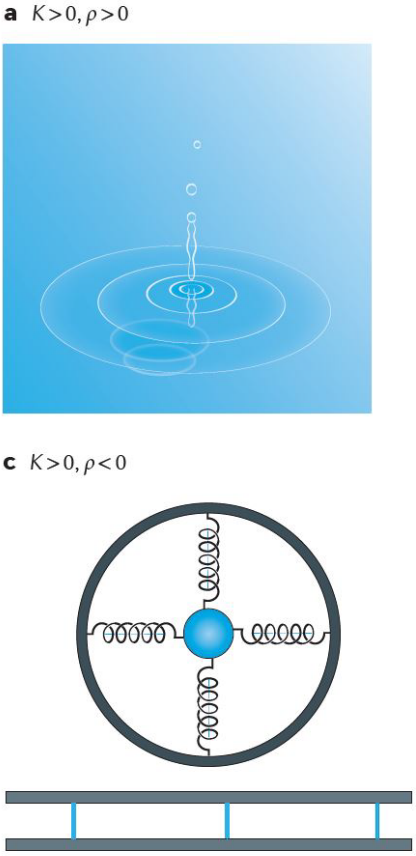

Figure 2: a) Ordinary material with positive stiffness $K > 0$ and positive density $\rho > 0$. b) Metamaterial with negative stiffness $K < 0$ and positive density $\rho > 0$. (c) Metamaterial with positive stiffness $K > 0$ and negative density $\rho < 0$. (c) Double negative $K < 0$, $\rho < 0$ metamaterial. (From Ref. [26]).

1.1.3 *Applications and open challenges*

Periodic and locally resonant media are an active and promising research field, with high potential for the development of new technologies for wave propagation control. Since the wave-scattering and resonance based phenomena exploited by these materials can be explored at different length/frequency scales, a large number of applications has been envisioned, from thermal vibrations control at the nanoscale-terahertz [43, 44], to the attenuation of seismic waves at the geophysical scale [45–47].

Design strategies based on computational approaches play a fundamental role in the search of optimal properties of phononic materials [48] or novel/peculiar dynamic properties of metamaterials [49] across all the length scales. To this reason, faster numerical tools able to support the design of these materials are of crucial importance. Nonetheless, given the interest in exploring the wave filtering properties of such materials, fast numerical methodologies with the ability of fully predicting

the spatial wave decay are desirable
On the other hand, when applications of periodic media and metamaterials are specifically investigated at the geophysical scale, the key challenge is to translate their filtering properties into physical devices, which are at the same time of feasible dimensions and practical implementations.

1.2 THESIS OBJECTIVES

Based on the above initial discussion, in this dissertation two primary objectives are set, which are pursued within two distinct Parts:

- The objective of Part I of the thesis is to develop/extend fast numerical approaches able to provide a complete description of the phononic/locally resonant materials dynamics allowing to investigate both the dispersive and attenuation properties of the materials and to incorporate material energy dissipation.
- The objective of Part II of the thesis is to investigate the possibility of realizing a seismic isolation device based on periodic locally resonant structures able to significantly attenuate the propagation of surface seismic waves.

1.3 ORGANIZATION OF THE THESIS

As above mentioned, the thesis is organized in two parts: Part I and Part II. Part I deals with fast Finite Element based numerical strategies for the calculation of elastic band structures of periodic and locally resonant media and is composed of 3 chapters (from Chapter 2 to Chapter 4). Part II deals with the use of periodic and locally resonant media at the geophysical scale for the attenuation of seismic waves and is composed of 3 chapters (from Chapter 5 to Chapter 7).
Chapter 2 provides an overview of the most relevant numerical strategies for calculating material dispersive properties. An in-depth overview of Finite Element (FE) based approaches for the calculation of complex band structures is also provided.
Chapter 3 proposes an FE-based technique for fast extraction of complex band structures of elastic/viscoelastic periodic/locally resonant media. The method combines a model reduction approach, the Component Mode Synthesis (CMS), with the Wave Finite Element method. The combination of CMS and WFEM, originally developed for speeding up the calculation of real band structures is extended and validated also to calculate the evanescent/complex wave solutions and assess the attenuation properties of the materials.
In Chapter 4 the CMS-WFEM technique is combined with a reduced wave-based description of the dynamics of the periodic/locally resonant media to further speed the complex band structure calculation of periodic waveguides. The numerical technique, originally proposed and discussed for the calculation of propagative waves in two-dimensional periodic systems, is extended to the analysis of highly

damped, evanescent/complex wave solutions in one-dimensional viscoelastic media. Criteria for an appropriate selection of the wave basis to capture both propagative and highly decaying waves are discussed analyzing both uniform structural waveguides and periodic/resonant systems.

In Chapter 5 the use of periodic and locally resonant media and structures for seismic wave attenuation is discussed by critically reviewing the most recent developments in the field. These approaches are presented as alternative solutions to isolation and dissipative devices already available for seismic resistant structures, briefly recalled in the same chapter. The overview aims at highlighting limits and promising aspects of a phononic/metamaterial based approach for earthquake engineering applications and at summarizing the state-of-the-art of this young and growing research field.

Chapter 6 presents the "seismic metabarrier", an innovative isolation device to attenuate the propagation of seismic Rayleigh waves. The metabarrier is a periodic locally resonant structure realized by burying subwavelength meter-size resonant units under the soil surface. An analytical model to guide the design of the metabarrier for varying soil conditions is presented and validated using FE simulations. Moreover, the results of a scaled experimental campaign realized to validate the numerical/analytical predicted ground motion attenuation are presented. The findings are finally discussed on the lights of the simplified assumptions of the analytical/numerical/experimental model.

Chapter 7 discusses the feasibility of the "seismic metabarrier", analyzing the required dimensions and mass to achieve a sensible ground motion attenuation. To minimize the metabarrier dimensions and to broaden the frequency spectrum of attenuation, a multi-mass barrier is proposed. The multi-mass metabarrier is optimized using Genetic Algorithms, which search the resonant unit's design with minimal mass.

Finally, Chapter 8 summarizes the main findings/conclusions of the previous chapters, discuss the ongoing research activity and provides possible directions for future investigations.

Part I

PERIODIC AND LOCALLY RESONANT MEDIA: DISPERSION CURVE FROM FINITE ELEMENT APPROACHES

2

DISPERSION ANALYSIS OF PERIODIC AND LOCALLY RESONANT MEDIA: AN OVERVIEW

ABSTRACT

The objective of this Chapter is to review the available numerical approaches to evaluate the dispersion properties of periodic elastic materials and locally resonant materials. First, the Floquet-Bloch theorem and the elastic band structure concept are recalled as fundamental tools to investigate the dynamic of these media. Then, the most relevant numerical strategies for calculating the elastic band structures are reviewed, highlighting the importance of extracting the full complex band structures to quantify the material attenuation properties. Finally, an in-depth overview of Finite Element approaches for the calculation of complex band structures is provided.

2.1 INTRODUCTION

Applications of phononic materials and resonant metamaterials for wave propagation control have been proposed by exploiting different physical phenomena across different length scales. However, the fundamental dynamics of such materials can be mostly disclosed by investigating their elastic-acoustic band structure. The elastic band structure concept has been derived from the parallel concept of the electronic band structure of electrons in semiconductors. In solid-state physics, the electronic band structure of a solid identifies the energy levels that an electron can possess within the solid. Similarly, the energy bands not allowed are identified, which are called band gaps or forbidden bands. For acoustic/elastic waves pass bands and stop bands can be evaluated by translating the electronic band structure concept to elastodynamics. The band structure of an elastic medium, also referred as dispersion relation, provides all the waves supported by the material, and thus constitute the "map" of its dynamic properties. By engineering the materials constituent/geometry to modify at will their dispersion relations, it is possible to obtain unusual dynamic properties, as the ones possessed by phononic and acoustic metamaterials. In what follows, an overview of the available techniques required to extract elastic band structures is provided.

2.2 BLOCH THEOREM AND BAND STRUCTURE OF PERIODIC AND LOCALLY RESONANT MEDIA

The propagation of elastic waves in any periodic material/structure is governed by the Bloch or Floquet-Bloch theorem, originally applied to the Schrödinger equation

with periodic potential [50]. A detailed explanation of the application of the Bloch theorem in elastodynamics can be found in [50]. Here, for the sake of brevity, only the fundamental statements of the theorem are recalled.
Let us consider a medium, for which the generic property M satisfies the periodic condition:

$$M(\mathbf{x}) = M(\mathbf{x} + \mathbf{Rm}) \tag{1}$$

where $\mathbf{m}$ are integers, and $\mathbf{R} = [\mathbf{r}_1, \mathbf{r}_2, \mathbf{r}_3]$ contains the three lattice vectors $\mathbf{r}_j$, $j = 1, 2, 3$ of the medium (see Fig. 3a). The primitive unit cell belongs to the generic polyhedron in the domain Ω_r (Fig. 3b). The reciprocal unit cell, in the domain Ω_g (Fig. 3c), is defined by the reciprocal lattice vector basis $\mathbf{g}_k$ for which the following relation holds:

$$\mathbf{r}_j \cdot \mathbf{g}_k = 2\pi\delta_{jk} \tag{2}$$

where δ_{jk} is the Kronecker delta.

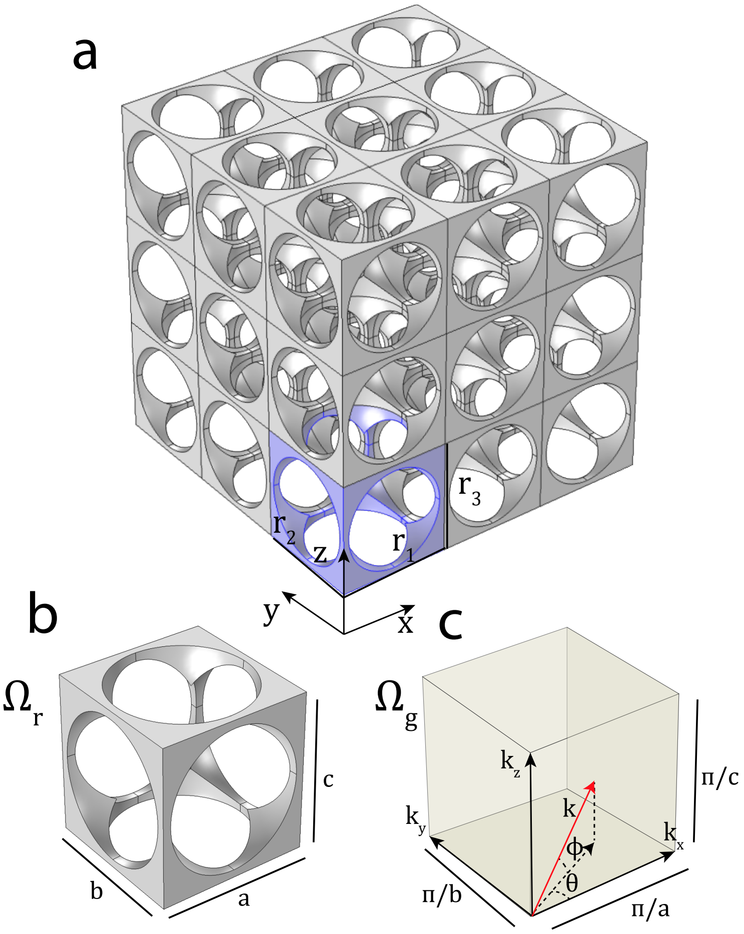

Figure 3: a) Generic 3D periodic media. b) Unit Cell geometry. c) Reciprocal lattice space.

For such periodic media, the Bloch theorem stipulates that any functions $\mathbf{u}(\mathbf{x})$, can be expressed as:

$$\mathbf{u}(\mathbf{x}) = \int_{\Omega_g} \tilde{\mathbf{u}}(\mathbf{k}, \mathbf{x}) e^{i\mathbf{k}\cdot\mathbf{x}} d\mathbf{k} \tag{3}$$

where $\tilde{\mathbf{u}}(\mathbf{k}, \mathbf{x})$ are the Bloch amplitudes, which are periodic in the reciprocal lattice space.

In particular, the theorem states that a solution of an elastic problem defined over a periodic domain Ω_r can be expressed on a basis which is periodic and uniquely identified in the unit cell reciprocal lattice space Ω_g.

Thus, to apply the Bloch theorem one has to identify the unit cell, also referred as Wigner-Seitz cell, which is the minimum portion of the material that possesses all its symmetric properties. Then, from the unit cell, and in particular from its representation in the reciprocal vector space, the range of wave vectors k spanned by the Bloch solution basis, namely the first Brillouin zone, can be identified. Nonetheless, given the symmetric properties in the reciprocal lattice, the wave vectors space can be further restricted to the Irreducible Brillouin Zone (IBZ), where all the wavenumbers are positive. In Fig. 4 two examples of different unit cell reciprocal lattice spaces and Irreducible Brillouin Zones are provided.

Using a basis of Bloch solutions spanning the Irreducible Brillouin Zone (IBZ) the elastic band structure can be calculated. Indeed, a more concise description of the elastic band structure can be provided by spanning only the contour of the IBZ where the band extrema almost always occur [23]. The band extrema are of interest as they allow to identify the stop bands (band gaps) where elastic/acoustic waves cannot propagate freely. In the following section, the elastic band structure of a simple 1D spring-mass system is calculated to clarify the application of the Bloch theorem.

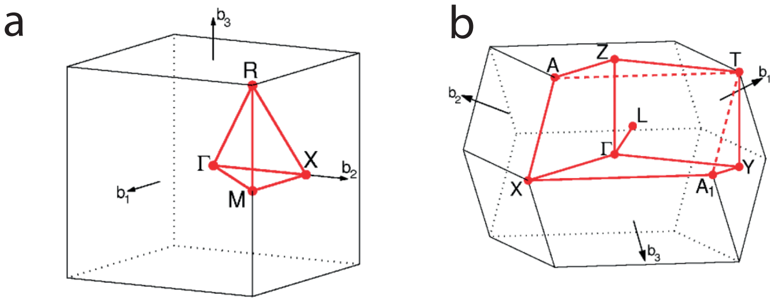

Figure 4: a) First Brillouin zone of cubic lattice unit cell. b) First Brillouin zone of an orthorhombic lattice unit cell. In red the boundaries of the Irreducible Brillouin Zone. (From Ref. [51]).

2.3 ELASTIC BAND STRUCTURE: REAL $\omega(k)$ VS. COMPLEX $k(\omega)$ APPROACH

To quickly explain the concept of elastic band structure, the simplest case of a one-dimensional spring-mass system, originally described in [5] is here reviewed. The spring-mass system is composed of a chain of masses m interacting each other by springs of stiffness $\tilde{k}$ (see Fig. 5a).The system has a lattice distance (i.e. unit cell length) a and first Brilloiun Zone $k=[-\frac{\pi}{a}\ \frac{\pi}{a}]$ (see Fig. 5b). The IBZ, which covers only positive wavenumber, is $k=[0\ \frac{\pi}{a}]$.

A Bloch form of the displacement is assumed to derive the spring-mass system band structure; in particular, the displacement of the n^{th} mass takes the form:

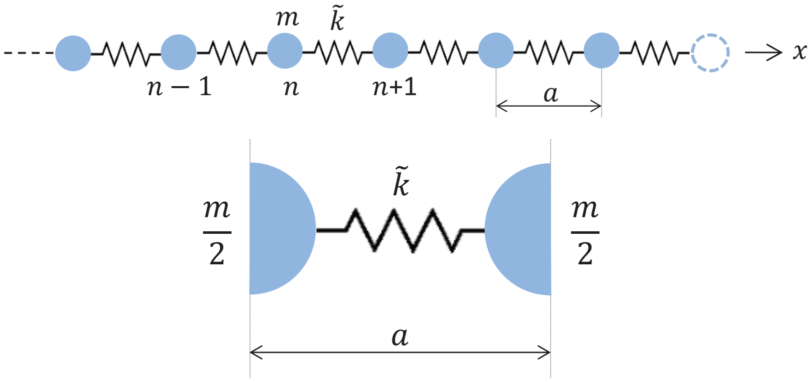

Figure 5: a) Discrete mass-spring chain. b) Mass-spring unit cell.

$$u_n(t) = \tilde{u}(k(\omega))e^{i(kx_n-\omega t)} \tag{4}$$

where x_n is the coordinate of the generic n^{th} mass and ω is the wave angular frequency.

The characteristic equation of the system, which is obtained by evaluating the chain's dynamic equilibrium with the Bloch form of the displacement in Eq. 4, reads:

$$[-\omega^2 m + 2\tilde{k} - \tilde{k}(e^{ika} + e^{-ika})] = 0 \tag{5}$$

Equation 5 has the form of a Bloch eigenvalue problem whose solution provides the elastic band structure of the system. The real elastic band structure $\omega(k)$ is extracted by feeding the characteristic equation in Eq. 5 with real wavenumber k within the IBZ. In doing so, all the propagative waves supported by the medium are identified. Nonetheless, the same equation can be solved by providing real angular frequency ω as input and extracting complex wavenumber $k = k_r + ik_i$ as output. In this case, purely propagating, attenuated and evanescent waves are found [52, 53]. The wave spatial attenuation is provided by the imaginary component k_i of the wavenumber. The $k(\omega)$ approach is fundamental when the filtering properties and the evanescent wave field of a periodic medium are of interest as well as when material energy dissipation is accounted, which inevitably leads to attenuated solutions within all the IBZ. In Fig. 6 the band structures of a linear elastic and two viscoelastic (Kelvin-Voigt (KV) and Standard Linear Solid (SLS) model), mass-spring system are reported as an example.

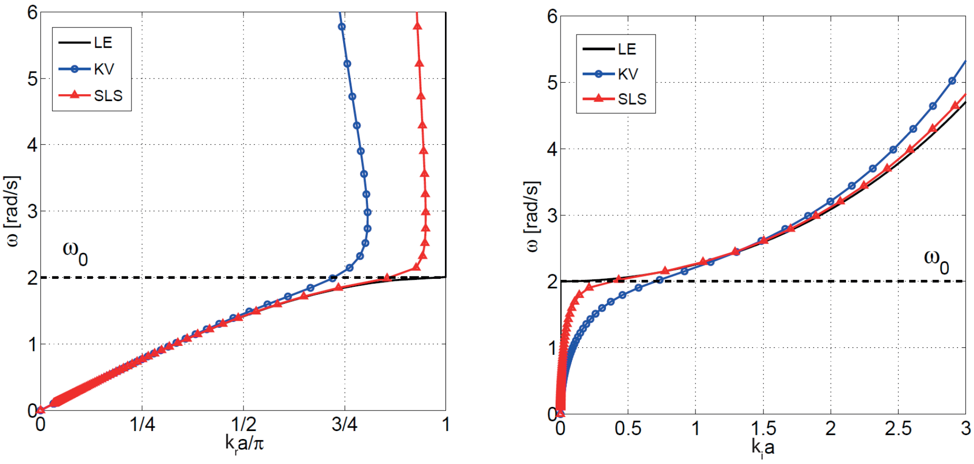

Figure 6: a) Complex band structure curves of a LE, a KV and a SLS mass-spring chain.

For the LE case, propagative solutions ($k_i = 0$, $k_r \neq 0$) are found within the IBZ below the frequency ω_0 which marks the starting point of the mass-spring band gap. No propagative waves are found within the band gap, where only evanescent solutions exist, found using the inverse approach. Similarly, when material damping is accounted (Kelvin-Voigt (KV) and Standard Linear Solid (SLS) model), all the solutions are characterized by a non-zero spatial attenuation which can be determined only using the inverse approach.

2.4 COMPUTATIONAL METHOD FOR ELASTIC BAND STRUCTURE CALCULATION

Different computational techniques exist for the calculation of periodic media band structures, developed both in the context of solid-state physics and material science for phononic crystals and acoustic metamaterial analysis. Nonetheless, further numerical techniques have also been developed in the context of structural engineering for the evaluation of the dynamics of periodic structures. Among others, the Plane Wave Expansion (PWE) technique, and the Finite Element (FE) method are the most adopted for solving periodic elastic problems. Here, a short description of the Plane Wave Expansion (PWE) technique is presented, together with a more detailed review on Finite Element based approaches, which are later applied and extended in Chapts. 3 and 4.

2.4.1 *Plane-Wave Expansion Method*

The Plane-Wave expansion technique is based on the projection of the unknown displacement solution field and the known material properties of the periodic media on a Fourier basis. By exploiting the orthogonality of such basis functions, the solution field is found by solving each orthogonal equation independently for the unknown Fourier solution coefficients. The method has been widely used for the analysis of acoustic and elastic composites [8, 9, 54, 55]. The methodology can be briefly illustrated using the example of a continuous one-dimensional periodic medium, as in [4]. For this system the governing periodic equilibrium equation reads:

$$\rho\frac{\partial^2 u}{\partial t^2} = \frac{\partial}{\partial x}\left(\rho c^2 \frac{\partial u}{\partial x}\right) \tag{6}$$

where $u(x,t)$ denotes the displacement field, $\rho(x)$ the density, and $c(x)$ the speed of sound through the media. The material properties $\rho(x)$ and $c(x)$ vary periodically with period a, such that the generic lattice vector $\mathbf{R_m}$ and the related reciprocal lattice vector $\mathbf{G_m}$ read:

$$\mathbf{R_m} = m \cdot a\mathbf{x} \quad \mathbf{G_m} = \frac{m}{a\mathbf{x}} \tag{7}$$

where $\mathbf{x}$ denotes a unit vector and m is a generic integer.
According to the PWE method, the following Fourier expansions are introduced:

$$\begin{aligned} u(x,t) &= e^{i(\mathbf{k}\cdot\mathbf{r}-\omega t)} \sum_{\mathbf{G_l}} u_k(\mathbf{G_l}) e^{(i\mathbf{G_l}\cdot\mathbf{r})} \\ \rho(x) &= \sum_{\mathbf{G_m}} \rho(\mathbf{G_m}) e^{i\mathbf{G_m}\cdot\mathbf{r}} \\ \rho(x)c^2(x) &= \sum_{\mathbf{G_m}} \tau(\mathbf{G_m}) e^{i\mathbf{G_m}\cdot\mathbf{r}} \end{aligned} \tag{8}$$

where $\mathbf{r}$ denotes position, $\mathbf{k}$ denotes the wavevector, ω the angular frequency and $\sum_{\mathbf{G_i}}$ the sum over all the reciprocal lattice space vectors. It is remarked that the displacement solution embodies the Bloch theorem. The expansions introduce the transformed density $\rho(\mathbf{G_m})$ and the transformed stiffness $\tau(\mathbf{G_m})$, as well as the transformed displacements $u_k(\mathbf{G_l})$.
Substituting the expansions into Eq. 6 leads:

$$\sum_{\mathbf{G_l}} [-\omega^2\rho(\mathbf{G_n}-\mathbf{G_l}) + (k+\mathbf{G_l})(k+\mathbf{G_n})\tau(\mathbf{G_n}+\mathbf{G_l}]u_k(\mathbf{G_l}) = 0 \tag{9}$$

The only nonzero terms in the inner product are those satisfying $\mathbf{G_l}+\mathbf{G_m}-\mathbf{G_n}=0$ leading to the condensing of the summation over $\mathbf{G_m}$. By truncating the expansions for $\mathbf{G_l}$, and evaluating Eq. 9 for a similarly truncated set of $\mathbf{G_n}$, a well-posed Bloch

eigenvalue problem in the eigenfrequencies $\omega(k)$ is defined. The band structure is then obtained by sampling the wavenumber k in the Irreducible Brillouin Zone and extracting the related angular frequency ω.
An extension to the original PWE method, namely the Extended Plane Wave Expansion, has been proposed to the calculation of the complex band structure [55]. The method projects the sought wavefield over a basis of solutions with unknown complex wavenumber $k = k_r + k_i$, extracted along the analyzed direction of wave propagation. The approach has been used to investigate the nature and feature of the evanescent field within the frequency band gap as well as to address the effect of viscoelasticity on the material dispersion properties [55, 56],.

2.4.2 *Finite Element based techniques*

The Finite Element method is a standard numerical technique to solve PDEs arising from elasticity problems. Its wide application is related to the possibility of modeling complex geometry and material rheology with relative effort. For this reason, FE methodologies have also been adopted also in the context of periodic media, with the aim of evaluating elastic band structures by analyzing the dynamic equilibrium of the material unit cell. The construction of the Bloch eigenvalue problem needed for calculating the material band structure can be achieved following two different strategies based on a FE discretization. One of the approach undertakes a Bloch operator transformation of the governing differential equation, builds its weak form and discretizes it over the unit cell domain using finite elements [50, 57, 58]. The second one applies directly Bloch boundary conditions to the unit cell mass and stiffness matrices with proper defined Bloch operators. In this latter approach, referred in literature also as Wave Finite Element Method (WFEM) [19, 20], only the mass and stiffness matrices of the unit cell, typically found using commercial FE packages, are needed, requiring minimum code implementation. In both methodologies, the obtained Bloch eigenvalue problems can be solved by seeking unknown frequencies ω for given real wave numbers k_r, providing the real band structure, or conversely, by seeking complex wave numbers $k = k_r + ik_i$, for given real frequencies ω as input, leading to the full complex band structure. In what follows, a review of the FE Bloch operator transformation approach and the WFEM approach is given, detailing the required strategy to obtain both real $\omega(k)$ and complex $k(\omega)$ band structures.

2.5 REVIEW OF BLOCH OPERATOR TRANSFORMATION APPROACH

In this section, the Bloch operator transformation approach required to define the eigenvalue problem for periodic continuous media is reviewed, following the formalism presented by Collet et al. in Ref. [50].

2.5.1 *Strong formulation of the elastic Bloch eigenvalue problem*

Let us consider a generic infinite periodic elastic medium as the one in Fig. 3, for which the dynamic equilibrium equation reads:

$$\rho(\mathbf{x})\omega^2\mathbf{u}(\mathbf{x}) + \nabla\mathbf{C}\nabla^S\mathbf{u}(\mathbf{x}) = 0 \qquad \mathbf{x} \in \mathbf{R}^3 \tag{10}$$

with $\rho(\mathbf{x})$ the mass density, ω the angular frequency, $\mathbf{C}$ the elastic tensor and $\mathbf{u}(\mathbf{x})$ the displacement vector. Bloch solutions of the elastic problem in Eq. 10 defined over the unit cell domain Ω_r are sought in the form:

$$\mathbf{u}(\mathbf{x}) = \mathbf{u}_{n,k}(\mathbf{x},\mathbf{k})e^{i\mathbf{kx}} \tag{11}$$

where $\mathbf{u}_{n,k}(\mathbf{x},\mathbf{k})$ are periodic in the unit cell domain. Substitution of Eq. 11 in Eq. 10, leads to the generalized eigenvalues problem :

$$\begin{aligned}\rho(\mathbf{x})\omega_n^2(\mathbf{k})\ \mathbf{u}_{n,k}(\mathbf{x}) + \nabla\mathbf{C}\nabla^S\mathbf{u}_{n,k} - i\mathbf{C}\nabla^S\mathbf{u}_{n,k}\cdot\mathbf{k}\\ -i\nabla\mathbf{C}\frac{1}{2}(\mathbf{u}_{n,k}(\mathbf{x})\cdot\mathbf{k}^T + \mathbf{k}\cdot\mathbf{u}_{n,k}(\mathbf{x})^T)\\ +\mathbf{C}\frac{1}{2}(\mathbf{u}_{n,k}(\mathbf{x})\cdot\mathbf{k}^T + \mathbf{k}\cdot\mathbf{u}_{n,k}(\mathbf{x})^T)\cdot\mathbf{k} = 0\end{aligned} \tag{12}$$

for which symmetrical boundary conditions defined on the boundary faces of the unit cell hold:

$$\mathbf{u}_{n,k}(\mathbf{x} - \mathbf{R}\cdot\mathbf{n}) - \mathbf{u}_{n,k}(\mathbf{x}) = 0 \tag{13}$$

The Bloch eigenproblem in Eq. 12 has the form of a complex Quadratic Eigenvalue Problem (QEP) in the variables ω and $\mathbf{k}$. Thus, it has to be solved either by fixing ω and the complex amplitude $|k|$, or ω and the cosine directions of $\mathbf{k}$ (see Fig. 3b):

$$\mathbf{k} = |k|\boldsymbol{\Phi} = |k|\begin{bmatrix}\cos\theta\cos\phi\\ \cos\theta\sin\phi\\ \sin\theta\end{bmatrix} \tag{14}$$

From the eigenproblem strong formulation, an easier numerical implementation can be achieved by first obtaining its weak formulation and then discretizing it with a standard FE approach.

2.5.1.1 *Weak formulation and FE discretization*

The weak form of the generalized eigenproblem is obtained by projecting Eq. 12 onto a Bloch periodic test function $\tilde{\mathbf{u}}_{n,k}(\mathbf{x})$ defined over the unit cell domain, and integrating the projection over the same domain (see Ref.[50] for the details). The numerical implementation is then obtained by using a standard FE discretization resulting in the set of equations:

$$[\mathbf{K} + \lambda\mathbf{L}(\boldsymbol{\Phi}) - \lambda^2\mathbf{H}(\boldsymbol{\Phi}) - \omega_n^2(\lambda,\boldsymbol{\Phi})\mathbf{M}]\mathbf{u}_{n,k}(\boldsymbol{\Phi}) = \mathbf{0} \tag{15}$$

where:

$$
\begin{aligned}
\mathbf{K} &= \int_{\Omega} \boldsymbol{\epsilon}_{n,k}(\mathbf{x})\mathbf{C}(\mathbf{x})\tilde{\boldsymbol{\epsilon}}_{n,k}(\mathbf{x})\partial\Omega \\
\mathbf{M} &= \int_{\Omega} \rho(\mathbf{x})\mathbf{u}_{n,k}(\mathbf{x})\tilde{\mathbf{u}}_{n,k}(\mathbf{x})\partial\Omega \\
\mathbf{L} &= \int_{\Omega} -\tilde{\boldsymbol{\kappa}}_{n,k}(\mathbf{x})\mathbf{C}(\mathbf{x})\boldsymbol{\epsilon}_{n,k}(\mathbf{x}) + \tilde{\boldsymbol{\epsilon}}_{n,k}(\mathbf{x})\mathbf{C}(\mathbf{x})\boldsymbol{\kappa}_{n,k}(\mathbf{x})\partial\Omega \\
\mathbf{H} &= \int_{\Omega} \tilde{\boldsymbol{\kappa}}_{n,k}(\mathbf{x})\mathbf{C}(\mathbf{x})\boldsymbol{\kappa}_{n,k}(\mathbf{x})\partial\Omega
\end{aligned}
\tag{16}
$$

where $\lambda = ik$, $\boldsymbol{\epsilon}_{n,k}(\mathbf{x})$ is the strain tensor, $\boldsymbol{\kappa}_{n,k}(\mathbf{x})$ the symmetric dyadic product of the displacement $\mathbf{u}_{n,k}(\mathbf{x})$ and the direction vector Φ, **M** and **K** are respectively the standard mass and stiffness matrices, **L** is a skew-symmetric matrix and **H** is a symmetric semi-definite positive matrix.
By sampling the system in Eq. 15 with given wavevectors, i.e. given $|k|$ and $\boldsymbol{\Phi}$ in the unit cell first Brillouin zone, a linear eigenvalue problem is obtained which allows computing the real dispersion functions ωk and the associated Bloch eigenvector $\mathbf{u}_{n,k}$ of the periodic system.
Conversely, rearranging the generalized eigenvalue problem as:

$$[(\mathbf{K} - \omega^2\mathbf{M}) - \lambda(\omega, \Phi)\mathbf{L})(\Phi) - \lambda^2(\omega, \Phi)\mathbf{H}(\Phi)]\mathbf{u}_{n,k}(\boldsymbol{\Phi}) = \mathbf{0} \tag{17}$$

for given real frequency ω and the wave direction angle Φ, the wavenumbers λ_n = ik_n and associated Floquet vectors $\mathbf{u}_{n,k}$ are computed. Such approach allows the calculation of the complex dispersion curve along any direction, ensuring the collinearity between imaginary and real part of the wave vector (i.e. the attenuation is collinear with the direction of propagation). The approach also allows the introduction of generalized damping terms to account for dissipation in materials. However, further numerical processing is required to restrict the obtained solutions within the IBZ.

2.6 REVIEW OF WAVE FINITE ELEMENT METHOD

The application and refinement of Wave Finite Element methodologies for the analysis of periodic materials and structures is a topic of great interest, as demonstrated by the continuous research effort devoted to this field in the recent years [4, 17]. Indeed, the Wave finite element methodology is a simple but useful tool to calculate the dispersion and attenuation properties of periodic media as well as of uniform waveguides, considered as the limiting case of a periodic assembly. For such reasons the method has been used for multiple applications, from simple one-dimensional systems [52] to complex 2D periodic media [23, 59] and structural systems [19, 20, 60]. In what follows, the WFEM is reviewed for the extraction of real band structure and attenuation dispersive properties in one-dimensional and two-dimensional elastic (and viscoelastic) periodic systems.

2.6.1 *Wave Finite Element Method for 1D periodic waveguides*

The starting point of the WFE procedure is the identification of the waveguide unit cell, obtained by cutting a portion of the waveguide of length L along its longitudinal axis x, to which correspond an IBZ $k = [0 \quad \pi/L]$. The unit cell is then meshed with a standard FE software ensuring an identical discretization at the left and right boundaries of the cell, later required for one-to-one mapping of the boundary nodes (see Fig. 7).

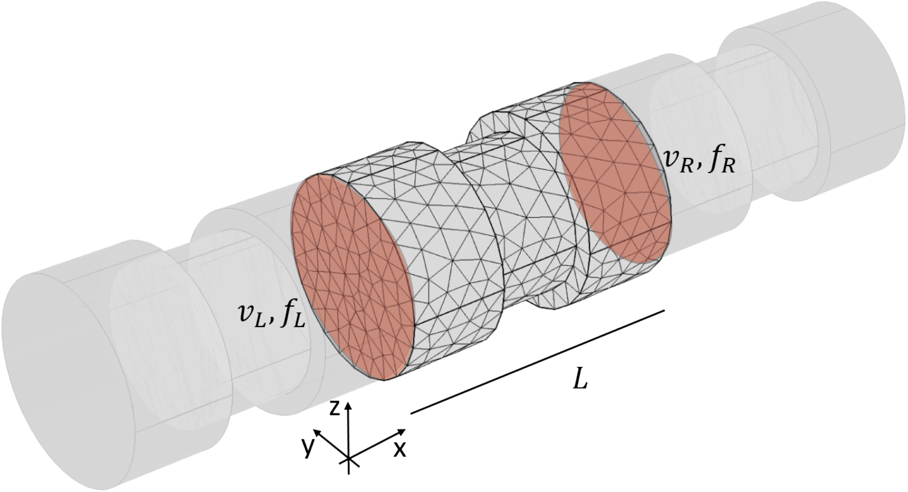

Figure 7: Generic 1D waveguide unit cell.

Energy dissipation in the material can be accounted by means of linear viscoelasticity. The beauty of linear viscoelasticity is that, in force of the correspondence principle, it can be introduced by simply replacing the linear elastic coefficients with their corresponding linear viscoelastic [61]. The approach is here detailed for a hysteretic frequency independent viscoelastic material but applies for any linear frequency dependent rheological models.

Standard FE assembly procedure leads to the definition of the unit cell equation of motion:

$$(\mathbf{K} - \omega^2 \mathbf{M})\mathbf{v} = \mathbf{f} \tag{18}$$

with $\mathbf{K} = \mathbf{K_r} - i\mathbf{K_i}$ and $\mathbf{M}$ the complex stiffness matrix and the mass matrix, respectively, $\mathbf{v}$ the vector of nodal displacements and $\mathbf{f}$ the vector of nodal forces. By introducing the subsets of nodal degree-of-freedoms (DOFs) belonging to the left (L) edge of the unit cell, the right (R) edge of the unit cell and the interior (i) DOFs, the discrete operators in the unit cell equation of motion can be partitioned as follows:

$$\left(\begin{bmatrix} \mathbf{K}_{LL} & \mathbf{K}_{LR} & \mathbf{K}_{Li} \\ \mathbf{K}_{RL} & \mathbf{K}_{RR} & \mathbf{K}_{Ri} \\ \mathbf{K}_{iL} & \mathbf{K}_{iR} & \mathbf{K}_{ii} \end{bmatrix} - \omega^2 \begin{bmatrix} \mathbf{M}_{LL} & \mathbf{M}_{LR} & \mathbf{M}_{Li} \\ \mathbf{M}_{RL} & \mathbf{M}_{RR} & \mathbf{M}_{Ri} \\ \mathbf{M}_{iL} & \mathbf{M}_{iR} & \mathbf{M}_{ii} \end{bmatrix}\right) \begin{bmatrix} \mathbf{v}_L \\ \mathbf{v}_R \\ \mathbf{v}_i \end{bmatrix} = \begin{bmatrix} \mathbf{f}_L \\ \mathbf{f}_R \\ \mathbf{0} \end{bmatrix} \tag{19}$$

where no external forces on the interior nodal DOFs have been considered. The equation can be further simplified introducing the dynamic stiffness matrix $\mathbf{D} = \mathbf{K} - \omega^2\mathbf{M}$ of the unit cell:

$$\begin{bmatrix} \mathbf{D}_{LL} & \mathbf{D}_{LR} & \mathbf{D}_{Li} \\ \mathbf{D}_{RL} & \mathbf{D}_{RR} & \mathbf{D}_{Ri} \\ \mathbf{D}_{iL} & \mathbf{D}_{iR} & \mathbf{D}_{ii} \end{bmatrix} \begin{bmatrix} \mathbf{v}_L \\ \mathbf{v}_R \\ \mathbf{v}_i \end{bmatrix} = \begin{bmatrix} \mathbf{f}_L \\ \mathbf{f}_R \\ \mathbf{0} \end{bmatrix} \tag{20}$$

For free waves propagating along the waveguide, displacements and forces at successive cross sections can be related as:

$$\begin{bmatrix} \mathbf{v}_R \\ \mathbf{f}_R \end{bmatrix} = \lambda \begin{bmatrix} \mathbf{v}_L \\ \mathbf{f}_L \end{bmatrix} \tag{21}$$

where $\lambda = e^{ikL}$ is the Floquet-Bloch propagator and $k = k_r + ik_i$ the complex wavenumber.

The Floquet-Bloch boundary operators $\boldsymbol{\Lambda}$ and $\overline{\boldsymbol{\Lambda}}$ can be introduced, respectively, to impose the periodicity of the displacements along successive cross sections $\mathbf{v} = \boldsymbol{\Lambda}\mathbf{v}_{red}$ [52]:

$$\begin{bmatrix} \mathbf{v}_L \\ \mathbf{v}_R \\ \mathbf{v}_i \end{bmatrix} = \begin{bmatrix} \mathbf{I}_L & \mathbf{0} \\ \mathbf{I}_L\lambda & \mathbf{0} \\ \mathbf{0} & \mathbf{I}_i \end{bmatrix} \begin{bmatrix} \mathbf{v}_L \\ \mathbf{v}_i \end{bmatrix} \tag{22}$$

and to enforce the equilibrium of the unit cell $\overline{\boldsymbol{\Lambda}}^T \mathbf{f} = \mathbf{0}$:

$$\begin{bmatrix} \mathbf{I}_L & \mathbf{I}_L\lambda^{-1} & \mathbf{0} \\ \mathbf{0} & \mathbf{0} & \mathbf{I}_i \end{bmatrix} \begin{bmatrix} \mathbf{f}_L \\ \mathbf{f}_R \\ \mathbf{0} \end{bmatrix} = \begin{bmatrix} \mathbf{0} \\ \mathbf{0} \\ \mathbf{0} \end{bmatrix} \tag{23}$$

where the reduced set of nodal displacements $\mathbf{v}_{red}$ reads:

$$\mathbf{v}_{red} = \begin{bmatrix} \mathbf{v}_L \\ \mathbf{v}_i \end{bmatrix} \tag{24}$$

In both the operators $\boldsymbol{\Lambda}$ and $\overline{\boldsymbol{\Lambda}}$ the identity matrices $\mathbf{I}_L$ and $\mathbf{I}_i$ have dimension $(n_L \times n_L)$ and $(n_i \times n_i)$, respectively. Pre- and post-multiplying the unit cell equation of motion with the Bloch boundary operators $\overline{\boldsymbol{\Lambda}}^T$ and $\boldsymbol{\Lambda}$, leads to eigenvalue problem:

$$\overline{\boldsymbol{\Lambda}}^T(\lambda^{-1})\mathbf{D}(\omega)\boldsymbol{\Lambda}(\lambda)\mathbf{v}_{red} = \mathbf{0} \tag{25}$$

The Bloch eigenvalue problem in Eq. (25) is a function of two parameters, namely the angular frequency ω and the Floquet-Bloch propagator λ. If the Floquet-Bloch propagator λ is specified (i.e. if a real wavevector k is given as input), all the eigenfrequency solutions corresponding to the propagative waves supported by the periodic media are found. Conversely, when harmonic solutions are sought, the eigenvalue problem is solved by providing real frequencies ω as input. In that case, the eigenvalue problem in Eq. 25 is rearranged in the quadratic form:

$$\left[\mathbf{D}_0 + \lambda \mathbf{D}_1 + \lambda^2 \mathbf{D}_2\right] \mathbf{v}_{red} = \mathbf{0} \tag{26}$$

where:

$$\mathbf{D}_0 = \begin{bmatrix} \mathbf{D}_{RL} & \mathbf{D}_{Ri} \\ \mathbf{0} & \mathbf{0} \end{bmatrix} \quad \mathbf{D}_1 = \begin{bmatrix} \mathbf{D}_{LL} + \mathbf{D}_{RR} & \mathbf{D}_{Li} \\ \mathbf{D}_{iL} & \mathbf{D}_{ii} \end{bmatrix} \quad \mathbf{D}_2 = \begin{bmatrix} \mathbf{D}_{LR} & \mathbf{0} \\ \mathbf{D}_{iR} & \mathbf{0} \end{bmatrix} \tag{27}$$

The solution of the eigenproblem for different frequencies ω provides the waveguide complex dispersion relation $k(\omega)$.
Similar results can be obtained following the approach detailed by Mace et al. [19] where the definition of the unit cell transfer matrix $\mathbf{T}$ is required:

$$\mathbf{T} = \begin{bmatrix} -\tilde{\mathbf{D}}_{LR}^{-1} \tilde{\mathbf{D}}_{LL} & -\tilde{\mathbf{D}}_{LR}^{-1} \\ -\tilde{\mathbf{D}}_{RL} + \tilde{\mathbf{D}}_{RR} \tilde{\mathbf{D}}_{LR}^{-1} \tilde{\mathbf{D}}_{LL} & -\tilde{\mathbf{D}}_{RR} \tilde{\mathbf{D}}_{LR}^{-1} \end{bmatrix} \tag{28}$$

with:

$$\begin{aligned} \tilde{\mathbf{D}}_{LL} &= \mathbf{D}_{LL} - \mathbf{D}_{Li} \mathbf{D}_{ii}^{-1} \mathbf{D}_{iL} \quad & \tilde{\mathbf{D}}_{LR} &= \mathbf{D}_{LR} - \mathbf{D}_{Li} \mathbf{D}_{ii}^{-1} \mathbf{D}_{iR} \\ \tilde{\mathbf{D}}_{RL} &= \mathbf{D}_{RL} - \mathbf{D}_{Ri} \mathbf{D}_{ii}^{-1} \mathbf{D}_{iL} \quad & \tilde{\mathbf{D}}_{RR} &= \mathbf{D}_{RR} - \mathbf{D}_{Ri} \mathbf{D}_{ii}^{-1} \mathbf{D}_{iR} \end{aligned} \tag{29}$$

In this case, the complex dispersion relation $k(\omega)$ is obtained by solving the eigenproblem:

$$\mathbf{T} \begin{bmatrix} \mathbf{v}_L \\ \mathbf{f}_L \end{bmatrix} = \lambda \begin{bmatrix} \mathbf{v}_L \\ \mathbf{f}_L \end{bmatrix} \tag{30}$$

2.6.2 *Wave Finite Element Method for 2D periodic waveguides*

Similarly to the 1D case, a two-dimensional periodic media is considered by tessellating the generic unit cell of Fig. 8a along x and y directions. The unit cell dimensions along x, y, and z axes are a, b and h; the rectangular reciprocal lattice space (in gray) and the Irreducible Brillouin Zone (in blue), whose boundaries are marked by the high-symmetry corner positions Γ-X-M, are shown in Fig. 8b.
The unit cell equation of motion, as obtained from a standard Finite Element approach, reads:

$$[\mathbf{K} - \omega^2 \mathbf{M}]\mathbf{v} = \mathbf{D}(\omega)\mathbf{v} = \mathbf{0} \tag{31}$$

where $\mathbf{K}$ is the stiffness matrix of the unit cell (eventually complex if a viscoelastic material is considered), $\mathbf{M}$ is the mass matrix, $\mathbf{D}(\omega)$ the dynamic matrix and $\mathbf{v}$ the

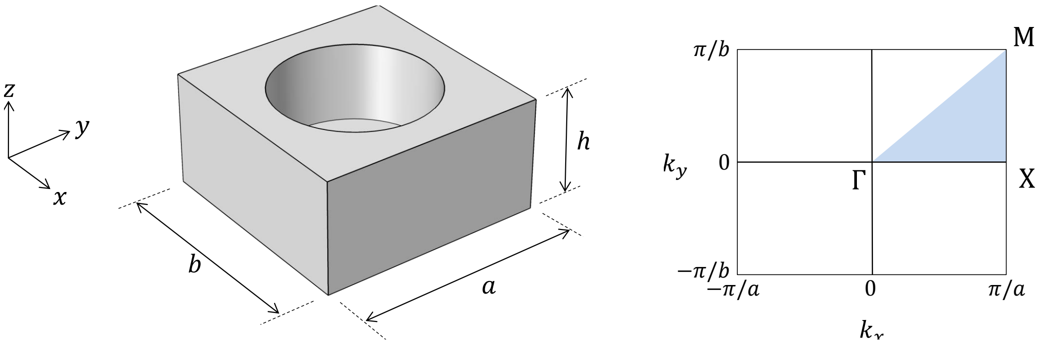

Figure 8: a) Unit cell geometry and b) Unit cell Brillouin Zone.

vector of unit cell nodal displacements. Floquet-Bloch periodicity is introduced by applying Bloch boundary conditions (BBCs) along x and y directions. As for the 1D waveguide, the imposition of BBCs requires a proper discretization of the unit cell boundaries, such that a one-to-one correspondence between boundary nodes can be established. As such, a convenient arrangement of the unit cell nodal displacements and of the dynamic stiffness matrix is given according to the node numbering of Fig. 9 as:

$$\mathbf{v} = \begin{bmatrix} \mathbf{v}_i \\ \mathbf{v}_{b_1} \\ \mathbf{v}_{b_2} \\ \mathbf{v}_{b_3} \\ \mathbf{v}_{b_4} \\ \mathbf{v}_{b_5} \\ \mathbf{v}_{b_6} \\ \mathbf{v}_{b_7} \\ \mathbf{v}_{b_8} \end{bmatrix} \qquad \mathbf{D} = \begin{bmatrix} \mathbf{D}_{ii} & \cdots & \mathbf{D}_{ib_8} \\ \vdots & \ddots & \vdots \\ \mathbf{D}_{b_8 i} & \cdots & \mathbf{D}_{b_8 b_8} \end{bmatrix} \tag{32}$$

where the vector $\mathbf{v}_i$ retains the n_i internal dofs of the unit cell; vectors $\mathbf{v}_{b1}$ and $\mathbf{v}_{b4}$ retain, respectively, the n_{b1} and n_{b4} boundaries dofs of nodes at $[0 < x < a, y = 0, 0 \leqslant z \leqslant h]$ and $[0 < x < a, y = b, 0 \leqslant z \leqslant h]$; vectors $\mathbf{v}_{b2}$ and $\mathbf{v}_{b5}$ the n_{b2} and n_{b5} boundary dofs of nodes at $[x = 0, 0 < y < b, 0 \leqslant z \leqslant h]$ and $[x = a, 0 < y < b, 0 \leqslant z \leqslant h]$, respectively, whereas vectors $\mathbf{v}_{b3}$, $\mathbf{v}_{b6}$, $\mathbf{v}_{b7}$ and $\mathbf{v}_{b8}$ retain the $n_{b3} = n_{b6} = n_{b7} = n_{b8}$ corner boundary dofs with coordinates $[x = 0, y = 0, 0 \leqslant z \leqslant h]$, $[x = a, y = 0, 0 \leqslant z \leqslant h]$, $[x = 0, y = b, 0 \leqslant z \leqslant h]$ and $[x = a, y = b, 0 \leqslant z \leqslant h]$, respectively. It follows that the BBCs can be imposed

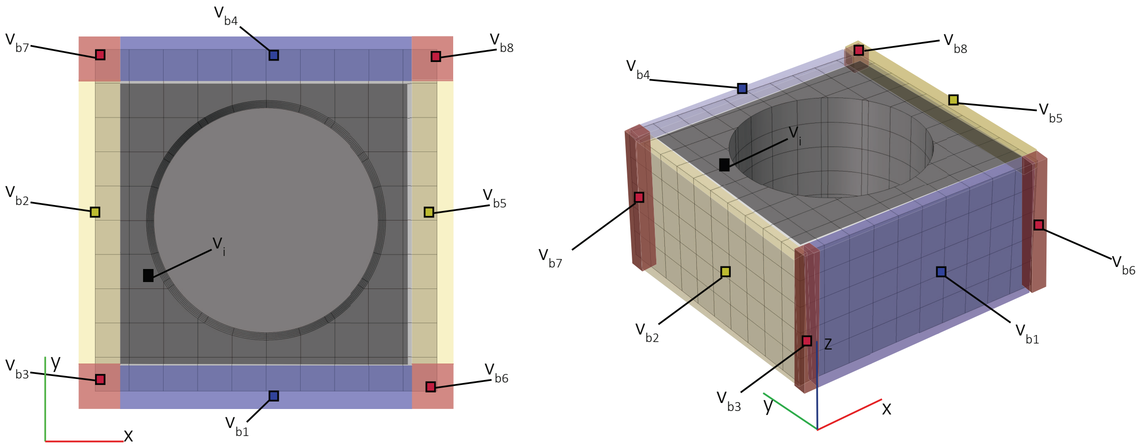

Figure 9: Unit cell node numbering.

with the following relationships:

$$\mathbf{v} = \begin{bmatrix} \mathbf{v}_i \\ \mathbf{v}_{b_1} \\ \mathbf{v}_{b_2} \\ \mathbf{v}_{b_3} \\ \mathbf{v}_{b_4} \\ \mathbf{v}_{b_5} \\ \mathbf{v}_{b_6} \\ \mathbf{v}_{b_7} \\ \mathbf{v}_{b_8} \end{bmatrix} = \begin{bmatrix} \mathbf{v}_i \\ \mathbf{v}_{b_1} \\ \mathbf{v}_{b_2} \\ \mathbf{v}_{b_3} \\ \mathbf{v}_{b_1}\lambda_y \\ \mathbf{v}_{b_2}\lambda_x \\ \mathbf{v}_{b_3}\lambda_x \\ \mathbf{v}_{b_3}\lambda_y \\ \mathbf{v}_{b_3}\lambda_x\lambda_y \end{bmatrix} \tag{33}$$

where $\lambda_x = e^{ik_x a}$, $\lambda_y = e^{ik_y b}$ are the Floquet-Bloch multipliers in which $k_x = k_{x,r} + ik_{x,i}$ and $k_y = k_{y,r} + ik_{y,i}$ are the complex wavenumber components along x and y directions, respectively. Equations (33) can be rearranged in the operatorial form:

$$\mathbf{v} = \mathbf{\Lambda}(\lambda_x, \lambda_y)\mathbf{v}_{red} = \begin{bmatrix} \mathbf{I}_i & 0 & 0 & 0 \\ 0 & \mathbf{I}_{b_1} & 0 & 0 \\ 0 & 0 & \mathbf{I}_{b_2} & 0 \\ 0 & 0 & 0 & \mathbf{I}_{b_3} \\ 0 & \mathbf{I}_{b_1}\lambda_y & 0 & 0 \\ 0 & 0 & \mathbf{I}_{b_2}\lambda_x & 0 \\ 0 & 0 & 0 & \mathbf{I}_{b_3}\lambda_x \\ 0 & 0 & 0 & \mathbf{I}_{b_3}\lambda_y \\ 0 & 0 & 0 & \mathbf{I}_{b_3}\lambda_x\lambda_y \end{bmatrix} \begin{bmatrix} \mathbf{v}_i \\ \mathbf{v}_{b_1} \\ \mathbf{v}_{b_2} \\ \mathbf{v}_{b_3} \end{bmatrix} \tag{34}$$

where $\boldsymbol{\Lambda}$ is the Floquet-Bloch boundary operator, that reduces the unit cell nodal displacements to the set $\mathbf{v}_{red}$. In $\boldsymbol{\Lambda}$, the identity matrix $\mathbf{I}_j$ has dimension (n_j, n_j), with j=i, b_1, b_2, b_3. Substituting λ_x and λ_y in $\boldsymbol{\Lambda}$ with λ_x^{-1} and λ_y^{-1}, respectively, the linear operator $\overline{\boldsymbol{\Lambda}}$ is obtained, whose transpose $\overline{\boldsymbol{\Lambda}}^T$, reads:

$$\overline{\boldsymbol{\Lambda}}^T(\lambda_x, \lambda_y) = \begin{bmatrix} \mathbf{I}_i & 0 & 0 & 0 & 0 & 0 & 0 & 0 & 0 \\ 0 & \mathbf{I}_{b_1} & 0 & 0 & \mathbf{I}_{b_1}\lambda_y^{-1} & 0 & 0 & 0 & 0 \\ 0 & 0 & \mathbf{I}_{b_2} & 0 & 0 & \mathbf{I}_{b_2}\lambda_x^{-1} & 0 & 0 & 0 \\ 0 & 0 & 0 & \mathbf{I}_{b_3} & 0 & 0 & \mathbf{I}_{b_3}\lambda_x^{-1} & \mathbf{I}_{b_3}\lambda_y^{-1} & \mathbf{I}_{b_3}\lambda_x^{-1}\lambda_y^{-1} \end{bmatrix} \tag{35}$$

At this stage, the Bloch eigenvalue problem for the infinite periodic media is obtained by pre- and post-multiplying Eq. (31) with the Floquet-Bloch boundary operators $\overline{\boldsymbol{\Lambda}}^T$ and $\boldsymbol{\Lambda}$, respectively:

$$\overline{\boldsymbol{\Lambda}}^T(\lambda_x^{-1}, \lambda_y^{-1})\mathbf{D}(\omega)\boldsymbol{\Lambda}(\lambda_x, \lambda_y)\mathbf{v}_{red} = \mathbf{0} \tag{36}$$

The Bloch eigenvalue problem in Eq. (36) appears as a function of three parameters, namely the angular frequency ω and the two Floquet-Bloch propagators λ_x, λ_y (and thus k_x and k_y) so that two sets of parameters need to be specified to solve it. Moreover, different eigenvalue problems are obtained depending on the nature of the assumed solutions. When harmonic solutions are sought, the eigenvalue problem is solved by providing real frequencies ω as input and specifying either the direction or one of the wavenumber vector components. In particular, when the direction $\mu = \frac{\lambda_y}{\lambda_x}$ is specified, either a polynomial or a transcendental eigenproblem is obtained, depending if μ assumes a rational or irrational value, respectively [20]. Whereas, if one of the wavevector component k_x, k_y is specified, a quadratic eigenvalue problem is obtained. For phononic materials, a compact representation of the wave properties is provided by seeking eigensolutions along the boundaries Γ-X-M of the IBZ. In some cases this compact representation is not sufficient to capture the extension of bandgap for phononic structures [62]. However, it is undoubtedly the most effective and used representation in the literature [4], and therefore it will be adopted in the following Chapters.
Along the Γ-X direction the wavevector component $k_y = 0$, i.e. $\lambda_y = 1$, and the resulting eigenproblem:

$$\overline{\boldsymbol{\Lambda}}^T(\lambda_x^{-1})\mathbf{D}(\omega)\boldsymbol{\Lambda}(\lambda_x)\mathbf{v}_{red} = \mathbf{0} \tag{37}$$

can be rearranged in the following quadratic form:

$$[\mathbf{D}_{0x}(\omega) + \mathbf{D}_{1x}(\omega)\lambda_x + \mathbf{D}_{2x}(\omega)\lambda_x^2]\mathbf{v}_{red} = \mathbf{0} \tag{38}$$

Along the X-M direction, where the wavevector components $k_x = \pi/a$, with $\lambda_x = -1$, the eigenvalue problem takes the form:

$$\overline{\boldsymbol{\Lambda}}^T(\lambda_y^{-1})\mathbf{D}(\omega)\boldsymbol{\Lambda}(\lambda_y)\mathbf{v}_{red} = \mathbf{0} \tag{39}$$

and leads to the quadratic eigenproblem:

$$[\mathbf{D}_{0y}(\omega) + \mathbf{D}_{1y}(\omega)\lambda_y + \mathbf{D}_{2y}(\omega)\lambda_y^2]\mathbf{v}_{red} = \mathbf{0} \tag{40}$$

Finally, along the M-Γ direction the normalized wavevector components $k_x a = k_y b$, i.e. $\lambda_x = \lambda_y = \lambda$ and the eigenvalue problem:

$$\overline{\boldsymbol{\Lambda}}^{T}(\lambda^{-1})\mathbf{D}(\omega)\boldsymbol{\Lambda}(\lambda)\mathbf{v}_{red} = \mathbf{0} \tag{41}$$

can be rearranged in the quartic form:

$$[\mathbf{D}_0(\omega) + \mathbf{D}_1(\omega)\lambda + \mathbf{D}_2(\omega)\lambda^2 + \mathbf{D}_3(\omega)\lambda^3 + \mathbf{D}_4(\omega)\lambda^4]\mathbf{v}_{red} = \mathbf{0} \tag{42}$$

Solutions of quadratic and quartic Bloch type eigenvalue problems of Eqs. (38), (42) and (40) are tackled by linearization, leading respectively to standard eigenproblem with $2n$ and $4n$ equations, being n the total number of dofs of the unit cell ($n = n_{b1} + .. + n_{b8}$). Details on the matrices $\mathbf{D}_i$ and on the adopted linearization schemes are provided in Appendix A.

Questions have been raised about the validity of the WFEM approach along X-M direction for dissipative systems due to the losing of collinearity between attenuation and direction of propagation (i.e $k_{xr} = \pi/a k_{xi} = 0$, $k_{yr} \neq 0 k_{yi} \neq 0$) [58]. Nevertheless, the analysis of these solutions along X-M direction has still significance in the context of forced harmonic problem as they represent known wave incident on the x straight boundary so that the real trace of the wavenumber k_x is given and all possible solutions for k_y are sought [20] .

2.7 CONCLUSION

In this Chapter a review of the elastic band structure concept and the available numerical techniques for its calculation has been provided. For all the discussed methodologies, the band structure is calculated analyzing the dynamic of the material unit-cell and assuming a periodic form of the unknown solution, by the Floquet-Bloch theorem. The approach results in a Bloch eigenvalue problem which relates the frequency ω and the wavenumber k of the elastic vibrations supported by the medium. When propagative waves are sought the eigenproblem is solved giving real wavenumber k_r within the IBZ and calculating the frequencies of the propagative solutions. However, a richer information can be accessed solving the Bloch eigenvalue problem for known frequencies and extracting complex wavenumber $k = k_r + k_i$ which identify both propagative and evanescent waves. Knowledge of the wave spatial decay $k_i(\omega)$ has great importance for understanding the filtering properties of periodic and locally resonant media as well as for investigating energy dissipation induced by material damping.

Different numerical techniques allow the solution of Bloch eigenproblem for both propagative and highly decaying waves: the PWE technique is an intuitive methodology for band structure calculation but its application in the elastodynamic problems is limited due to convergence issues [63] and required coding for implementation. Similarly, the FE based Bloch transformation approach is a versatile method to calculate complex band structure but again limited in application due to the required coding. The WFEM approach, instead, is largely diffused given its easiness in implementation and the possibility of use in commercial FE software. However, when 2D (or 3D) periodic systems are investigated, large higher order eigenproblems are found, which limit the applicability of the WFEM for the analysis of complex phononic/locally resonant materials. For such problems, model reduction techniques able to lower the computational requirements for the unit cell modeling can be highly beneficial, as it will be shown in the next Chapters.

3

A CMS REDUCTION TECHNIQUE FOR COMPLEX BAND STRUCTURES CALCULATION

ABSTRACT

This Chapter[1] proposes and validates an efficient numerical technique, based on the combination of the Component Mode Synthesis (CMS) and Wave Finite Element method, for fast calculation of complex band structures of elastic/viscoelastic periodic media. The combination of CMS and WFEM, originally presented as Bloch Mode Synthesis for speeding up the calculation of real band structures, is here extended to evaluate also evanescent/complex wave solutions by solving a $k(\omega)$ *Bloch eigenvalue problem. The* $k(\omega)$ *Bloch eigenvalue problem is setup up by means of the Wave Finite Element and is reduced in dimensions by means of the Component Mode Synthesis approach. The Component Mode Synthesis is based on the Craig Bampton model reduction technique which substitutes the unit cell interior degree-of-freedoms with a reduced number of modal coordinates. The methodology performance in terms of band structure accuracy and computational saving are demonstrated on one-dimensional and two-dimensional periodic structures. It is shown that the computational time required to extract complex band structures can be reduced up to two orders of magnitudes from the initial full model computational time with negligible errors for both real and evanescent/complex solutions.*

3.1 INTRODUCTION

The calculation of periodic media band structures is a demanding computational process as it requires the solution of large eigenvalue problems at multiple locations (wavenumbers k for an $\omega(k)$ approach, frequencies ω for the related $k(\omega)$ approach). Therefore, numerical strategies for speeding up band structure calculations are highly desirable and widely investigated in the literature. Among the others, techniques based on the use of fast iterative solvers have been proposed for both phononic and photonic applications [66–68]. Multiscale finite elements have been used to extract dispersion curves of 2D phononic crystals [69, 70] and homogenization techniques based on multiscale methodologies have been proposed to analyze periodic heterogeneous media [71, 72]. Within the context of FE-based techniques, an intuitive way to reduce the band structure computational demand is to perform a model reduction of the unit cell domain. Model reduction techniques have been originally developed and applied in the context of structural dynamics. For example, in the simple static Guyan reduction [73] technique, the internal dofs of a system are removed by static condensation. Similarly, when steady-state waves are sought using a WFEM approach, a dynamic condensation of the interior dofs can be performed to reduce the dimensions of the eigenvalue problem [19] (refer to Chapt. 2 sect. 2.6.1). However, this step requires a computational effort comparable to the eigensolution of the full system. On the other hand, different model reduction strategies can be followed to lower the band structure computational effort effectively. In particular, two distinct classes of approaches can be applied when FE solutions of an elastic periodic media are sought. One class of method is based on a reduced description of the non-periodic dynamic equilibrium equation of the system and is derived from the Component Mode Synthesis (CMS) technique [74], used in structural dynamics to obtain reduced models of complex dynamic systems. The second class of method relies on a wave-based reduction to scale the dimensions of the Bloch eigenproblem using a proper set of wave shapes extracted at either selected wave vector positions [57] or selected frequencies [75]. In this Chapter, the first class of model reduction technique is investigated and extended for the calculation of elastic and viscoelastic complex band structures; wave-based model reduction techniques will be discussed in Chapt. 4.

---

[1] The results presented in this Chapter are largely based on two recent works published by the author [64, 65]

Several variations of the CMS technique exist, all of them based on an initial subdivision of the FE domain in subdomains and on a reduced description of each subsystem. The whole domain is then reassembled by coupling the reduced representations of the different subdomains, leading to a smaller size model of the initial structure. For a periodic medium the subdomain is constituted by the unit cell itself, while the full domain is simply reconstructed using periodic boundary conditions, within the framework of the WFEM. Among the possible model reduced description available for the CMS technique, the Craig Bampton (CB) reduction [74] is particularly suitable for periodic domains. In the CB technique the internal dofs of each subsystem are substituted by constrained modes while the boundary dofs are left untouched for the application of periodic boundary conditions.

The combination of a WFEM approach with a CMS-Craig Bampton reduction has been originally proposed by Krattiger et al. [76], under the name of Bloch Mode Synthesis (BMS), for 2D periodic elastic waveguides and later recalled by Zhou et al. [77], for 1D periodic waveguides and 2D periodic waveguides [78]. In both Ref. [76] and Ref. [77] the CMS approach has been used to investigate only propagative waves in undamped 2D periodic media, utilizing a reduced $\omega(k)$ approach. Conversely in Ref. [77] the methodology has been applied to investigate both propagative and evanescent wave solutions of elastic one-dimensional periodic waveguides, by means of a reduced $k(\omega)$ approach.

Here, the CMS-WFEM approach is first extended and validated for one-dimensional periodic viscoelastic waveguides. To this aim, both standard uniform waveguides and periodic waveguides are analyzed, focusing on the evaluation of the accuracy of the method in the calculation of the dispersive attenuation $k_i(\omega)$. Next, the CMS-WFEM approach for 2D periodic media, i.e. the Bloch Mode Synthesis, is extended to extract the complex band structure $k(\omega)$ of two-dimensional periodic waveguides, leading to the original formulation of the Extended Bloch Mode Synthesis. The numerical tool is validated discussing its accuracy and computational cost. Nonetheless, an in-depth analysis of the complex band structure of a periodic stubbed plate is conducted, to highlight the rich dynamic of periodic system accessible by means of a $k(\omega)$ approach.

3.2 CMS WFEM FOR ONE-DIMENSIONAL PERIODIC WAVEGUIDE

The Component Mode Synthesis is here combined with a WFEM approach for fast extraction of complex dispersion curves in viscoelastic 1D periodic waveguides. To this aim, let us reconsider the unit cell of the generic 1D waveguide previously presented in Chapt. 2, here schematically shown in Fig. 10a. The displacement vector $\mathbf{v}$ of the FE discretized unit cell can be partitioned in internal i (nodes in blue) and boundary b (nodes in red) displacement vectors (see Fig. 10b):

$$\mathbf{v} = \begin{bmatrix} \mathbf{v}_i \\ \mathbf{v}_b \end{bmatrix} \quad \text{with} \quad \mathbf{v}_b = \begin{bmatrix} \mathbf{v}_L \\ \mathbf{v}_R \end{bmatrix} \tag{43}$$

Accordingly, the complex stiffness matrix $\mathbf{K}$, obtained assuming an hysteretic material damping model, and the mass matrix $\mathbf{M}$, both resulting from a standard FE discretization of the unit cell domain, are partitioned in the sub-matrices:

$$\mathbf{K} = \begin{bmatrix} \mathbf{K}_{ii} & \mathbf{K}_{ib} \\ \mathbf{K}_{ib} & \mathbf{K}_{bb} \end{bmatrix} \qquad \mathbf{M} = \begin{bmatrix} \mathbf{M}_{ii} & \mathbf{M}_{ib} \\ \mathbf{M}_{ib} & \mathbf{M}_{bb} \end{bmatrix} \tag{44}$$

At this stage, the Craig Bampton transformation operator $\mathbf{T}_{CB}$ is introduced as:

$$\mathbf{v} = \mathbf{T}_{CB}\mathbf{v}_{CB} \qquad \begin{bmatrix} \mathbf{v}_i \\ \mathbf{v}_b \end{bmatrix} = \begin{bmatrix} \mathbf{\Phi}_i & \mathbf{\Psi}_{ib} \\ \mathbf{0} & \mathbf{I} \end{bmatrix} \begin{bmatrix} \boldsymbol{\eta} \\ \mathbf{v}_b \end{bmatrix} \tag{45}$$

where $\mathbf{\Phi}_i$ is a set of n_{fi} fixed-interface modes (see Fig. 10c), i.e. the eigenvectors ϕ_i associated to the first smallest n_{fi} eigenfrequencies of the eigen problem:

$$[\mathbf{K}_{ii} - \omega^2 \mathbf{M}_{ii}]\phi_i = \mathbf{0} \tag{46}$$

and $\mathbf{\Psi}_{ib} = -\mathbf{K}_{ii}^{-1}\mathbf{K}_{ib}$ is the set of constrained boundary modes (see Fig. 10c), i.e. static deformations of the system resulting from the application of a unit displacement to one boundary dof, with all other boundary dofs restrained.

As such, the interior nodes are substituted by a reduced number $n_{fi} << n_i$ of modal coordinates $\boldsymbol{\eta}$, while boundary displacements $\mathbf{v}_b$ are left untouched. Accordingly, the CB reduced stiffness $\mathbf{K}_{CB}$ and mass matrix $\mathbf{M}_{CB}$ are obtained as:

$$\mathbf{K}_{CB} = \mathbf{T}_{CB}^T \mathbf{K} \mathbf{T}_{CB} \qquad \mathbf{M}_{CB} = \mathbf{T}_{CB}^T \mathbf{M} \mathbf{T}_{CB} \tag{47}$$

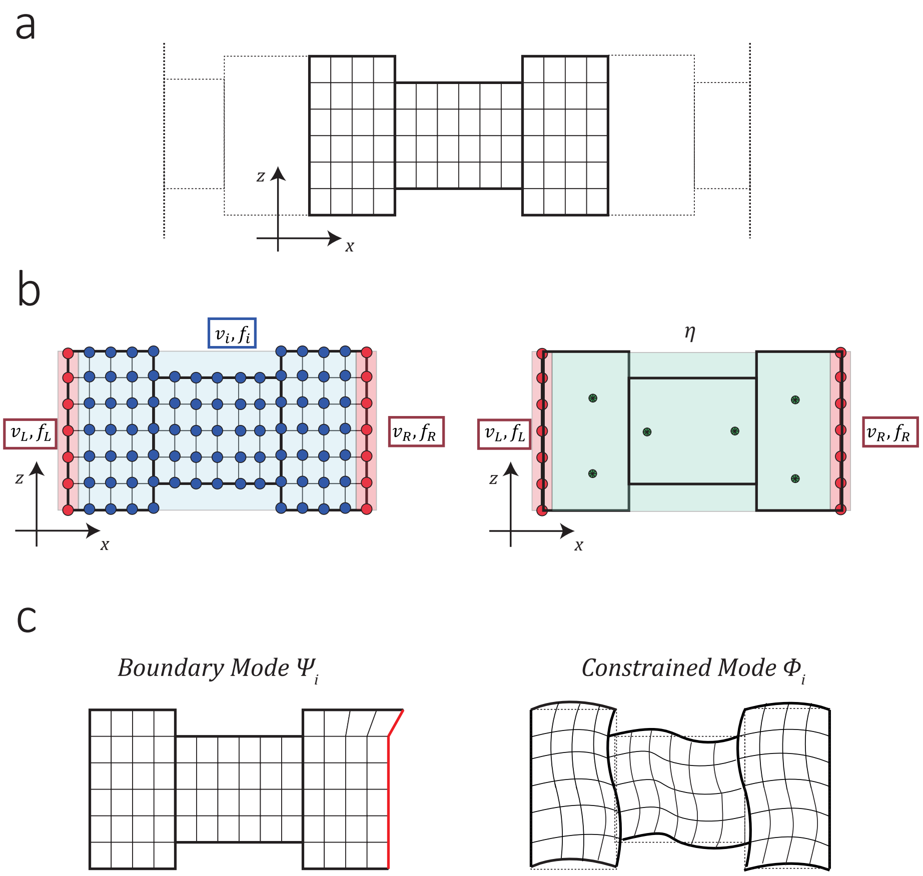

Figure 10: a) Schematic of the generic 1D waveguide unit cell. b).1) Unit cell node partition .2) Modal reduced unit cell description. c) Schematic of boundary and constrained modes.

and from the reduced operators $\mathbf{K}_{\mathrm{CB}}$ and $\mathbf{M}_{\mathrm{CB}}$, the reduced dynamic stiffness matrix is assembled as:

$$\mathbf{D}_{\mathrm{CB}} = \mathbf{K}_{\mathrm{CB}} - \omega^2 \mathbf{M}_{\mathrm{CB}} \quad \mathbf{D}_{\mathrm{CB}} = \begin{bmatrix} \mathbf{D}_{\mathrm{LL}} & \mathbf{D}_{\mathrm{LR}} & \mathbf{D}_{\mathrm{Lfi}} \\ \mathbf{D}_{\mathrm{RL}} & \mathbf{D}_{\mathrm{RR}} & \mathbf{D}_{\mathrm{Rfi}} \\ \mathbf{D}_{\mathrm{fiL}} & \mathbf{D}_{\mathrm{fiR}} & \mathbf{D}_{\mathrm{fifi}} \end{bmatrix} \tag{48}$$

The reduced Bloch operators $\boldsymbol{\Lambda}_{\mathrm{CB}}$ and $\overline{\boldsymbol{\Lambda}}^{\mathrm{T}}_{\mathrm{CB}}$ can be obtained from the related full operators $\boldsymbol{\Lambda}$ and $\overline{\boldsymbol{\Lambda}}^{\mathrm{T}}$ in Eqs. 22,23 by replacing the identity operator $\mathbf{I}_i$ with $\mathbf{I}_{f_i}$, i.e. an identity operator with n_{fi} x n_{fi} elements:

$$\boldsymbol{\Lambda}_{\mathrm{CB}} = \begin{bmatrix} \mathbf{I}_{\mathrm{L}} & \mathbf{0} \\ \mathbf{I}_{\mathrm{L}}\lambda & \mathbf{0} \\ \mathbf{0} & \mathbf{I}_{\mathrm{fi}} \end{bmatrix} \qquad \overline{\boldsymbol{\Lambda}}^{\mathrm{T}}_{\mathrm{CB}} = \begin{bmatrix} \mathbf{I}_{\mathrm{L}} & \mathbf{I}_{\mathrm{L}}\lambda^{-1} & \mathbf{0} \\ \mathbf{0} & \mathbf{0} & \mathbf{I}_{\mathrm{fi}} \end{bmatrix} \tag{49}$$

Pre-and post-multiplying the reduced dynamic stiffness matrix $\mathbf{D}_{CB}$ by the reduced Bloch operators $\overline{\boldsymbol{\Lambda}}_{CB}^{T}$ and $\boldsymbol{\Lambda}_{CB}$, respectively, leads to a reduced Bloch eigenvalue problem as:

$$\overline{\boldsymbol{\Lambda}}_{CB}^{T}(\lambda^{-1})\mathbf{D}_{CB}(\omega)\boldsymbol{\Lambda}_{CB}(\lambda)\mathbf{v}_{red,CB} = \mathbf{0} \quad \text{with} \quad \mathbf{v}_{red,CB} = \begin{bmatrix} \mathbf{v}_L \\ \boldsymbol{\eta} \end{bmatrix} \tag{50}$$

As for a standard WFEM approach, the resulting Bloch eigenvalue problem is a function of the angular frequency ω and the Floquet-Bloch propagator λ. For a viscoelastic waveguide, when the interest is to assess the dispersive attenuation properties $k_i(\omega)$ of the waveguide, the eigenvalue problem should be solved by providing real frequencies ω. Thus, the eigenproblem is rearranged in the quadratic form:

$$\left[\mathbf{D}_{0,CB} + \lambda\mathbf{D}_{1,CB} + \lambda^2\mathbf{D}_{2,CB}\right]\mathbf{v}_{red,CB} = \mathbf{0} \tag{51}$$

where:

$$\begin{aligned} \mathbf{D}_{0,CB} &= \begin{bmatrix} \mathbf{D}_{RL} & \mathbf{D}_{Rfi} \\ \mathbf{0} & \mathbf{0} \end{bmatrix} \\ \mathbf{D}_{1,CB} &= \begin{bmatrix} \mathbf{D}_{LL} + \mathbf{D}_{RR} & \mathbf{D}_{Lfi} \\ \mathbf{D}_{fiL} & \mathbf{D}_{fifi} \end{bmatrix} \\ \mathbf{D}_{2,CB} &= \begin{bmatrix} \mathbf{D}_{LR} & \mathbf{0} \\ \mathbf{D}_{fiR} & \mathbf{0} \end{bmatrix} \end{aligned} \tag{52}$$

The solution of the reduced eigenvalue problem of Eq. (51) at the given frequency steps ω_i provides the waveguide complex dispersion curve.

3.2.1 *Numerical applications*

3.2.1.1 *Octagonal steel bar*

The proposed framework is applied to compute the real dispersion $k_r(\omega)$ and attenuation curves $k_i(\omega)$ of an octagonal steel bar, whose mechanical properties are given in Table 1. To this aim, a finite length bar with octagonal cross-section has been modeled in COMSOL® (see Fig. 11a). The length of the bar is taken equal to $L = 0.0075$ m to map real wavenumbers k_r in the IBZ up to $\pi/a = 418.88$ [1/m]. The material bulk speeds and attenuation are given in Table 1. The complex Young's modulus E^* and the complex Poisson ratio ν^* required for the FE formulation are easily derived from these parameters using the relationship given in [79].

The unit cell of the octagonal bar is meshed using 4064 tetrahedral elements with

Table 1: Mechanical parameters of the octagonal steel bar.

Material	ρ [kg/m^3]	c_L [m/s]	c_T [m/s]	α_L [Np/λ]	α_T [Np/λ]
Steel	7800	5960	3190	0.003	0.043

10 nodes per element for a total of 17739 dofs (with 486 boundary dofs), which ensures at least 10 nodes along the direction of propagation for the smallest wavelength $\lambda = L/2$, as suggested in [20].

The complex dispersion curves are extracted in the frequency range $0 - f_{max} = 180$ kHz with a frequency step $\Delta f = 1$kHz. At each frequency value, the quadratic eigenvalue problem is linearized and subsequently solved by using the SPTARN Matlab eigensolver. This iterative solver allows seeking for the eigenvalues of the pencil $(\mathbf{A} - \lambda \mathbf{B})\, \mathbf{x} = \mathbf{0}$ with a real part in the interval $[-1, 1]$ and closest to the real axis. It is based on the Arnoldi method with spectral transformation where the shift is randomly chosen in the defined interval. The algorithm allows defining the number of Arnoldi runs, typically chosen as large as the maximum multiplicity of any eigenvalue. This criterion should ensure no missing roots. Direct solvers, which naturally ensure that all the eigensolutions are extracted, could also be used. The choice between iterative or direct solvers is a trade-off between computational resources and dimension of the problem. Here, an iterative solver is used in order to deal with the dimensions of the full model, as its number of dofs is prohibitive for a direct solver.

The dispersion curves are provided in terms of phase velocity $c_{ph} = \omega / k_r$ and attenuation k_i; the representation in terms of phase velocity c_{ph} is a standard for uniform waveguides where no frequency gaps are expected. The complex dispersion curves of the octagonal bar, computed for the full model (17739 dofs) and for a CB reduced model with 80 fixed interface modes (for a total of $486 + 80 = 566$ boundary-modal coordinates), are represented in Fig. 11c and Fig. 11d, respectively. Damped wave solutions with $k_i > 2$ are filtered out. As far as the number of fixed interface modes is concerned, Zhou et al. [78] suggest retaining all the fixed-interface modes with a frequency of vibration $f_{mode} \leqslant 3 f_{max}$, where f_{max} is the maximum frequency at which real band solutions are calculated. This selection criterion, which ensures accurate solutions for elastic waveguide, is here applied for the analysed viscoelastic waveguide, resulting in 80 fixed interface modes.

The full and reduced curves are validated with those obtained using a semi analytical finite element (SAFE) formulation, similar to that proposed in Ref. [79]. The SAFE mesh, represented in Fig. 11b, is built using linear strain triangular elements with the nodes of the tetrahedral elements belonging to the cross-section surface of the 3D unit cell mesh in Fig. 11a. As it can be noted, for both the full and reduced model the phase velocity $c_{ph}(\omega)$ and attenuation $k_i(\omega)$ curves perfectly match with those computed by using a SAFE scheme (Fig. 11c,b).

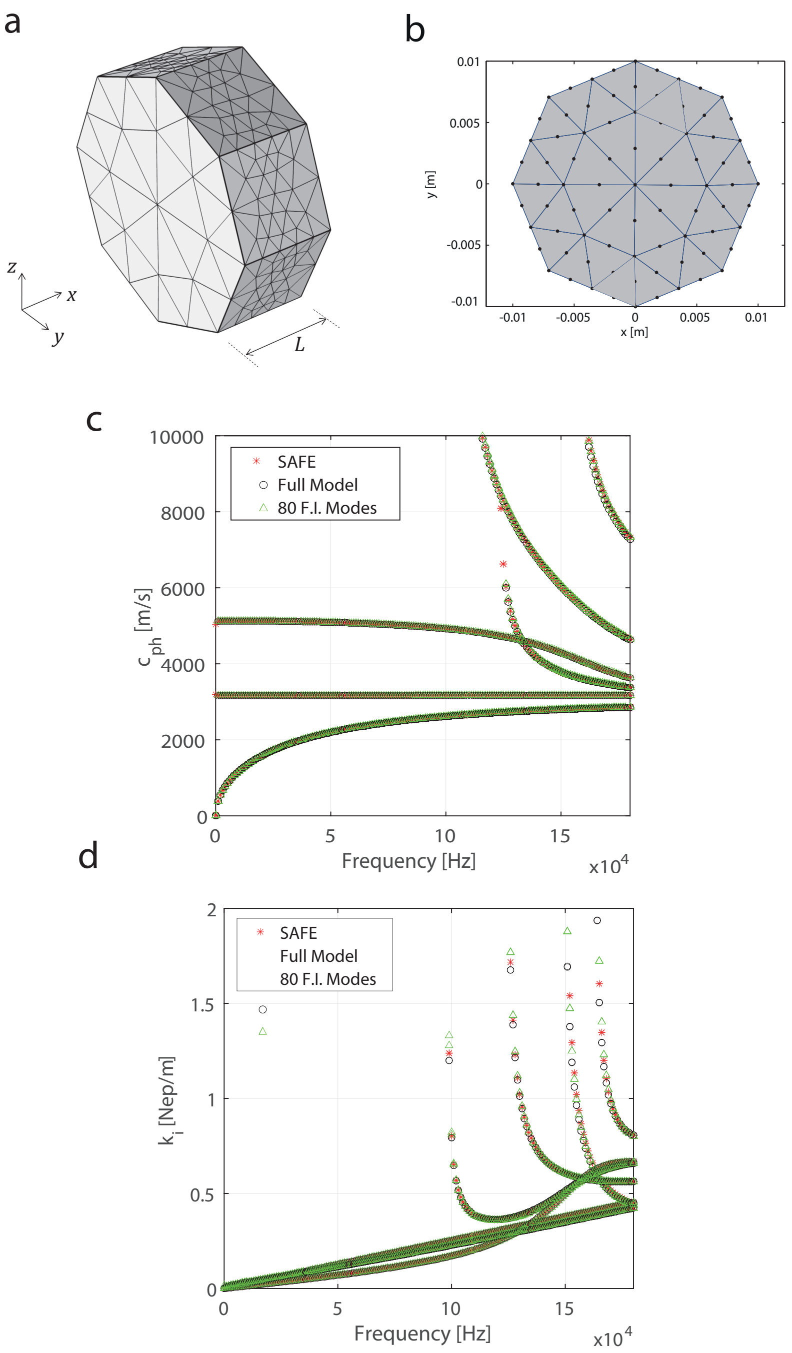

Figure 11: a) Mesh of the finite length portion of the octagonal waveguide built in COMSOL. b) Cross-section mesh used in the SAFE formulation. c) Phase velocity and d) attenuation dispersion curves.

As regards to the computational time saving, the performance of the reduction technique is measured by calculating the time fraction defined as [76]:

$$T_{fr} = \frac{t^{RED}}{t^{FULL}} = \frac{t_{CB} + n_{\omega} t_{\omega}^{RED}}{n_{\omega} t_{\omega}^{FULL}} \tag{53}$$

where t^{RED} and t^{FULL} are the computational times for the reduced and full-dof band structures, respectively, t_{CB} is the computational time needed to computed the reduced $\mathbf{K}_{CB}$ and $\mathbf{M}_{CB}$ matrices, t_{ω}^{RED} and t_{ω}^{FULL} are the computational times required to solve the reduced and full eigenproblems at the given frequency ω_i, respectively, and n_{ω} is the number of frequency steps at which the band structures are evaluated.

The reduced model with 80 fixed interface modes requires just the 1.9% of the full model computational time, with an error in the real and imaginary wavenumber component prediction below the 2% (see details in Table 2). The error in real and imaginary wavenumber components are calculated as:

$$\text{err.}_{k_r} = \max\left|\frac{k_{j,r}^{RED} - k_{j,r}^{FULL}}{k_{j,r}^{FULL}}\right| \qquad \text{err}_{k_{Im}} = \max\left|\frac{k_{j,i}^{RED} - k_{j,i}^{FULL}}{k_{j,i}^{FULL}}\right| \tag{54}$$

where $k_{j,r(i)}$ is the real (imaginary) wavenumber component of the j branch intercepted at the given frequency ω. Higher accuracy can be easily achieved by enriching the basis of the CB reduction. For example, considering 500 fixed interface modes the error in the prediction of both imaginary and real wavenumber components can be reduced below 0.2% with a small increase in the required computational time (i.e. 5% of the full model computational time). The accuracy of the method shows a clear frequency dependence, with lower frequencies characterized by smaller errors as shown in Fig.12a and Fig.12b. This trend is consistent with the criteria used for the modes selection.

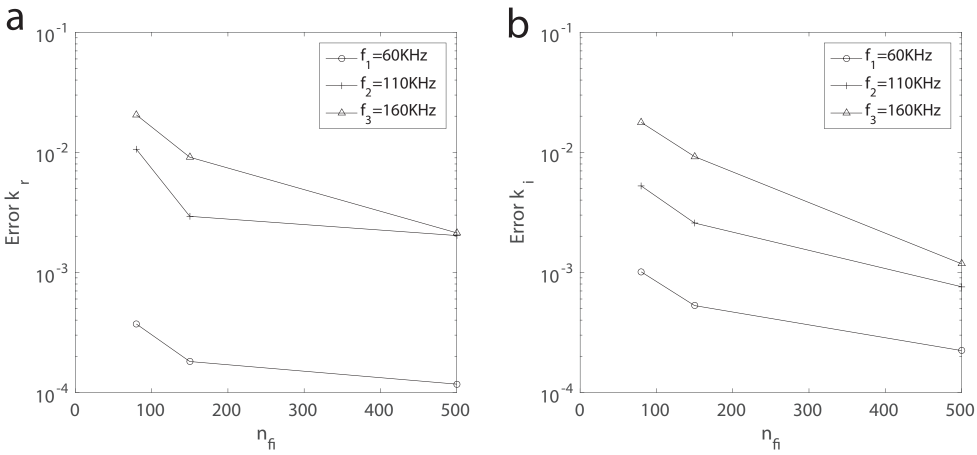

Figure 12: a) Error real wavenumber prediction k_r vs. number of fixed-interface mode n_{fi}. b) Error imaginary wavenumber prediction k_i vs. number of fixed-interface mode n_{fi}.

Table 2: Octagonal beam: Computational time vs. accuracy.

	Computational time [s]			Max Error [@160kHz]	
—	CMS Reduction	EVP Solution (1 step)	$\frac{\mathrm{timeF.I}}{\mathrm{timeF.M}}$ (180 steps)	err. k_{Re}	err. k_{Im}
Full Model (FM)	-	77 s	-		
80 F.I. modes	140 s	0.8 s	1.9 %	2 %	1.8 %
150 F.I. modes	161 s	1 s	2.3 %	0.9 %	0.9 %
500 F.I. modes	326 s	2.7 s	5.5 %	0.2 %	0.1 %

3.2.1.2 *Periodic stubbed beam*

The CMS-WFEM reduction technique is here applied to compute the complex band structure of an aluminum periodic beam with squared pillars, depicted in Fig. 13, whose real dispersion curve has been numerically and experimentally investigated in Ref. [80]. The elastic constants and mass density used in the FE simulations are C11=10.62 GPa, C12 $= 52.05$ GPa, C44 $= 27.07$ GPa, and $\rho = 2830 Kg/m^3$, with an assumed loss factor $\eta = 0.01$. The lattice unit cell length and the thickness of the beam are equal to a (see Fig. 13). The square pillars have a relative height and a relative geometric length h/a and d/a, respectively.

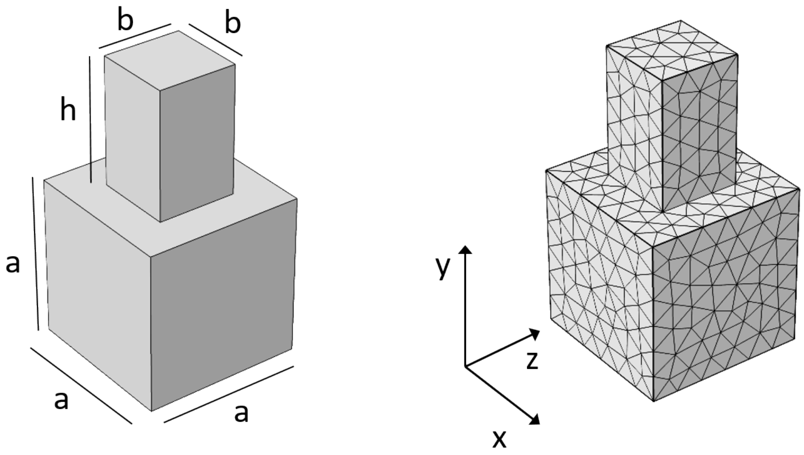

Figure 13: Unit cell of the phononic stubbed beam. Dimension and FE mesh

In Ref. [80] a parametric study on the relative height and length of the pillars is developed to analyze the shift and bandwidth of the lowest frequency band gap supported by the periodic beam. Here the beam complex band structure is calculated for a relative length of the pillars $d = 0.5a$ and a relative $h = 0.8a$ which maximize the lowest frequency band gap [80]. The unit cell FE model counts 2367 T10 tetrahedral elements for a total of 11256 dofs (942 boundary dof), which ensures at least 10 dofs for the shorter wavelength considered. Dispersion curves are provided in terms of relative frequency f/a as in [80] in the range $0 - f_{max} \cdot a = 1500m/s$ with a relative frequency step $\Delta f \cdot a = 5m/s$. As for the standard waveguide, wave solutions with $k_i a > 2$ are filtered out. Both linear elastic and viscoelastic (hysteretic) dispersion curves are analysed, with the aim of highlighting the effect of material absorption on the complex band structures (see Figs.14a,b). The real dispersion curves are extracted from both the $\omega(k)$ eigenproblem (continuous blue line) and the $k(\omega)$ approach (blue markers) for the linear elastic case. Conversely, only the $k(\omega)$ approach is used for the hysteretic case, due to the inherently complex nature of the wave solutions for a damped system.

The size of the markers are decreased proportionally to the increasing the wave attenuation, to more easily distinguish propagative (or light damped) solutions from evanescent complex waves. Indeed, in an elastic periodic medium, three distinct classes of solutions are found, namely purely propagative waves ($k_i = 0$), evanescent modes ($k_i \neq 0$) which lie at the edges of the IBZ and complex modes which connect propagating modes with same symmetry [59]. Where a bang gap is identified, in the range between f/a $[1190 - 1240]m/s$ for the analyzed beam (the light blue region in the Fig.14a and inset) no propagative solutions are supported by the media and only evanescent/complex modes are found. Further details on the nature of these complex/evanescent modes for an elastic periodic media will be given in the description of the band structure of the phononic plate provided in the next section. On the contrary, for a viscoelastic periodic media all the solutions are complex ($k_i \neq 0$) due to the material absorption (see Fig.14a and inset). In particular light damped propagative solutions are characterized by increasing values of attenuation as their group velocity decreases, finally resulting in high damped flat branches (see Fig.14b and inset). Similarly, the evanescent edge solutions and complex modes connecting flat propagative branches are transformed into complex high damped solutions which merge to low damped propagative waves blurring the clear distinction between different families of modes existing in LE periodic media. As regards to the accuracy of the proposed model reduction, the complex dispersion curves of the hysteretic periodic beam, computed with a CB reduced model with 60 fixed interface modes, which span the frequency range [0-3 f_{max}], are provided in Fig. 15. The reduced model counts a total of $942 + 60 = 1020$ boundary-modal coordinates. Similarly to the standard waveguide, the CB reduced method ensures accurate solutions (i.e. $err.k_r$ & $err.k_i \approx 1\%$) in the prediction of low damped propagative waves. Moreover, also high damped solutions extracted within the beam band gap, or at the IBZ edges are obtained with sufficient accuracy (i.e. $err.k_r$ & $err.k_i \approx 5\%$) (see Fig. 16). As regards to the computational time saving, when numerous frequency steps ($n_\omega > 100$) are required to accurately capture flat branches, the computational time for calculating the reduced $\mathbf{K}_{CB}$ and $\mathbf{M}_{CB}$ matrices becomes negligible, and the time fraction

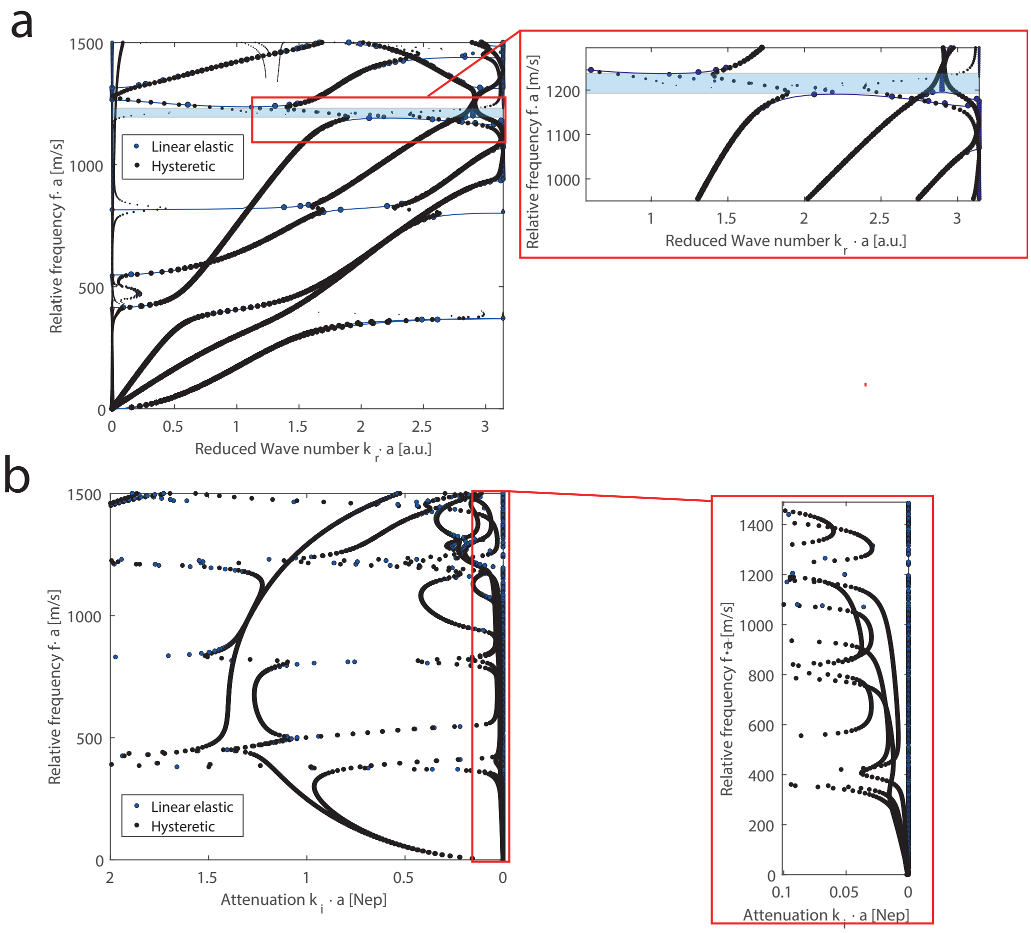

Figure 14: a) Dispersion and b) attenuation curve for a linear elastic and a viscoelastic (hysteretic) stubbed beam.

T_{fr} approaches the ratio between the time required to solve the reduced and full eigenproblem at each frequency step:

$$T_{fr} \simeq \frac{t_{\omega}^{RED}}{t_{\omega}^{FULL}} \tag{55}$$

As a result, the computational time is reduced to only some percents of the related full model. For the stubbed beam with 60 fixed interface modes a computational time of less than 2% of the full model is spent for the complex band structure calculation. Further details on the performances of the method for increasing number of fixed interface modes are given in Table 3.

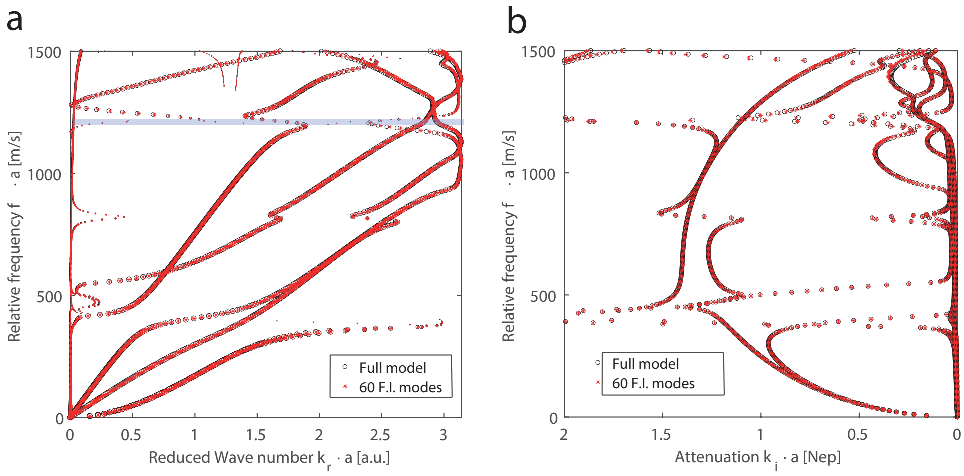

Figure 15: a) Dispersion and b) attenuation curve for the hysteretic stubbed beam. Full vs. CB reduced results.

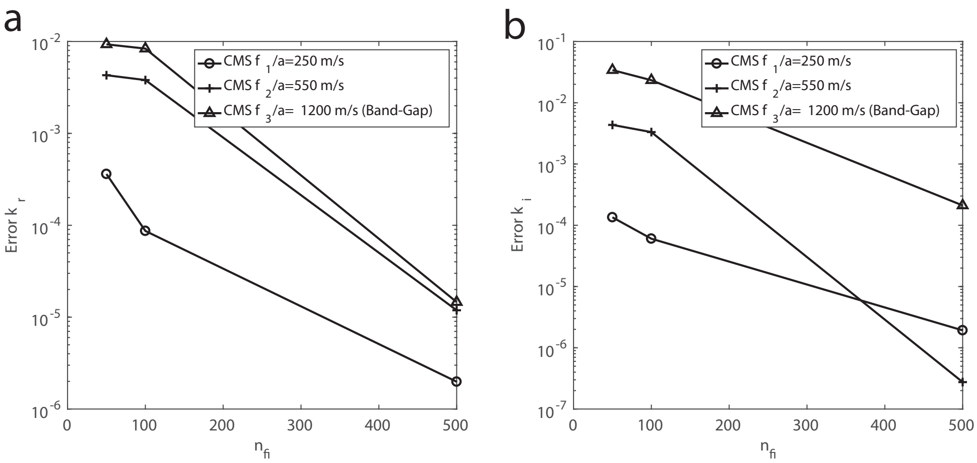

Figure 16: a) Error real wavenumber prediction k_r vs. number of fixed-interface mode n_{fi}. b) Error imaginary wavenumber prediction k_i vs. number of fixed-interface mode n_{fi}.

	Computational time [s]			Max Error BG frequency: [@f/a=1200 m/s]	
—	CMS Reduction	EVP Solution (1 step)	$\frac{timeF.I}{timeF.M}$ (300 steps)	err. k_r	err. k_i
Full Model (FM)	-	77 s	-		
60 F.I. modes	177 s	0.8 s	1.9 %	1 %	2 %
100 F.I. modes	199 s	1 s	2.3 %	0.8 %	2 %
500 F.I. modes	309 s	2.7 s	5.5 %	0.01 %	0.02 %

Table 3: Stubbed beam: Computational time vs. accuracy.

3.3 CMS-WFEM FOR TWO-DIMENSIONAL PERIODIC WAVEGUIDES: THE EBMS METHOD

The combination of a CMS reduction with a WFEM approach for the calculation of the real band structures of two-dimensional periodic waveguides, originally developed by Krattiger et al. [76] under the name of Bloch Mode Synthesis, is here extended to calculate the complex band structures, leading to the formulation of the Extended Bloch Mode Synthesis (EBMS). To this aim, as already shown for 1D waveguides, a Craig Bampton modal reduction of the unit cell is performed. First, the unit cell nodal displacements are subdivided in interior (i) and boundary (b) displacements. For a generic 2D unit cell, like the one in Fig. 9, the nodal displacement $\mathbf{v}$ are rearranged in the sets:

$$\mathbf{v} = \begin{bmatrix} \mathbf{v}_i \\ \mathbf{v}_b \end{bmatrix} \quad \text{with} \quad \mathbf{v}_b = \begin{bmatrix} \mathbf{v}_{b1} \\ \mathbf{v}_{b2} \\ \mathbf{v}_{b3} \\ \mathbf{v}_{b4} \\ \mathbf{v}_{b5} \\ \mathbf{v}_{b6} \\ \mathbf{v}_{b7} \\ \mathbf{v}_{b8} \end{bmatrix} \tag{56}$$

Accordingly, the stiffness matrix $\mathbf{K}$ and the mass matrix $\mathbf{M}$ are partitioned in the sub-matrices:

$$\mathbf{K} = \begin{bmatrix} \mathbf{K}_{ii} & \mathbf{K}_{ib} \\ \mathbf{K}_{ib} & \mathbf{K}_{bb} \end{bmatrix} \qquad \mathbf{M} = \begin{bmatrix} \mathbf{M}_{ii} & \mathbf{M}_{ib} \\ \mathbf{M}_{ib} & \mathbf{M}_{bb} \end{bmatrix} \tag{57}$$

By means of the Craig Bampton transformation operator $\mathbf{T}_{CB}$, the reduced modal-boundary stiffness $\mathbf{K}_{CB}$ and mass matrix $\mathbf{M}_{CB}$ are obtained as:

$$\mathbf{K}_{CB} = \mathbf{T}_{CB}^T \mathbf{K} \mathbf{T}_{CB} \qquad \mathbf{M}_{CB} = \mathbf{T}_{CB}^T \mathbf{M} \mathbf{T}_{CB} \tag{58}$$

and the reduced dynamic stiffness matrix of dimension $n_{CB} \times n_{CB}$ is:

$$\mathbf{D}_{CB}(\omega) = \mathbf{K}_{CB} - \omega^2 \mathbf{M}_{CB} \tag{59}$$

At this stage, the modal-reduced Bloch operators $\mathbf{\Lambda}_{CB}$ and $\overline{\mathbf{\Lambda}}_{CB}^T$ are obtained from the related full operators $\mathbf{\Lambda}$ and $\overline{\mathbf{\Lambda}}^T$ in Eqs. 34,35 by replacing the identity operator $\mathbf{I}_i$ with $\mathbf{I}_{f_i}$, and the reduced Bloch eigenvalue problem is obtained as:

$$\overline{\mathbf{\Lambda}}_{CB}^T(\lambda_x^{-1}, \lambda_y^{-1}) \mathbf{D}_{CB}(\omega) \mathbf{\Lambda}_{CB}(\lambda_x, \lambda_y) \mathbf{v}_{CB} = \mathbf{0} \tag{60}$$

Solution of the eigenproblem in Eq. (60) at the given frequency ω_i is tackled following the same procedure described in Chapt. 2 for the full eigenvalue problem of Eq. (36). As a result, Floquet-Bloch multipliers $\lambda_x = e^{ik_x a}$, $\lambda_y = e^{ik_y b}$ as function of frequency ω, i.e. the complex band structure $k(\omega)$, are obtained together with the CB reduced Bloch modal shapes $\mathbf{v}_{CB}$. The reduced periodic eigenvectors $\mathbf{v}_{CB}$ can be expanded to reconstruct the full modal shapes of the unit cell according to the relationship:

$$\mathbf{v} = \mathbf{T}_{CB} \mathbf{\Lambda}_{CB} \mathbf{v}_{CB} \tag{61}$$

3.3.1 *Numerical application*

In the next section, the complex band structure of a phononic stubbed plate is analyzed with the aim of highlighting the richer information provided by the $k(\omega)$ approach, compared to the $\omega(k)$ approach, for the characterization of the dynamic behavior of periodic systems. As first, an in-depth study of the band structure of this phononic material is provided using the full model computation. Later, the accuracy of the reduced EBMS complex band structures in relation to the number of fixed-interface modes is discussed.

3.3.1.1 *Complex band structures of an aluminum stubbed plate*

The analysed phononic plate (Fig. 17) has been originally designed and studied by Wu et al. [32, 33] as a linear elastic media and later by Collet et al. [50] assuming a hysteretic viscoelastic constitutive model. It consists of a 1 mm thick 6063-T83 aluminum plate with periodically cylindrical stubs of 5 mm height and 3.5 mm radius placed on its face. Here, the material is assumed to be isotropic with density ρ=2700 $\mathrm{kg/m^3}$, Young's modulus E=69 GPa and Poisson's ratio ν=0.33. The material dissipation is not accounted to avoid the collinearity issues between wave attenuation k_i and wave direction of propagation k_r along X-M direction discussed in Chapt. 2. The whole numerical approach is implemented in Matlab environment by using the open source FE library Fineale [81]. The band structures along the Γ-X-M high-symmetry directions, shown in Fig. 18, 19a and 19b, are calculated in the frequency range between 0-200 kHz with a frequency step of 500 Hz (400 steps) to capture and track flat branches accurately. At each frequency value, the quadratic and quartic eigenproblems of Eqs. (38), (40) and (42) are linearized and subse-

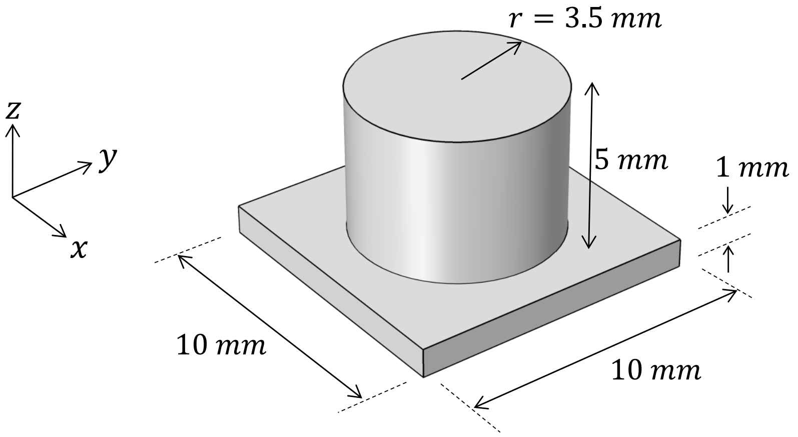

Figure 17: Unit cell of the considered aluminum stubbed plate.

quently solved by using the SPTARN Matlab eigensolver. For each λ the real and imaginary wavenumber components in the IBZ are obtained as:

$$k_r = \frac{1}{d} \arctan\left(\frac{\mathrm{Im}(\lambda)}{\mathrm{Re}(\lambda)}\right), \qquad k_i = -\frac{\ln|\lambda|}{d} \tag{62}$$

where $d = a$ for the computation of the wavenumber component along the x-axis whereas $d = b$ for the computation of the wavenumber component along the y-axis.

For easiness/clarity of representation, wave solutions with $k_{i,x}a > 4$ or $k_{i,y}b > 4$ are filtered out. The results refer to a FE model with 1415 quadratic T10 tetrahedral elements and 7341 dofs (with 600 boundary dofs) and have been validated with a refined mesh with 2977 elements for a total of 14559 dofs, using 800 frequency steps. Here, the 3D representation (k_r, k_i, ω) shown in Fig. 18, suggested by Veres in [59], is provided to get a further insight of the relationship between the different families of solutions calculated according to the $k(\omega)$ approach. As anticipated in section 3.2.1, three distinct types of solution can be identified in a periodic elastic media: purely propagative modes (PM), here marked with black dots, evanescent edge modes (EM), marked with green dots and complex modes (CM) in red dots. As in Ref. [59] the class of evanescent modes comprises both purely imaginary $k_r = 0$ modes and complex $k_r = \pi/a, \pi/b$ modes, i.e. all the complex modes existing at the edges of the IBZ. The real band structures of the stubbed plate are

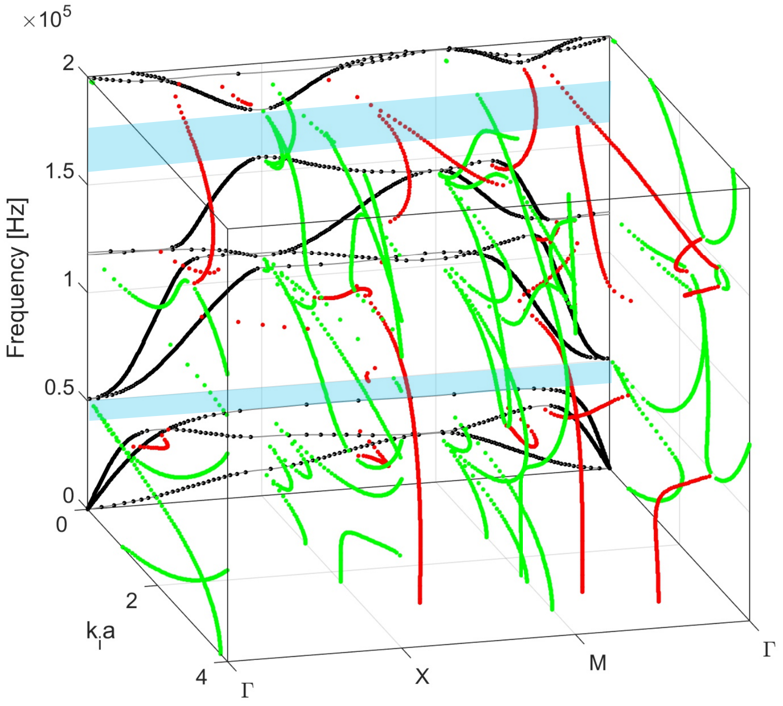

Figure 18: Complex band structures of the aluminum stubbed plate:full 3D representation (ω, k_r, k_i).

characterized by two band-gaps BG (highlighted in light blue in Figs. 18 and 19a), the lowest one in the frequency range between $40-50$ kHz, the highest one between $156-176$ kHz.

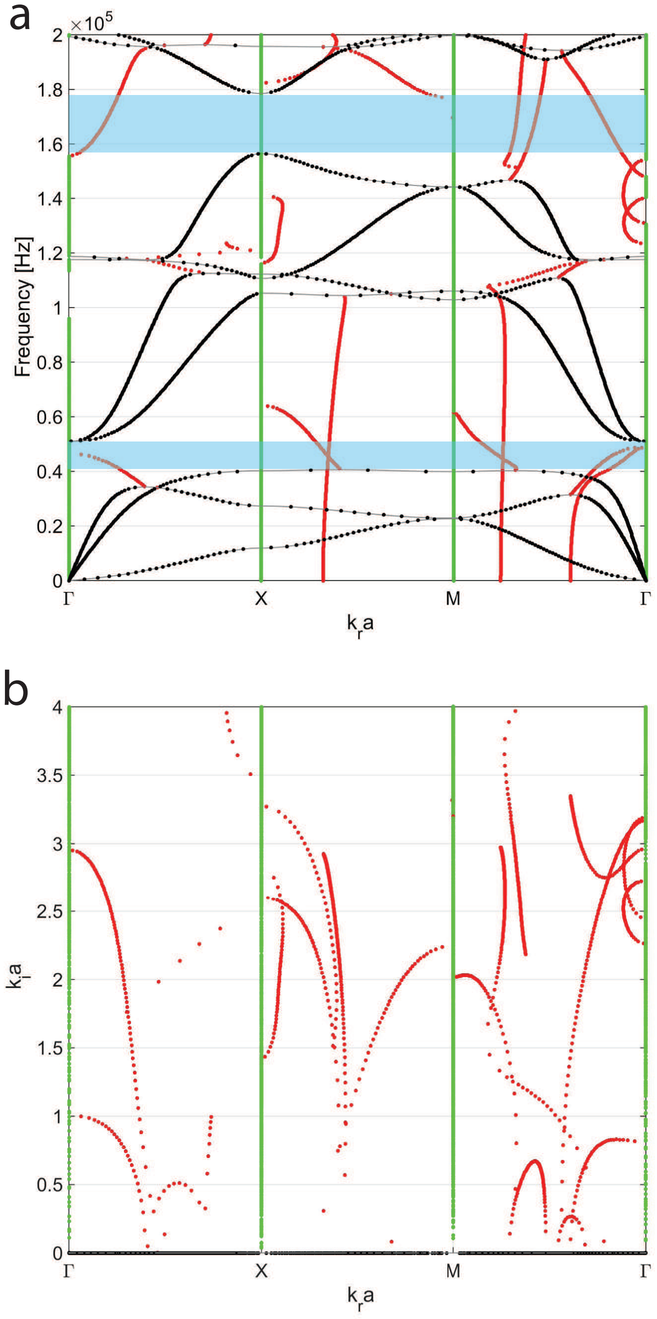

Figure 19: Complex band structures of the aluminum stubbed plate:a) ω vs. k_r and b) k_i vs. k_r.

Across these frequency ranges no purely propagative modes are found, while evanescent and complex modes still exist as shown for 2D phononic structures [59] and sonic crystals [55, 82]. Purely propagative modes are in excellent accordance with the real band structures (continuous gray lines in Figs. 18 and 19a) calculated with a standard $\omega(k)$ approach, as in Wu et al. [32]. A selection of propagative mode shapes along the Γ-X direction is provided in Fig. 20. The reader can qualitatively compare the calculated modal shapes PM3, PM4, PM5, with those proposed by Wu et al. in Ref. [32] (indicated as L1, U1 and L2, respectively) for a similar

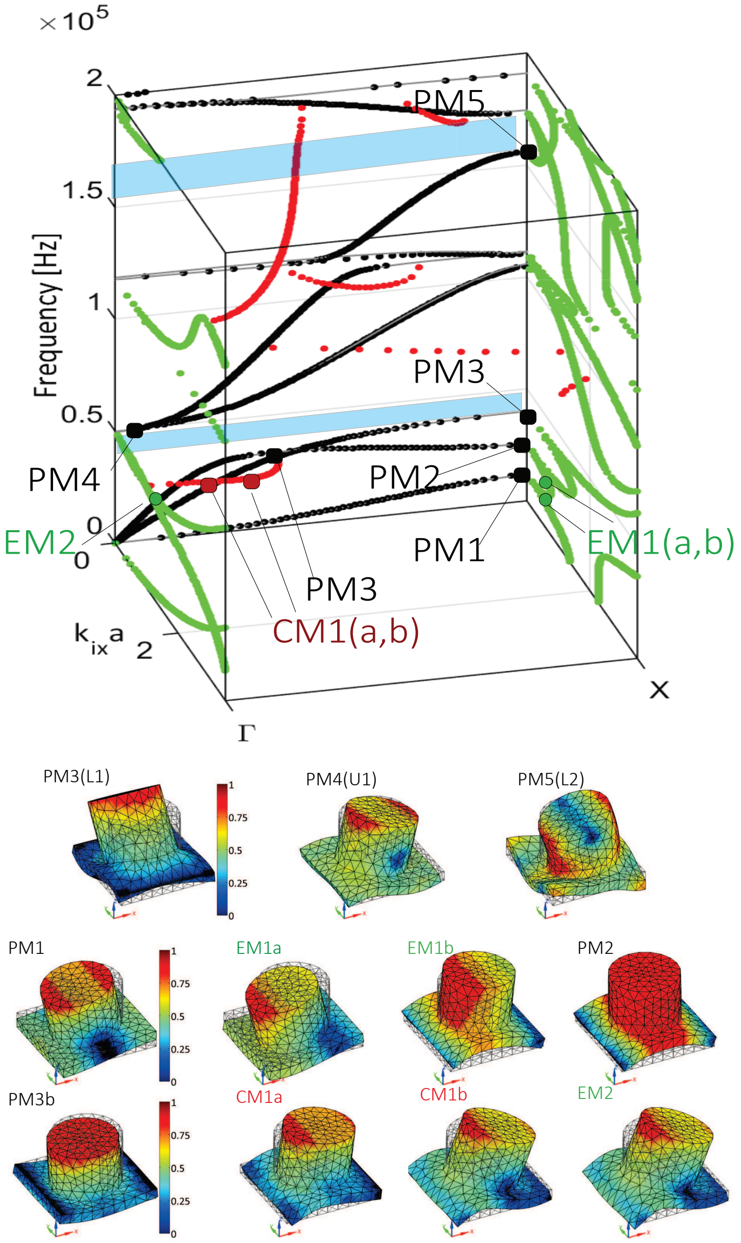

Figure 20: Band structures and selected mode shapes of the stubbed plate along Γ-X direction obtained with a refined mesh of 14559 dofs.

stubbed plate. As already pointed out in Refs.[55, 59] evanescent branches connect neighboring Bloch harmonics with the same symmetry and transfer this symmetry from one branch to the other. This aspect is clearly shown by the modal shapes EM1a and EM1b, selected along the evanescent branch that connects propagative modes PM1 and PM2 with the same symmetry. Moreover, the asymmetric-fano like profile of the X-edge evanescent modes around the BG frequencies (see Fig. 20) confirms the resonant nature of these BGs as already highlighted by Wu et al. [32] discussing the modal shapes of the propagative modes that exist at frequencies close to those of the BG. As far as complex modes are concerned, they connect stationary points (minima and maxima) between propagative branches, propagative-evanescent branches and evanescent-evanescent branches [55, 59]. As the evanescent ones, complex modes preserve the symmetry of the connected branches (see for example CM1a and CM1b in Fig. 20).
As shown, the adoption of a WFEM $k(\omega)$ approach for the calculation of the complex band structures provides a complete picture of the dynamic behavior of a phononic system. However, the richer information from the $k(\omega)$ approach comes with a much higher computational cost if compared to the related WFEM $\omega(k)$ technique, which can be significantly reduced with the CMS reduction.

3.3.1.2 *Complex band structures with CMS-WFEM method: accuracy vs. computation time*

The proposed EBMS method is here applied to compute the complex band structures of the stubbed plate described in the previous section. For the sake of conciseness, the comparison between full and reduced models is shown and discussed for the Γ-X domain in the frequency range 0-160 kHz (referred later as f_{max}) only. Analogous results are found along both X-M and M-Γ directions. In Fig. 21 the reduced complex band structure solutions calculated with 100 fixed-interface modes for a total of 700 dofs (marked with crosses) are compared with the complex band structure solutions computed using a full model of 7341 dofs (marked with dots). The computed reduced complex band structures provide an excellent approximation of those computed using the full model in the selected frequency range with only the 2% of the full model computational time ($t_{full} \simeq$ 2h 15m, $t_{red} \simeq$ 2m 30s). A quantitative analysis of the accuracy and computational time performances of the EBMS methodology is conducted by calculating the reduced complex band structures for increasing number of fixed interface modes ϕ_i, i.e. n_{fi}=[10, 30, 50, 100, 200, 500, 1000]. Fig. 22a shows the real band structures calculated with 30, 100, 500 fixed-interface modes ϕ_i and the frequencies steps at which the error analysis has been conducted, i.e. 20 kHz, 60 kHz, 100 kHz and 140 kHz. As for the one-dimensional case, the $k(\omega)$ solutions (shown with markers) are in excellent agreement with the related $\omega(k)$ ones (continuous lines). For the analyzed phononic plate, 30 fixed-interface modes are required to span the frequency range [0 $3f_{max}$], with an error in the real wavenumber $err_{k_r} \simeq 0.2\%$ and a related shift in frequency with the same order of magnitude. Higher accuracy is achievable with an increas-

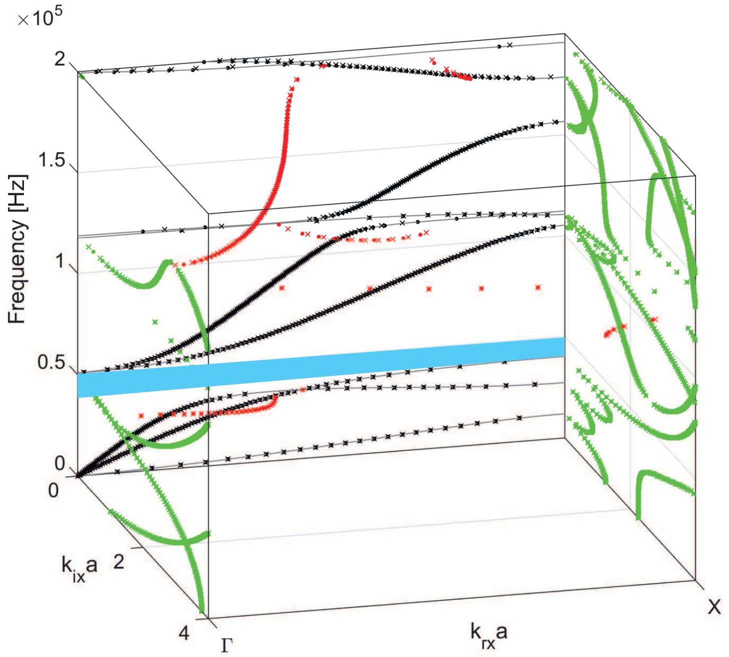

Figure 21: Full vs. reduced complex band structures along the Γ-X direction. Dots represent solutions of the full-dof model (7341 dofs) whereas crosses denote solutions of the reduced model with 100 interface modes (700 dofs).

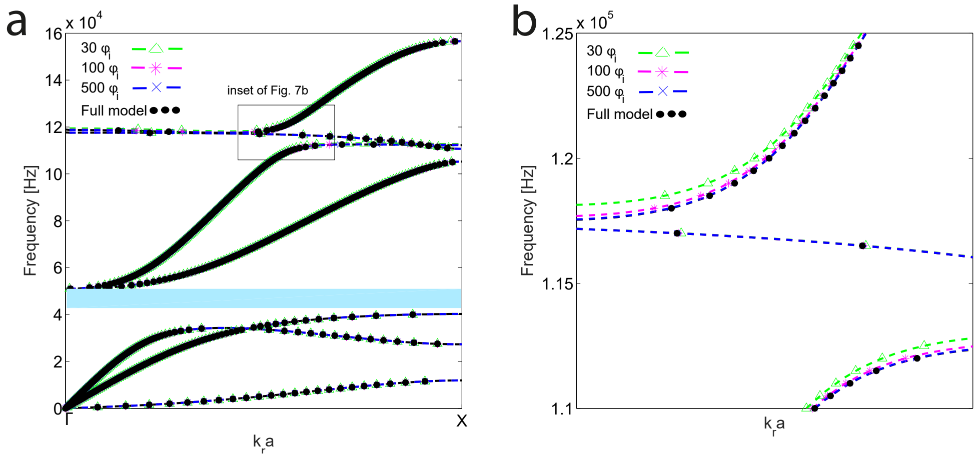

Figure 22: a) Propagative modes along the Γ-X direction computed considering 30 (green), 100 (magenta) and 500 (blue) interface modes as well as considering the full model (black); b) the inset shows the modal dependency.

ing number of fixed-interface modes, with lowest frequency branches showing smaller errors, as expected from the nature of the applied modal reduction (see Fig. 23). As for the one-dimensional case, that the accuracy of the method shows some modal dependency, has highlighted in Fig. 22b, where branches around the same frequency (115 kHz) show different levels of accuracy. The observed feature is consistent with the modal nature of the reduction technique, in which the chosen fixed-interface modal base could be more/less appropriate to reconstruct different periodic modal shapes.

Figure 23b shows that accurate solutions ($err_{k_r} \leqslant 10^{-2}$) are obtained with almost 1% of the full computational time, with fully convergent solutions ($err_{k_r} \simeq 10^{-4} - 10^{-5}$) achieved with less than 15% of full computational time. Similarly to propagative solutions, the accuracy of evanescent and complex modes is analyzed by calculating the maximum error over the imaginary wavenumber component. In Fig. 24 a selection of X-edge evanescent modes calculated with $n_{fi} = 30, 100$ and 500 fixed-interface modes ϕ_i as well as considering the full model is shown.

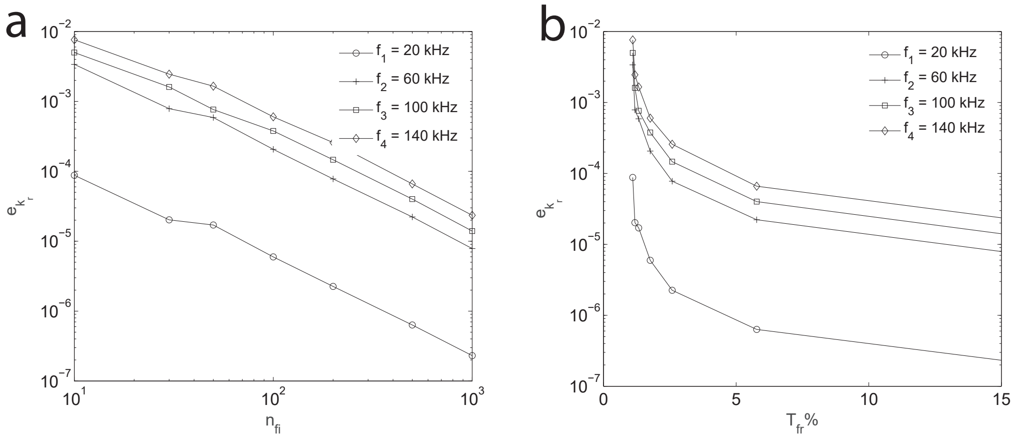

Figure 23: Propagative modes: a) error e_{k_r} versus number of fixed-interface modes n_{fi}. b) error e_{k_r} versus the computational time fraction T_{fr}.

The error analysis is conducted at the frequency values of 20 kHz, 60 kHz, 100 kHz and 140 kHz. Lower accuracy is shown by the reduced modal technique in the prediction of evanescent modes, with an error on the imaginary wavenumber component $e_{k_i} \simeq 5 \cdot 10^{-2}$ when 30 fixed-interface modes are used (see Fig. **??**). The reason of the slightly poorer performances of the modal reduction technique in the evaluation of evanescent modes could be related both to the chosen modal base that do not contain evanescent modal shapes and to the chosen eigensolver (based on the Arnoldi algorithm) that typically provides better accuracy in searching for largest magnitude eigenvalue solutions λ (i.e. propagative solutions and evanescent/complex solutions with $k_i < \varepsilon$). Indeed, as shown in Fig. 23, accurate solutions $err_{k_i} < 10^{-2}$ are easily achievable by slightly increasing the number of selected fixed-interface modes (i.e 50 or 100) with computational time still below the 2% of the total computational time (see Fig. 25).

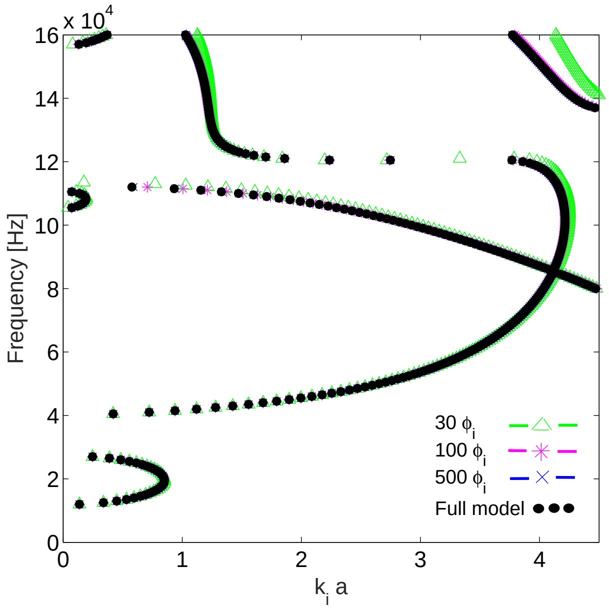

Figure 24: Evanescent X-edge modes calculated for $n_{fi} = 30$ (green triangle), 100 (magenta star) and 500 (blu cross) fixed-interface modes ϕ_i vs the evanescent X-edge modes calculated using the full model (black dot).

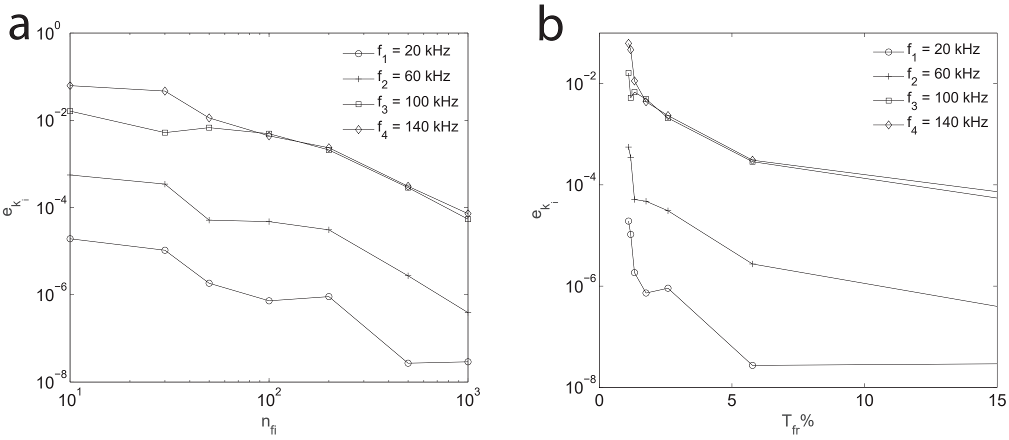

Figure 25: a) Error e_{k_i} versus the number of fixed-interface modes n_{fi} for the evanescent X-edge modes at four considered frequencies. b) Error e_{k_i} versus the computational time fraction T_{fr} (in percentage) for the evanescent X-edge modes at four considered frequencies.

3.4 CONCLUSIONS

In this Chapter, a numerical strategy for the fast calculation of complex band structures in elastic and viscoelastic periodic media has been presented and validated. The proposed numerical technique combines the Component Mode Synthesis and WFEM for the calculation of the full complex elastic band structures, by solving the $k(\omega)$ Bloch eigenvalue problem. The method uses a WFEM approach allowing for a simple discretization of the unit cell Bloch wave equation, by means of standard FE routines. The Component Mode Synthesis with a Craig Bampton technique reduces the dimensions of the interior unit cell dofs leaving the boundary ones available for a standard WFEM approach. The resulting $k(\omega)$ approach for solving Bloch eigenvalue problems provides the complete set of real (propagative) and complex (decay/evanescent) solutions and damped solutions (for a viscoelastic material) supported by the periodic media, needed to characterize the far field and near field (filtering) response of the phononic media. The methodology has been detailed and validated for 1D viscoelastic waveguides and 2D periodic unit cells, focusing both on the prediction of the dispersive attenuation $k_i(\omega)$ in structural waveguides and on the prediction of evanescent solutions in the band gaps of periodic systems. The accuracy and efficiency of the method have been tested on waveguides already used as a benchmark for other Bloch computational methods. It has been shown that the computational time can be reduced up to some percents only of the full model computational time with negligible errors for both real and evanescent/complex modes. As such, the methodology appears suitable to reduce enormously the computational effort preserving the full description of the dynamic behavior achieved with a $k(\omega)$ approach.

4

A COMBINED CMS-WAVE REDUCTION FOR COMPLEX BAND STRUCTURES CALCULATION

ABSTRACT

This chapter analyzes and validates a combined modal-wave reduction technique to further speed up the complex band structures calculation of periodic waveguides. The method is based on the combination of the CMS technique and a frequency interpolation scheme where the Bloch eigenproblem is projected onto a reduced space of eigenfunctions. The numerical technique, originally proposed for the calculation of propagative waves in two-dimensional systems, is here extended to extract both highly damped and low decaying propagative wave solutions in one-dimensional periodic viscoelastic media. To this aim, the reduced CMS $k(\omega)$ *eigenproblem is projected onto a set of Bloch wave shapes selected within a small frequency subset spanning the frequency range of interest. As a result, a smaller dimension eigenproblem is obtained from which the complex dispersion curve is calculated within the full range of frequencies. The performance of the method is discussed, analyzing both standard (uniform) and periodic waveguides. Selection criteria for the appropriate wave basis to capture both propagative and highly decaying waves are provided. It is shown that accurate complex band structures can be calculated with a computational time reduced by up to two orders of magnitudes from the initial full model and up to 50% from the CMS reduced model.*

4.1 INTRODUCTION

It is known that the dynamic response of a vibrating medium can be viewed either as a superposition of modes or as a superposition of elastic waves, as discussed and proved by Langley [83] for one-dimensional structures. If a wave-based description is assumed, the harmonic response of a one-dimensional system can be reconstructed as the sum of left and right going waves. In the literature, different numerical strategies have been proposed to select the smallest set of waves to reconstruct the system/material dynamic response with a lower computational demand. Among the others, model reduction strategies to compute the low-and mid-frequency forced response of single and coupled elastic waveguides have been proposed [84, 85], as well as to analyze the response of periodic structures with local perturbations [86]. These techniques allow reducing the effort for computing the forced response of a dynamic system but do not speed up the calculation of the initial wave basis, as well as the related extraction of the dispersion properties. For this last purpose, according to the best knowledge of the author, only two wave-based techniques are now available. The first one, proposed by Hussein

et al. [57], is based on a projection of the Bloch eigenproblem resulting from a $\omega(k)$ WFE approach on a reduced set of waves selected at specific locations of the IBZ. This method, referred as Reduced Bloch Mode Expansion, ensures accurate real band structures calculation with significant time savings. Conversely, Droz et al. [75] presented a frequency interpolation method based on the projection of the $k(\omega)$ Bloch eigenproblem over a subset of propagative solutions selected at specific frequencies. The methodology has been used to correctly predict the real dispersion properties (k_r vs. ω) of uniform composite waveguides. Moreover, the described wave-based reduction can be easily coupled with a reduced description of the unit cell domain provided by the CMS technique, to enhance the computational savings. Indeed, such coupled CMS-Wave reduction has been recently investigated by the same Droz et al. [87] for the evaluation of the real band structure of two-dimensional periodic systems, with excellent performances both in terms of accuracy and computational savings. Indeed, the methodology can be in principle exploited also for the prediction of the attenuation properties k_i vs. ω of waveguides, that are similarly extracted within the context of a WFE $k(\omega)$ approach. However, it is necessary to investigate the appropriate wave basis required to predict the waveguide attenuation properties correctly.
As such, in what follows the CMS-Wave reduction is extended and validated for the analysis viscoelastic one-dimensional periodic (and uniform) waveguides. First, the wave-based model reduction technique introduced by Droz et al. [75] is reviewed and detailed for the analysis of one-dimensional periodic viscoelastic waveguides. The methodology is then coupled with the CMS reduction leading to the formulation of a CMS-Wave technique for one-dimensional waveguides. The combined method is detailed for 1D viscoelastic waveguides, focusing on the wave basis selection strategies required to capture both low damped propagative waves as well as highly decaying evanescent solutions. The efficiency and accuracy of the numerical technique is investigated by means of two numerical examples: (i) a rail steel section, as an example of a uniform (non-periodic) waveguide for which the prediction of low decaying waves are of interest (ii) a periodic stubbed beam (presented in Chapt. 3) to discuss the required wave basis to reconstruct the evanescent field in periodic media.

4.2 A WAVE-BASED MODEL REDUCTION FOR $k(\omega)$ WFE APPROACH

The idea behind the wave-based model reduction proposed by Droz et al. [75] is to project the Bloch eigenproblem obtained from a standard WFE approach, here recalled from Eq. 25 for the sake of clarity:

$$\overline{\boldsymbol{\Lambda}}^{T}(\lambda^{-1})\mathbf{D}(\omega)\boldsymbol{\Lambda}(\lambda)\mathbf{v}_{red} = \mathbf{0}$$

onto a reduced subset of solutions of the same system. Such solutions correspond to the set of wave shapes $X=\{\chi_1, \dots, \chi_n\}$ associated to the Bloch propagators $\lambda = \{\lambda_1, \dots, \lambda_n\}$ extracted at given frequency ω_i. Since the displacement field in a waveg-

uide subjected to harmonic excitation can be reconstructed as a sum of wave amplitudes, a limited set of wave shapes can be selected at given frequencies $\tilde{\omega}$={ω_0, ..., ω_m} to construct a sufficient basis. In this respective, the method can be seen as a frequency interpolation scheme where a reduced set of eigenvectors at given frequency ω_i are used to interpolate the original eigenproblem over the whole frequency range of interest [75]. Thus, the crucial aspect of the methodology is the selection criterium for the frequency values ω_i where the wave shapes are sought as well as the criterium to select the appropriate number wave shapes at the given frequency ω_i.
According to Droz et al.[75], the reduced basis can be built selecting positive going waves with the lowest decay. Nonetheless, for an accurate description of the waveguide low-frequency behavior, rigid body wave shapes need to be added to the basis. Then, the extracted wave basis can be further post-processed to remove similar wave shapes selected at different frequencies to avoid the construction of large bases with redundant vectors. This post-process is based on a Modal Assurance Criterion (MAC) to check the orthogonality between the modes. In summary, the construction of the reduced wave basis for the WFE eigenproblem requires the following steps:

- Extraction of waveguide rigid body motions;
- Definition of the frequency subset $\tilde{\omega} = \{\omega_0, \dots, \omega_m\}$ where the eigenproblem is solved;
- Extraction of the wave shapes X={$\chi_1, \dots, \chi_n$}, identification of positive going waves with lower decay and removal of redundant wave shapes;

Indeed, nothing prevents to apply the same wave-based reduction procedure on the CMS-reduced Bloch eigenproblem (Eq. 50), here recalled for the sake of clarity:

$$\overline{\mathbf{\Lambda}}^T_{CB}(\lambda^{-1})\mathbf{D}_{CB}(\omega)\mathbf{\Lambda}_{CB}(\lambda)\mathbf{v}_{red,CB} = \mathbf{0}$$

In the following subsections, the steps necessary to apply the combined CMS-Wave-based reduction on viscoelastic waveguides are detailed.

4.2.1 *Extraction of waveguide rigid body motions*

The wave basis should contain the waveguide's rigid modes to represent its low-frequency dynamic correctly. Waveguide's rigid body motions can be extracted as the rigid displacement solutions associated with the static problem:

$$\mathbf{K}_{red,CB}\mathbf{v}_{red,CB} = \mathbf{0} \tag{63}$$

with:

$$\mathbf{K}_{red,CB} = \begin{bmatrix} \mathbf{K}_{RL} + \mathbf{K}_{LL} + \mathbf{K}_{RR} + \mathbf{K}_{LR} & \mathbf{K}_{Rfi} + \mathbf{K}_{Lfi} \\ sym & \mathbf{K}_{fifi} \end{bmatrix} \tag{64}$$

which results from the equilibrium equation in Eq. 50 calculated at $k_r = 0$, $\omega = 0$. The extracted i rigid modes are denoted as $\chi_{rig,i}$.

4.2.2 *Definition of the cut-on frequency subset $\tilde{\omega}$*

The wave basis $X=\{\chi_1 \dots \chi_n\}$ is extracted at selected frequencies $\tilde{\omega} = \{\omega_0, \dots, \omega_m\}$ within the range of interest for the complex dispersion curve calculation. In Ref. [87], for 2D periodic media, mid-alias frequencies (i.e eigenfrequency selected at mid-position of the IBZ $k_r = \pi/(2a)$) are used to build the subset $\tilde{\omega}$. Conversely, cut-on frequencies can be used to build the frequency subset when one-dimensional waveguides are investigated[75]. In fact, cut-on frequencies mark the appearance of new propagative waves in the dispersion curve, and for this reason they represent suitable candidates for the frequency interpolation scheme. The cut-on frequency subset $\tilde{\omega}$ is built from the solutions of $\omega(k)$ eigenproblem for $k_r = 0$:

$$\begin{aligned} \overline{\Lambda}_{CB}^{T}(\lambda^{-1} = 1)\mathbf{D}_{CB}(\omega)\Lambda_{CB}(\lambda = 1)\mathbf{v}_{red,CB} = \mathbf{0} \\ (\mathbf{K}_{red,CB} - \omega^2\mathbf{M}_{red,CB})\mathbf{v}_{red,CB} = \mathbf{0} \end{aligned} \tag{65}$$

When viscoelasticity is accounted in the model, complex frequencies $\omega^* = \omega_r + i\omega_i$ are obtained. Here, only the real parts ω_r are stored in the frequency subset and later used as input for the definition of the reduced basis.

4.2.3 *Extraction of the wave shapes Φ and construction of the reduced basis*

Once the frequency subset $\tilde{\omega} = (\omega_{r,1} ... \omega_{r,m})$ is defined, the wave basis can be constructed from a reduced number of wave solutions subsequently calculated at all the frequencies of the subset $\tilde{\omega}$:

$$\begin{cases} \overline{\Lambda}_{CB}^{T}(\lambda^{-1})\mathbf{D}_{CB}(\omega_{r,1})\Lambda_{CB}(\lambda)\mathbf{v}_{red,CB} = \mathbf{0} \\ \overline{\Lambda}_{CB}^{T}(\lambda^{-1})\mathbf{D}_{CB}(\omega_{r,2})\Lambda_{CB}(\lambda)\mathbf{v}_{red,CB} = \mathbf{0} \\ \vdots \\ \overline{\Lambda}_{CB}^{T}(\lambda^{-1})\mathbf{D}_{CB}(\omega_{r,m})\Lambda_{CB}(\lambda)\mathbf{v}_{red,CB} = \mathbf{0} \end{cases} \tag{66}$$

In particular, from the full set of eigenvectors $\mathbf{v}_{red,CB}^{i}$ extracted at each frequency step $\omega_{r,i}$, only the positive propagative low decaying waves are retained. In Droz et al. [75] least decaying positive propagative waves are selecting retaining solutions with $k_r >> |k_i|$. The criteria are further detailed in Ref. [87] for 2D periodic media where the set of positive propagative waves is identified as:

$$\begin{cases} 0 \leqslant k_{r,j} \leqslant \pi/L \\ k_{i,j} > 0 \\ |k_{i,j}| < \alpha k_{r,j} \quad \alpha \approx 0.01 \end{cases} \tag{67}$$

However, for viscoelastic media the condition $|k_{i,j}| < \alpha k_{r,j}$ (or similarly $k_r >> |k_i|$) is prone to miss the appearance of propagative solutions at cut-on frequencies, i.e. solutions with $k_r \approx 0$ and $k_i \neq 0$. Indeed, in periodic viscoelastic media, several flat branches are found, typically characterized by high values of damping around the cut-on points (see for example the dispersion curve of the stubbed beam presented in Chapt. 3 Fig. 14). For such reasons, the wave selection criterium is here rearranged as:

$$\gamma \leqslant |\lambda_j| \leqslant 1 \quad 0 \leqslant \gamma \leqslant 1 \tag{68}$$

Using the criterium in Eq. 68 all the non growing waves (i.e. $|\lambda_j| \leqslant 1$) with an amplitude attenuation across one unit cell length lower or equal to $|\lambda_j|$ are selected for the basis. The choice of the parameter γ to obtain accurate solutions for both low and highly damped solutions will be discussed in the numerical section.

When numerous frequency points ω_i are used, a large basis with redundant solutions (i.e. correlated wave shapes) can be generated, possibly limiting the computational saving of the method. Thus, a recursive strategy based on the modal assurance criteria (MAC) can be adopted to select only uncorrelated wave shapes, as proposed in [75]. Starting from a fundamental basis built with waveguide rigid modes $X = \{\chi_{r,1}, \dots, \chi_{r,n_r}\} = \{\chi_1, \cdots, \chi_{n_r}\}$, the basis X is recursively enriched at each frequency step ω_i with the non-growing wave vectors ν_j^i selected according the criteria in Eq. 68 fulfilling the relation:

$$\text{if} \quad \frac{|(\phi_k^T \overline{\nu^i}_j)({\nu^i}_j^T \overline{\phi^k})|}{|(\phi_k^T \overline{\phi_k})({\nu_j^i}^T \overline{\nu_j^i})|} < \epsilon \Rightarrow \nu_j^i \in X \quad \text{with} \quad 0 < \epsilon < 1 \tag{69}$$

4.3 NUMERICAL APPLICATIONS

In this section, two numerical applications of the combined CMS-Wave model reduction are presented and discussed. In the first, the dispersion and attenuation curves of a rail steel section are calculated. Dispersive properties of guided waves in rails have been largely analyzed in the literature [79, 88–91] given their importance for noise reductions applications at low frequencies and for long-range defect detections at high frequencies. In the second example, the dispersion curves of the stubbed beam described in Chapter 3 are calculated with the combined CMS-Wave approach to investigate the required reduced basis to capture the complex evanescent solutions existing in such periodic waveguide.

4.3.1 *A.R.E.M.A. rail steel section*

The purpose of this section is to demonstrate the applicability of the combined CMS-Wave reduced approach to model uniform waveguides of arbitrary cross-section, as a typical 115-lb A.R.E.M.A. rail steel section (see Figure 26). The rail section mechanical properties are given in Table 4.

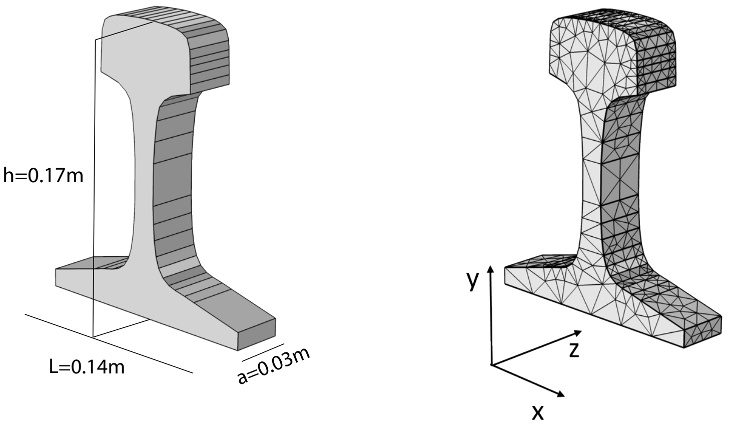

Figure 26: Geometry and FE mesh of the finite length portion of the A.R.E.M.A waveguide built in COMSOL®.®

Material	ρ [kg/m^3]	c_L [m/s]	c_T [m/s]	α_L [Np/λ]	α_T [Np/λ]
Steel	7800	5960	3190	0.003	0.043

Table 4: A.R.E.M.A. rail steel section mechanical parameters.

For the WFEM discretization, a finite length $L = 0.03$ m of the rail track is modeled in COMSOL® (see Fig. 26), in order to map real wavenumbers up to $\pi/a = 104.7198$ [rad/m]. The adopted rail WFE mesh, required to obtain convergent solutions up to 30 kHz, consists of 2685 tetrahedral elements with 10 nodes per element for a total of 14304 dofs, with 2028 cross section boundary dofs. The dispersion curves, calculated in the frequency range [0-30] kHz with 100 frequency steps of $\Delta f = 3$kHz, are presented in terms of phase velocity $c_{ph} = \omega/k_r$ (Fig. 27a) and attenuation k_i (Fig. 27b). Wave solutions with attenuation $k_i > 1$ are filtered out, given the typical interest on long-range propagative waves for NDE defects detection in rail sections.

The accuracy of the CMS-Wave method is discussed by comparing the dispersion curves extracted from the full model, a CMS reduced model with 50 interface modes, and a CMS-Wave reduced model with a threshold value for the propagative damped solutions $\gamma = 0.9$ and a correlation parameter $\epsilon = 0.99$. It is worth noticing that 50 fixed interface modes, span a frequency range up to $3 * f_{max}$, and that such model counts for a total of $2028 + 50 = 2078$ boundary-modal coordinates, which roughly corresponds to the 15% of the initial number of nodal coordinates. On the contrary the CMS-Wave reduced model is built on a basis of 147 least decaying propagative waves (4 rigid modes), extracted at the first 15 dispersion cut-on frequencies f_{cut}={1192, 3916, 5123, 5904, 10172, 10214, 14267, 15050, 16858, 21813, 22164, 23636, 24948, 27721, 30415} Hz, marked with dashed lines in Fig. 27a.

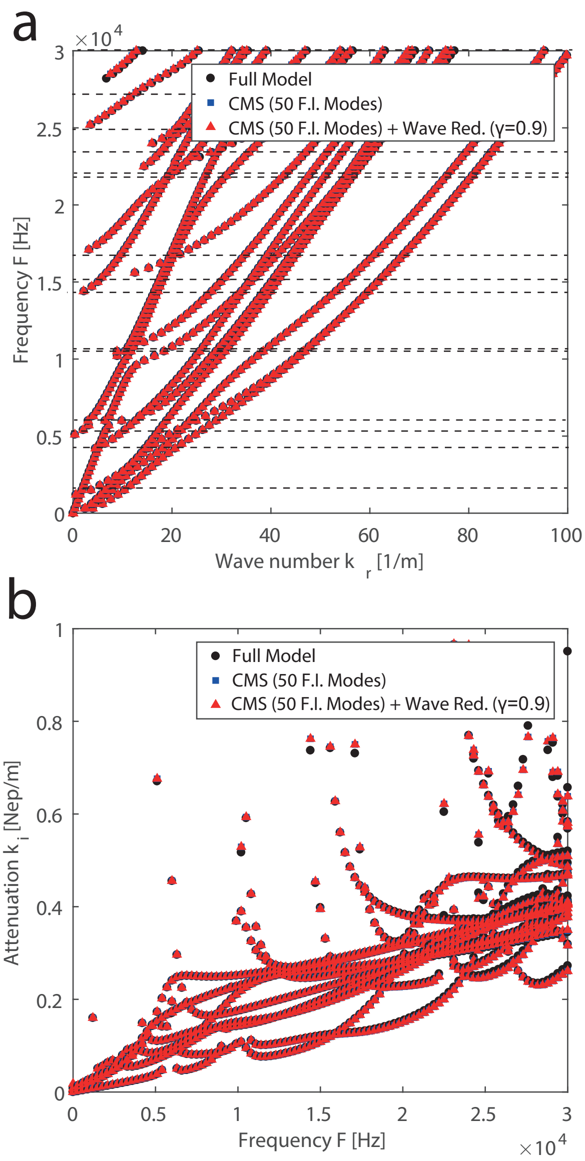

Figure 27: Dispersion k_r vs. f and attenuation k_i vs. f curve for the Full Model, CMS reduced model and CMS-Wave reduced model.

From visual inspection of Fig.27a,b, dispersion and attenuation curves extracted from the CMS-Wave reduced model perfectly match the full model results, similarly to the CMS reduced results. A more in-depth analysis on the accuracy and computational savings of the method is performed by varying the number of interface modes n_{fi}={50,100,250,500} as well as the attenuation threshold parameter γ={0.9, 0.5, 0.1}. The accuracy of the method is investigated calculating the errors on the real and imaginary components of the wavenumber (i.e. $Err.k_r$ and $Err.k_i$) between the full and CMS-Wave reduced results:

$$\begin{aligned} Err._{k_r} &= \max \left| \frac{k_{j,r}^{CMS-W,RED} - k_{j,r}^{FULL}}{k_{j,r}^{FULL}} \right| \\ Err_{k_i} &= \max \left| \frac{k_{j,i}^{CMS-W,RED} - k_{j,i}^{FULL}}{k_{j,i}^{FULL}} \right| \end{aligned} \tag{70}$$

Similarly, the relative errors between the CMS reduction and the combined CMS-Wave reduction results are calculated as:

$$\begin{aligned} err._{k_{r,rel.W-red}} &= \max \left| \frac{k_{j,r}^{CMS-W,RED} - k_{j,r}^{CMS,RED}}{k_{j,r}^{CMS,RED}} \right| \\ err._{k_{i,rel.W-red}} &= \max \left| \frac{k_{j,i}^{CMS-W,RED} - k_{j,i}^{CMS,RED}}{k_{j,i}^{CMS,RED}} \right| \end{aligned} \tag{71}$$

The errors $Err.k_r$ and $Err.k_i$ calculated on the first four propagative solutions within the whole frequency range of interest are reported in Fig. 28a,b. The method ensures a discrepancy lower than 1% for both the real and attenuation dispersion curves, which is fully comparable with the related CMS solutions. Moreover, there is no significant benefit in using a larger basis (i.e. 194 modes) of propagative solutions for the wave reduction as resulting from a smaller threshold value $\gamma = 0.5$. In fact, the relative errors introduced by the wave-based reduction are at least two orders of magnitude lower than the error introduced by the CMS reduction alone, as highlighted in Figs.29a,b. Nonetheless, when a richer CMS reduction (i.e. $n_{fi} = \{100, 250, 500\}$) is used to achieve a higher level of accuracy, appropriate wave bases, extracted with lower attenuation threshold parameters $\gamma = \{0.9, 0.5, 0.1\}$, have to be chosen to ensure negligible relative error introduced by the wave reduction (Figs. 30a,b). As far as the computational savings of the method are concerned, it is worth remarking that for the analyzed system the performance of the CMS reduction alone is poorer compared to the previously analyzed cases (Chapter 3). In particular, a computational time for the CMS alone approximately equal to 37 % of the full computational time is obtained. This result is due to the consistent number of boundary dofs (compared to the total number of dofs) required to ensure an accurate description of waveguide cross-section deformations. In this context, the adoption of a further wave-based reduction is highly beneficial as it leads to a computational time reduction up to the 17% of the full computational time, thus less than 50% of the CMS reduction alone. As expected, for the CMS-Wave reduction the most expensive step is the calculation of the reduced stiffness and mass matrix (the CB reduction) which counts 67% of the total computational time. Conversely,

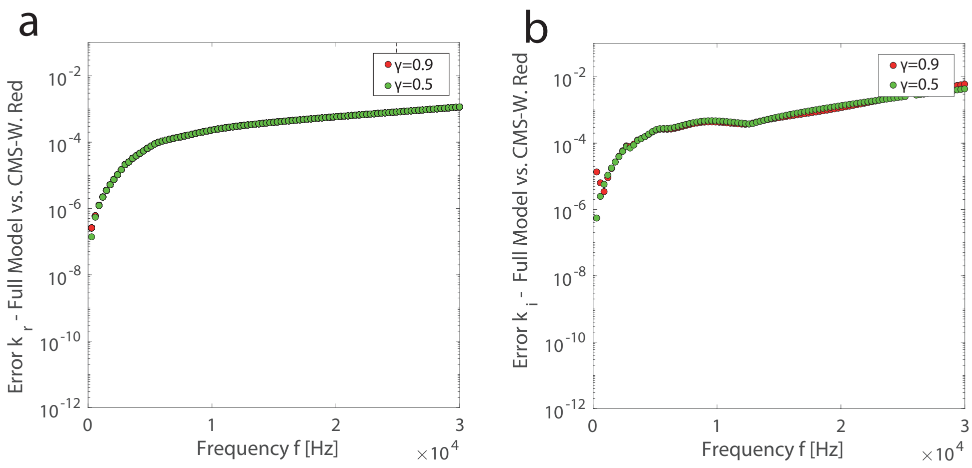

Figure 28: Errors in the real and imaginary wavenumber predictions for the first 4 propagative modes for the CMS-Wave reduced model vs. Full model.

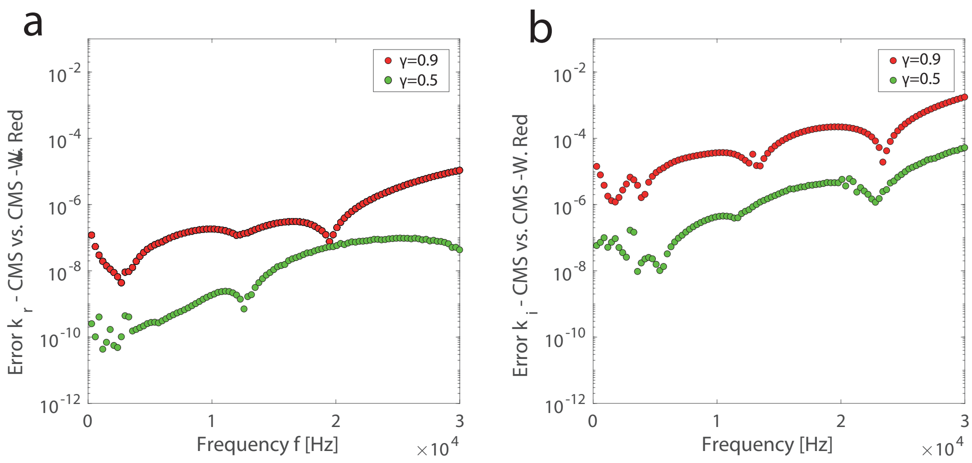

Figure 29: Relative errors in the real and imaginary wavenumber predictions for the first 4 propagative modes for the CMS-Wave reduced model vs. CMS reduced model.

the wave basis construction and reduction require a computational effort almost equal to the time needed to solve the CMS-reduced eigenproblem at n different cut-on frequency points. Further details on the computational time savings and the accuracy achieved with the different CMS and CMS-Wave reduced configurations are given in Table 5. It is worth remarking that in the case of small wave basis (i.e. high values of γ) either a direct solver or an iterative solver can be used for the solution of the CMS-Wave reduced eigenproblem with no substantial difference in the computational performance of the method. On the contrary, for larger basis (i.e. $\gamma = 0.1$) the use of an iterative solver (as the SPTARN-Arnoldi algorithm described in Chapt. 3) is beneficial to ensure a substantial speed up the method.

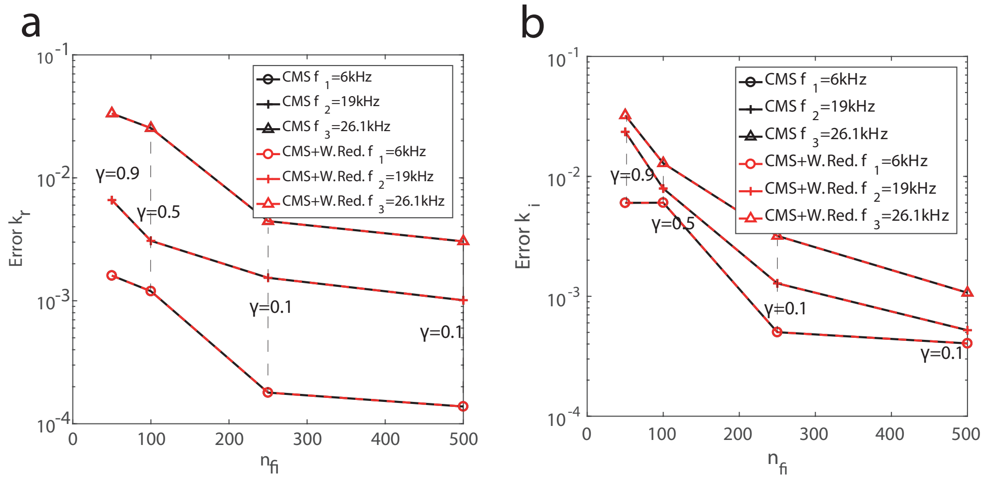

Figure 30: Errors in real and imaginary wavenumber predictions vs. number of fixed-interface mode. In black lines are shown the errors for the CMS models, while in red lines the errors for the related CMS-Wave models.

Table 5: A.R.E.M.A: Computational time vs. accuracy.

	Computational time [s]				Max Error [@26.1kHz]	
—	CMS Reduction	Wave-base Extraction (15 cut freq.)	EVP Solution (1 step) (Direct Solver DS) (Iterative Solver IS)	$\frac{\mathrm{timeF.I}}{\mathrm{timeF.M}}$ (100 steps)	Err. k_r	Err. k_i
Full Model (FM)	-	-	37 s (IS)	-		
50 F.I. modes	436 s	-	9.6 s (IS)	37 %	3.3 %	3.3 %
50 F.I. modes ($\beta = 0.9$)	436 s	144 s [145modes]	0.7 s (DS)	17 %	3.3 %	3.3 %
100 F.I. modes	491 s	-	10.1 s (IS)	40 %	2.5 %	1.2 %
100 F.I. modes ($\beta = 0.5$)	491 s	177 s [187modes]	1 s (DS)	21%	2.5 %	1.2 %
250 F.I. modes	665 s	-	12.3 s (IS)	51%	0.4 %	0.3 %
250 F.I. modes ($\beta = 0.1$)	665 s	212 s [361modes]	6 s (DS) ; <1 s (IS)	39 % (DS); 27% (IS)	0.4 %	0.3 %
500 F.I. modes	742 s	-	17.1s	66 %	0.3 %	0.1 %
500 F.I. modes ($\beta = 0.1$)	742 s	259 s [364modes]	6 s (DS); <1 s (IS)	43 % (DS); 29% (IS)	0.3 %	0.1 %

4.3.2 *Periodic stubbed beam*

The combined CMS-Wave reduction is here applied to calculate the complex band structure of the periodic stubbed beam presented in Chapt. 3 (cf. **??**). Indeed, such periodic waveguide would not require a further reduction, given the excellent performance of the CMS technique alone discussed in the previous Chapter. However, it is of interest to investigate the required reduced basis (i.e. the appropriate choice of the parameter γ) to reconstruct the complex evanescent solutions. To this aim, the phononic beam is discretized with the same mesh like the one presented in Chapt. 3, i.e. 2367 T10 tetrahedral elements for a total of 11256 dofs (942 boundary dof), and a CMS reduction with 60 fixed interface modes is applied.

The wave-based reduction is performed by building a basis of least decaying waves selected at the waveguide cut-on frequencies lying in the relative frequency range of interest, i.e. f_{cut}/a={369.1 801.6 935.4 1068.6 1164.8 1180.1 1312.8 1439.5 1491.3} m/s. Wave basis of 21 and 41 least-decaying propagative waves are obtained, for γ values of 0.9 and 0.5, respectively. In Fig. 31 the complex dispersion curves as obtained for the two CMS-Wave reduced models are reported. Figure 31 shows

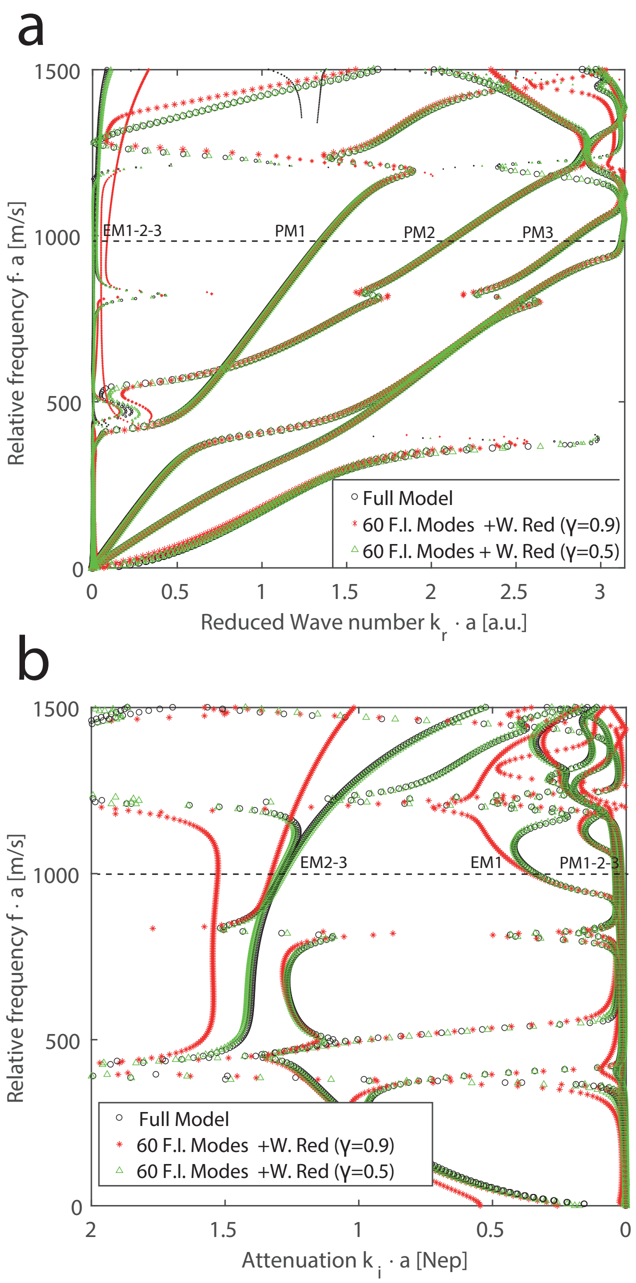

Figure 31: Complex dispersion curve of an hysteretic periodic stubbed beam. Full model vs. CMS-Wave reduced models.

that the selection of the least decaying propagative waves associated to a $\gamma = 0.9$ is not sufficient to ensure an accurate description of the complex/evanescent modes lying at the edge of the IBZ and within the band gap of the periodic beam (solutions in red of Figs. 31a,b). The prediction on the attenuation of complex/edge modes as obtained from the reduced wave basis with $\gamma = 0.9$ is poor (err.$k_i \approx 10\%$) within the whole frequency range of interest. Indeed a $\gamma = 0.9$ allows selecting only the low damped propagative modes with an attenuation $k_i \approx 0.1$, which are not able to reconstruct the evanescent field related to the complex waves. On the contrary a $\gamma = 0.5$ retains all the solutions with an attenuation $k_i < 0.7$ which is sufficient to accurately estimate (err.$k_i \approx 1\%$) the evanescent modes up to $k_i < 2$. A quantitative evaluation of the discrepancies obtained for selected propagative low damped solutions and complex/edge waves are given in Table 6. The modes selected for the error analysis are highlighted by the dashed lines in Figs.31. As regards to the computational saving of the method, the benefits of the CMS-Wave reduction for this periodic system are hidden by the excellent performance of the CMS alone, which is able to reduce the computational time of approximately two order of magnitudes. However, the relative time reduction between the CMS and

Table 6: Stubbed Beam: Error analysis for propagative low damped solutions and complex/edge modes.

	Err. [@f/a=1000 m/s]						Computational time
	PM1	PM2	PM3	EM1	EM2	EM3	time fract.
(Err.kr, Err.ki)	(Err.kr, Err.ki)	(Err.kr, Err.ki)	(Err.ki)	(Err.ki)	(Err.ki)	time fract.	
Full Model (FM)	-	-	37 s (IS)	-	-	-	-
60 F.I. modes ($\beta = 0.9$)	0.3 %, 1.2%	0.2 %, 10 %	0.5 %, 3 %	6%	4 %	12 %	1.4%
60 F.I. modes ($\beta = 0.5$)	0.2 %, 0.9 %	0.1 %, 0.3 %	0.1 %, 0.4 %	1%	1 %	1.46%	

the CMS-Wave reduction of approximately 50% is an indication of the potential of the method when more complex periodic systems are considered.

4.3.3 *Conclusions*

In this Chapter, a CMS-Wave reduction technique has been presented and applied to the study one-dimensional periodic viscoelastic media with the aim of analyzing both dispersion $k_r(\omega)$ and attenuation $k_i(\omega)$ properties of such waveguides. The method combines a reduced unit cell description by the CMS method with a frequency interpolation scheme resulting from a wave-based reduction. The criteria to select appropriate wave shapes to obtain accurate predictions of both light and highly attenuated waves have been discussed using two numerical applications, i.e. a uniform structural waveguide and a periodic stubbed beam. For the uniform structural waveguide, a selection of least decaying propagative waves ($\gamma = 0.9$) is sufficient to ensure an accurate prediction of real dispersion and attenuation of guided waves for long-range NDE applications. Conversely, for periodic viscoelastic waveguides, the investigation of the evanescent/complex field requires a basis of wave shapes that also contain high damped solutions. It is here remarked that a similar wave basis is also required when the wave reduction is performed without a preliminary CMS transformation (as in Ref. [75]), and damped periodic systems are of interest. Further investigations are necessary to extend the criteria for the choice of the wave basis to the case of viscoelastic two-dimensional media.

Part II

PERIODIC AND LOCALLY RESONANT MEDIA FOR SEISMIC WAVE ATTENUATION: A SEISMIC METABARRIER

5

PERIODIC AND LOCALLY RESONANT MEDIA FOR SEISMIC WAVE ATTENUATION: AN OVERVIEW

ABSTRACT

In this Chapter, an overview of the most recent developments in the field of seismic wave attenuation using periodic and locally resonant media is provided. Periodic and locally resonant media for earthquake engineering applications, which are sometimes referred as "seismic metamaterials", are a fast developing research topic, as demonstrated by the growing related literature published in the last two decades. As such, a comprehensive review of the relevant contributions in this field is needed to summarize the state-of-the-art and understand the possible research directions to be explored in the next years. First, a short overview of the modern seismic design criteria and protective devices already available for the design of seismic resistant structures is provided. Then, different strategies to control the propagation of seismic waves utilizing artificial periodic/resonant structures in the soil or periodic/locally resonant foundations are described, starting from the first attempts of the early 1960's using single trenches and holes to the recent ideas for "cloaking" entire urbanized areas.

5.1 INTRODUCTION: A SHORT HISTORICAL PERSPECTIVE ON EARTHQUAKE ENGINEERING

Earthquake engineering is a multidisciplinary subject which aims at improving the resistance of man-made structures against earthquake events. The history of earthquake engineering goes back to the centuries as testified by the conscious attempts made in ancient Greece and China to improve the resistance of temples and monumental structures. However, it is from the end of 19th century that some European engineers started to designing structures accounting for the horizontal loads generated by a seismic event [92]. After the three major earthquake events of 1906 in San Francisco (US) (Magnitude $M_w = 7.9$), 1908 in Messina (Italy) (Magnitude $M_w = 7.5$) and 1923 in Kanto (Japan) (Magnitude $M_w = 8.3$), commissions and research society (as the Seismological Society of America and the Earthquake Research Institute in Japan), were founded to provide first prescriptions for earthquake resistant structures. Building codes started to adopt specific prescriptions for equivalent lateral static loads applied to the structures, and later on, appropriate factors were introduced to account for the peculiar dynamic characteristics of the buildings, related for example to their height and flexibility. However, only after the 1950s, structural dynamics concepts started to be systematically applied to the field of earthquake engineering, with several publications and books published in the 1960s on the topic [92]. From the 1960-70s earthquake engineering started to evolve as a multidisciplinary approach to reduce the risks related to seismic events. In the early 70s, such risks were identified with the life safety of building occupants. Later on, also financial risks and risks of disruption of normal life for extended periods of time were encompassed. At the present *"earthquake engineering encompasses multidisciplinary efforts from various branches of science and engineering with the goal of controlling the seismic risks to socio-economically acceptable levels"*, as excellently summarized by Bertero (1992).

In the last two decades, an approach toward the design of earthquake resistant structures for different levels of acceptable risks has been developed under the name of Performance-Based Seismic Design (P-BSD). Within the P-BSD, different Performance Objectives (POs) can be established for different levels of seismic ground motion (i.e. different levels of hazards), which in turn require appropriate seismic provisions to be achieved. Performance Objectives can range between minimum code requirements, like the avoidance of collapse under very rare earthquakes, to no damages at all under the same rare seismic events. Standard seismic provisions could result to be inadequate to meet high POs. For these cases, additional prescriptions are needed, based for example on the use of seismic isolation systems or energy dissipation devices.

5.2 STANDARD AND MODERN STRATEGIES FOR EARTHQUAKE RESISTANT STRUCTURES

Performance-Based Seismic Design (P-BSD), proposed by the SEAOC Vision 2000 Committee in 1995, aims at designing predictable and controlled structural performances within established levels of risks [92]. Within this framework, specific Performance Objectives, identified in terms of life-safety, damageability, and functionality of the building can be selected for different levels of seismic hazards, accounting also for the "importance" of the building itself (see Fig 32). For example, for a building of basic "importance" (i.e. apartment, detached house), the P-BSD identifies the following Performance Objectives:

- *Fully Operational* performance level, i.e. no damages either at structural and non-structural components, under frequent earthquakes;
- *Operational* performance level, i.e. structure undamaged with only minor damages at the non-structural components, for an occasional earthquake;
- *Life Safety* performance level, i.e. the safety of the occupants has to be guaranteed, for a rare earthquake;
- *Near Collapse* performance level for a very rare earthquake, i.e. the global stability of the structure has to be guaranteed.

Such performance levels are the results of a compromise between a safe and cost-effective seismic design of structures.

The definition of different performance objectives, characterized by increasing levels of damage in the structure, naturally implies the exploitation of the inelastic response of the structure to accommodate part of the input energy provided by the seismic event. As such, the structure should be designed to ensure adequate ductility for a controllable/predictable seismic behavior in the inelastic regime. However, material elasticity and related structural damages are not always desirable/acceptable and appropriate devices to control (reduce) the damage of the primary structural members as well as non-structural members need to be used. In particular, four distinct classes of protective devices are now available [92]:

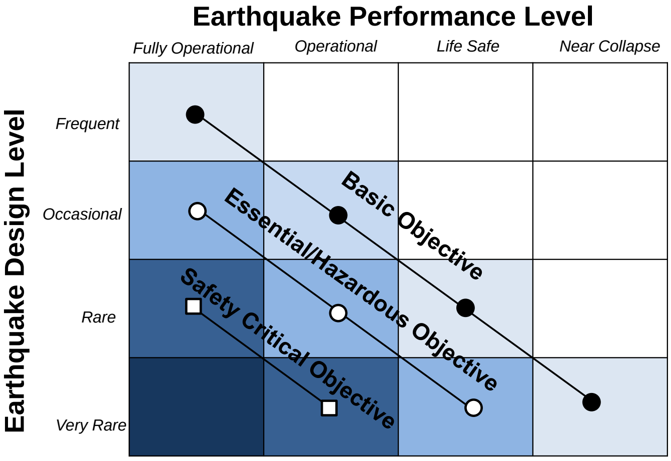
Earthquake Performance Level
Fully Operational
Operational
Life Safe
Near Collapse
Earthquake Design Level
Frequent
Occasional
Rare
Very Rare
Basic Objective
Essential/Hazardous Objective
Safety Critical Objective

Figure 32: Performance objectives for buildings (Adapted from SEAOC 1995).

- Seismic isolation systems which are designed to decouple the structure from the most damaging components of the seismic input. The isolation system is typically realized by supporting the structure on discrete isolators made of elastomeric, friction or sliding devices, to shift the fundamental horizontal frequency from the predominant component of the ground motion.

- Passive energy dissipative systems designed to add significant damping to the structure for dissipating part of the seismic input energy and reduce the structural response (and damage). Viscoelastic (solid and fluid) dampers, metallic-yielding and friction based devices are examples of dissipative devices.

- Active control systems which counteract the earthquake-induced forces by imposing a set of forces to the structures using computer-controlled actuators.

- Hybrid control systems, obtained as a combination of passive and active systems with reduced power demands and higher robustness compared to the related active systems.

The above solutions have proved to be effective in controlling the seismic response of building and reducing their damages and are paving the way for the earthquake-proof design of new structures. However, in spite of the available technical solutions for seismic resistant structures, earthquakes remain the most harmful natural hazards. In fact, only a minor portion of the current building heritage is designed and realized according to current seismic provisions, even in some first world countries. Indeed, the possibility of retrofitting the whole existing building heritage with advanced protective devices is remote and new design strategies to enhance the safety of existing urbanized areas are highly desirable. In this regards the idea of designing a "defense structure" to prevent the arrival of seismic waves at vulnerable buildings could represent a new paradigm of seismic isolation, grounded on the physical concepts established in the field of phononic crystals and acoustic metamaterials to control the propagation of elastic/acoustic waves.

5.3 NEW DEVICES AND STRATEGIES TOWARDS THE CONTROL OF SEISMIC WAVES

Seismic waves are mechanical vibrations that travel through the earth carrying the elastic energy released during an earthquake. When a seismic event occurs both body waves and surface wave are generated. As in any solid, body waves traveling in the interior of the earth are of two types: fast longitudinal (L) or primary waves, for which the particles motion induces compression and rarefaction of the material along the direction of propagation and slower shear (S) or secondary waves, where particles move in the direction perpendicular to the wave propagation. The perpendicular planes where the particle motion occurs allows distinguishing between the two components of the shear waves, namely vertical (SV) and horizontal (SH).
Surface waves arise due to the interaction of body waves and the free surface or superficial layering of the earth. They travel at a lower speed than the shear waves and are characterized by an exponential decay with the depth. Surface waves are prominent at longer distances from the earthquake source where they may be responsible for peak ground motions [93]. Rayleigh waves and Love waves are the most relevant type of surface waves. Rayleigh waves are produced by the interaction between longitudinal waves and vertical shear waves at the free surface of a homogenous soil, which results in a combined horizontal and vertical particle motion in an elliptical retrograde shape [94]. Love waves arise when a low velocity (i.e. a softer) superficial layer lies over high velocity (i.e. stiffer) sub-layers, a situation that typically occurs in the upper layers of the earth crust. The particle motion of a Love wave lies in the horizontal plane perpendicular to the direction of propagation (i.e. transverse waves).
Both bulk and surface waves generated during an earthquake have their major fre-

quency content below 20 Hz [93], with related wavelengths varying from few tens to some hundreds of meters depending on the wave velocities of the uppermost crust layers. Moreover, the same frequency content roughly corresponds to the frequency range of the fundamental modes of many man-made structures, which results in large, possibly unbearable, dynamic actions on the structures.

Several research groups have tried to "translate" phononic and acoustic metamaterial concepts at the geophysical scale to achieve control of the propagation of such low-frequency seismic waves and prevent their arrival at vulnerable structures. The resulting applications, typically obtained by artificially patterning the soil with holes, piles or resonant structures, are commonly referred in the literature as "seismic metamaterials" to underline the connection with the phononic/metamaterial research field. Indeed, the idea of creating wave barriers in the soil is not originally coming from the phononic/acoustic metamaterial community, since several researchers in the geotechnical field performed experimental and theoretical studies on the attenuation performances of trenches and piles for anthropic (traffic or machinery) induced vibrations in soils.

In the next section, the major contributions presented in the above mentioned research fields are reviewed to summarize the state-of-the-art techniques for the control and attenuation of seismic waves.

5.3.1 *Periodic structures for seismic wave attenuation*

The first attempts to design wave barriers made of trenches or sheet-pile in soils for vibration isolation purpose are from the 1960s [95]. Barkan [96] in 1960, reported some unsuccessful applications of soil-trenches for vibration isolation motivating the poor performance of such barriers with the lack of rationale design according to surface wave propagation theory. In 1968 Woods [95] tried to investigate the scattering of trenches within the context of Rayleigh wave propagation. Trenches with different dimensions were analyzed together with sheet-wall barriers of the same size (see a schematic of the analyzed trench in Fig. 33). Series of field model tests were performed to investigate the trenches performance in terms of reduction in vibration amplitude, shape, and extent of the screened zone. A minimum dimensionless trench height $h/\lambda_r = 0.6$ (where λ_r is the Rayleigh wavelength) was prescribed for achieving a significant attenuation of the soil ground motion, while no important influence for the trenches width was identified.

From this seminal experimental work, several analytical, numerical and experimental studies on the propagation of surface waves across barriers and in-filled trenches followed. Aboudi [97] used perturbation expansion and Finite Difference Method to obtain approximated solutions of Rayleigh wave diffraction over a thin barrier. Haupt [98] employed a FE formulation in the frequency domain to assess the attenuation of surface waves from open and in-fill trenches. Similarly, Segol et al. [99] used FEM and a two-dimensional slab-type model for studying vibration screening by open trenches and in-filled trenches in layered soils, with results in

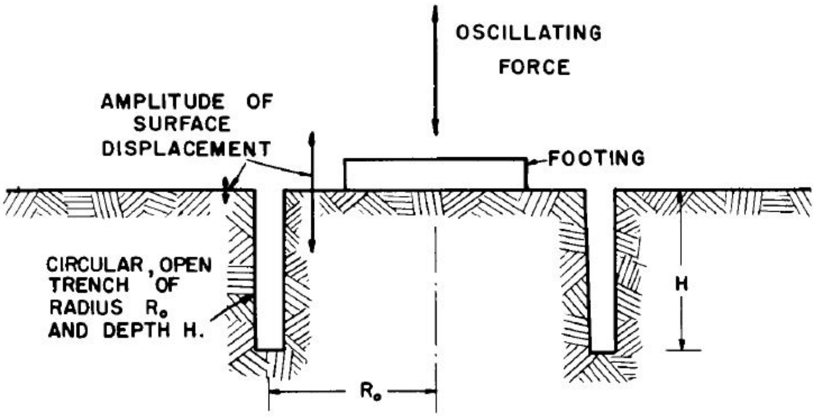
OSCILLATING FORCE
AMPLITUDE OF SURFACE DISPLACEMENT
FOOTING
CIRCULAR, OPEN TRENCH OF RADIUS R₀ AND DEPTH H.
H
R₀

Figure 33: Schematic of the investigated soil trench. (From Ref. [95]).

qualitative agreement with Woods's findings. Conversely, Fuyuki and Matsumoto [100] investigated surface wave propagation through rectangular open trenches showing significant influence on the effect of the width, in contrast to what shown by Woods and Segol. Beskos [101] analyzed open and infilled trenches in linear elastic or viscoelastic, homogeneous and isotropic using an efficient Boundary Element Formulation highlighting the superior performances of open trenches compared to identical infilled ones. Finally, more recent numerical studies focused on the problem of soil vibrations induced by high-speed trains investigating optimal solutions for different train speeds and load frequencies (see for example [102–104]).

Besides the numerous studies on trenches-piles presented in the geotechnical community, the first attempt to exploit the collective scattering effect generated by a periodic structure in soils was proposed by Mesenguer et al. [13], which experimentally and numerically analyzed the attenuation of surface elastic waves by a periodic array of cylindrical holes in a meter size marble quarry. Honeycomb and triangular lattice arrangements of centimeter-size holes were analyzed, both able to open up absolute Bragg-scattering band gaps for surface waves in the kHz range. By scaling the results obtained for such centimeter-size periodic system in a marble quarry, the authors predicted the possibility of attenuating real scale surface waves in the low frequency (1-10 Hz range) with giant (>200m) periodic structures. Such huge, basically unfeasible, periodic structures are indeed required to manipulate long wavelength low frequency surface waves traveling in high stiff soil (soil shear velocity $c_s > 3000$ m/s).

Indeed, when higher-frequency ranges are of interest, as in the case of anthropic vibrations generated by the railways, the use of smaller, meter size, periodic structures can be adequate to effectively screen surface waves, as demonstrated by Huang et al. [105]. In their work, the authors numerically investigated the use of periodic pile barriers in a triangular lattice arrangement, showing significant attenuation (20 dB) in a band gap frequency range consistent with mid-frequency

railway vibrations [20-50 Hz].
Nonetheless, for softer sedimentary soils ($c_s < 500$ m/s) which usually characterize the upper crust layers, periodic structures of meter size dimensions can be envisioned also for controlling the propagation of seismic surface waves. This possibility was experimentally investigated by Brüle et al. in 2012 [45] with a real scale seismic test carried out using seismic waves generated by a monochromatic vibrocompactation probe at 50 Hz (Fig. 34). The test zone located in the alpine city of Grenoble (France), consisted in a regular rectangular mesh of vertical cylindrical boreholes of 0.32 m in diameter and 5 m depth, located at a relative distance of 1.7 m. The aim of the test was to point out the possibility of exploiting simple linear elastic phononic plate models to predicted the shielding capabilities of such periodic grid in soils.

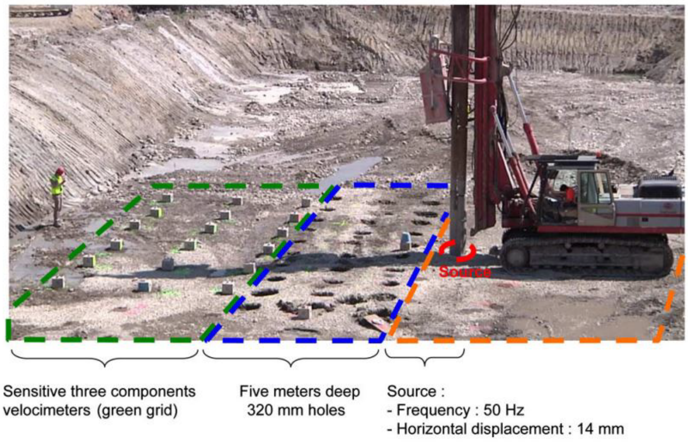
Source
Sensitive three components velocimeters (green grid)
Five meters deep 320 mm holes
Source :
- Frequency : 50 Hz
- Horizontal displacement : 14 mm

Figure 34: a) The test zone located in the alpine city of Grenoble (France). (Adapted from Ref. [45]).

Indeed, soils can be characterized by inhomogeneous stratification, anisotropicity, nonlinearities, which could strongly influence the propagation pattern of waves. However, the measurements of the ground velocities in the presence of the meter size phononic structure were in agreement with numerical simulations using the simple plate model. For complex materials such as soils, this large-scale experiment paved the way for the realization of "seismic metamaterials" for civil engineering applications. Besides the relevance of such work, the frequency range targeted in the test was still too high compared the relevant frequency content of seismic waves (<20 Hz).
More recently, Miniaci et al. [106] extensively investigated the feasibility of different period structures (cross-shaped, hollow and locally resonant) to attenuate both Rayleigh and bulk waves in the 1 to 10 Hz frequency range with extended FE numerical simulations. Results revealed that in really low stiff sedimentary soil ($c_s < 100$ m/s) both surface and bulk seismic waves can be considerably attenu-

ated uilizing phononic seismic metamaterials with small size unit cell dimensions (≈ 10 m).

A parallel/complimentary phononic-based strategy aimed at designing vibration immune buildings consists in the use of periodic foundations to isolate the building superstructure. This concept was numerically investigated by Bao et al. [107] and later experimentally tested by Xiang et al. [108] with laboratory reduced scale models. Numerical showed that periodic foundations obtained by subsequent layers of concrete and rubber (materials typically used in civil engineering) can open up band gaps in the low frequency range [1-10] Hz with significant attenuation when more than 3 unit cells are used. Experimental tests performed on reduced scale 3-storey steel frame attached to a periodic concrete-rubber foundation confirmed the numerical findings (see Fig. 35).

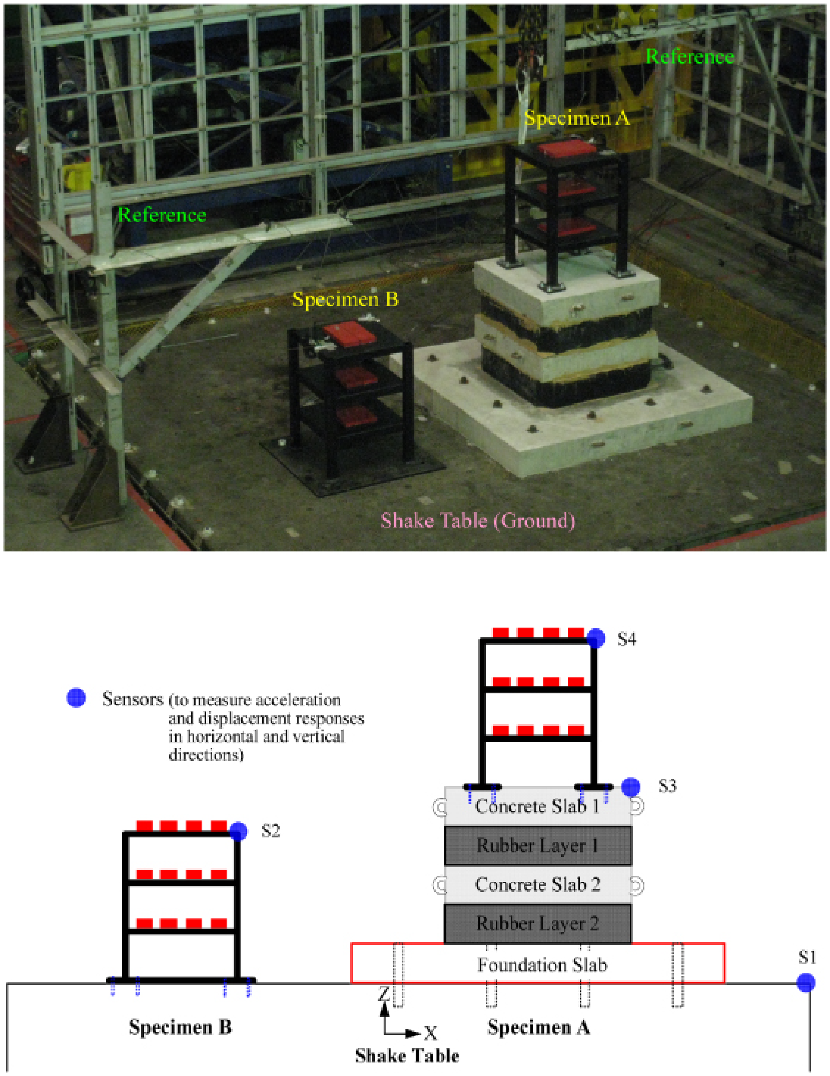
Reference
Specimen A
Reference
Specimen B
Shake Table (Ground)
S4
Sensors (to measure acceleration and displacement responses in horizontal and vertical directions)
S3
Concrete Slab 1
Rubber Layer 1
Concrete Slab 2
Rubber Layer 2
Foundation Slab
S2
S1
Z
X
Specimen B
Specimen A
Shake Table

Figure 35: Test setup for specimens A (with a periodic foundation) and B (without a periodic foundation). (From Ref. [108]).

However, similarly to the case of phononic wave-barriers, phononic foundations of considerable dimensions need to be designed to achieve low-frequency band gaps. Nonetheless, periodic foundations are appropriate for the design of new buildings, for which standard (and possibly economically convenient) isolation systems are already available.

In summary, although the use of phononic base concepts can lead to significant attenuation of seismic induced vibrations, the dimensions of the required periodic structures, dictated by the wavelength of the seismic waves, are almost prohibitive for practical applications or limited to really low-stiff sedimentary deposits. For such reasons design strategies based on the use of sub wavelength resonators may represent a more feasible solution for seismic waves control.

5.3.2 *Resonant structures for seismic wave attenuation*

Locally resonant metamaterials allow achieving control on the propagation of low-frequency long-wavelength elastic waves exploiting the equivalent effective properties assumed by the supporting medium around the material resonance frequency. The first attempt to make use of such properties in the context of seismic wave control is the one proposed by Kim et al. [109], which consists in an earthquake proof barrier realized by an array of Helmholtz resonators (see Fig. 36). The array

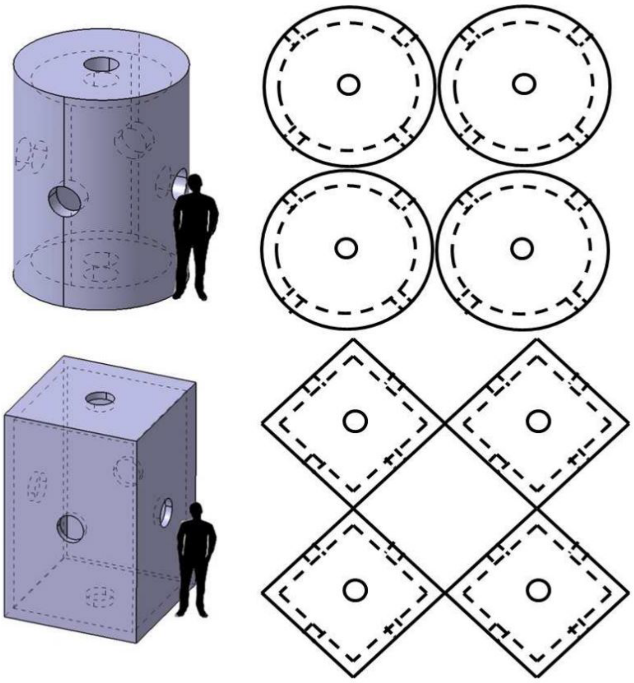

Figure 36: Schematic of the Helmotz resonators for seismic attenuation. (From Ref. [109]).

of Helmholtz resonator attenuate shear seismic waves by means of an equivalent negative shear modulus. When the shear modulus becomes negative, the shear velocity and so the refractive index become imaginary, and the wave mode becomes evanescent. The evanescent wave field implies that seismic shear waves amplitude is attenuated. From a physical perspective, the negative shear modulus is generated by the resonance of sound waves generated and accumulated in the Helmholtz resonators which react against the applied pressure at some specific frequency ranges. Although the working principle of such wave barrier is grounded on physical concepts demonstrated for elastic waves, no experimental demonstration has been given for such barrier.

In parallel to the concept of negative elastic moduli, an effective negative inertia can be used to attenuate the propagation of elastic waves. Such equivalent property can be obtained by embedding locally resonant masses in the supporting media. In the context of seismic wave control, meter-size locally resonant structures have been proposed by Krodel et al. [46] to control the propagation of seismic waves. The designed "metastructure"’ consists of arrays of resonant units, able to reflect incident longitudinal and shear seismic waves. Each resonant unit consists of a heavy steel cylindrical mass, suspended by commercial elastic rubber bearings encased in an external concrete cylindrical shell (Fig. 37).

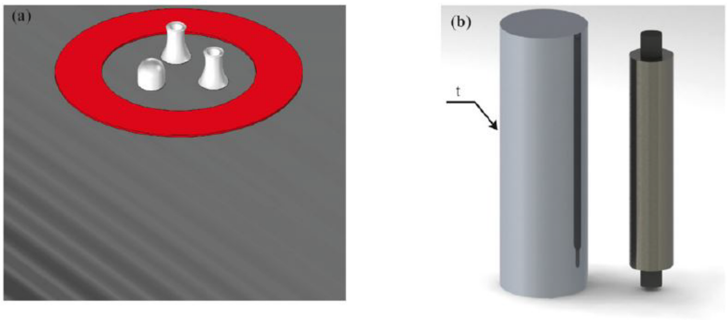

Figure 37: a) Schematic diagram showing vulnerable buildings (white structures) that are endangered by incoming seismic waves. The red ring around the buildings represents the area with buried local resonators. b) Components in a resonator, consisting of a cylindrical hollow tube (left), containing a heavy bulk cylinder (right, shown separately) suspended by polymeric springs (black). (From Ref. [46]).

The authors analyzed the attenuation capabilities of this seismic barrier against longitudinal and shear seismic excitations in the frequency range [1-10] Hz using an equivalent 2D FE model. Arrays of units resonating at different frequencies were exploited to broaden the frequency range of attenuation provided by the single frequency resonators. This concept, proposed earlier in acoustic systems as rainbow trapping [110], is based on the idea of splitting propagating waves into a spatial spectrum. The principle can be translated to seismic excitations, such that the different frequency components of the incident wave are attenuated by different spatial regions of the barrier. The design concept was verified in a scaled experimental setup, embedding scaled metastructure in a box of sedimentary soil. The attenuation capabilities and the feasibility of a similar resonant metabarrier have been recently investigated in the really lower frequency range [0.5 5.0] Hz using simplified mass-in-mass 1D analytical approaches [111] and full 3D FE simulations [112]. Cacciola et al. [113], instead, proposed the use of a single resonant structure, referred as ViBa (Vibrating Barrier), designed for absorbing a portion of the shear ground motion energy directed to the building. In their numerical and experimental analysis, the authors considered the full "building–soil–vibrating structure" interaction to investigate the reduction in the building acceleration response due to the vibration barrier mitigating effects.

Far from the earthquake epicenter, bulk waves convey just a minor portion of the energy released in a seismic event, which travels, instead, in the form of surface waves. To this reason, adequate strategies/devices have to be designed to target specifically surface wave propagation. In this regards, Colombi and coauthors recently showed that Rayleigh waves interacting with an array of trees can create hybridization band gaps [47, 114], where surface waves are attenuated. The longitudinal resonances of trees couple with the vertical component of the Rayleigh wave and attenuate the surface ground motion by redirecting part of the elastic energy into the bulk (Fig. 38) (an extended analytical study on the surface-to-shear wave conversion mechanism can be found in Ref. [115]). Such surface-to-shear wave conversion appears particularly suitable for seismic isolation given that earthquake energy is redirected into the depth and not back reflected on the surface where it could remain harmful for other buildings.

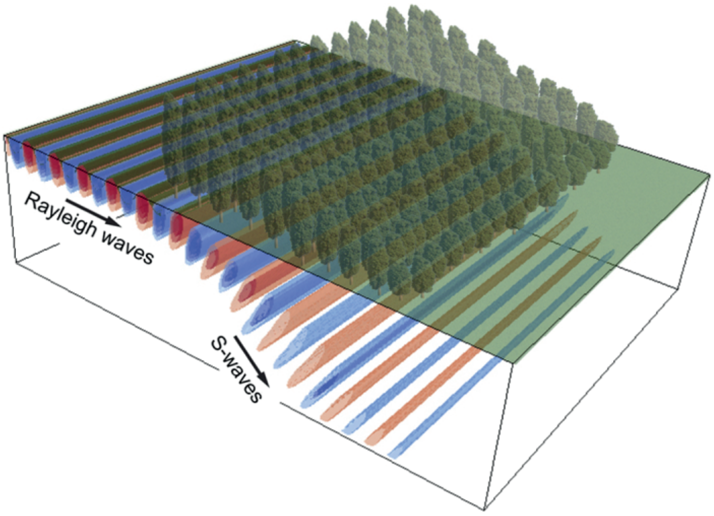

Figure 38: Surface-to-shear waves conversion of a forest. (From Ref. [114]).

However, this natural "forest metamaterial" showed a working frequency range around 40 Hz, well above of the relevant seismic frequency range.

As for the phononic case, in parallel to locally resonant seismic barriers, resonant foundations have been proposed to isolate the building superstructure. Among the others, Cheng and Shi [116, 117] numerically investigated the performance of local-resonant panels and local-resonant plate foundations, made of concrete and rubber, showing attenuation zones in the low-frequency region (below 20 Hz), useful for mitigating vibrations. Local resonances have also been designed with isochronous mechanical oscillators realized with spheres rolling over a cycloidal trajectory [118].
Besides the promising efficiency of such resonant foundation systems, the use of these devices would remain limited to new buildings, similarly to related periodic foundations, for which standard isolation and energy dissipation devices possibly represent a more competitive/reliable solution.

5.3.3 *Further strategies to control seismic waves: Lensing, cloaking, and clamped metamaterials*

Strategies to control the propagation of elastic waves are not limited to the use of phononic and locally resonant material to create bulk and surface wave band gaps. Since elastic waves are subjected to the Snell's law which governs the wave refraction according to the material refractive index, gradient index lenses (GRIN), obtained by varying the refractive index of the medium, can be used to steer elastic waves [119]. This concept has been translated to the geophysics scale to design seismic lenses able to reroute wave around buildings [120]. As GRIN lenses are not based on subwavelength control of wave propagation, giant lenses (>100 m) would be required (see Fig. 39), making questionable their use in practical applications.

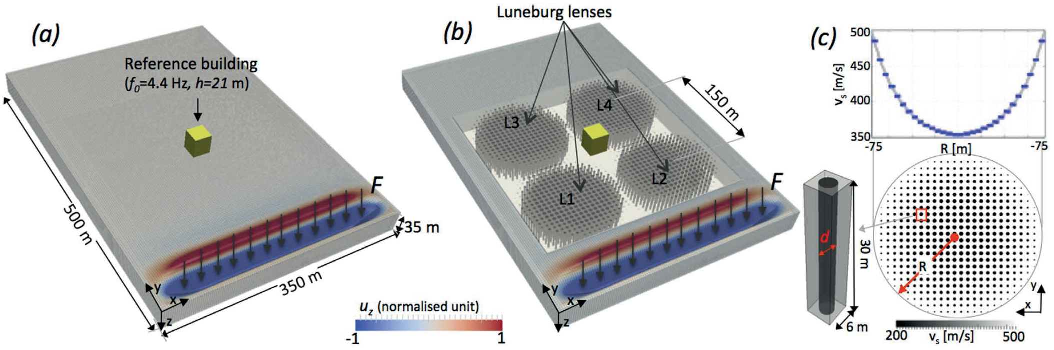

Figure 39: Composite soil lenses. (From Ref. [120]).

Similarly, concepts of transformation optics have been applied to the elastodynamic domain to design cloaks for flexural waves in thin plates [121], as well as Rayleigh waves in semi-infinite domain [122]. A cloak is a structure which aims at making a region of a medium effectively "invisible" to waves by rerouting the wave pattern around the structure (see Fig. 40 as an example of a cloak for flexural waves [121]). However, similarly to the case of GRIN lensing, the complex structure required to realize the cloak would result in a protecting system of the order of a hundred meters for geophysical applications.

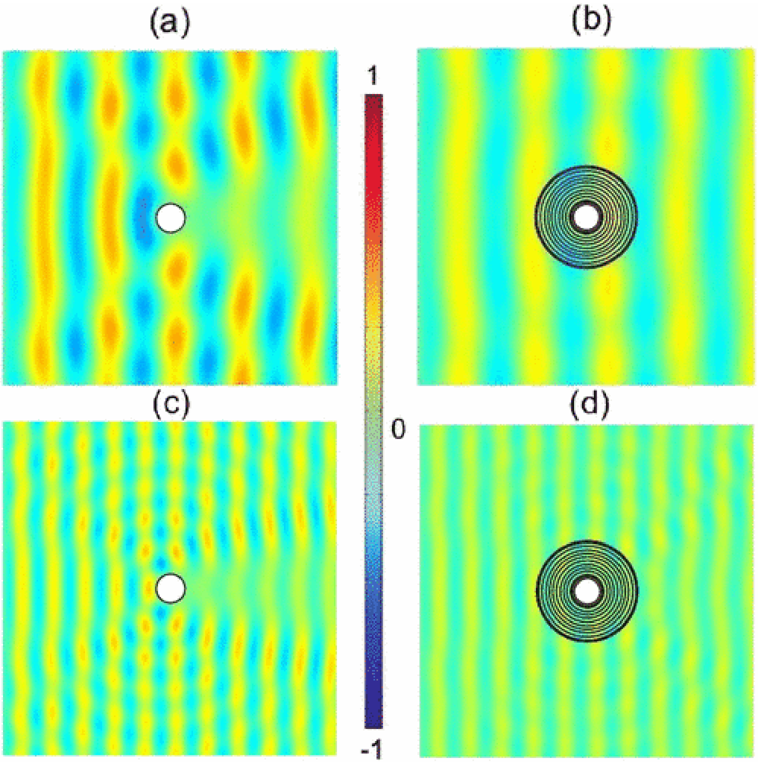

Figure 40: Examples of uncloaked (a,c) and cloaked objects (a,c). (From Ref. [121]).

Finally, "clamped seismic metamaterials" [123] have been recently proposed to create low and broad frequency stop bands in shallow sedimentary deposits. These metamaterials, as suggested by the name, consist in a periodic arrangement of stiff inclusions (for example concrete piles) in sedimentary soil clamped to the bedrock. The stiff inclusions realize an elastic layer periodically clamped to a rigid substrate which is characterized by a zero frequency stop band, suitable for seismic wave attenuation. This concept has been applied to the case of a sedimentary basin of 15 meters deep, where a theoretical zero frequency stop-band covering the frequency range of 0 to 30 Hz has been identified.

5.4 CONCLUSIONS

In this Chapter, the major contributions in the field of wave propagation control for earthquake engineering applications have been reviewed. Earthquake engineering, born as a branch of civil engineering to account for seismic induced loads, has now become a multidisciplinary subject which needs to encompass several branches of science, economics, and engineering to reduce the seismic risk at acceptable levels. Major achievements have been reached employing modern seismic design criteria and isolation/dissipation devices which now almost ensure the possibility of designing safe buildings and infrastructures in seismic areas. However, further efforts are still required to ensure the same level of safety for the existing building heritage, not designed with modern seismic design criteria. New design strategies based on the control of seismic waves exploiting phononic and metamaterial concepts can be of help for this task and the first achievements by the seismic metamaterial community show a potential for reaching this scope. In particular, locally resonant materials/structures which are able to control the propagation of waves with sub-wavelength units, represent a more viable solution for earthquake engineering applications. Although numerous promising solutions have been recently presented to control the propagation of seismic waves, most of them are still limited to theoretical formulations which need an experimental verification and a robust feasibility analysis to become an effective alternative for earthquake proofing of large urbanized areas.

6

AN ENGINEERED METABARRIER FOR SEISMIC SURFACE WAVE ATTENUATION

ABSTRACT

In this Chapter [1]*, a seismic metabarrier to attenuate the propagation of Rayleigh waves is presented. The metabarrier is able to convert seismic Rayleigh waves into shear bulk waves which travel away from the ground surface. The metabarrier is realized by burying sub-wavelength resonant structures under the soil surface. Each resonant structure consists of a cylindrical mass suspended by elastomeric springs within a concrete case and can be tuned to the resonance frequencies of interest. The design allows controlling seismic waves with wavelengths from ten-to-hundreds meters with meter-size resonant structures. An analytical model based on effective medium theory able to capture the wave conversion mechanism is developed. The model is used to guide the design of metabarriers for varying soil conditions and is validated using finite-element simulations. Numerical simulations show the possibility of reducing the surface ground motion up to 50% in frequency regions below* 10 Hz*, relevant for the protection of buildings and civil infrastructures. A scaled experimental setup with centimeter-size resonators is realized to validate the numerically predicted ground motion attenuation. The experimental data confirm the wave conversion mechanism and provide indications consistent with the numerical data for the achievable ground motion attenuation by the metabarrier.*

6.1 INTRODUCTION

The study of surface waves and the possibility of achieving control of their propagation using phononic crystals, metamaterials and more in general artificial composite media has attracted the attention of numerous researchers in the last decades, who applied these concepts across different length scales. At the micro scale, the confinement of surface acoustic waves (SAW) finds application in the context of micro-electro-mechanical systems (MEMS) for advanced wave filtering applications [125]. SAW filters have been obtained for example by exploiting the full Bragg scattering band-gaps of air/silicon phononic crystals [126] and piezoelectric phononic crystals [127]. Similarly, numerical and experimental studies have reported the possibility of filtering the propagation of surface waves utilizing periodic arrangements of pillars [34, 128] or by the contact of silica microspheres arranged in a two-dimensional crystal over a substrate [129]. Both pillars and microspheres generate surface band gaps thanks to the interaction of their local resonance modes with surface Rayleigh waves, which allows filtering waves in the sub-wavelength regime.

---

[1] The results presented in this Chapter are largely based on a recent work published by the author [124].

A similar behavior has been experimentally observed at the geophysical scale for surface waves traveling within a forest [47, 114]. Rayleigh waves interacting with an array of trees can create surface wave band gaps, where surface waves are converted into shear ones which travel away into the soil bulk. This surface-to-shear wave conversion is promising for earthquake engineering applications but occurs in nature in the frequency range around 40 Hz (i.e. the typical longitudinal frequency of medium size, 15 m height, trees), thus well above of the relevant seismic frequency range. Indeed, one can envision an engineered array of vertical pillars to reach the desired frequency target. Nonetheless, a forest of man-made pillars would result in a strongly intrusive and practically unfeasible solution in a highly urbanized context.

For this reason, a more feasible and effective seismic metabarrier in which soil-embedded surface resonators are used to redirect the surface waves into the bulk is here presented. Soil-embedded resonators, with a single [111] or varying natural frequencies [46], can target the required frequency range and constitute the building block of the seismic metabarrier. In what follows, first an analytical model to guide the design of the resonant structures of the metabarrier is presented. Next, through FE numerical simulations the effectiveness of the seismic metabarrier in attenuating surface ground motion within the 1–10 Hz range is discussed. Finally, Rayleigh waves attenuation is demonstrated on scaled experiments, which quantitatively agree with the attenuation predicted by the numerical simulations.

6.2 CONCEPT

A seismic metabarrier consisting of an array of resonators buried at the soil surface around sensitive buildings (Fig. 41) is here proposed as an innovative isolation strategy for seismic surface waves. The resonant units are realized with materials commonly used in civil engineering and construction: each resonator contains a heavy cylindrical mass in steel (Young's modulus $E_s = 210$ GPa, Poisson's ratio $\nu_s = 0.3$, mass density $\rho_s = 7800$ kg/m^3, with radius r_r and height h_r, and an overall mass m) encased in a concrete hollow tube ($E_c = 30$ GPa, $\nu_c = 0.3$, $\rho_c = 2500$ kg/m^3, with outer radius r_c and height h_c) and suspended by elastic bearings ($E_b = 1.9$ MPa, $\nu_b = 0.3$). Arrays of these resonators proved to be effective in attenuating shear and longitudinal seismic excitations at their horizontal resonances [46]. Here for each resonator, the horizontal, rotational and vertical mode of vibration, with their resonant frequencies f_h, f_r and f_v, respectively, are considered, as all the three modes are potentially excited by the elliptical surface motion of the Rayleigh waves, as shown in Fig. 41b. Variations in the resonator mass/geometry as well as in the bearing stiffness/dimensions allow tuning the resonance frequencies within the relevant spectrum of seismic events [1-10] Hz.

The resonators are designed to be embedded in low-speed sedimentary soils (e.g.

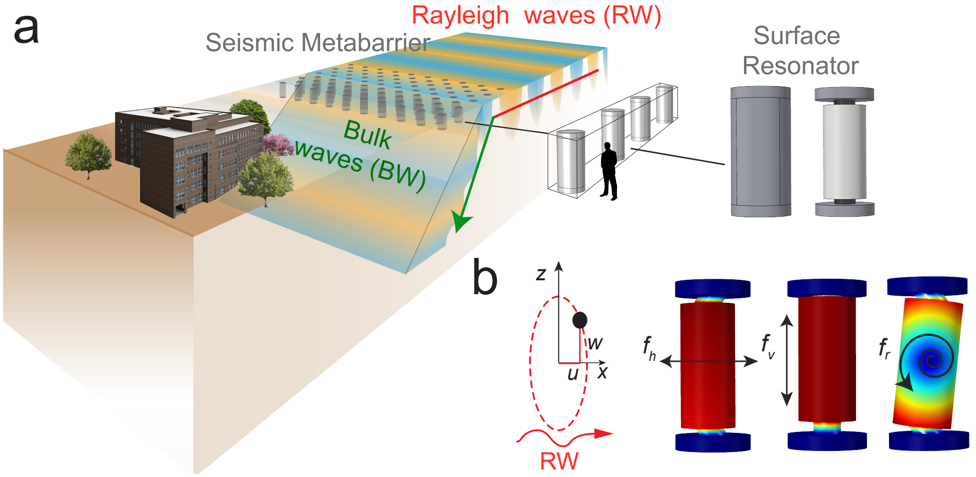

Figure 41: a) The seismic metabarrier. b) The resonant unit.

shear velocity $c_{S,s} = 100 - 500$ m/s) and can be arranged in different spatial configurations. Here, a triangular lattices arrangement, with a lattice constant a, is chosen as it ensures the highest density of resonators per unit area. The resonant unit dimensions and the resonator spacing a are subwavelength in the frequency range of interest, i.e. $\frac{a}{\lambda_r}, \frac{r_c}{\lambda_r} < \frac{1}{10}$, where $\lambda_r = \frac{c_{R,s}}{f}$ is the Rayleigh wavelength at given frequency f and $c_{R,s}$ the Rayleigh wave velocity in the sedimentary soil.

6.3 ANALYTICAL MODEL

The dynamic coupling between Rayleigh waves and surface resonant structures is studied by adopting and extending an analytical model, previously proposed to capture the interaction between surface acoustic waves and contact resonances induced by silica microspheres adhered to a substrate [129]. This analytical model is schematically shown in Fig. 42a: the soil is modelled by a semi-infinite homogeneous elastic space ($z<0$) and each resonator by a three degree-of-freedom (3-dofs) system (i.e. X, Z are respectively the horizontal and vertical displacements of the resonator relative to the ground surface, θ the rotation of the resonator with respect to its center of mass). Each resonator has a mass $m = \pi r_r^2 h_r \rho_s$, and a rotational inertia $I = m h_r^3/12$, where h_r is the height of the resonator. The resonator translational stiffness in the horizontal and vertical directions are:

$$
\begin{aligned}
& K_h = K_{h,1} + K_{h,2} \\
& K_v = K_{v,1} + K_{v,2} \\
\text{with} \quad & K_{h,i} = \frac{G_b A_{b,i}}{h_{b,i}} \quad i = 1,2 \\
\text{and} \quad & K_{v,i} = \frac{M_b A_{b,i}}{h_{b,i}} \quad i = 1,2
\end{aligned}
$$

where G_b and M_b are the shear and bulk moduli of the elastic bearing material and $A_{b,i}$ and $h_{b,i}$ the area and the height of the bearing. The resonator rotational stiffness is calculated from the bearing horizontal stiffness $K_{h,i}$ as:

$$K_r = \frac{K_{h,2}\alpha h_r^2}{(1+\alpha)} \quad \text{with} \quad \alpha = \frac{K_{h,1}}{K_{h,2}}$$

with the coupling between horizontal and rotational motion accounted by the coupled stiffness term (see Fig. 42b):

$$K_{rh} = K_{hr} = \frac{K_{h,2}(1-\alpha)h_r}{2}$$

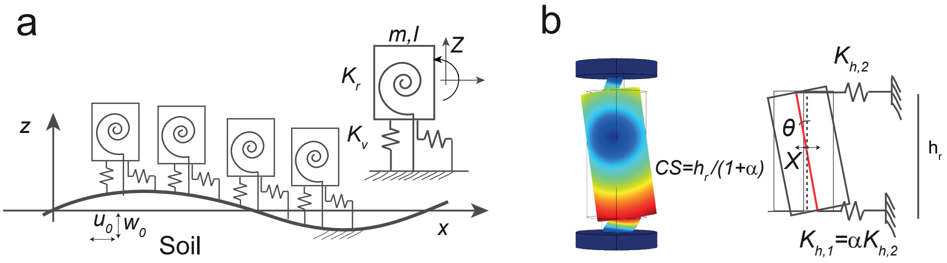

Figure 42: Schematic of the analytical model. a) Dynamic of 3DOFS resonators excited by Rayleigh waves. b) Rotational and coupled horizontal-rotational stiffness of the resonator.

The dynamic of such three-degree-of-freedom (3-DOFs) system is analyzed to derive the dispersion curve of the metabarrier. In particular, an approach with increasing levels of complexity is followed to understand the contribution of each resonant mode to the dynamic of the metabarrier subjected to surface waves. First, the coupling between Rayleigh waves and each single mode is analyzed separately (i.e. Rayleigh waves + single-dof (SDOF) resonator metabarrier). Next, a two degree-of-freedom (2DOFs) horizontal and vertical metabarrier model is used to understand the influence of the cross coupling between horizontal and vertical motion induced by the elliptical motion of the Rayleigh waves. Finally, the 3-DOFs resonator model is considered to obtain the full Rayleigh waves-metabarrier dispersion curve.

6.3.1 *Single-dof surface resonators: Behavior at vertical and horizontal resonance*

The dynamic of a vertical SDOF resonator (Fig. 43a.) subjected to a base excitation induced by the vertical soil surface displacement $w(z=0) = w_0$ is described by the equation:

$$m(\ddot{Z} + \ddot{w}_0) - K_v Z = 0 \tag{72}$$

The stresses exchanged from soil and resonator at the surface are calculated as:

$$\sigma_{xz,res} = 0 \quad \sigma_{zz,res} = \frac{F_v}{A} = \frac{K_v}{A} Z \tag{73}$$

where is $A = \frac{a^2\sqrt{3}}{2}$ the area of the triangular unit cell over which each resonator exerts its force. Here, it is implied that:

- the stress exerted by each resonator are uniform over the unit cell area;
- the particular lattice symmetry of the resonator does not introduce directional effects on the soil-resonator dispersive properties. This assumption has been numerically proven for resonant pillars over silica substrate in Ref. [34] and holds as long as the subwavelength regime of the resonators is respected.

The analytical expression for the surface wave dispersion relation is obtained following a standard approach for Rayleigh waves [94], where the stress-free boundary conditions are substituted with the stresses in Eq.73. The approach is detailed in the following.

Elastic waves traveling in the soil substrate are described by the wave equations:

$$\begin{aligned} \nabla^2 \phi &= \frac{1}{c_{L,s}^2} \frac{\partial^2 \phi}{\partial t^2} \\ \nabla^2 H_y &= \frac{1}{c_{S,s}^2} \frac{\partial^2 H_y}{\partial t^2} \end{aligned} \tag{74}$$

where $c_{L,s}$ ($c_{S,s}$) are the longitudinal (shear) velocity in the soil, t is time, ϕ and H_y are the dilatational and transverse potentials that for a semi-infinite elastic space take the form [94]:

$$\begin{aligned} \phi &= A e^{kz\sqrt{1-\frac{\omega^2}{k^2 c_{L,s}^2}}} e^{i(\omega t - kx)} \\ H_y &= B e^{kz\sqrt{1-\frac{\omega^2}{k^2 c_{S,s}^2}}} e^{i(\omega t - kx)} \end{aligned} \tag{75}$$

where ω is the circular frequency of the surface wave, k the wavenumber along the horizontal propagation direction (x) of the wave.

The vertical and horizontal displacement components u and w of the wave field relate to the potentials ϕ and H_y reads:

$$u = \frac{\partial \phi}{\partial x} - \frac{\partial H_y}{\partial z} \quad w = \frac{\partial \phi}{\partial z} + \frac{\partial H_y}{\partial x} \tag{76}$$

It is worth remarking that the potentials in Eq. 75 (and the related displacements u and w) are characterized by an inhomogeneous (exponentially decaying) shape in z, which confer the surface characteristic to wave solutions. Such property of the potentials hold true if the apparent wave velocity along the surface $c = \frac{\omega}{k} < c_{L,s}, c_{S,s}$.

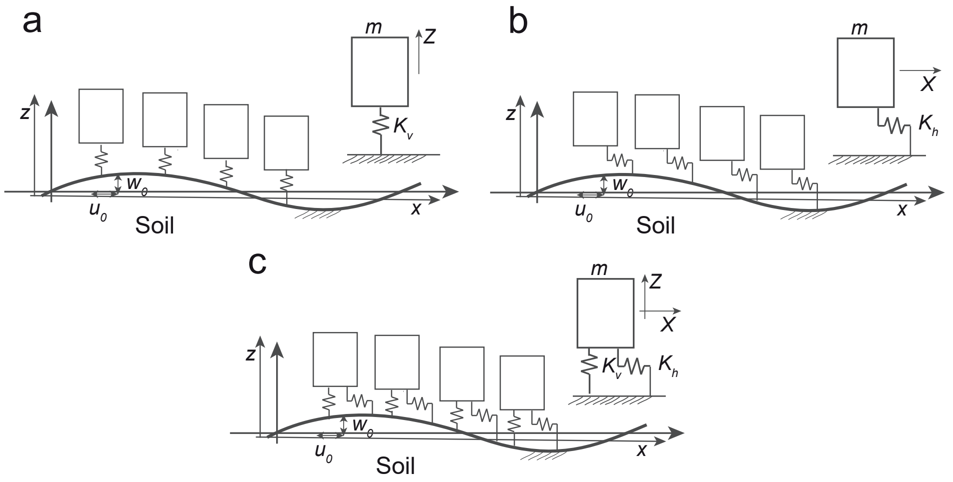

Figure 43: Simplified analytical models. a) SDOF vertical resonators excited by Rayleigh waves. b) SDOF horizontal resonators excited by Rayleigh waves. c) 2DOFs vertical-horizontal resonators excited by Rayleigh waves.

For the vertical motion of the resonator, a wave solution of the form $Z = Z_0 e^{i(\omega t - kx)}$ is assumed and substituted it into Eq. 72 to obtain the amplitude of the resonator vertical displacement:

$$Z_0 = \frac{\omega^2}{\omega_v^2 - \omega^2} w_0 \tag{77}$$

where $\omega_v^2 = \frac{K_v}{m}$ is the vertical eigenfrequency of the resonator. By substituting Eqs. 77, into Eq. 73, the stress boundary conditions in terms of vertical surface displacements w_0 are obtained:

$$\sigma_{xz,res} = 0 \quad \sigma_{zz,res} = \frac{F_v}{A} = \frac{K_v}{A} \frac{\omega^2}{\omega_v^2 - \omega^2} w_0 \tag{78}$$

At this stage, using Eqs. 75, 76, 78 and isotropic linear elastic stress-strain relations [94], the dispersion relation for surface Rayleigh waves coupled with the SDOF vertical resonators is obtained:

$$\begin{aligned} &\left(2 - \frac{\omega^2}{k^2 c_{S,s}^2}\right)^2 - 4\sqrt{1 - \frac{\omega^2}{k^2 c_{L,s}^2}}\sqrt{1 - \frac{\omega^2}{k^2 c_{S,s}^2}} \\ &= -\left(\frac{\omega_v^2}{\omega^2 - \omega_v^2}\right) \frac{m\omega^4}{A c_{S,s}^4 \rho_s k^3} \sqrt{1 - \frac{\omega^2}{k^2 c_{L,s}^2}} \end{aligned} \tag{79}$$

In Eq. 79 where one can easily recognize the standard Rayleigh dispersion term:

$$\left(2 - \frac{\omega^2}{k^2 c_{S,s}^2}\right)^2 - 4\sqrt{1 - \frac{\omega^2}{k^2 c_{L,s}^2}}\sqrt{1 - \frac{\omega^2}{k^2 c_{S,s}^2}} \tag{80}$$

and the additional term related to the vertical resonances:

$$\left(\frac{\omega_v^2}{\omega^2-\omega_v^2}\right)\frac{m\omega^4}{Ac_{S,s}^4\rho_s k^3}\sqrt{1-\frac{\omega^2}{k^2c_{L,s}^2}} \tag{81}$$

Solutions of Eq. 79 are obtained as real eigenfrequency ω for given wavenumber k provided as input, using a standard numerical algorithm in a Matlab® environment.

In particular, the dispersion relation for an array of resonators of mass $m = 6700$ kg, vertical resonances $f_v = 4.9$ Hz embedded in a soft sedimentary soil $c_{S,soil} = 121$ m/s with a triangular arrangement of lattice constant a=1.3 m, is provided in Fig. 44a. All the other relevant geometrical dimensions and mechanical parameters of the designed resonators and selected sedimentary soil are collected in Table 1.

The inspection of the dispersion relation in Fig. 44a reveals the emergence of an interesting dynamic coupling between Rayleigh waves and resonator vertical resonance. The Rayleigh mode hybridizes with the surface resonances and splits into two branches following a typical avoided crossing behavior [129, 130]. Above the vertical resonant frequency, the solutions become dispersive and terminate at the sound line, i.e. the dispersion relation of the shear bulk mode in the substrate ($\frac{\omega}{k} = c_{S,s}$). In the sound cone $\frac{\omega}{k} > c_{S,s}$, represented in light orange, surface solutions cannot exist as the transverse potential loses its exponential decaying shape (refer to Eq. 75). As a result, surface waves are radiated into the soil bulk. Indeed, such radiative modes are bulk shear waves that escape from the surface [114]. The elastic energy traveling on the surface as Rayleigh waves is deviated into the bulk and the surface motion is strongly attenuated. The mode conversion results in a band gap for surface waves, bounded between the vertical resonance frequency of the resonator and the intersection point between the dispersion curve and the sound line $\frac{\omega}{k} = c_{S,soil}$ (see inset Fig. 44a). Inspection of the dispersion relation in Eq. 79 allows identifying the band gap lower (BG^-) and upper edges (BG^+):

$$\begin{aligned}
&BG^-: \quad \text{for} \quad k \to \infty \qquad (\frac{\omega^2}{\omega_v^2}-1) = 0 \quad \omega^- = \omega_v \\
&BG^+: \quad \text{for} \quad \omega = kc_S, s \qquad (\frac{\omega^2}{\omega_v^2}-1) = \frac{m\omega}{Ac_{S,s}^4\rho_s k^3}\sqrt{1-\frac{c_{S,s}^2}{c_{L,s}}} \\
&\text{introducing} \quad \beta = \frac{m\omega_v}{Ac_{S,s}\rho_s}\sqrt{1-\frac{c_{S,s}^2}{c_{L,s}}} \\
&\omega^+ = \omega_v(\beta+\sqrt{\beta^2+1}))
\end{aligned} \tag{82}$$

From the BG lower and upper edges the band gap normalized width is obtained:

$$\Delta\Omega = \frac{\omega^+ - \omega^-}{\frac{1}{2}(\omega^+ + \omega^-)} = \frac{2(\beta+\sqrt{\beta^2+1}-1)}{\beta+\sqrt{\beta^2+1}+1} \tag{83}$$

For the designed resonators a non-dimensional parameter $\beta = 0.377$ is found

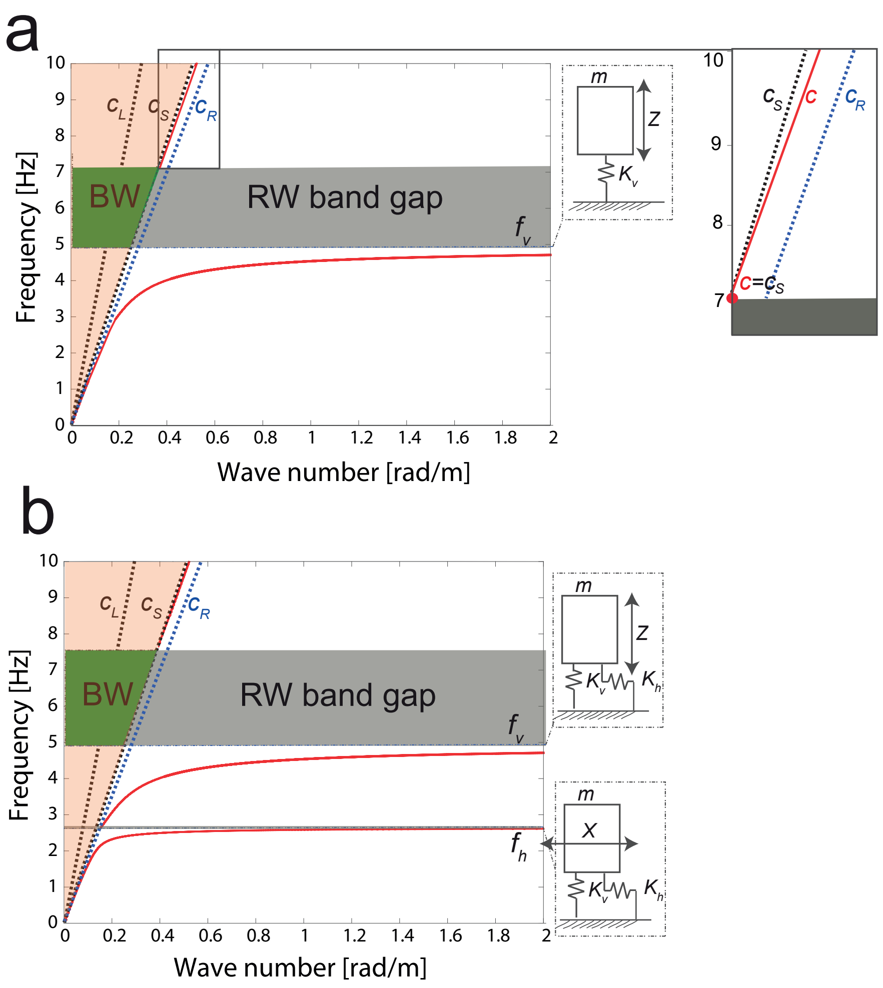

Figure 44: Simplified analytical models. a) SDOF vertical resonators excited by Rayleigh waves. b) 2DOFs vertical-horizontal resonators excited by Rayleigh waves.

which corresponds to a band gap between 4.9 Hz and 7.1 Hz and a normalized frequency range $\Delta\Omega = 0.367$. Moreover, the non-dimensional parameter β can be interpreted as the ratio between the resonator mass and the mass of the soil excited by the surface wave at the vertical resonance frequency. Higher parameters β result in wider band gaps, with an approximately linear relationship between β and normalized bandwidth $\Delta\Omega$ (for $\beta \to 0$).

Following the same approach detailed for vertical resonators, the dynamic coupling between Rayleigh waves and horizontal resonators around their horizontal resonance can be investigated. To this aim, an array of resonators, targeting a horizontal resonance $f_h = 2.6$, subjected to base motion u_0 induced by Rayleigh waves is studied (see Fig. 43b). Starting from the resonator equation of motion:

$$m(\ddot{X} + \ddot{u}_0) - K_h X = 0 \tag{84}$$

and assuming a wave solution of the form $X = X_0 e^{i(\omega t - kx)}$, the resonator horizontal response is obtained as:

$$X_0 = \frac{\omega^2}{\omega_h^2 - \omega^2} u_0 \tag{85}$$

where $\omega_h^2 = \frac{K_h}{m}$ is the horizontal eigenfrequency of the resonator. Such resonator exerts the following stresses at the soil surface:

$$\sigma_{xz,res} = \frac{F_h}{A} = \frac{K_h}{A} \frac{\omega^2}{\omega_h^2 - \omega^2} u_0 \quad \sigma_{zz,res} = 0 \tag{86}$$

At this stage, using Eqs. 75, 76, 86 and isotropic linear elastic stress-strain relations [94], the dispersion relation for surface Rayleigh waves coupled with the SDOF horizontal resonators is obtained:

$$\begin{aligned} &\left(2 - \frac{\omega^2}{k^2 c_{S,s}^2}\right)^2 - 4\sqrt{1 - \frac{\omega^2}{k^2 c_{L,s}^2}}\sqrt{1 - \frac{\omega^2}{k^2 c_{S,s}^2}} \\ &\quad = -\left(\frac{\omega_h^2}{\omega^2 - \omega_h^2}\right) \frac{m\omega^4}{A c_{S,s}^4 \rho_s k^3} \sqrt{1 - \frac{\omega^2}{k^2 c_{S,s}^2}} \end{aligned} \tag{87}$$

where one can easily recognize the standard Rayleigh dispersion term:

$$\left(2 - \frac{\omega^2}{k^2 c_{S,s}^2}\right)^2 - 4\sqrt{1 - \frac{\omega^2}{k^2 c_{L,s}^2}}\sqrt{1 - \frac{\omega^2}{k^2 c_{S,s}^2}} \tag{88}$$

and the additional term related to the horizontal resonances:

$$\left(\frac{\omega_h^2}{\omega^2 - \omega_h^2}\right) \frac{m\omega^4}{A c_{S,s}^4 \rho_s k^3} \sqrt{1 - \frac{\omega^2}{k^2 c_{S,s}^2}} \tag{89}$$

Although Eq.87 presents a structure similar to the related vertical dispersion relation, the dynamic coupling between Rayleigh waves and resonators is strongly different. Indeed, no surface band gaps emerge due to the horizontal resonances as highlighted by the analytical inspection of dispersion relation in Eq. 87 around the horizontal resonance:

$$\begin{aligned} &BG^-: \quad \text{for} \quad k \to \infty \qquad \left(\frac{\omega^2}{\omega_h^2} - 1\right) = 0 \quad \omega^- = \omega_h \\ &BG^+: \quad \text{for} \quad \omega = kc_S, s \qquad \left(\frac{\omega^2}{\omega_h^2} - 1\right) = \frac{m\omega}{A c_{S,s}^4 \rho_s k^3} \sqrt{1 - \frac{c_{S,s}^2}{c_{S,s}}} = 0 \\ &\omega^+ = \omega_h \end{aligned} \tag{90}$$

Although the presence of an array of horizontal resonators in the soil may introduce a dispersive behavior (a flat branch) around the resonance, the wave conversion mechanism does not occur given that the upper branch of the dispersion curve intersects the sound line exactly at the horizontal resonance.

Table 7: Dimensions and mechanical parameters of resonators and sedimentary soil

		Dimensions	Mechanical Parameters
Soil			$E_s = 50\mathrm{MPa}$ $\nu_s = 0.3$ $\rho_s = 1300\frac{kg}{m^3}$
Res.	Steel mass	$r_r = 0.4m$ $h_r = 1.7m$	$E_{st} = 210\mathrm{GPa}$ $\nu_{st} = 0.3$ $\rho_{st} = 7800\frac{kg}{m^3}$
	Bearing	$r_b = 0.2m$ $h_b = 0.1m$	$E_b = 1.9\mathrm{MPa}$ $\nu_b = 0.3$ $\rho_b = 1100\frac{kg}{m^3}$
	Concrete shell	$r_c = 0.55m$ $t_c = 0.05m$ $h_c = 2.5m$	$E_c = 30\mathrm{GPa}$ $\nu_c = 0.3$ $\rho_c = 2500\frac{kg}{m^3}$

6.3.2 *Horizontal-Vertical coupling and full 3-DOFs metabarrier*

In the following a combined horizontal-vertical resonator as depicted in Fig. 43c is analyzed. As Rayleigh waves are characterized by an elliptical surface motion, a small coupling between the vertical and horizontal response of the resonator is expected. To verify this assumption, the response of an array of vertical-horizontal resonators subjected to a coupled horizontal-vertical base excitation is evaluated:

$$m(\ddot{X} + \ddot{u}_0) - K_h X = 0 \qquad m(\ddot{Z} + \ddot{w}_0) - K_v Z = 0 \tag{91}$$

Assuming the vertical and horizontal resonator response of Eqs. 77,85 the stresses exchanged by the resonators at the soil surface are obtained as:

$$\sigma_{xz,res} = \frac{K_h}{A}\frac{\omega^2}{\omega_h^2 - \omega^2}u_0 \qquad \sigma_{zz,res} = \frac{K_v}{A}\frac{\omega^2}{\omega_v^2 - \omega^2}w_0 \tag{92}$$

Following the identical procedure adopted for the sdofs resonators, the dispersion relation for surface Rayleigh waves coupled with the 2DOFs resonators is obtained:

$$\begin{aligned}
&\left(2 - \frac{\omega^2}{k^2 c_{S,s}^2}\right)^2 - 4\sqrt{1 - \frac{\omega^2}{k^2 c_{L,s}^2}}\sqrt{1 - \frac{\omega^2}{k^2 c_{S,s}^2}} \\
&+ \left(\frac{\omega_v^2}{\omega^2 - \omega_v^2}\right)\frac{m\omega^4}{A c_{S,s}^4 \rho_s k^3}\sqrt{1 - \frac{\omega^2}{k^2 c_{L,s}^2}} \\
&+ \left(\frac{\omega_h^2}{\omega^2 - \omega_h^2}\right)\frac{m\omega^4}{A c_{S,s}^4 \rho_s k^3}\sqrt{1 - \frac{\omega^2}{k^2 c_{S,s}^2}} \\
&+ \left(\frac{\omega_h^2}{\omega^2 - \omega_h^2}\right)\left(\frac{\omega_v^2}{\omega^2 - \omega_v^2}\right)\frac{m^2\omega^4}{A^2 c_{S,s}^4 \rho_s^2 k^2}\sqrt{1 - \frac{\omega^2}{k^2 c_{S,s}^2}}
\end{aligned} \tag{93}$$

where a further which couples the horizontal and vertical resonances (fourth line of Eq. 93) arises. The numerical solution of dispersion relation in Eq. 93 is provided for the resonators described in Table 1.

For the designed resonators two surface waves band gaps emerge, each one bounded between a resonant frequency and the intersection of the upper dispersive branch and the sound line. The band gap above the horizontal frequency is extremely narrow (2.6–2.7 Hz, normalized bandwidth $\Delta\Omega = 0.05$) and thus unsuitable for seismic shielding purposes. Above the vertical resonance, a wider band gap emerges (4.9–7.5 Hz, normalized bandwidth $\Delta\Omega = 0.42$), which is suitable for large spectrum seismic isolation. Thus the coupling response results in the presence of a small band gap around the horizontal resonance as well as in a larger gap at the vertical resonance.

Finally, the rotational mode of the resonator can by integrated by analyzing the horizontal-rotation response using the coupled set of equations:

$$\begin{gathered}\begin{bmatrix} m & 0 \\ 0 & I \end{bmatrix}\left(\begin{bmatrix} \ddot{X} \\ \ddot{\theta} \end{bmatrix} + \ddot{u}_0 \begin{bmatrix} 1 \\ 0 \end{bmatrix}\right) + \begin{bmatrix} K_h & K_{hr} \\ K_{rh} & K_r \end{bmatrix}\begin{bmatrix} X \\ \theta \end{bmatrix} = \begin{bmatrix} 0 \\ 0 \end{bmatrix} \\ m(\ddot{Z} + \ddot{w}_0) - K_v Z = 0 \end{gathered} \tag{94}$$

The horizontal-rotational Eqs. 94 can be uncoupled by means of standard modal analysis, as:

$$\ddot{\eta}_i + \omega_i^2 \eta_i = \Gamma_i \ddot{u}_0 \quad i = 1,2 \tag{95}$$

where ω_i is the natural frequency, Γ_i the modal participation factors.

Assuming a modal response of the form:

$$\eta_{i,0} = -\frac{\omega^2}{\omega_i^2 - \omega^2}\Gamma_i u_0 \tag{96}$$

the resonator horizontal-rotational response is evaluated as:

$$\begin{bmatrix} X_0 \\ \theta_0 \end{bmatrix} = \sum_{i=1}^{2} \eta_{i,0} U_i \tag{97}$$

where U_i is the modal shape.

Once the horizontal response X_0 is obtained, the standard set of Eqs. 92 is used to calculated the stresses at the soil surface so that the dispersion relation of the 3DOFS metabarrier can be evaluated. Indeed, for the analyzed symmetric resonator, the two resonant modes are uncoupled and correspond to a pure horizontal translation and a pure rotation of the resonator with eigenfrequencies $f_h = 2.6$ Hz and $f_r = 4.6$ Hz. However, in a full uncoupled system, the rotational motion cannot be excited by the horizontal base displacement. On the contrary in the real system, the variation of the surface wave horizontal displacement along the resonator depth would always induce a resonator rotation. To account for this fact, a small numerical asymmetry $\alpha = 1.01$ is assumed. As shown in Fig. 45, accounting for the rotational motion does not substantially affect the position and size of the occurring band gaps. However, a further flat branch is observed at the rotational resonance frequency.

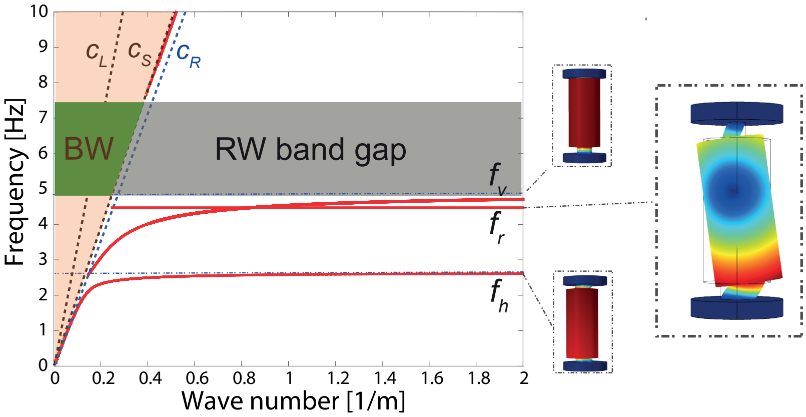

Figure 45: Dispersion relation for the 3DOFs metabarrier.

It is worth underlining that the use of the modal analysis to extract the response of the resonator can be extended to multi-dofs and multi-mass resonator systems, to generalize the design of the metabarrier, as will be shown in the next chapter. However, when a single-mass metabarrier is considered, the use of a simple SDOF vertical resonators model allows capturing the main wave-conversion phenomena and estimating (in a conservative approach) the range of frequency where the wave conversion occurs. In this regards, the definition of a closed analytical formulation for the band gap width represents a powerful tool (Eq. 83) to quickly investigate the performances of the designed metabarrier for different analyzed sedimentary soil. For example, Eq. 83 can be used to calculate the normalized bandwidth of resonators with different mass over resonator lattice area $\frac{m}{A}$, embedded in sedimentary soil with shear wave speed $c_{S,s}$ in the range between 100–500 m/s. In Fig. 46 the normalized bandwidth for different resonators with a vertical frequency $f_v = 4.9\text{Hz}$ is shown. In the plot, solid lines identify iso-bandwidths.

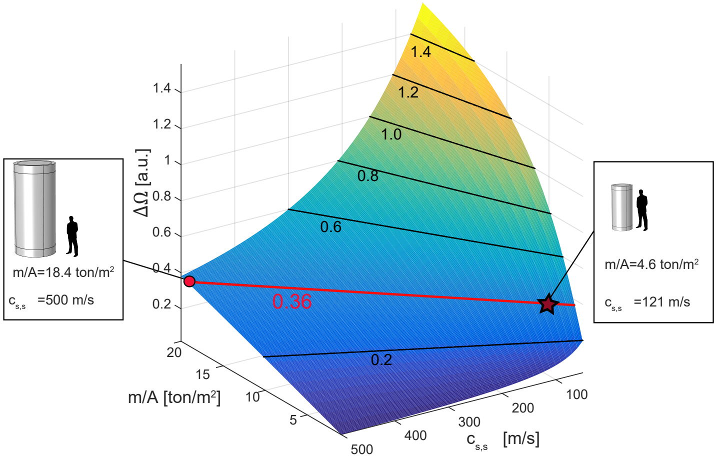

Figure 46: Normalized bandwidth for varying soils vs. resonator design.

The star represents the considered case, the dot represents a resonator with the same bandwidth embedded in a soil with 5 time higher shear velocity $c_{S,s}$ (assuming a constant soil density $\rho_s = 1300 \text{ kg/m}^3$ and a constant soil Poisson ratio $\nu_s = 0.3$, i.e. a constant ratio between soil longitudinal and shear wave speed). The plot clearly indicates that similar resonators can be designed to achieve different normalized bandwidths (i.e. desired attenuation capabilities) for different sedimentary soils, thus supporting the initial design of the seismic metabarrier. A more extended parametric study on the performance of single-mass resonators will be presented in Chapter 7, using the simple SDOF model.

6.4 NUMERICAL MODEL

6.4.1 *Numerical dispersion relation*

The numerical dispersion relation of the soil-metabarrier system is evaluated using full 3D FE models, using a $\omega(k)$ Bloch operator (WFEM) approach in COMSOL® Multiphysics. The unit cell dimensions for the assumed triangular lattice arrangement of the resonators are reported in Fig. 47. In the frequency range where resonances occur, (2.6 Hz and 4.9 Hz) the Rayleigh waves wavelength λ_r is at least 50 m. Thus a unit cell depth $h = 100$ m is adequate to simulate the semi-infinite half space assumption required to capture correctly the surface nature of Rayleigh waves. A shorter depth h would lead to a plate-like behavior, leading to an incorrect estimation of the dispersion relation [47].

Standard Bloch boundary conditions are applied on the vertical side of the unit cell, while traction-free conditions are imposed on the surface. The computed dis-

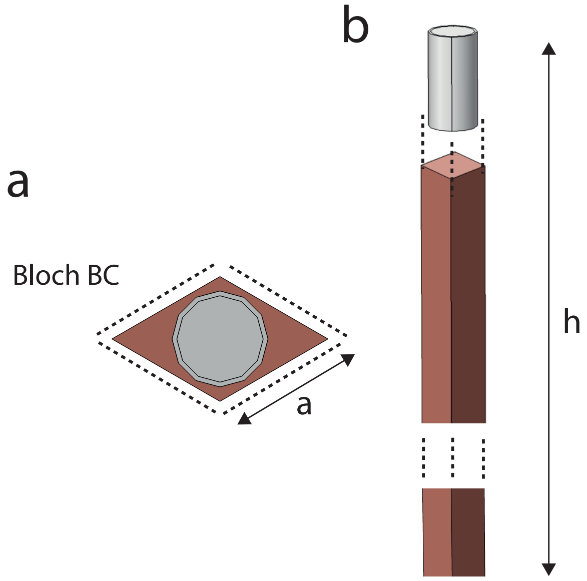

Figure 47: Metabarrier unit cell. a) Planar view. b) 3D view.

persion curve and the graphical representation of the three resonant eigenmodes are reported in Fig. 48. The numerical dispersion curve confirms the behavior observed from the analytical model. Around all the resonant frequencies the wave solutions are strongly dispersive and the branches are flattened.

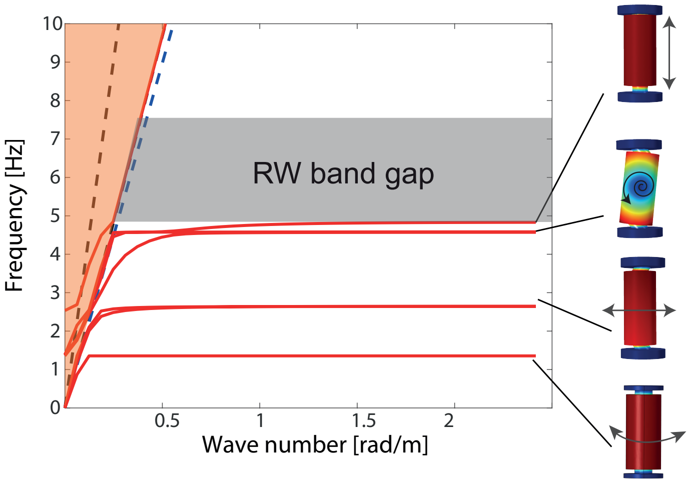

Figure 48: Numerical dispersion relation.

Interestingly, the FE model identifies a first flat branch related to the torsional response of the resonator, not accounted in the analytical model. However, such torsional response does not introduce further band gap in the metabarrier response. Moreover, given the 3D nature of the model, two identical (degenerate) horizontal modes, as well as two flexural modes, are identified. As regards to upper region of the dispersion curve, multiple branches are found traveling at velocities close to the shear velocity of the soil. These solutions possess a hybrid shear-surface behavior from which is hard to identify the real band-gap upper edge. To this aim, further numerical simulations on a finite length stripe of soil engineered with a metabarrier and excited harmonically by surface waves are described in the next section to estimate the width of the band gap clearly.

6.4.2 *FE simulations on a finite length metabarrier*

Full-scale finite element simulations are used to confirm the analytical predictions and get further insights on the mode conversion mechanism and the band gap width. To this aim, a 3D stripe model with 12 lines of resonators in a triangular lattice arrangement is built (see Fig. 49a). The same mechanical and geometrical parameters as in the analytical model (Table 1) are used for this model. The stripe has a width w equal to the triangular lattice constant a, a length $l = 225$ m and a depth of $h = 60$ m sufficient to model the propagation of several Rayleigh wavelengths in the band gap frequency region. All materials are assumed to be linear elastic, and a small isotropic loss factor ($\xi_b = 0.05$) is used for the elastic bearing materials to avoid numerical issues at the resonators resonances. Periodic boundary conditions along y-direction (see inset Fig. 49a) and perfectly matched layer (PML) at the sides and at the bottom of the model avoid wave reflections from the boundaries.

Harmonic simulations from 1 to 10 Hz are performed with an imposed surface displacement ($u_0(\omega) = w_0(\omega) = d_0 e^{i\omega t}$, $d_0 = 0.01\text{m}$) applied as a line source (Fig. 49a). An identical 3D stripe model without resonators is used to obtain the reference displacement field in the analyzed frequency range. The line source is placed 140 m away from the first line of resonators and generates both bulk waves propagating in the soil as well as Rayleigh waves traveling at the surface. In the far field of the source, surface displacements are dominated by Rayleigh waves so that the interaction between resonators and bulk waves becomes negligible. The performance of the resonators is evaluated by looking at amplitude decay of the surface ground motion after the barrier compared to the model without barrier.

In the band gap frequency range (i.e. at 5.0 Hz), the Rayleigh waves incident to the resonator array excite the vertical resonance that in turn steers the elastic energy into the bulk, thus attenuating the surface ground motion (Fig. 49b). This phenomenon is in line with the expected surface mode conversion. For comparison, the reference displacement field at the same harmonic excitation (Fig. 49b) is shown. The amplitude of the horizontal ground motion $u(f)$ for the soil-resonator system (solid red line) and the reference model (solid black line) are evaluated 30 m away from the last line of resonators (Fig. 49c). As the distance between the actuation and the measurement (output) point is maintained constant and the wavelength of the surface waves varies with the excitation frequency, the measurement point can be located either in a valley or on a crest of the spatial wave profile, resulting in an apparent fluctuation of the surface displacement vs. the input wave frequency. No significant discrepancy between the reference and the soil-resonator displacement is observed at the horizontal resonant frequency f_h, confirming the negligible effect of such resonant mode for seismic wave attenuation. On the contrary, in the second band gap region predicted analytically, the soil-resonator ground motion is strongly attenuated, with a transmission dip up to 60% at 6 Hz (see inset Fig. 49c). The attenuated frequency range is slightly larger than the analytical prediction, with a narrow transmission dip occurring before the lower band gap limit caused by the coupling between surface waves and the resonator rotational. All the above observations remain valid for vertical ground motion w, given the elliptical nature of the surface wave.

Identical numerical models with increasing number of resonators are used to investigate the achievable attenuation performance of the proposed seismic barrier. In Fig. 49d the amplitude reduction at 5 Hz for seismic barriers with up to 32 lines of resonators is shown. With 32 lines of resonators the surface amplitude displacement is attenuated by approximately one order of magnitude. Further details on the attenuation performance of metabarrier with different length and different resonator masses will be provided in Chapter 7.

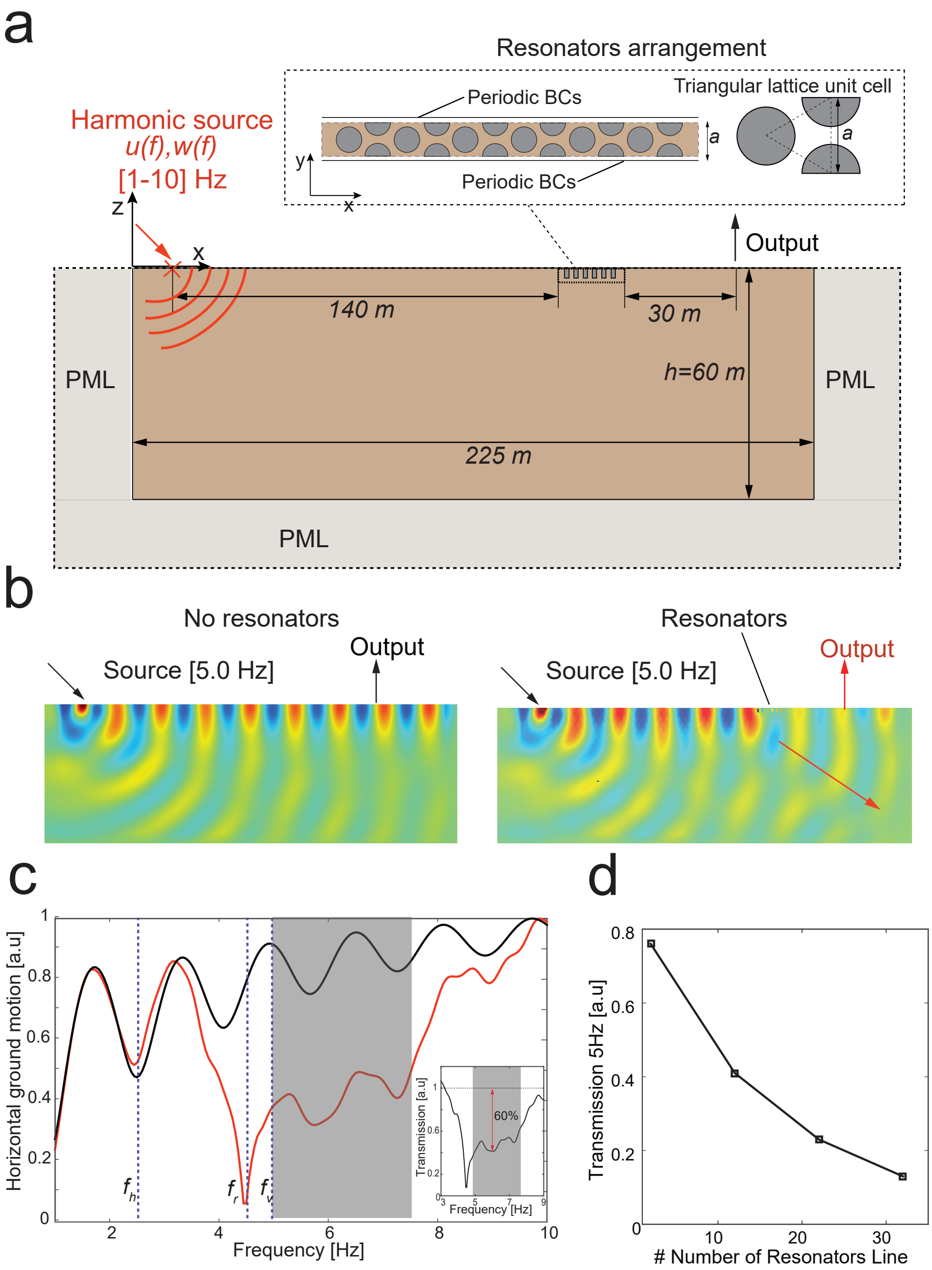

Figure 49: Numerical simulation of the wave conversion mechanism. a) 3D stripe finite element model of soil engineered with 12 lines of resonators. b) Harmonic response at 5 Hz with and without the resonators. c) Horizontal surface ground motion. d) Horizontal ground motion attenuation as a function of the number of resonators in the array (5.0 Hz), averaged over a distance of 20 m at 30 m away from the resonator barrier.

It is worth underlining that the adopted periodic resonator arrangement is not strictly required to induce band gaps formation, as the band gap mechanism does not rely on Bragg scattering. In fact, the effectiveness of band gap formation relies on the density of resonators and not on their actual arrangement [28]. Nonetheless, a triangular lattice arrangement is the optimal one, given that it shows the highest density for a given lattice constant.

6.5 EXPERIMENTAL TEST ON A SMALL SCALE METABARRIER

A tabletop setup is used to experimentally verify the analytical and numerical findings described in the previous sections. The setup consists of a polymer resin block where centimeter-size resonators are embedded to realize a small-scale seismic metabarrier with a non-dimensional parameter $\beta_{exp} = 0.372$ (Fig. 50). A polymer resin (Resinpal 1707 ®) with a density $\rho_{res} = 1180$ kg/m^3 a shear and longitudinal wave speeds $c_{S,res} = 1170$m/s and $c_{L,res} = 2540$ m/s was used to build a block with overall size of 1,2 x 0,3 x 0,21 m representing an ideal linear elastic homogeneous soil. Indeed, such polymer material is commonly used in geophysical experiments to build up small-scale setups [131, 132]. For fabrication of the experimental setup the block was poured layer by layer (2 cm thickness each) casting the resin into a wooden box. After having released the resin block from the wooden box, a reflective spray (Albedo 100®) was applied on its top and bottom surfaces later used for laservibrometric surface velocity measurements.

A set of 30 small-scale resonators were designed and placed in the resin block over 12 lines in a triangular packing with a lattice constant of 1.7 cm (Fig. 50a). Each resonator consists of three main parts: a rigid aluminum tube, a soft spring and a heavy mass $m_s = 4$g (Fig. 50b). The heavy steel mass is encased in the aluminum tube. A thin, threaded aluminum rod realizes the soft spring. Only the bottom side of the rigid tube is closed allowing for a direct optical measurement of the resonator mass response during the experiments. In the experiments, only the vertical resonance was considered. Tuning of this resonance was achieved by changing the free length of the threaded rod, up to a final value $f_{v,exp} = 11.5$kHz with a measured accuracy of $\pm 10\%$. An example of a resonator response is reported in Fig. 51. The above described configuration results in a $\beta_{exp} = 0.372$ with an analytically predicted band gap between 11.5 kHz and 16.4 kHz (corresponding to the effective band gap width of $4.9 - 7.5$ Hz in a real-size experiment). At the resonance frequency, the wavelength of the propagating Rayleigh waves ($\lambda = 0.1$m) is much larger than the lattice constant, in agreement with the subwavelength assumption of the model.

The out-of-plane v_z component of the surface velocity was measured by using a Laser Doppler Vibrometer mounted on a scanning stage (Fig. 50b). Rayleigh waves were excited by a piezoelectric transducer (Steminc ® , 20 × 15 × 1 mm, PZT-4) glued on the surface of the resin block 22 cm away from the resonator array. A signal generator (Agilent 3320 A®) connected to a voltage amplifier was used to drive the piezoelectric transducer. Signals were acquired by means of an oscillo-

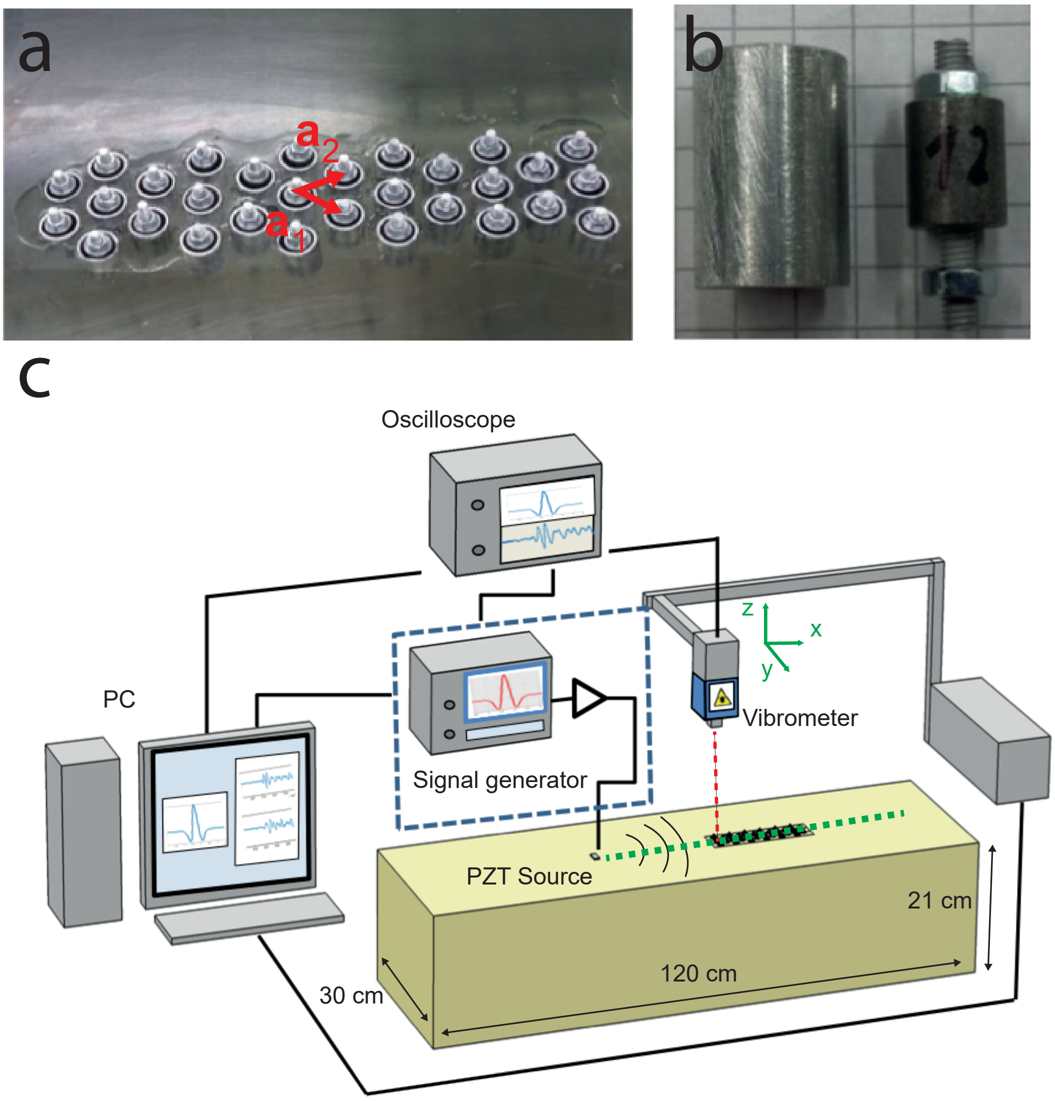

Figure 50: Tabletop experimental setup. a) Resin block with embedded 30 resonators in a triangular lattice. (b) The resonator consists of rigid aluminum shell, a heavy steel mass and soft spring. c) Experimental setup to measure the surface out-of-plane velocity wave field using a laser doppler vibrometer.

scope (Tektronix DPO3014®). At each acquisition point 32 signals were averaged to reduce the signal to noise ratio. All instruments were controlled using a Matlab® interface. Additionally, the same excitation setup was realized on the backside of the resin block, as control experiment to obtain the reference wave field without the influence of resonators.

The propagation of Rayleigh waves excited by a Ricker wavelet, centered at the resonance frequency $f_{v,exp}$ was investigated. Ricker wavelets are commonly used in seismology because they resemble the asymmetric frequency content of seismic

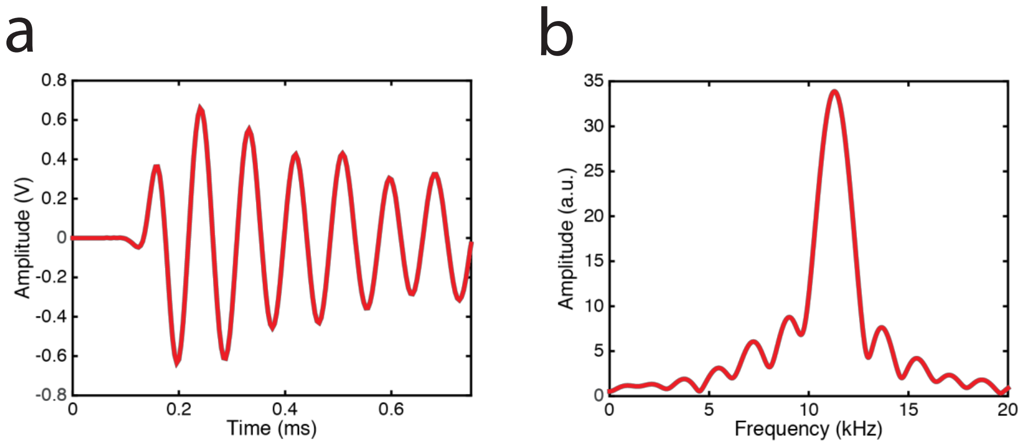

Figure 51: Resonator response. a) Typical transient response of the scaled resonator and b) the corresponding frequency spectrum.

waves [133]. By performing a line scan of measurements along the symmetry axis of the block, 1D seismographs were obtained from both sides of the resin block (Fig. 52a and 52d). The reference seismographs obtained from the resonator-free backside of the resin block is shown in Fig. 52a. A non-dispersive Rayleigh wave propagating at speed $c_{R,res} = 1100 m/s$ is observed, with a measured amplitude decay of 0.8 Np/m induced by material damping. Additionally, several hyperbolic wave arrivals occur, which stem from reflections of surface waves from the block's side edges.

A moving time window Δt of duration equal to the pulse length was applied to the acquired transients to extract the Rayleigh wave content at the different x positions (Fig. 52b). The frequency content of the arriving windowed pulses was analyzed at x=0.38 m away from the excitation point. In the case of free propagation, the frequency spectrum matches well the theoretical spectrum of the actuated Ricker's wavelet (Fig. 52c). The seismograph of the Ricker pulses traveling through the resonators array is depicted in Fig. 52d. As it can be seen, the surface motion excites the resonators. In turn, incident Rayleigh waves are highly attenuated after passing through the array, as predicted by the analytical model. Comparison between the initial pulse at the source (Fig. 52e, left) and the signal after the resonator chain (Fig. 52e, right) reveals strong attenuation and dispersion induced by the hybridization at resonance. Indeed, the frequency spectrum (Fig. 52f) shows a frequency dependent attenuation of up to 50%, centered in the predicted band gap highlighted in gray. The reached attenuation in the experimental setup is consistent with the one predicted for the real scale numerical model. The small discrepancy can be mainly attributed to transient effects due to the limited quality factor ($Q = 10$, see Fig. 52b) of the resonators, which creates a finite activation time of the resonators.

One the base of the 1D line measurements, experimental dispersion diagrams for the propagation of surface waves on the free surface (Fig. 53a) and along the resonators array (Fig. 53b) were obtained. The propagation through the resonator ar-

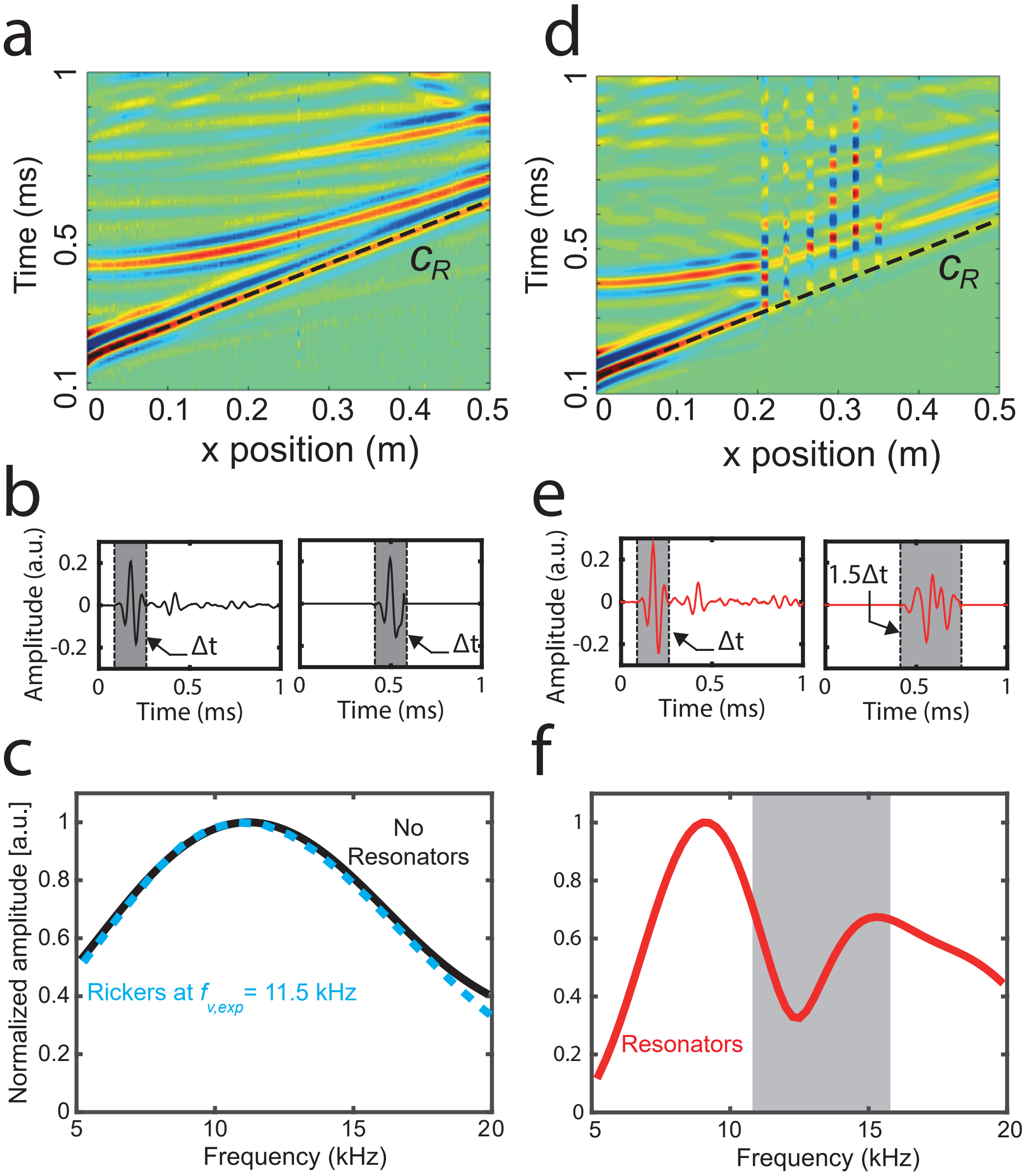

Figure 52: 1D seismographs and frequency transmission. a) Experimental seismograph of free propagation. b) Transient response at 5 cm and at 35 cm distance from the source. c) Normalized spectrum of the far field response compared to the spectrum of the adopted Ricker's wavelet pulse. d) Experimental seismograph of propagation with resonators. e) Transient response at 5 cm and at 35 cm (after the resonators) distance from the source. f) Normalized spectrum of the far field response.

ray shows a highly dispersive character, as opposed to the non-dispersive behavior of Rayleigh waves propagating on the free surface. The propagating components are spread over a broader range of wavenumbers around the resonator's frequency

$f_{\nu,exp} = 11.5$ kHz and match well with the predicted analytical dispersion curve. The harmonic response of the resonators dominates the spectrum, and the Rayleigh solutions above the upper edge of the predicted band gap are not clearly visible.

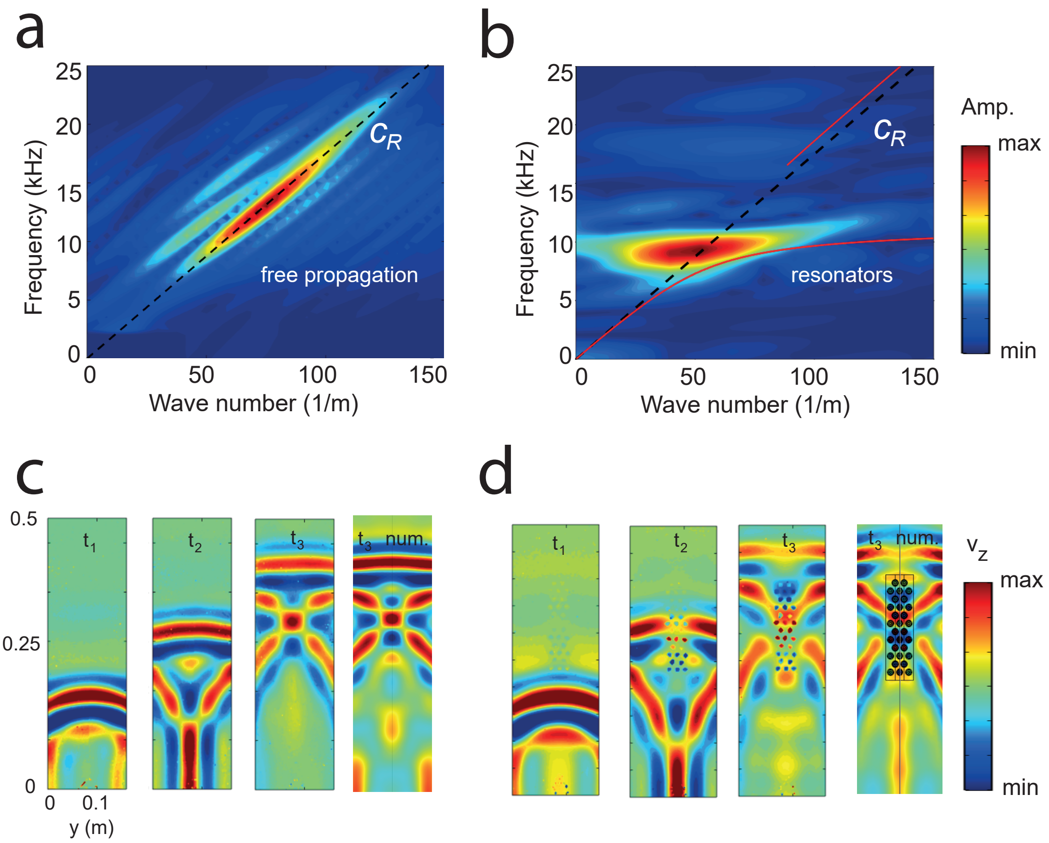

Figure 53: Experimental dispersion and surface velocity field. a) Experimental dispersion diagram of free propagation of Rayleigh waves. b) Experimental dispersion diagram of the propagation of Rayleigh through the metabarrier. c) Full velocity field of experimental Rayleigh wave propagation at 3 sequential time instants ($t_1 = 0.26$ ms, $t_2 = 0.38$ ms and $t_3 = 0.5$ ms) on the free surface. Numerical comparison for time instant t_3. d) Full velocity field of experimental Rayleigh wave propagation at 3 sequential time instants ($t_1 = 0.26$ ms, $t_2 = 0.38$ ms and $t_3 = 0.5$ ms) on the surface with the metabarrier. Numerical comparison for time instant t_3.

To obtain a full field visualization of Rayleigh wave propagation, 2D scans of the sample were performed using a grid of points on the block surface (Figs. 53c,d). In the sample without resonators, (Fig. 53c), a clear plane wavefront propagates, followed by wave reflections from the side boundaries of the block that generate interference figures. We performed time transient 3D finite element simulations to verify the experimental results. In the numerical simulations, a point load is assumed as a source of excitation, driven by the same Ricker wavelet as input pulse.

For the free propagation (Fig 53c), the measured experimental wave field at t_3 (third panel in Fig. 53c) agrees very well with full 3D numerically simulated wave field at the same time instant (fourth panel in the same figure). In the presence of the seismic metabarrier (Fig. 53d), the wave front impinging the resonators is split and the Rayleigh energy is confined between the array and the block boundaries. Again, excellent agreement with full 3D numerical simulations of the resin block can be observed for the time instant t_3 (compare the third and fourth panel of Fig. 53d). The Rayleigh waves passing through the resonators show large dispersion and wave attenuation. In addition, the second peak of the initial pulse is attenuated more than the first peak due to the fact that resonators are closer to steady state resonance. Far away from the array, the signal amplitude recovers due to diffraction of waves previously confined to the boundaries.

6.6 CONCLUSIONS

In this Chapter, a seismic metabarrier to attenuate the propagation of Rayleigh waves has been proposed and investigated. The metabarrier exploits the coupling between Rayleigh waves and surface resonances to redirect part of the surface ground motion into the soil bulk. The attenuation bandwidth and magnitude of surface waves obtained by the resonant metabarrier depend on the interaction between the dynamic mass of soil moved by Rayleigh waves and the moving mass of the resonators. By means of the simplified SDOF analytical model a unifying parameter β is derived able to describe such interactions. This parameter allows designing seismic barriers for varying soil conditions. Specifically, it has been numerically proven that in soft sedimentary soils beta values of the order of 0.38 can open band gaps in the 4-7.5 Hz providing a reduction in the surface ground motion up to the 60%. Similarly, the analytical model can guide the design of equivalent small-scale equivalent experimental setup to validate the numerically predicted performance of the metabarrier.

It is fundamental to recognize that both numerical findings and experimental results are derived under some limiting assumptions: the soil is modeled as a linear elastic material with a homogeneous stiffness profile along the depth, the resonators are modeled assuming a linear elastic behavior of the bearing connectors. As regards to the soil, it is known that it may present a complex stratigraphy, leading to depth dependent wave speeds that could result in complex wave propagation pattern, like ray-bending effects or multimodal surface propagations. In such case, multi-layered models are necessary to analyze the feasibility of the proposed seismic shielding solution. Additionally, both structural integrity and soil bearing capacity of the resonant barrier needs to be investigated for high dynamic loads induced by large magnitude events. Indeed, commercial elastomeric bearings, which are originally designed to isolate buildings and infrastructures, can certainly sustain the expected loads induced by the resonant mass exploiting either viscous or hysteretic dissipation. Finally, It has been shown that these barriers can be designed for a specific critical infrastructure, by targeting its resonance frequency. Additionally, to obtain a broadband performance of the seismic barrier, the resonators frequencies can be varied along the array, exploiting the rainbow trapping phenomenon [46, 114], or multi-mass resonator targeting multiple frequencies can be used. This can be particularly useful for shielding large urbanized areas where infrastructures and building resonances are spread over the full harmful seismic spectrum.

7

METABARRIER OPTIMIZATION WITH MULTI-MASS RESONATORS

ABSTRACT

This chapter proposes the use of multi-mass resonators to enhance the ground motion attenuation of a seismic metabarrier and achieve broadband wave filtering properties with more compact structures. First, the performance of the single mass metabarrier, presented in Chapter 6, is further investigated performing a parametric study varying the resonator mass m *and the total barrier length. Then, a multi-mass metabarrier is introduced providing an analytical approach to extract its dispersion curve. A double-mass resonator system is investigated in detail to show the superior performance of multi-mass resonators, either when specific frequencies are targeted and when a rainbow trapping arrangement is exploited. Finally, an optimization strategy based on the use of Genetic Algorithms is employed to design a multi-mass resonator with minimal mass* m *able to target selected frequency ranges at will. The optimization strategy is applied to design a structure to protect two concrete frame buildings of known dynamic properties, showing significant ground motion reduction with a more compact metabarrier design.*

7.1 INTRODUCTION

As shown in Chapter 1, locally resonant materials find several potential applications for wave attenuation and elastic energy absorption at low-frequency. However, as their band gaps are confined to a narrow frequency range which can be broadened only using massive resonators, their practical implementation is still limited. Several strategies have been proposed in the literature to broaden the metamaterial response. Among the others: the rainbow trapping concept [110], the inertial amplification [134, 135] the combination of phononic and locally resonant band gaps [136], chiral metamaterials [137] and architected lattices to exploit multiple resonant modes of a resonant inclusion [37]. However, only the rainbow trapping concept has been utilized at large scale for seismic isolation applications [46, 47], as all the other strategies require complex unit-cell/resonant structures of impractical design for earthquake engineering purposes. Nonetheless, the same rainbow trapping concept requires the use of an array of multiple single frequency resonators which can result in a barrier of significant length. Indeed, in urbanized areas, the metabarrier length can represent the primary limit for its implementation given the limited free space usually available. For this reason, this Chapter investigates the possibility of using multi-mass resonators to realize metabarriers able to target multiple frequency ranges and reduce the metabarrier total length. After a parametric investigation to assess performance and limitations of single mass resonators, an analytical model to extend the design of the metabarrier to multi-mass resonators is presented. FE numerical simulations are employed to show the superior attenuation of a double mass metabarrier. Optimal multi-mass resonators with minimal total mass are then sought using Genetic Algorithms. Finally, an optimal four mass metabarrier is designed to attenuate the base shear response of two concrete frame structures.

7.2 SINGLE MASS SEISMIC METABARRIER: PERFORMANCE AND LIMITATIONS

As shown in Chapter 6, an accurate (conservative) approximation of the metabarrier attenuation frequency range can be obtained by restricting the resonator dynamics to the interaction of the vertical resonance with surface Rayleigh waves. In this case the dispersion law, here recalled for the sake of the clarity, reads:

$$\left[\left(2-\frac{\omega^2}{k^2{c_S}^2}\right)^2-4\sqrt{1-\frac{\omega^2}{k^2{c_L}^2}}\sqrt{1-\frac{\omega^2}{k^2{c_S}^2}}\right]=-\frac{\overline{\sigma}_{zz}\omega^2}{\rho {c_S}^4k^3}\sqrt{1-\frac{\omega^2}{k^2{c_L}^2}} \tag{98}$$

where:

$$\overline{\sigma}_{zz}=-\frac{m\omega^2}{A}\left(\frac{\omega^2}{{\omega_v}^2}-1\right)^{-1} \tag{99}$$

is the vertical stress exchanged by a resonator with vertical resonance frequency ω_v. A numerical validation of the dispersion law has been provided in Chapter 6 using full 3D FE simulations. Here, the interest is to investigate barriers with varying length L_{res} and resonator mass m. Thus, a 2D simplified numerical model is adopted to simulate the performance of different barriers, reducing the required computational effort. A 2D FE soil-resonator unit cell with appropriate Bloch boundary conditions is used to extract numerically its dispersion curve (see Fig. 54a). The ground is modeled as an elastic plane strain medium, while the resonators as truss-point mass elements spread at the soil surface to simulate the local stress exchange assumed in the dispersion law. The model has a width $w = a/10$ (where $a = A/1$ [m]) and a height of $4\lambda_{\omega 1R}$ with clamped boundary conditions (BCs) at the lower edge and Bloch-Floquet periodic BCs on the side. Such dimensions ensure the correct representation of surface waves and avoid the occurrence of spurious flexural modes. An example of the analytic and numerical dispersion law for a SDOF resonator is provided in Fig. 54b. Resonator properties are collected in Table 8 while sedimentary soil properties are given in Table 9. It is here underlined that the considered resonator exerts a static vertical stress well below the bearing soil capacity, calculated according to the simplified Terzaghi's formulation.

The analyzed resonator generates a BG between ${f_{BG}}^- = 2.43$Hz and ${f_{BG}}^+ = 2.76$Hz with $\beta = 0.26$. Excellent agreement between analytic and FE results is obtained.

SDOF-Resonator properties

Mass	m	10500	kg
Stiffness	K_v	2.4416e6	N/m
Foundation surface	A	1.3	m^2

Table 8: SDOF-Resonator for numerical evaluations

Soil mechanical properties

Shear wave speed-S	c_S	250	m/s
Longitudinal wave speed-L	c_L	468	m/s
Rayleigh wave speed-R	c_R	232	m/s
Density	ρ	1600	kg/m^3

Table 9: Soil class C, in accordance with EC8 [**EC8**]

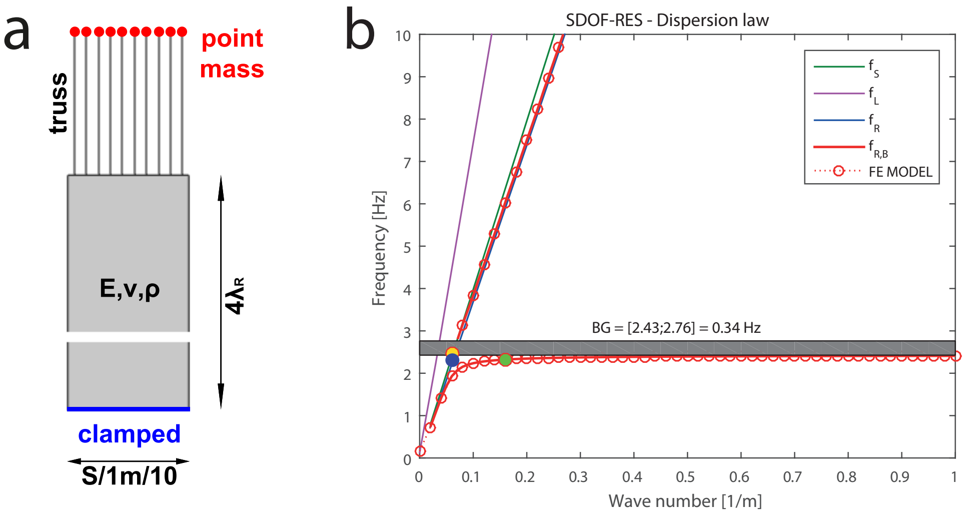

Figure 54: FE Dispersion law. a) FE model geometry. b) Dispersion law - SDOF resonators.

7.2.1 *Attenuation vs resonators mass and metabarrier length*

An extended 2D plane strain model is used to analyze the attenuation of the metabarrier varying the resonator mass m, keeping constant its resonant frequency ω_v. The geometry, provided in Fig. 55a, consists of a symmetric 2D soil model with a total length $L_{mod} = 16\lambda_{\omega_v} + 2L_{res}$, (where $\lambda_{\omega_v} = 96m$ is the Rayleigh wavelength at the resonator frequency ω_v and c_R is the Rayleigh velocity) and depth $d_{mod} = 2\lambda_{\omega_v}$. A harmonic point source in the middle of the ground surface (model symmetry line) is used to generate surface waves within the frequency range [1-10] Hz corresponding to Rayleigh wavelength [232-23] m. These surface waves can travel undisturbed on the left side of the model (used a reference wave field), while they are converted to shear waves by the metabarrier located at the right side of the harmonic source (see Fig. 55b). As for the numerical dispersion law, the metabarrier is modeled with truss-point mass elements and cover a total length $L_{res} = 0.5\lambda_{\omega_v}$=48 m. Perfectly Matched Layers (PMLs) are used to minimize the boundary reflections at the domain borders.

A parametric study is performed by varying the percentage of the initial mass m=10500 kg of the resonator, with the aim of assessing the ground motion attenuation of the metabarrier. The resonator mass is varied between 10%-200% of the initial mass, with an equivalent variation on the dimensionless parameter β which governs the width of the BG. The metabarrier ground motion attenuation is estimated using the average vertical ground acceleration evaluated over a length $L_{ave} = 2\lambda_{\omega_v}$ located behind the metabarrier (see Fig. 55a). It is here remarked that identical results are obtained for the horizontal acceleration given the coupled elliptical nature of Rayleigh waves.

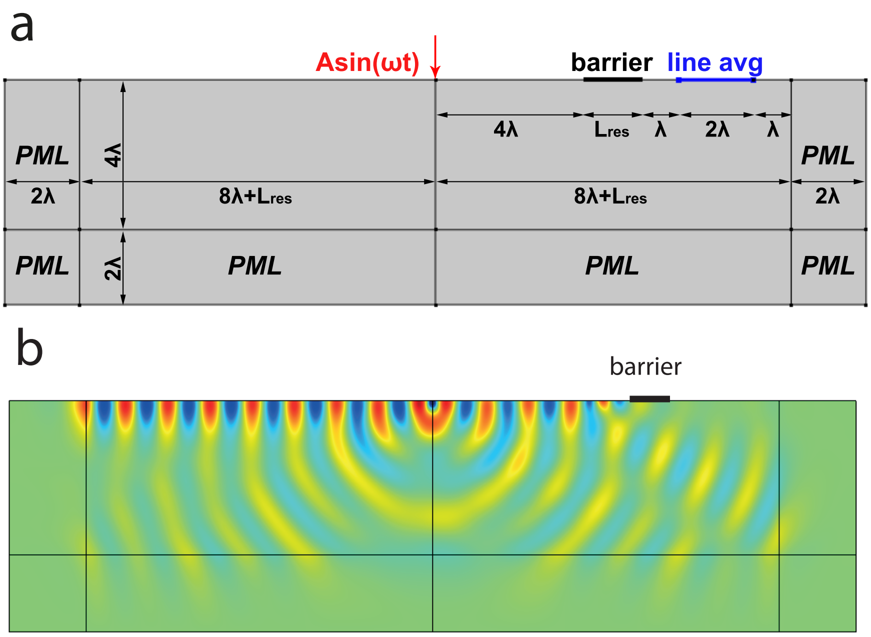

Figure 55: FE 2D Numerical Model. a) Schematic of the model geometry. b) Displacement field at the attenuation peak.

As expected, both the peak attenuation and the frequency width of the gap are substantially increased by an increase in resonator mass (see Fig. 56a). In particular, the BG width shows approximately a linear variation with an increase in mass following the dispersion law predictions (marked with dashed lines for the different resonators). However, a significant shift both in the frequency peak attenuation and in the upper BG edge is registered resulting in a larger effective gap for the metabarrier (see Fig. 56a). This larger band gap can be explained considering the wave coupling at the interface between the semi-infinite medium and

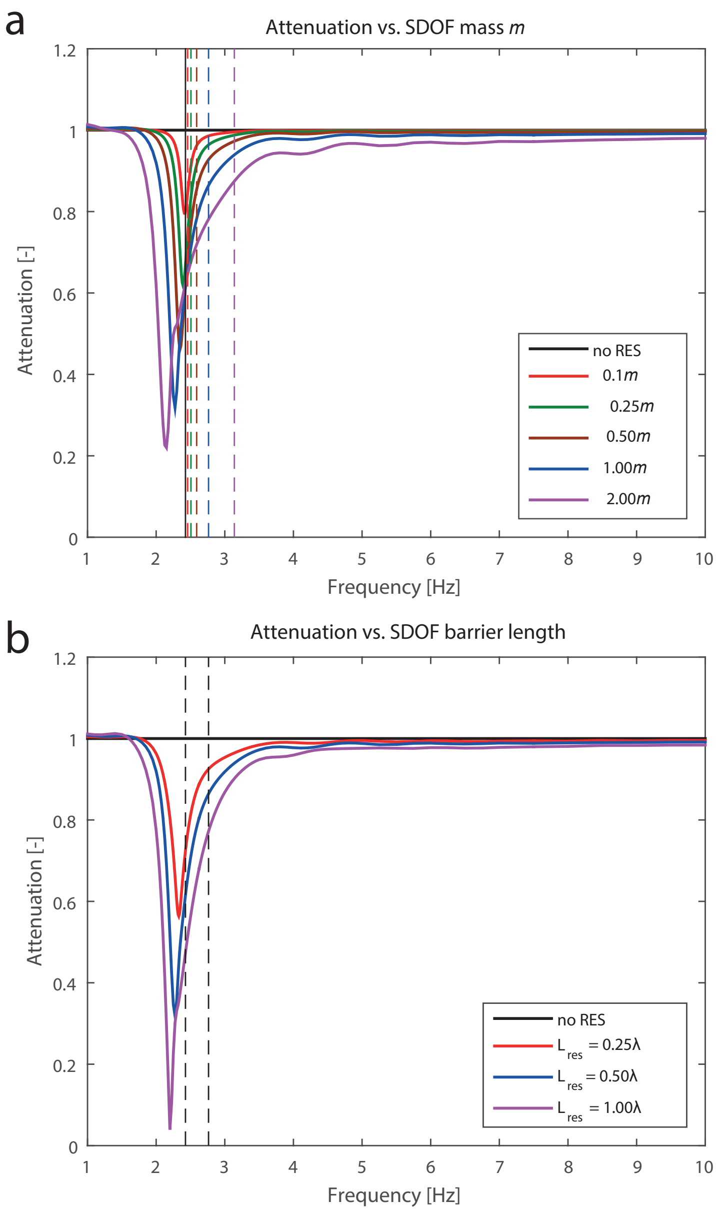

Figure 56: SDOF Parametric study. a) Normalized average vertical acceleration vs. resonator mass m. b) Normalized average vertical acceleration vs. metabarrier lenght L_{res}.

the same medium with vertical resonators. At the interface between pure soil and the metabarrier, Rayleigh waves at the given frequency ω_i are forced to transform to surface solutions with identical frequency (as stated by the Snell laws) which travel at different phase velocity and with a different wavelength, as shown in the metabarrier dispersion law (Fig. 54). Indeed, the metabarrier surface waves are not pure Rayleigh solutions and can be considered as Rayleigh-Bloch waves [115, 138] given that their nature is influenced by the presence of a periodic artificial media. When Rayleigh and Rayleigh-Bloch waves differ substantially, as in the region around the resonance frequency, the coupling between these waves is poor due to the significant difference in their phase, group velocity, and wave shape (see Fig. 57). This weak coupling results in a leakage of energy in the soil bulk which contributes to the surface ground motion attenuation.

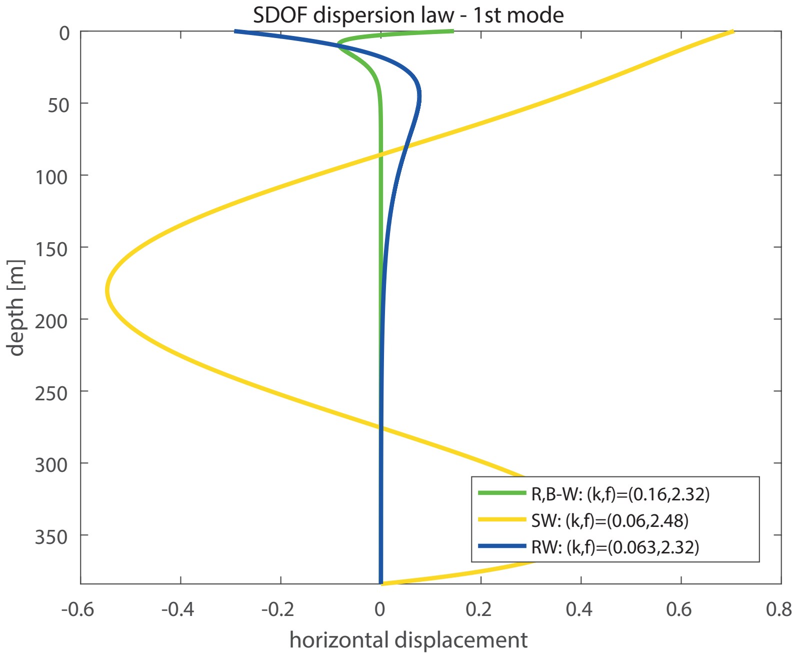

Figure 57: Rayleigh, Rayleigh-Bloch, and Shear wave shapes. The frequency-wavenumber values where the wave shapes are calculated are represented with colored dots in Fig. 54.

A second parametric study is performed to investigate the attenuation capabilities of metabarriers with different lengths. Here the focus is to assess the minimum barrier length required to achieve a significant attenuation of the surface ground motion. Indeed, metamaterial based approaches for vibration isolation rely on the assumption that arrangement of subwavelength units can be used to control the propagation of waves. However, it is of crucial importance to investigate the total length of such structure to analyze the feasibility of this isolation strategy. To this aim, the same 2D FE model is utilized to perform harmonic analysis with metabarrier of length $L_{res} = [0.25 - 1]\lambda_{\omega_v}$ and mass m=10500 kg. As for the mass-parametric study, results are presented in terms of normalized average vertical acceleration calculated after the metabarrier (see Fig. 56b). Approximately total isolation (i.e. attenuation $>$ 90% of the original signal) is obtained for a metabarrier of $L_{res} = \lambda_{\omega_v}$ while significant reduction (>60%) of the ground motion is ensured with half of this length.

7.2.2 *Results and Limitations*

Besides the significant ground motion attenuation achieved by the analyzed metabarriers, two main limitations characterize this device as presented: (i) the limited frequency width covered by the single mass resonator; (ii) the total metabarrier length required to achieve a significant attenuation. For this reason, in the next sections, multi-mass metabarriers to cover multiple frequency ranges with a single resonator and reduce the metabarrier total length are presented.

7.3 MULTI-MASS SEISMIC METABARRIER

In this section, the dispersion law and the attenuation capabilities of a multi-mass (MM) resonator metabarrier are described. First, the analytic dispersion relationship of a generic multi-mass resonator is derived using a modal analysis approach. The approach is then specified for the case of a double-mass (DM) resonator system for which the numerical dispersion relation is calculated utilizing the already discussed FE Bloch-Floquet approach. The attenuation of the double-mass resonator is then numerically investigated to understand the required mass m of the resonator and length of the barrier for a significant ground motion attenuation.

7.3.1 *Analytical model*

A surface resonator composed of a series of N vertical resonant masses (see Fig. 58) is subjected to the surface vertical ground motion w_g .

$$w_g = w_{g0} \exp[i(kx - \omega t)] \tag{100}$$

Introducing the diagonal resonator mass matrix $\mathbf{M}$ and the tridiagonal stiffness matrix $\mathbf{K}$ of the dynamical system, the equation of motion for the N-DOFs vertical displacement $\mathbf{w}$ relative to the ground is:

$$\mathbf{M}\ddot{\mathbf{w}} + \mathbf{K}\mathbf{w} = -\mathbf{M}\mathbf{i}\ddot{w}_g \tag{101}$$

where $\mathbf{i}$ is the influence vector (in this case is the identity vector). The displacement vector $\mathbf{w}$ is projected in the modal space:

$$\mathbf{w} = \boldsymbol{\Phi}\boldsymbol{\eta} \Rightarrow \ddot{\mathbf{w}} = \boldsymbol{\Phi}\ddot{\boldsymbol{\eta}} \tag{102}$$

where $\boldsymbol{\Phi}$ is the modal matrix and $\boldsymbol{\eta}$ is modal coordinates vector. Introducing for each mode r the modal mass $M_r = \boldsymbol{\Phi}_r^T \mathbf{M} \boldsymbol{\Phi}_r$ and modal stiffness $K_r = \boldsymbol{\Phi}_r^T \boldsymbol{\Phi}_r$, with the r vertical resonator eigenfrequency $\omega_r = \sqrt{K_r/M_r}$, the uncoupled set of equilibrium equations is obtained:

$$M_r \ddot{\eta}_r + K_r \eta_r = -\boldsymbol{\Phi}_r^T \mathbf{M}\mathbf{i}\ddot{w}_g \tag{103}$$

At this stage, assuming each modal coordinate is harmonically driven by the ground motion:

$$\eta_r = \eta_{0r} \exp[i(kx - \omega t)] \tag{104}$$

and introducing the participation factor for each mode r as $\Gamma_r = \boldsymbol{\Phi}_r^T \mathbf{M}\mathbf{i}/M_r$, the η_{0r} modal coordinate reads:

$$\eta_{0r} = \frac{\Gamma_r}{\frac{\omega_r^2}{\omega^2} - 1} w_{g0} \tag{105}$$

from which the force transmitted to the ground F_{tr} is found:

$$\mathbf{w}_0 = \boldsymbol{\Phi}\boldsymbol{\eta}_0 \Rightarrow \mathbf{F}_0 = \mathbf{K}\mathbf{w}_0 \Rightarrow F_{0,tr} = \sum_{i=1}^{n} F_{0,i} \tag{106}$$

and similarly the transmitted vertical stress:

$$\overline{\sigma}_{zz} = \frac{F_{0,tr}}{A} \tag{107}$$

Introducing the formulation of the vertical stress in Eq. 107 in the dispersion law in Eq. 98, this last relationship assumes general validity for any multi-mass vertical resonator system.

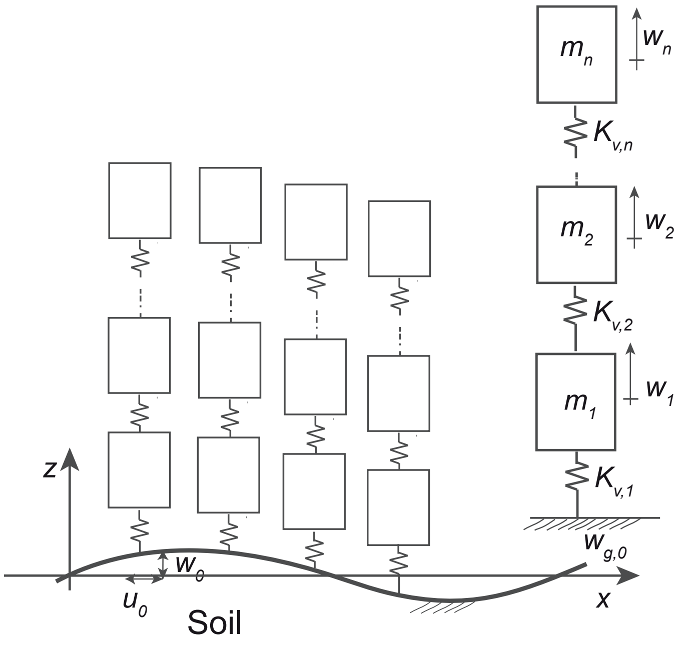

Figure 58: Schematic of the MDOF system

7.3.2 *A double-mass (DM) resonator*

The modal procedure described in the previous section is here applied to find the Rayleigh-Bloch dispersion law for a double-mass resonator system. For this case a close form solution for the transmitted vertical stress is given as:

$$\overline{\sigma}_{zz} = \frac{\omega^2 k_1}{A}\left[\frac{k_2\left(m_1+m_2\right)-\omega^2 m_1 m_2}{k_1 k_2-\omega^2\left(m_1 k_2+m_2 k_1+m_2 k_2+\omega^2 m_1 m_2\right)}\right] \tag{108}$$

The dispersion law plotted from Eq. 98 replacing the stress $\overline{\sigma}_{zz}$ in Eq. 108 is given in Fig. 59 for a double-mass resonator whose mechanical properties are collected in Table 10. In the same plot, the dispersion relation as obtained from a 2D unit-cell FE model is given.

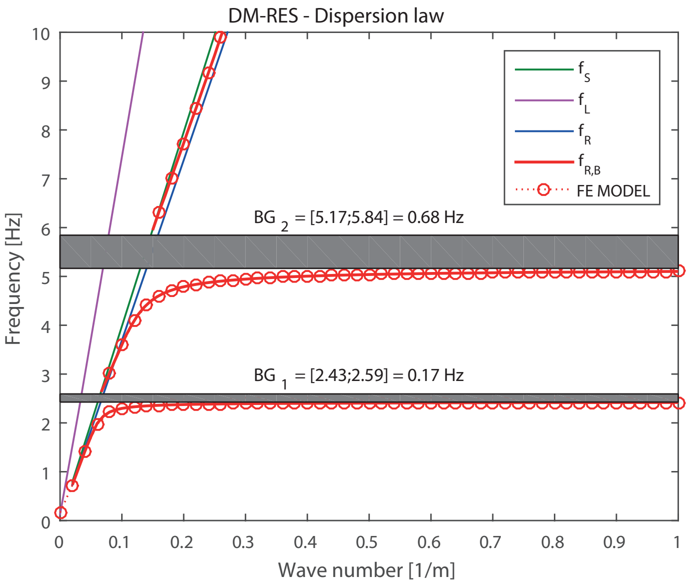

Figure 59: Dispersion law - DM resonator.

The analyzed DM resonators generate a first BG between $f^-_{BG_1} = 2.43$Hz and $f^+_{BG_1} = 2.59$Hz and an higher frequency BG between $f^-_{BG_2} = 5.17$Hz and $f^+_{BG_2} = 5.84$Hz. The FE model used for dispersion law numerical validation is similar to the one used in SDOF resonator case (Fig. 54), with double truss-mass resonators. As for the single-dof, excellent agreement between the numerical and the analytical dispersion relation is found.

7.3.3 *DM metabarrrier vs. Equivalent SDOF metabarrier*

The performance of this DM resonator barrier is analyzed using a 2D FE model geometrically similar to the one presented for the parametric study of the SDOF case (Fig. 55). Harmonic analysis in the [1-10] Hz frequency range are developed

DM-Resonator properties

DOF (from base)	r	1	2	
Mass	m_r	7000	3500	kg
Stiffness	k_r	6e6	1e6	N/m
Foundation surface	A	1.3		m^2

Table 10: DM-Resonator for numerical evaluations

considering two metabarrier lengths, L_{res}= [0.25 0.5]λ_{ω_R}. An identical region behind the metabarrier is used to estimate the ground acceleration attenuation. The normalized vertical acceleration is used as a measure of the metabarrier attenuation. The performance of the DM metabarrier is compared with an equivalent single mass metabarrier composed by series of 2 SDOFi (SDOF1, SDOF2) equivalent resonators (Fig. 60). The equivalent SDOFi resonator is designed to provide a band gap in the same frequency region of the i^{th} band gap of the related DM resonator. By recalling the expression of the coefficient β_i for the SDOF system:

$$\beta = \frac{m f_{BG}{}^{-} \pi}{\rho c_S A} \sqrt{1 - \left(\frac{c_S}{c_L}\right)^2} = \frac{R^2 - 1}{2R}; \qquad R = \frac{f_{BG}{}^{+}}{f_{BG}{}^{-}} \tag{109}$$

and approximating its expression for each of the two band gaps as:

$$\beta_i = \frac{R_i^2 - 1}{2R_i} \approx \frac{\Delta f_{BG}}{f_{BG,avg}} \tag{110}$$

the required mass $m_{i,eq}$ and the stiffness $K_{i,eq}$ of the equivalent resonator SDOFi reads:

$$m_{i,eq} = \frac{\beta_i \rho c_S A}{f_{BGi}^{-} \pi \sqrt{1 - \left(\frac{c_S}{c_L}\right)^2}} \qquad K_{i,eq} = \omega_{r,i}^2 m_{i,eq} = (2\pi f_{BGi}^{-})^2 m_{i,eq} \tag{111}$$

Using these expressions, it is possible to identify the equivalent SDOFi resonators whose mechanical parameter are collected in Table 11.

SDOF1-SDOF2 equivalent resonators

Resonator	SDOFn	SDOF1	SDOF2	
Mass	M	5343.63	4696.10	kg
Stiffness	K	1242561	4945855	N/m
Foundation surface	S	1.3	1.3	m^2

Table 11: Mechanical and geometrical properties of the equivalent SDOFi resonators.

It is here remarked that the total SDOF1+SDOF2 mass is about 10040 kg. The

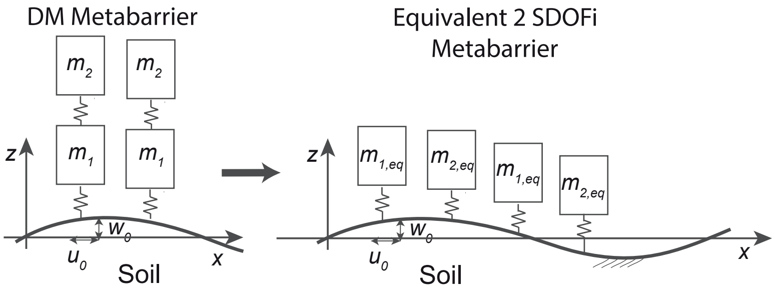
DM Metabarrier
m_2
m_2
m_1
m_1
z
w_0
u_0
Soil
x
Equivalent 2 SDOFi
Metabarrier
z
$m_{1,eq}$
$m_{2,eq}$
$m_{1,eq}$
$m_{2,eq}$
w_0
u_0
Soil
x

Figure 60: Equivalent 2SDOFi.

equivalent DM resonator has a mass of 10500 kg: the increment in used material is minimal, about 4.5%. However, the DM metabarrier requires half of the length space maintaining almost the same performances as the 2SDOFi barrier, as shown in Fig. 61.

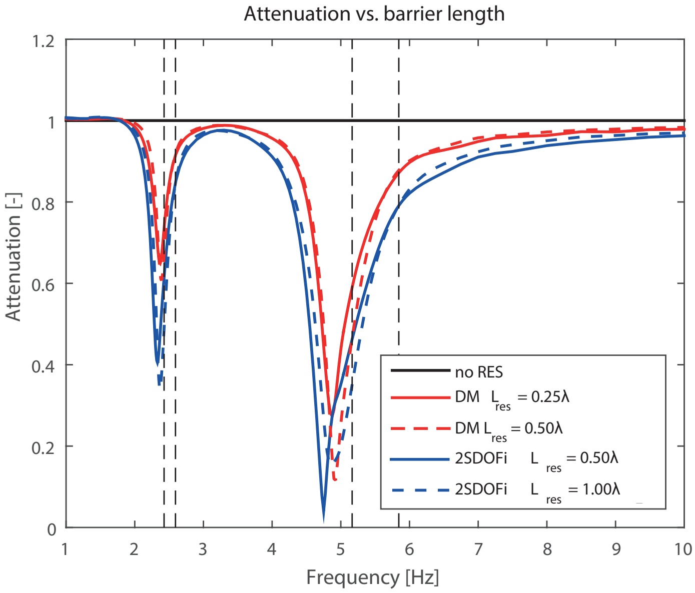

Figure 61: Attenuation vs barrier length - DM vs Equivalent 2SDOF.

7.3.4 *DM metawedge barrier vs. 2SDOF equivalent one*

The rainbow trapping concept [46, 110] can be employed to design a metabarrier of resonators with increasing frequency along the direction of wave propagation, also referred as metawedge in Ref. [47], which achieves a broader band surface wave-to-shear conversion and consequently a broader band ground motion attenuation. Here, the rainbow trapping approach is used to design a DM metawedge, with the aim of designing a more compact barrier with equivalent attenuation capabilities.

The DM metawedge is composed of 18 couples of DM resonators with increased frequency, obtained by simply scaling the stiffness of the DM resonators given in Table 10 with the factors provided in Table 15 (Appendix B), and keeping constant the masses of the resonators. By doing so, it is possible to generate complementary band gaps to cover the frequency range $2.43 \div 13.39$ Hz. As for the equivalent 2SDOF resonators metabarrier, an equivalent 2SDOF metawedge is obtained with 18 couples of 2SDOFi resonators matching the gaps of the DM resonators of the metawedge. The stiffness and masses of the 18 couples of 2SDOFi resonators are collected in Table 16 (Appendix B).
The DM metawedge shows almost the same attenuation performances of the related SDOF metabarrier, with half of the occupied length (see Fig. 62).

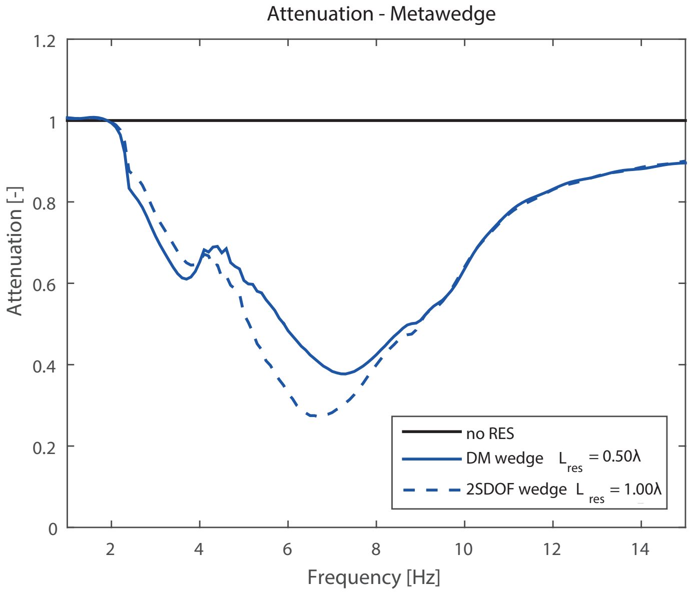

Figure 62: Attenuation - DM metawedge vs. equivalent 2SDOF metawedge

However, the wider range of frequency obtained with the metawedge arrangement is partially counteracted by the obtained lower mean attenuation. Indeed, if a metabarrier is designed to protect buildings with known dynamic properties, a more efficient solution can be achieved using resonators with multiple band gaps spanning the required frequency ranges to target all the relevant natural frequencies of such buildings. However, multiple band gaps require multi-mass resonators which in turn can result in massive devices of limited applicability. To this aim, in the next section, it is investigated the possibility of designing multi-mass resonators to target specific frequencies minimizing the total resonator mass. This design problem can be tackled using optimization strategies as the genetic algorithms (GAs).

7.4 MULTI-MASS METABARRIER: OPTIMIZATION WITH GAS

This section describes an optimization strategy based on the use of genetic algorithms (GA) to design a multi-mass metabarrier to protect a group of dynamically identified structures, i.e. structures for which the relevant natural frequencies are known. The optimization scheme aims at designing a metabarrier with n masses (i.e. n vertical modes and band-gaps) to target the first n relevant frequencies of a single or multiple structures that have to be protected, with the minimum amount of total mass of the resonator barrier. A detailed description of the characteristics and capabilities of GAs is beyond the scope of this work; the reader may refer to Ref. [139] for a more exhaustive explanation. A concise description of how the technique is used in this work is given in the following and is summarized in the flowchart of Fig. 63:

- The workflow of the optimization scheme starts with the dynamic analysis of the structures that have to protected by the metabarrier. From the modal analysis, the natural frequencies $f_r = \{f_{r,1}, ..., f_{r,n}\}$ related to significant mode shapes of the structures are selected. Here the attention is focused on the first horizontal modes of the structures, retaining all the modes with a participating modal mass along the horizontal direction > 0.05. Similarly, the transfer function $T_h(f)$ which links the applied base ground motion $U_g(f)$ to the total base shear of the structure $F(f)$ is calculated from harmonic analysis. From the structure transfer function, it is possible to identify the half-power points around each resonance to define the appropriate frequency width for the metabarrier band gaps $\Delta f_r = \{\Delta f_{r,1}, ..., \Delta f_{r,n}\}$.

- The GAs are initialized with a set of n identical masses and n identical stiffnesses $\alpha_0 = \{m_{0,1}, ..., m_{0,n}, k_{0,1}, ..., k_{0,n}\}$ based on experience and engineering judgment, such that the total mass generates a static stress below the bearing capacity of the soil. From this initial guess a population of k individuals α_j (with j=1,...,k) is created, in which one of the individuals is set equal to α_0 and the remaining ones are automatically generated varying the stiffness and mass within limits specified by upper and lower bounds (from 0.1 to 5 times the original values in α_0).

- By means of Eq. 98 with the vertical stress in Eq. 107, for each individual α_j the dispersion curve and the related n lower and upper edges $f^-_{BG,j}$, $f^+_{BG,j}$ band-gaps are calculated:

- For each individual α_j, it is verified that the n band-gaps fulfill the constraints:

$$\begin{aligned} f^-_{BG,j,n} &= \gamma f_{r,n} - \frac{\Delta f_{r,n}}{2} \\ f^+_{BG,j,n} &= \gamma f_{r,n} + \frac{\Delta f_{r,n}}{2} \end{aligned} \tag{112}$$

which ensure that the natural frequencies $f_{r,n}$ fall within the metabarrier BG and that the BG has sufficient width to cover the frequency range of interest $\Delta f_{r,n}$. A coefficient $\gamma \geqslant 1$ is used to account for the shift of the frequency peak observed in the attenuation curve.

- The population of individuals α_j which fulfill the nonlinear constraints is finally sorted according to the fitness function:

$$J(\alpha_j) = Min(\sum_{i=1}^{n} m_{j,i}) \tag{113}$$

The algorithm stops when the improvement of the best fitness value for a preset number of generations is less than a selected tolerance (stall toll) or if the maximum number of generations is reached (max num. gen.). Once convergence is reached, the best individual of the current generation is assumed as the final solution α^*. Until convergence is not reached, e elite members, i.e. the individuals α_j with the best fitness function values, are passed to the next generation, while a fraction of the remaining individuals α_j, the so-called parent individuals, are used to create the next generation, by crossover and mutation. The new generation is then used to restart the algorithm. The settings used in the following numerical applications are summarized in Table 12.

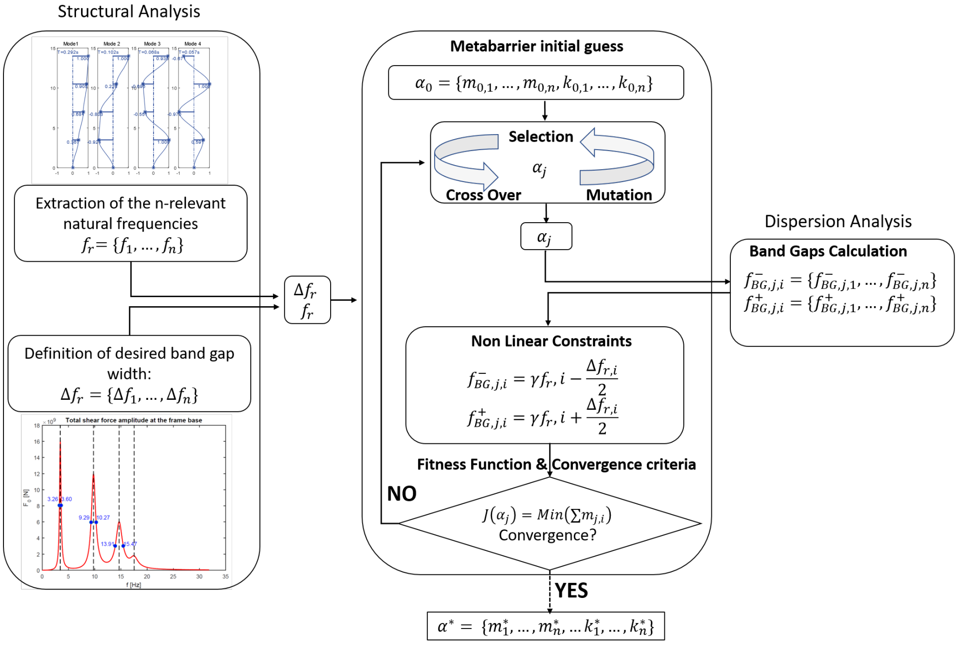
Structural Analysis
Mode 1
Mode 2
Mode 3
Mode 4
Extraction of the n-relevant natural frequencies $f_r = \{f_1, \dots, f_n\}$
Definition of desired band gap width: $\Delta f_r = \{\Delta f_1, \dots, \Delta f_n\}$
Total shear force amplitude at the frame base
f [Hz]
Δf_r
f_r
Metabarrier initial guess
$\alpha_0 = \{m_{0,1}, \dots, m_{0,n}, k_{0,1}, \dots, k_{0,n}\}$
Selection
α_j
Cross Over
Mutation
Dispersion Analysis
Band Gaps Calculation
$f^-_{BG,j,i} = \{f^-_{BG,j,1}, \dots, f^-_{BG,j,n}\}$
$f^+_{BG,j,i} = \{f^+_{BG,j,1}, \dots, f^+_{BG,j,n}\}$
Non Linear Constraints
$f^-_{BG,j,i} = \gamma f_r, i - \frac{\Delta f_{r,i}}{2}$
$f^+_{BG,j,i} = \gamma f_r, i + \frac{\Delta f_{r,i}}{2}$
Fitness Function & Convergence criteria
NO
$J(\alpha_j) = Min(\sum m_{j,i})$
Convergence?
YES
$\alpha^* = \{m_1^*, \dots, m_n^*, \dots k_1^*, \dots, k_n^*\}$

Figure 63: GA Optimization strategy

Genetic Algorithm settings

Individual	Elite	Stall criteria		
10	e=1	max time=24 h	max num. gen.=500	stall toll=10^{-10}

Table 12: Genetic Algorithm settings.

7.4.1 *Metabarrier Transfer Function and Frame response*

The GA optimization process provides an optimal resonator for a multi-mass metabarrier able to target given frequencies. Using the extended 2D FE model, the multi-mass metabarrier attenuation function is calculated within the frequency range of interest. The attenuation function $A(f)$ is a measure of the normalized residual acceleration ground motion after the metabarrier. Thus, it can be used to filter the known acceleration spectra of far-field earthquakes (which mainly contain surface waves [93]) and assess the structural response of buildings protected by the metabarrier. The procedure can be summarized in the following steps:

- From a given ground acceleration time history $\ddot{u}_g = \ddot{u}_g(t)$, the frequency spectrum $\ddot{U}_g(f)$ is obtained by applying the Fast Fourier Transform (FFT).
- Given the linearity of the system, the ground motion acceleration spectrum $\ddot{U}_g(f)$ is filtered by the metabarrier attenuation function $A(f)$, to obtain the reduced acceleration ground motion:

$$\ddot{U}_{g,red}(f) = A(f)\ddot{U}_g(f) \tag{114}$$

- The reduced acceleration spectrum can be multiplied to the structure transfer function $T_h(f)$ to obtain its shear base response:

$$F_{red}(f) = T_h(f)\ddot{U}_{g,red} \tag{115}$$

- The reduced shear response is compared to the shear response of the unprotected structure to evaluate the performance of the metabarrier.

In the following section, the optimization strategy and the metabarrier transfer function approach is applied to a case study to assess the performance of a multi-mass metabarrier.

7.4.2 *A case study: a multi-mass metabarrier for two concrete frames*

In this section, a metabarrier to protect two generic adjacent concrete-frame structures (see Fig. 64) is presented. Without loss of generality, the study of each concrete structure is performed by considering its main frame along the x direction. The frame's natural frequencies and participating masses are given in Table 13. Each frame has 40x60cm beams with 5m spans and 55x55cm columns with 3.5m storey height. The first frame has four storeys and 1 span; the second one has two storeys and four spans. Each storey is loaded with a quasi-permanent combination in accordance with the EC8. The RC structural elements (beams and columns) have a specific weight of $25\mathrm{kN/m^3}$.

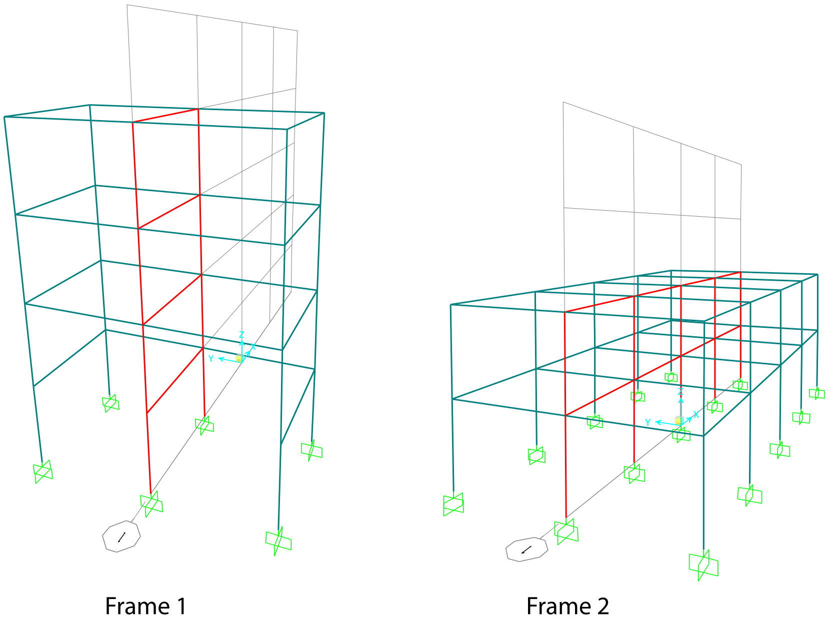

Figure 64: Concrete-frame structures. In red the main frames along the x direction.

Frequencies & modal participating masses

Frame	n.1		n.2	
1st mode	2.27Hz	82%	4.48Hz	90%
2nd mode	7.33Hz	12%	12.94Hz	10%

Table 13: First natural frequencies and modal participating masses of two 2D frames.

The frames horizontal transfer functions T_h for a unitary horizontal base acceleration are given in Fig. 65. From the transfer functions, four relevant frequency ranges are identified as the target for the metabarrier design: $BG_1 = f_{r,1} \pm \frac{\Delta f_{r,1}}{2} = 2.27 \pm 0.165$, $BG_2 = f_{r,2} \pm \frac{\Delta f_{r,2}}{2} = 4.48 \pm 0.32$, $BG_3 = f_{r,3} \pm \frac{\Delta f_{r,3}}{2} = 7.33 \pm 0.415$, $BG_4 = f_{r,4} \pm \frac{\Delta f_{r,4}}{2} = 12.94 \pm 0.735$. As a result of the GA-based optimization strategy, an optimal four-mass resonator (FM1) can be identified with a total mass $m_1 = 19817$ kg. Nonetheless, to further enlarge the attenuation band around the frame resonance frequencies, a second FM resonator (FM2) is designed starting from the best configuration of the FM1 resonator with a slight shift in the sought resonance frequencies. With this approach, the rainbow trapping concept is ex-

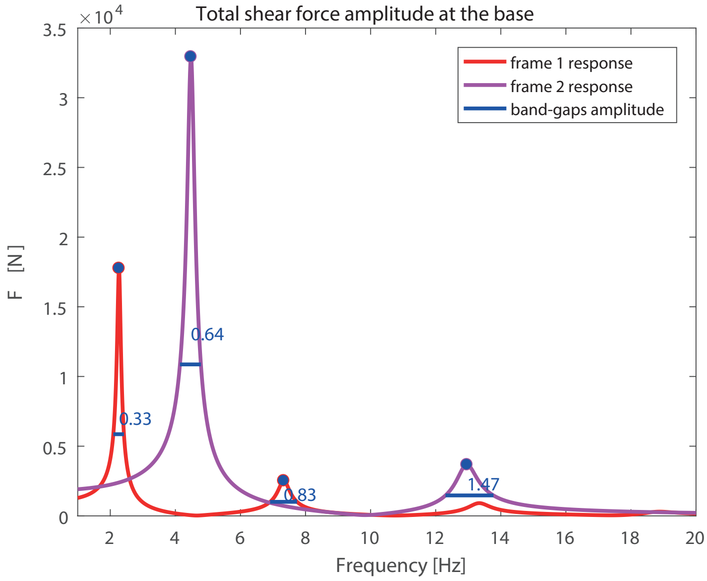

Figure 65: Concrete frame base shear transfer function T_h.

ploited just around the resonance frequencies of interest. As a result, a hybrid metawedge-metabarrier that targets specific frequencies is obtained. The mechanical properties of the designed four-mass resonators FM1 and FM2 are provided in Table 14.

Four Mass (FM) resonators properties

DOF	FM1			FM2		
r	m_r[kg]	k_r[N/m]	S [m^2]	m_r[kg]	k_r[N/m]	S [m^2]
1	5182.3	1.8772e7	1.3	4769.3	1.8702e7	1.3
2	6333.1	1.3646e7	1.3	5663.9	1.3144e7	1.3
3	4765.7	0.5067e7	1.3	4087.7	0.4652e7	1.3
4	3537.9	0.1730e7	1.3	3022.9	0.1580e7	1.3

Table 14: FM-Resonators for the metabarrier.

In Fig. 66 the attenuation function of the hybrid FM metabarrier is given. As significant attenuation (>60%) around the frame resonance frequency is achieved with a metabarrier of length $L_{res} = 0.25\lambda_{\omega_v}$ (see Fig. 66).
The metabarrier attenuation function is used to reduce the ground motion spectra of two far-field earthquake records, (i) ChiChi (TCU045 Station), (ii) Trinidad (CDMG090 Station) that are given as base motions to the analyzed frames. The normalized frames' shear base response, calculated according to Eq. 114, are shown in Fig. 67, where a significant attenuation of approximately 40% is found at the frames resonance peaks. It is here remarked that such attenuation has been obtained with

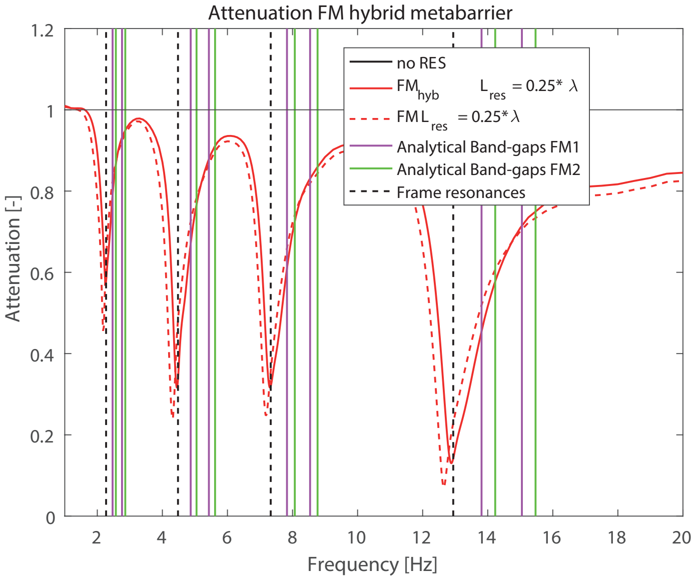

Figure 66: Attenuation function hybrid FM metabarrier

a metabarrier of subwavelength dimensions ($0.25\lambda_r$) with minimal mass resonators, which can be sustained by the analyzed sedimentary soil.

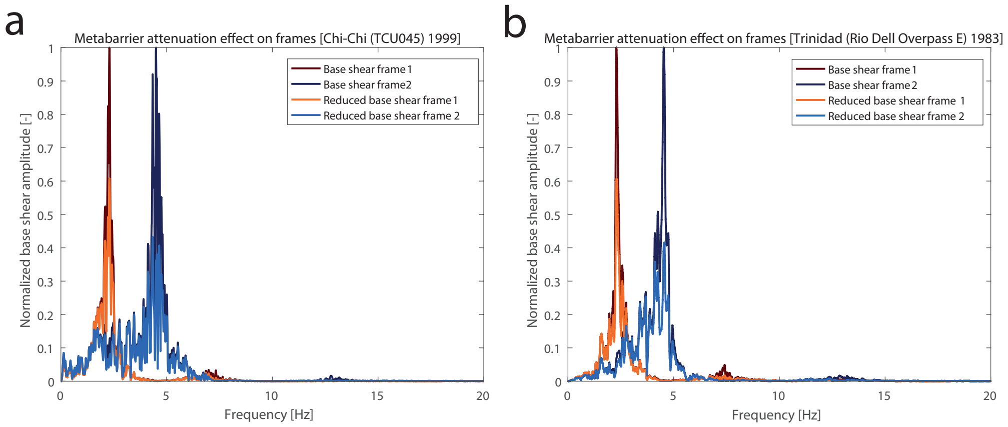

Figure 67: Frames base shear response. a) ChiChi (TCU045 Station) ground motion. b) Trinidad (CDMG090 Station) ground motion

7.5 CONCLUSION

In this Chapter, a design strategy to realize compact multi-mass metabarriers has been presented. It has been shown that a multi-mass metabarrier can be designed to target the relevant resonant frequencies of known buildings and reduce their response during an earthquake. Multi-mass resonant units can be used to substitute n single masses resonators resulting in a more compact structure for multi-frequency attenuation. The N-DOFS resonator dynamics has been predicted by means of an analytical-modal approach which extends the study of the metabarrier to multi-mass systems. Metabarriers to target known frequencies and metawedges (i.e. resonators in a rainbow trapping arrangement) to cover broader frequency range with minimal dimensions have been analysed. An optimization strategy based on the use of Genetic Algorithms has been proposed to design multi-mass resonators with minimal total mass. The metabarrier attenuation, obtained by means of FE models, has been used as a filter for incoming surface wave ground motion to analyze the response of protected buildings. The analyzed cases have demonstrated that a metabarrier with feasible dimensions (<25 m in length) may effectively reduce the seismic response of buildings with known dynamic properties.

8

CONCLUSIONS, ONGOING RESEARCH AND FUTURE OUTLOOK

The study presented in this dissertation focused on the analysis of dispersive properties of periodic and locally resonant media and the exploitation of their filtering properties for seismic wave attenuation. Part I presented the development and validation of fast FE-based numerical techniques for the extraction of complex dispersion properties of periodic/locally resonant media. Part II proposed the application of metamaterial concepts to design a metabarrier for surface seismic waves attenuation. A summary of the results was provided at the end of each chapter. Here, the main findings of this work are recapitulated, followed by a short description of the ongoing research activities and by suggestions for future research directions.

8.1 MAIN CONCLUSIONS OF PART I

In Part I, a brief overview of the available numerical techniques for complex dispersion analysis of periodic/locally resonant materials was provided. Two model reduction techniques to speed up the band structure calculation were presented and validated: the Component Mode Synthesis method and a Wave-based model reduction technique. In summary, the following conclusions are drawn:

- Knowledge of complex dispersion relation (i.e. real dispersion curve $k_r(\omega)$ and wave spatial decay $k_i(\omega)$) is fundamental for understanding the filtering properties of periodic and locally resonant media as well as for investigating energy dissipation induced by material damping.

- FE-based numerical techniques, and in particular WFE methodologies, are particularly suitable to study the complex dispersion properties of periodic/locally resonant media, given the possibility of modeling complex geometries and complex rheology. Modeling of complex 3D unit cells requires significant computational effort, which can be substantially reduced using model reduction techniques.

- The combination of a Component Mode Synthesis reduction and a WFEM $k(\omega)$ approach allows reducing the computational time for complex dispersion curves extraction up to two orders of magnitude with negligible errors for both real and evanescent/complex modes.

- A Wave-based model reduction technique can be used to project the WFEM $k(\omega)$ eigenproblem over a subset of wave shapes, significantly reducing the eigenproblem dimensions. When the filtering properties of periodic and locally resonant materials are of interest, wave shapes need to be carefully selected to reconstruct both the propagative and the highly decaying solutions. The Wave-based model reduction technique can be applied on the CMS reduced WFEM $k(\omega)$ eigenproblem to further reduce the band structure computational effort (up to 50%) with no significant additional discrepancy on the calculated solutions.

8.2 MAIN CONCLUSIONS OF PART II

In Part II, a comprehensive review of periodic and locally resonant structures for seismic wave propagation control was provided. A metabarrier of surface resonant units able to attenuate the propagation of seismic Rayleigh waves in the low-frequency range was proposed. Design strategies for single-mass and multi-mass metabarriers able to target multiple known resonance frequencies of buildings were discussed. In summary, the following conclusions are drawn:

- The application of phononic and metamaterial concepts can represent an alternative solution to protect existing buildings from seismic hazards.

- Locally resonant structures, which are able to control the propagation of waves with subwavelength units, are the best candidates to realize viable solutions for seismic isolation of large urbanized area.

- An array of locally resonant units, each one made of a steel mass encased in a concrete cylinder buried at the soil surface, can realize a metabarrier able to convert Rayleigh waves into shear bulk waves, attenuating the surface ground motion. Surface waves deflection is an advantageous concept for seismic wave isolation since the elastic energy is neither reflected nor rerouted on the surface, where waves could remain harmful for surrounding regions.

- Single-mass resonator metabarrier are effective in a narrow frequency range around the resonator vertical frequency. However, single-mass barriers of significant length and mass are required to achieve a substantial ground motion attenuation. An arrangement of resonators with increasing frequencies (rainbow trapping concept) can be used to broaden the barrier attenuation range, still requiring the same total length.

- Multi-mass resonators can substitute n single-mass resonators for a more compact metabarrier able to target multiple frequency ranges. The multi-mass resonators can be used both in a rainbow trapping arrangement to cover wide ranges of frequency or to target specific resonance frequencies of the buildings that have to be protected.

- Multi-mass resonators with minimal mass can be designed utilizing an optimization strategy based on Genetic Algorithms. A compact metabarrier of optimal multi-mass resonators can achieve a significant reduction in the shear base response of buildings subjected to far-field earthquakes.

8.3 ONGOING RESEARCH

This section provides a brief description of some of the research activities currently in progress, related both to the development of numerical methods for band structures calculation and to extend the study of the proposed seismic metabarrier.

8.3.1 *Model reduction technique for the FE Bloch operator transformation approach*

As discussed in Chapt.2 sect. 2.5, the FE Bloch operator transformation approach requires an ad-hoc implementation which has limited its application in comparison to the simplest WFE approach. However, the Bloch operator transformation presents a key advantage for the study of complex dispersion curves as it allows spanning all the directions of propagation without increasing the order of the eigenvalue problem [50]. On the contrary, the WFE approach results in high order polynomial (or transcendental) eigenproblems when 3D periodic structures are of interest [20]. For this reason, the Bloch operator transformation is suitable to investigate the wave directional effects of 2D (or even 3D) periodic system employing directivity plots, which provide information on the wave decay along different spatial directions. However, the study of directivity/beaming effects requires the solution of Bloch eigenproblems at multiple frequency steps and along multiple directions, resulting in an expensive computational procedure.

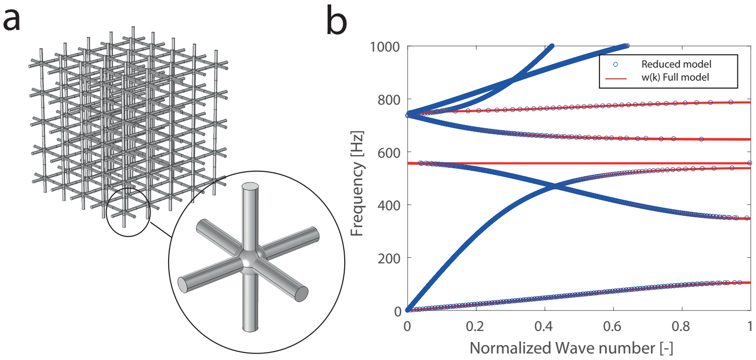

Figure 68: a) 3D Lattice structure. b) Real dispersion curve: Full $\omega(k)$ solution vs. Reduced $k(\omega)$ Bloch transformation approach.

At the moment no model reduction techniques are available to reduce the computational effort of the Bloch operator transformation approach. Indeed, a Wave-base reduction strategy based on a reduced set of wave shapes selected at specific directions and specific frequencies could be used to construct a reduced base for such formulation. The first results obtained utilizing such approach are promising, as it can be seen from the dispersion curve of a 3D lattice system, provided in Fig. 68. An extended investigation on the criteria for the appropriate wave shape selection as well as on the accuracy and computational benefit of the method is now in progress.

8.3.2 *Metabarriers in inhomogeneous soil profile*

Soils can be characterized by strongly inhomogeneous velocity profiles along the depth which lead to the propagation of surface modes with dispersive and multimodal nature [140]. As such, it is of primary interest to investigate if surface waves traveling in an inhomogeneous soil can be controlled by means of surface resonators. The nature of surface waves traveling in a medium with inhomogeneous depth profile has been thoroughly studied in the literature [141–143]. In particular, mechanical waves guided along the free surface of a granular medium have been used to extract the equivalent elastic profiles of the unconsolidated medium [144] and study the propagation of seismic waves in sedimentary soils [145]. At the moment, an experimental and numerical campaign is in progress to assess the possibility of attenuating surface waves in an inhomogeneous granular medium through surface resonators. The small scale experimental setup consists of a wooden box (2mX1.5mx1m) filled with a granular medium (Glass beads) characterized by a power law inhomogeneous velocity profile (see Fig. 69). Scaled 3D printed resonators are embedded in this medium to realize metabarrier of different lengths.Preliminary experimental and numerical results suggest that surface waves in inhomogeneous soils can be still deflected by a metabarrier of vertical resonators (see Fig. 70a,b).

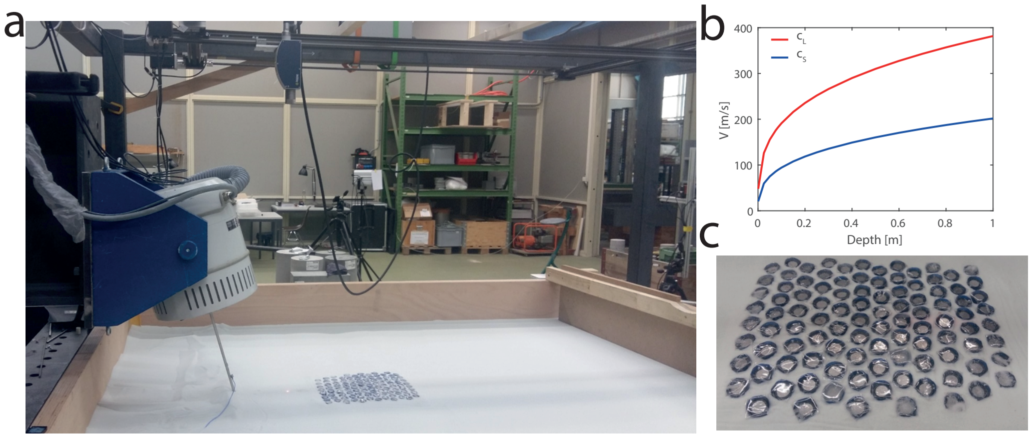

Figure 69: a) Small scale experimental setup. b) Granular medium velocity profile. c) Embedded scaled metabbarier.

However, far from the metabarrier, part of the elastic energy is rerouted to the surface due to the increasing stiffness of the medium (Fig. (70)d). Further numerical and experimental studies are now in progress to clarify/investigate this aspect and quantify the amount of energy back reflected into the surface for real soil stratigraphy.

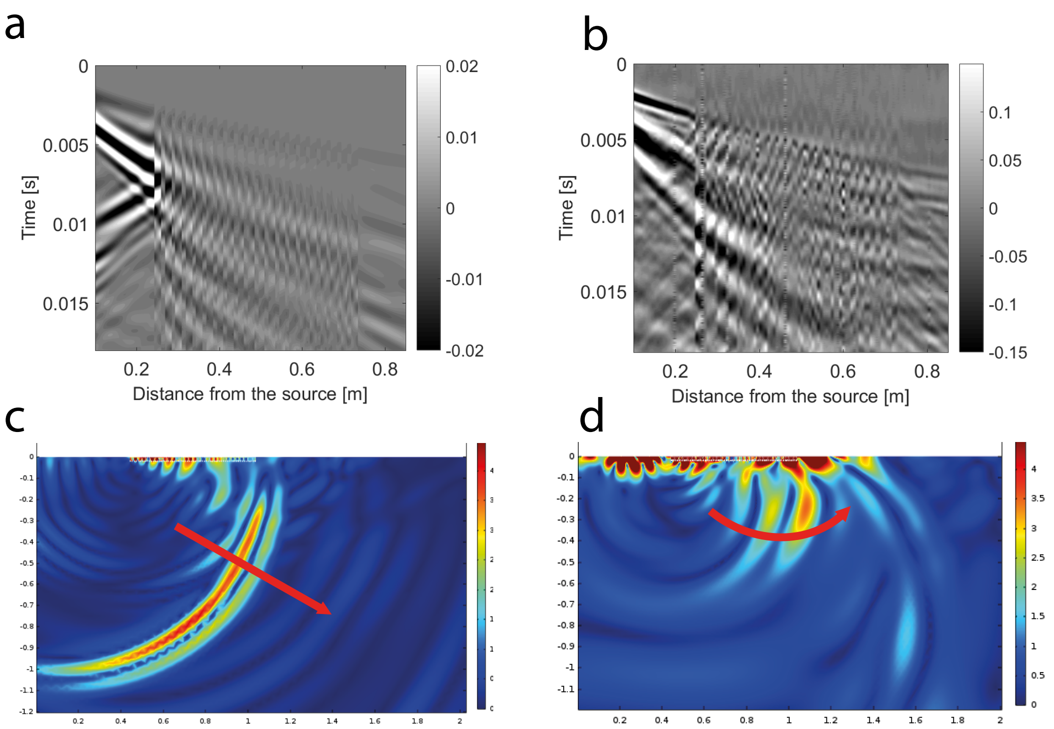

Figure 70: a) Numerical and b) Experimental velocity seismographs of surface waves traveling through the metabarrier in the granular medium. c) Wave conversion of a metabarrier in a homogeneous soil. d) Wave conversion and back reflection in the inhomogeneous soil.

8.4 FUTURE OUTLOOK

Building on the results shown in the dissertation, the future research activity should aim at assessing the performance of seismic metabarries, and more in general seismic metamaterials, under more realistic earthquake scenarios. To this purpose, an accurate description of the soil-metamaterial interaction, which accounts for soil and metamaterial non-linearities, is required. Similarly, a richer description of near-surface soil stratigraphy and topography, which can significantly influence the wave propagation pattern due to specific site effects like waves focusing, energy trapping or basin effects [146], is desirable.

This challenge can be tackled within a multi-scale computational framework able to provide both a detailed description of the local soil-metamaterial-structure interaction and a global/site description of the seismic wave propagation pattern in real soils with complex stratigraphy and topography.

Model reduction strategies presented within the context of this dissertation can serve as a base for the development of reduced models to accurately describe the soil-metamaterial dynamics at the local scale. The attenuation of seismic waves could be then investigated at the site scale by introducing such reduced models in available computational tools for sophisticated geotechnical earthquake simulations. The simulations should allow investigating the coupling of site effects (i.e. ground response effects, basin-edge effects and topography effects) and metamaterial induced attenuation, giving more complete indications on the performance of these isolation systems and ultimately serving as a guideline for real scale test of seismic metamaterials.

Part III

APPENDIX

.1 APPENDIX A

In this appendix the coefficient matrices and the linearizations of the eigenvalue problems in Eqs. (38), (40) and (42) are provided.
Along the Γ-X direction the eigenproblem reads:

$$[\mathbf{D}_{0x}(\omega) + \mathbf{D}_{1x}(\omega)\lambda_x + \mathbf{D}_{2x}(\omega)\lambda_x^2]\mathbf{v}_R = 0$$

with:

$$\mathbf{D}_{0x} = \begin{bmatrix} \mathbf{0} & \mathbf{0} & \mathbf{0} & \mathbf{0} \\ \mathbf{D}_{b_4 i} & \mathbf{D}_{b_4 b_1} & (\mathbf{D}_{b_4 b_2} + \mathbf{D}_{b_4 b_5}) & (\mathbf{D}_{b_4 b_3} + \mathbf{D}_{b_4 b_7}) \\ \mathbf{0} & \mathbf{0} & \mathbf{0} & \mathbf{0} \\ (\mathbf{D}_{b_6 i} + \mathbf{D}_{b_8 i}) & (\mathbf{D}_{b_6 b_1} + \mathbf{D}_{b_8 b_1}) & (\mathbf{D}_{b_6 b_2} + \mathbf{D}_{b_6 b_5} + \mathbf{D}_{b_8 b_2} + \mathbf{D}_{b_8 b_5}) & (\mathbf{D}_{b_6 b_3} + \mathbf{D}_{b_6 b_7} + \mathbf{D}_{b_8 b_3} + \mathbf{D}_{b_8 b_7}) \end{bmatrix}$$

$$\mathbf{D}_{1x} = \begin{bmatrix} \mathbf{D}_{ii} & \mathbf{D}_{ib_1} & (\mathbf{D}_{ib_2} + \mathbf{D}_{ib_5}) & (\mathbf{D}_{ib_3} + \mathbf{D}_{ib_7}) \\ (\mathbf{D}_{b_1 i} & (\mathbf{D}_{b_1 b_1} + \mathbf{D}_{b_4 b_4}) & (\mathbf{D}_{b_1 b_2} + \mathbf{D}_{b_1 b_5}) & (\mathbf{D}_{b_1 b_3} + \mathbf{D}_{b_1 b_7}\mathbf{D}_{b_4 b_6} + \mathbf{D}_{b_4 b_8}) \\ \mathbf{D}_{b_2 i} + \mathbf{D}_{b_5 i} & (\mathbf{D}_{b_2 b_1} + \mathbf{D}_{b_5 b_1}) & (\mathbf{D}_{b_2 b_2} + \mathbf{D}_{b_2 b_5} + \mathbf{D}_{b_5 b_2} + \mathbf{D}_{b_5 b_5}) & (\mathbf{D}_{b_2 b_3} + \mathbf{D}_{b_2 b_7} + \mathbf{D}_{b_5 b_3} + \mathbf{D}_{b_5 b_7}) \\ (\mathbf{D}_{b_3 i} + \mathbf{D}_{b_7 i}) & (\mathbf{D}b3b_1 + \mathbf{D}_{b_6 b_4} + \mathbf{D}_{b_7 b_1} + \mathbf{D}_{b_8 b_4}) & (\mathbf{D}_{b_3 b_2} + \mathbf{D}_{b_3 b_5} + \mathbf{D}_{b_7 b_2} + \mathbf{D}_{b_8 b_5}) & (\mathbf{D}_{b_3 b_3} + \mathbf{D}_{b_3 b_7} + \mathbf{D}_{b_6 b_6} + \mathbf{D}_{b_6 b_8} + \mathbf{D}_{b_7 b_3} + \mathbf{D}_{b_7 b_7} + \mathbf{D}_{b_8 b_6} + \mathbf{D}_{b_8 b_8} \end{bmatrix}$$

$$\mathbf{D}_{2x} = \begin{bmatrix} \mathbf{0} & \mathbf{D}_{ib_4} & \mathbf{0} & (\mathbf{D}_{ib_6} + \mathbf{D}_{ib_8}) \\ \mathbf{0} & (\mathbf{D}_{b_1 b_4} + \mathbf{D}_{b_4 b_5}) & \mathbf{0} & (\mathbf{D}_{b_1 b_6} + \mathbf{D}_{b_1 b_8}) \\ \mathbf{0} & (\mathbf{D}_{b_2 b_4} + \mathbf{D}_{b_5 b_4}) & \mathbf{0} & (\mathbf{D}_{b_2 b_6} + \mathbf{D}_{b_2 b_8} + \mathbf{D}_{b_5 b_6} + \mathbf{D}_{b_5 b_8}) \\ \mathbf{0} & (\mathbf{D}_{b_3 b_4} + \mathbf{D}_{b_7 b_4}) & \mathbf{0} & (\mathbf{D}_{b_3 b_6} + \mathbf{D}_{b_3 b_8} + \mathbf{D}_{b_7 b_6} + \mathbf{D}_{b_7 b_8}) \end{bmatrix}$$

Along the X-M direction the eigenproblem reads:

$$[\mathbf{D}_{0y}(\omega) + \mathbf{D}_{1y}(\omega)\lambda_y + \mathbf{D}_{2y}(\omega)\lambda_y^2]\mathbf{v}_R = 0$$

with:

$$\mathbf{D}_{0y} = \begin{bmatrix} \mathbf{0} & \mathbf{0} & \mathbf{0} & \mathbf{0} \\ \mathbf{D}_{b_4 i} & \mathbf{D}_{b_4 b_1} & (\mathbf{D}_{b_4 b_2} - \mathbf{D}_{b_4 b_5}) & (\mathbf{D}_{b_4 b_3} - \mathbf{D}_{b_4 b_6}) \\ \mathbf{0} & \mathbf{0} & \mathbf{0} & \mathbf{0} \\ (\mathbf{D}_{b_7 i} - \mathbf{D}_{b_8 i}) & (\mathbf{D}_{b_7 b_1} - \mathbf{D}_{b_8 b_1}) & (\mathbf{D}_{b_7 b_2} - \mathbf{D}_{b_7 b_5} - \mathbf{D}_{b_8 b_2} + \mathbf{D}_{b_8 b_5}) & (\mathbf{D}_{b_7 b_3} - \mathbf{D}_{b_7 b_6} - \mathbf{D}_{b_8 b_3} + \mathbf{D}_{b_8 b_6}) \end{bmatrix}$$

$$\mathbf{D}_{1y} = \begin{bmatrix} \mathbf{D}_{ii} & \mathbf{D}_{ib_1} & (\mathbf{D}_{ib_2} - \mathbf{D}_{ib_5}) & (\mathbf{D}_{ib_3} - \mathbf{D}_{ib_6}) \\ \mathbf{D}_{b_1 i} & (\mathbf{D}_{b_1 b_1} + \mathbf{D}_{b_4 b_4}) & (\mathbf{D}_{b_1 b_2} - \mathbf{D}_{b_1 b_5} & (\mathbf{D}_{b_1 b_3} - \mathbf{D}_{b_1 b_6} + \mathbf{D}_{b_4 b_7} - \mathbf{D}_{b_4 b_8}) \\ (\mathbf{D}_{b_2 i} - \mathbf{D}_{b_5 i}) & (\mathbf{D}_{b_2 b_1} - \mathbf{D}_{b_5 b_1}) & (\mathbf{D}_{b_2 b_2} - \mathbf{D}_{b_2 b_5} - \mathbf{D}_{b_5 b_2} + \mathbf{D}_{b_5 b_5}) & (\mathbf{D}_{b_2 b_3} - \mathbf{D}_{b_2 b_6} - \mathbf{D}_{b_5 b_3} + \mathbf{D}_{b_5 b_6}) \\ (\mathbf{D}_{b_3 i} - \mathbf{D}_{b_6 i}) & (\mathbf{D}_{b_3 b_1} - \mathbf{D}_{b_6 b_1} + \mathbf{D}_{b_7 b_4} - \mathbf{D}b8b4) & (\mathbf{D}b3b2 - \mathbf{D}_{b_3 b_5} - \mathbf{D}_{b_6 b_2} + \mathbf{D}_{b_6 b_5}) & (\mathbf{D}_{b_3 b_3} - \mathbf{D}_{b_3 b_6} - \mathbf{D}_{b_6 b_3} + \mathbf{D}_{b_6 b_6} + \mathbf{D}_{b_7 b_7} - \mathbf{D}_{b_7 b_8} - \mathbf{D}_{b_8 b_7} + \mathbf{D}_{b_8 b_8}) \end{bmatrix}$$

$$\mathbf{D}_{2y} = \begin{bmatrix} \mathbf{0} & \mathbf{D}_{ib_4} & \mathbf{0} & (\mathbf{D}_{ib_7} - \mathbf{D}_{ib_8}) \\ \mathbf{0} & \mathbf{D}_{b_1 b_4} & \mathbf{0} & (\mathbf{D}_{b_1 b_7} - \mathbf{D}_{b_1 b_8}) \\ \mathbf{0} & (\mathbf{D}_{b_2 b_4} - \mathbf{D}_{b_5 b_4}) & \mathbf{0} & (\mathbf{D}_{b_2 b_7} - \mathbf{D}_{b_5 b_7} - \mathbf{D}_{b_2 b_8} + \mathbf{D}_{b_5 b_8}) \\ \mathbf{0} & (\mathbf{D}_{b_3 b_4} - \mathbf{D}_{b_6 b_4}) & \mathbf{0} & (\mathbf{D}_{b_3 b_7} - \mathbf{D}_{b_3 b_8} - \mathbf{D}_{b_6 b_7} + \mathbf{D}_{b_6 b_8}) \end{bmatrix}$$

Along the M-Γ direction the eigenproblem reads:

$$[\mathbf{D}_0(\omega) + \mathbf{D}_1(\omega)\lambda + \mathbf{D}_2(\omega)\lambda^2 + \mathbf{D}_3(\omega)\lambda^3 + \mathbf{D}_4(\omega)\lambda^4]\mathbf{v}_R = 0$$

with:

$$\mathbf{D}_0 = \begin{bmatrix} \mathbf{0} & \mathbf{0} & \mathbf{0} & \mathbf{0} \\ \mathbf{0} & \mathbf{0} & \mathbf{0} & \mathbf{0} \\ \mathbf{0} & \mathbf{0} & \mathbf{0} & \mathbf{0} \\ \mathbf{D}_{b_8 i} & \mathbf{D}_{b_8 b_1} & \mathbf{D}_{b_8 b_2} & \mathbf{D}_{b_8 b_3} \end{bmatrix}$$

$$\mathbf{D}_1 = \begin{bmatrix} \mathbf{0} & \mathbf{0} & \mathbf{0} & \mathbf{0} \\ \mathbf{D}_{b_4 i} & \mathbf{D}_{b_4 b_1} & \mathbf{D}_{b_4 b_2} & \mathbf{D}_{b_4 b_3} \\ \mathbf{D}_{b_5 i} & \mathbf{D}_{b_5 b_1} & \mathbf{D}_{b_5 b_2} & \mathbf{D}_{b_5 b_3} \\ (\mathbf{D}_{b_6 i} + \mathbf{D}_{b_7 i}) & (\mathbf{D}_{b_6 b_1} + \mathbf{D}_{b_7 b_1} + \mathbf{D}_{b_8 b_4}) & (\mathbf{D}_{b_6 b_2} + \mathbf{D}_{b_7 b_2} + \mathbf{D}_{b_8 b_5}) & (\mathbf{D}_{b_6 b_3} + \mathbf{D}_{b_7 b_3} + \mathbf{D}_{b_8 b_6} + \mathbf{D}_{b_8 b_7}) \end{bmatrix}$$

$$\mathbf{D}_2 = \begin{bmatrix} \mathbf{D}_{ii} & \mathbf{D}_{ib_1}) & \mathbf{D}_{ib_2} & \mathbf{D}_{ib_3} \\ \mathbf{D}_{b_1 i} & (\mathbf{D}_{b_1 b_1} + \mathbf{D}_{b_4 b_4}) & (\mathbf{D}_{b_1 b_2} + \mathbf{D}_{b_4 b_5}) & (\mathbf{D}_{b_1 b_3} + \mathbf{D}_{b_4 b_6} + \mathbf{D}_{b_4 b_7}) \\ \mathbf{D}_{b_2 i} & (\mathbf{D}_{b_2 b_1} + \mathbf{D}_{b_5 b_4}) & (\mathbf{D}_{b_2 b_2} + \mathbf{D}_{b_5 b_5}) & (\mathbf{D}_{b_2 b_3} + \mathbf{D}_{b_5 b_6} + \mathbf{D}_{b_5 b_7}) \\ \mathbf{D}_{b_3 i} & (\mathbf{D}_{b_3 b_1} + \mathbf{D}_{b_6 b_4} + \mathbf{D}_{b_7 b_4}) & (\mathbf{D}_{b_3 b_2} + \mathbf{D}_{b_6 b_5} + \mathbf{D}_{b_7 b_5}) & (\mathbf{D}_{b_3 b_3} + \mathbf{D}_{b_6 b_6} + \mathbf{D}_{b_6 b_7} + \mathbf{D}_{b_7 b_6} + \mathbf{D}_{b_7 b_7} + \mathbf{D}_{b_8 b_8}) \end{bmatrix}$$

$$\mathbf{D}_3 = \begin{bmatrix} \mathbf{0} & \mathbf{D}_{ib_4} & \mathbf{D}_{ib_5} & (\mathbf{D}_{ib_6} + \mathbf{D}_{ib_7}) \\ \mathbf{0} & \mathbf{D}_{b_1 b_4} & \mathbf{D}_{b_1 b_5} & (\mathbf{D}_{b_1 b_6} + \mathbf{D}_{b_1 b_7} + \mathbf{D}_{b_4 b_8}) \\ \mathbf{0} & \mathbf{D}_{b_2 b_4} & \mathbf{D}_{b_2 b_5} & (\mathbf{D}_{b_2 b_6} + \mathbf{D}_{b_2 b_7} + \mathbf{D}_{b_5 b_8}) \\ \mathbf{0} & \mathbf{D}_{b_3 b_4} & \mathbf{D}_{b_3 b_5} & (\mathbf{D}_{b_3 b_6} + \mathbf{D}_{b_3 b_7} + \mathbf{D}_{b_6 b_8} + \mathbf{D}_{b_7 b_8}) \end{bmatrix}$$

$$\mathbf{D}_4 = \begin{bmatrix} \mathbf{0} & \mathbf{0} & \mathbf{0} & \mathbf{D}_{ib_8} \\ \mathbf{0} & \mathbf{0} & \mathbf{0} & \mathbf{D}_{b_1 b_8} \\ \mathbf{0} & \mathbf{0} & \mathbf{0} & \mathbf{D}_{b_2 b_8} \\ \mathbf{0} & \mathbf{0} & \mathbf{0} & \mathbf{D}_{b_3 b_8} \end{bmatrix}$$

The quadratic and quartic eigenvalue problems in Eqs. (38), (40) and (42) are linearized in the form:

$$(\mathbf{A} - \lambda \mathbf{B})\mathbf{x} = \mathbf{0} \tag{116}$$

For the quadratic eigenproblems along Γ-X and X-M directions the operators **A** and **B** are defined as:

$$\mathbf{A} = \begin{bmatrix} -\mathbf{D}_0 & \mathbf{0} \\ \mathbf{0} & \mathbf{D}_1 \end{bmatrix} \qquad \mathbf{B} = \begin{bmatrix} \mathbf{D}_1 & \mathbf{D}_2 \\ \mathbf{D}_1 & \mathbf{0} \end{bmatrix}$$

For the quartic eigenproblem along M-Γ directions the operators **A** and **B** are defined as:

$$\mathbf{A} = \begin{bmatrix} \mathbf{0} & -\mathbf{I} & \mathbf{0} & \mathbf{0} \\ \mathbf{0} & \mathbf{0} & -\mathbf{I} & \mathbf{0} \\ \mathbf{0} & \mathbf{0} & \mathbf{0} & -\mathbf{I} \\ \mathbf{D}_0 & \mathbf{D}_1 & \mathbf{D}_2 & \mathbf{D}_3 \end{bmatrix} \qquad \mathbf{B} = \begin{bmatrix} -\mathbf{I} & \mathbf{0} & \mathbf{0} & \mathbf{0} \\ \mathbf{0} & -\mathbf{I} & \mathbf{0} & \mathbf{0} \\ \mathbf{0} & \mathbf{0} & -\mathbf{I} & \mathbf{0} \\ \mathbf{0} & \mathbf{0} & \mathbf{0} & -\mathbf{D}_4 \end{bmatrix}$$

where **I** is the identity operator or any multiple of the identity operator. To avoid ill-conditioning, we used a multiple of the identity operator with the same order of magnitude of the average of the non-zero diagonal elements of the operator $\mathbf{D}_1$.

.2 APPENDIX B

In this appendix the mechanical properties of the DM metawedges described in Chapter 7, sect. 1.3.4 are given.

Resonator Couple	Scaling Factor	f_{BG1}^{-} [Hz]	f_{BG2}^{-} [Hz]
1	1.00	2.43	5.17
2	1.05^2	2.55	5.43
3	1.10^2	2.67	5.69
4	1.15^2	2.79	5.95
5	1.20^2	2.92	6.20
6	1.25^2	3.04	6.46
7	1.30^2	3.16	6.72
8	1.35^2	3.28	6.98
9	1.40^2	3.40	7.24
10	1.45^2	3.53	7.50
11	1.50^2	3.65	7.76
12	1.55^2	3.77	8.01
13	1.60^2	3.89	8.27
14	1.65^2	4.01	8.53
15	1.70^2	4.13	8.79
16	1.80^2	4.37	9.31
17	1.90^2	4.62	9.82
18	2.00^2	4.86	10.34

Table 15: Stiffness scaling factors for the DM metawedge

Mass [kg]	Stiffness [N/m]	f^{-}_{BG}[Hz]	f^{+}_{BG}[Hz]	β
5343.63	1242561	2.43	2.59	0.066
5304.84	1359980	2.55	2.73	0.069
5266.32	1481747	2.67	2.87	0.072
5228.07	1607750	2.79	3.01	0.075
5190.09	1737877	2.91	3.15	0.077
5152.39	1872019	3.03	3.29	0.080
5114.98	2010072	3.16	3.43	0.082
5077.85	2151931	3.28	3.57	0.085
5041.00	2297494	3.40	3.71	0.087
5004.45	2446662	3.52	3.85	0.090
4968.20	2599339	3.64	3.99	0.092
4932.24	2755429	3.76	4.13	0.095
4896.59	2914840	3.88	4.28	0.097
4861.23	3077483	4.00	4.42	0.099
4826.18	3243268	4.13	4.57	0.102
4757.00	3583927	4.37	4.86	0.106
4689.04	3936157	4.61	5.15	0.110
4622.32	4299331	4.85	5.44	0.115
4696.10	4945855	5.17	5.84	0.124
4711.86	5471104	5.42	6.18	0.130
4727.40	6024370	5.68	6.51	0.137
4742.72	6605821	5.94	6.86	0.144
4757.81	7215621	6.20	7.20	0.151
4772.69	7853928	6.46	7.55	0.157
4787.34	8520893	6.71	7.91	0.164
4801.78	9216658	6.97	8.27	0.171
4815.99	9941362	7.23	8.63	0.178
4829.99	10695137	7.49	9.00	0.185
4843.78	11478109	7.75	9.37	0.192
4857.34	12290397	8.01	9.75	0.199
4870.69	13132116	8.26	10.14	0.206
4883.83	14003375	8.52	10.52	0.213
4896.76	14904277	8.78	10.92	0.220
4922.00	16795396	9.30	11.72	0.234
4946.41	18806200	9.81	12.54	0.248
4970.01	20937337	10.33	13.39	0.262

Table 16: 2SDOF resonators properties for equivalent metawedge

BIBLIOGRAPHY

[1] V. M. Shalaev. "Optical negative-index metamaterials." In: *Nature photonics* 1.1 (2007), pp. 41–48.

[2] J. D. Joannopoulos, S. G. Johnson, J. N. Winn, and R. D. Meade. *Photonic crystals: molding the flow of light*. Princeton university press, 2011.

[3] M. Maldovan. "Sound and heat revolutions in phononics." In: *Nature* 503.7475 (2013), pp. 209–217.

[4] M. I Hussein, M. J Leamy, and M. Ruzzene. "Dynamics of Phononic Materials and Structures: Historical Origins, Recent Progress, and Future Outlook." In: *Applied Mechanics Reviews* 66.4 (2014), p. 040802.

[5] L. Brillouin. *Wave Propagation in Periodic Structures: Electric Filters and Crystal Lattices*. Dover phoenix editions. Dover Publications, 2003.

[6] M-H Lu, L. Feng, and Y-F Chen. "Phononic crystals and acoustic metamaterials." In: *Materials Today* 12.12 (2009), pp. 34 –42. ISSN: 1369-7021.

[7] M. M. Sigalas and E. N. Economou. "Elastic and acoustic wave band structure." In: *Journal of Sound and Vibration* 158.2 (1992), pp. 377–382.

[8] M. M. Sigalas and E. N. Economou. "Band structure of elastic waves in two dimensional systems." In: *Solid State Communications* 86.3 (1993), pp. 141 – 143. ISSN: 0038-1098.

[9] M. S. Kushwaha, P. Halevi, L. Dobrzynski, and B. Djafari-Rouhani. "Acoustic band structure of periodic elastic composites." In: *Phys. Rev. Lett.* 71 (13 1993), pp. 2022–2025.

[10] M. S. Kushwaha, P. Halevi, G. Martínez, L. Dobrzynski, and B. Djafari-Rouhani. "Theory of acoustic band structure of periodic elastic composites." In: *Phys. Rev. B* 49 (4 1994), pp. 2313–2322.

[11] E. N. Economou and M. M. Sigalas. "Stop bands for elastic waves in periodic composite materials." In: *The Journal of the Acoustical Society of America* 95.4 (1994), pp. 1734–1740.

[12] Y. Tanaka and S. Tamura. "Surface acoustic waves in two-dimensional periodic elastic structures." In: *Physical Review B* 58.12 (1998), p. 7958.

[13] F. Meseguer, M. Holgado, D. Caballero, N. Benaches, J. Sánchez-Dehesa, C. López, and J. Llinares. "Rayleigh-wave attenuation by a semi-infinite two-dimensional elastic-band-gap crystal." In: *Physical Review B* 59.19 (1999), p. 12169.

[14] C. Jiu-Jiu, Q. Bo, and C. Jian-Chun. "Complete band gaps for lamb waves in cubic thin plates with periodically placed inclusions." In: *Chinese Physics Letters* 22.7 (2005), p. 1706.

[15] J.O. Vasseur, P.A. Deymier, B. Djafari-Rouhani, Y. Pennec, and A.C. Hladky-Hennion. "Absolute forbidden bands and waveguiding in two-dimensional phononic crystal plates." In: *Physical Review B* 77.8 (2008), p. 085415.

[16] T-T Wu, J-C Hsu, and J-H Sun. "Phononic plate waves." In: *IEEE transactions on ultrasonics, ferroelectrics, and frequency control* 58.10 (2011), pp. 2146–2161.

[17] D. M. Mead. "Wave propagation in continuous periodic structures: research contributions from Southampton, 1964–1995." In: *Journal of Sound and Vibration* 190.3 (1996), pp. 495–524.

[18] R.M. Orris and M. Petyt. "A finite element study of harmonic wave propagation in periodic structures." In: *Journal of Sound and Vibration* 33.2 (1974), pp. 223 –236. ISSN: 0022-460X.

[19] B. R. Mace, D. Duhamel, M. J. Brennan, and L. Hinke. "Finite element prediction of wave motion in structural waveguides." In: *The J. of the Acoustical Society of America* 117.5 (2005), pp. 2835–2843.

[20] B. R. Mace and E. Manconi. "Modelling wave propagation in two-dimensional structures using finite element analysis." In: *Journal of Sound and Vibration* 318.4 (2008), pp. 884–902.

[21] M. Ruzzene, F. Scarpa, and F. Soranna. "Wave beaming effects in two-dimensional cellular structures." In: *Smart Materials and Structures* 12.3 (2003), p. 363.

[22] M. Ruzzene and F. Scarpa. "Directional and band-gap behavior of periodic auxetic lattices." In: *physica status solidi (b)* 242.3 (2005), pp. 665–680.

[23] A. Srikantha Phani, J. Woodhouse, and N. A. Fleck. "Wave propagation in two-dimensional periodic lattices." In: *The Journal of the Acoustical Society of America* 119.4 (2006), pp. 1995–2005.

[24] S. Gonella and M. Ruzzene. "Analysis of in-plane wave propagation in hexagonal and re-entrant lattices." In: *Journal of Sound and Vibration* 312.1 (2008), pp. 125–139.

[25] A. Spadoni, M. Ruzzene, S. Gonella, and F. Scarpa. "Phononic properties of hexagonal chiral lattices." In: *Wave motion* 46.7 (2009), pp. 435–450.

[26] S. A. Cummer, J. Christensen, and A. Alù. "Controlling sound with acoustic metamaterials." In: *Nature Reviews Materials* 1 (2016), p. 16001.

[27] J. B. Pendry. "Negative refraction makes a perfect lens." In: *Physical review letters* 85.18 (2000), p. 3966.

[28] Z. Liu, X. Zhang, Y. Mao, Y. Y. Zhu, Z. Yang, C. T. Chan, and P. Sheng. "Locally resonant sonic materials." In: *Science* 289.5485 (2000), pp. 1734–1736.

[29] J-Ch Hsu and T-T Wu. "Lamb waves in binary locally resonant phononic plates with two-dimensional lattices." In: *Applied physics letters* 90.20 (2007), p. 201904.

[30] D. Yu, Y. Liu, H. Zhao, G. Wang, and J. Qiu. "Flexural vibration band gaps in Euler-Bernoulli beams with locally resonant structures with two degrees of freedom." In: *Phys. Rev. B* 73 (6 2006), p. 064301.

[31] M. Nouh, O. Aldraihem, and A. Baz. "Vibration characteristics of metamaterial beams with periodic local resonances." In: *Journal of Vibration and Acoustics* 136.6 (2014), p. 061012.

[32] T-T Wu, Z-G Huang, T-C Tsai, and T-C Wu. "Evidence of complete band gap and resonances in a plate with periodic stubbed surface." In: *Applied Physics Letters* 93.11 (2008), p. 111902.

[33] Tzung-Chen Wu, Tsung-Tsong Wu, and Jin-Chen Hsu. "Waveguiding and frequency selection of Lamb waves in a plate with a periodic stubbed surface." In: *Physical Review B* 79.10 (2009), p. 104306.

[34] A. Khelif, Y. Achaoui, and B. Aoubiza. "Locally Resonant Structures for Low Frequency Surface Acoustic Band Gap Applications." In: *Acoustic Metamaterials*. Springer, 2013, pp. 43–59.

[35] C. Yilmaz, G. M. Hulbert, and N. Kikuchi. "Phononic band gaps induced by inertial amplification in periodic media." In: *Phys. Rev. B* 76 (5 2007), p. 054309.

[36] E. Baravelli and M. Ruzzene. "Internally resonating lattices for bandgap generation and low-frequency vibration control." In: *Journal of Sound and Vibration* 332.25 (2013), pp. 6562–6579.

[37] K. H. Matlack, A. Bauhofer, S. Krödel, A.o Palermo, and C. Daraio. "Composite 3D-printed metastructures for low-frequency and broadband vibration absorption." In: *Proceedings of the National Academy of Sciences* 113.30 (2016), pp. 8386–8390.

[38] N. Fang, D. Xi, J. Xu, M. Ambati, W. Srituravanich, C. Sun, and X. Zhang. "Ultrasonic metamaterials with negative modulus." In: *Nature materials* 5.6 (2006), pp. 452–456.

[39] Z. Yang, J. Mei, M. Yang, N. H. Chan, and P. Sheng. "Membrane-type acoustic metamaterial with negative dynamic mass." In: *Physical review letters* 101.20 (2008), p. 204301.

[40] J. Li and C. T. Chan. "Double-negative acoustic metamaterial." In: *Physical Review E* 70.5 (2004), p. 055602.

[41] Y. Lai, Y. Wu, P. Sheng, and Z-Q Zhang. "Hybrid elastic solids." In: *Nature materials* 10.8 (2011), pp. 620–624.

[42] G. Ma, C. Fu, G. Wang, P. Del Hougne, J. Christensen, Y. Lai, and P. Sheng. "Polarization bandgaps and fluid-like elasticity in fully solid elastic metamaterials." In: *Nature Communications* 7 (2016).

[43] A. Balandin and K. L. Wang. "Significant decrease of the lattice thermal conductivity due to phonon confinement in a free-standing semiconductor quantum well." In: *Physical Review B* 58.3 (1998), p. 1544.

[44] J-K Yu, S. Mitrovic, D. Tham, J. Varghese, and J. R. Heath. "Reduction of thermal conductivity in phononic nanomesh structures." In: *Nature nanotechnology* 5.10 (2010), pp. 718–721.

[45] S. Brûlé, E. H. Javelaud, S. Enoch, and S. Guenneau. "Experiments on seismic metamaterials: Molding surface waves." In: *Physical review letters* 112.13 (2014), p. 133901.

[46] S. Krödel, N. Thomé, and C. Daraio. "Wide band-gap seismic metastructures." In: *Extreme Mechanics Letters* 4 (2015), pp. 111–117.

[47] A. Colombi, P. Roux, S. Guenneau, P. Gueguen, and R. V. Craster. "Forests as a natural seismic metamaterial: Rayleigh wave bandgaps induced by local resonances." In: *Scientific reports* 6 (2016).

[48] G. Yi and B. D. Youn. "A comprehensive survey on topology optimization of phononic crystals." In: *Structural and Multidisciplinary Optimization* 54.5 (2016), pp. 1315–1344.

[49] K. H. Matlack, M. Serra-Garcia, A. Palermo, S. D. Huber, and C. Daraio. "Designing Perturbative Metamaterials from Discrete Models: From Veselago lenses to topological insulators." In: *arXiv preprint arXiv:1612.02362* (2016).

[50] M. Collet, M. Ouisse, M. Ruzzene, and M. N. Ichchou. "Floquet-Bloch decomposition for the computation of dispersion of two-dimensional periodic, damped mechanical systems." In: *International Journal of Solids and Structures* 48.20 (2011), pp. 2837–2848.

[51] W. Setyawan and S. Curtarolo. "High-throughput electronic band structure calculations: Challenges and tools." In: *Computational Materials Science* 49.2 (2010), pp. 299–312.

[52] F. Farzbod and M. J. Leamy. "Analysis of Bloch's method in structures with energy dissipation." In: *Journal of Vibration and Acoustics* 133.5 (2011), p. 051010.

[53] R. P. Moiseyenko and V. Laude. "Material loss influence on the complex band structure and group velocity in phononic crystals." In: *Phys. Rev. B* 83 (6 2011), p. 064301.

[54] P. Langlet, AC HladkyHennion, and JN Decarpigny. "Analysis of the propagation of plane acoustic waves in passive periodic materials using the finite element method." In: *The Journal of the Acoustical Society of America* 98.5 (1995).

[55] V. Laude, Y. Achaoui, S. Benchabane, and A. Khelif. "Evanescent Bloch waves and the complex band structure of phononic crystals." In: *Phys. Rev. B* 80 (9 2009), p. 092301.

[56] R. P. Moiseyenko and V. Laude. "Material loss influence on the complex band structure and group velocity in phononic crystals." In: *Physical Review B* 83.6 (2011), p. 064301.

[57] M. I. Hussein. "Reduced Bloch mode expansion for periodic media band structure calculations." In: *Proceedings of the Royal Society of London A: Mathematical, Physical and Engineering Sciences* 465.2109 (2009), pp. 2825–2848.

[58] E. Andreassen and J. S. Jensen. "Analysis of phononic bandgap structures with dissipation." In: *Journal of Vibration and Acoustics* 135.4 (2013), p. 041015.

[59] I. A. Veres, T. Berer, and O. Matsuda. "Complex band structures of two dimensional phononic crystals: Analysis by the finite element method." In: *Journal of Applied Physics* 114.8 (2013), p. 083519.

[60] E. Manconi and B. R. Mace. "Estimation of the loss factor of viscoelastic laminated panels from finite element analysis." In: *Journal of Sound and Vibration* 329.19 (2010), pp. 3928 –3939. ISSN: 0022-460X.

[61] R.M. Christensen. *Chapter 1 - Viscoelastic Stress Strain Constitutive Relations*. Ed. by R.M. Christensen. Academic Press, 1982, pp. 1 –34.

[62] F. Farzbod and M. J. Leamy. "Analysis of Bloch's Method and the Propagation Technique in Periodic Structures." In: *Journal of vibration and acoustics* 133.3 (2011), p. 031010.

[63] Y. Cao, Z. Hou, and Y. Liu. "Convergence problem of plane-wave expansion method for phononic crystals." In: *Physics Letters A* 327.2 (2004), pp. 247–253.

[64] A. Palermo and A. Marzani. "Ultrafast Wave Finite Element Method for the computation of dispersion properties in periodic viscoelastic waveguides." In: *Proceedings of the 8th European Workshop On Structural Health Monitoring (EWSHM 2016)*. 2016.

[65] A. Palermo and A. Marzani. "Extended bloch mode synthesis: Ultrafast method for the computation of complex band structures in phononic media." In: *International Journal of Solids and Structures* 100 (2016), pp. 29–40.

[66] W. Axmann and P. Kuchment. "An Efficient Finite Element Method for Computing Spectra of Photonic and Acoustic Band-Gap Materials." In: *Journal of Computational Physics* 150.2 (1999), pp. 468 –481. ISSN: 0021-9991.

[67] D. C. Dobson. "An Efficient Method for Band Structure Calculations in 2D Photonic Crystals." In: *Journal of Computational Physics* 149.2 (1999), pp. 363 –376. ISSN: 0021-9991.

[68] S. G. Johnson and J. D. Joannopoulos. "Block-iterative frequency-domain methods for Maxwell's equations in a planewave basis." In: *Opt. Express* 8.3 (2001), pp. 173–190.

[69] F. Casadei, Rimoli J.J., and Ruzzene M. "A geometric multiscale finite element method for the dynamic analysis of heterogeneous solids." In: *Computer Methods in Applied Mechanics and Engineering* 263 (2013), pp. 56 –70.

[70] F. Casadei, J.J. Rimoli, and M. Ruzzene. "Multiscale finite element analysis of wave propagation in periodic solids." In: *Finite Elements in Analysis and Design* 108 (2016), pp. 81 –95.

[71] T.W. McDevitt, G.M. Hulbert, and N. Kikuchi. "An assumed strain method for the dispersive global–local modeling of periodic structures." In: *Computer Methods in Applied Mechanics and Engineering* 190.48 (2001), pp. 6425 –6440. ISSN: 0045-7825.

[72] M. I. Hussein and G. M. Hulbert. "Mode-enriched dispersion models of periodic materials within a multiscale mixed finite element framework." In: *Finite Elements in Analysis and Design* 42.7 (2006). The Seventeenth Annual Robert J. Melosh Competition, pp. 602 –612.

[73] R. J. Guyan. "Reduction of stiffness and mass matrices." In: *AIAA journal* 3.2 (1965), pp. 380–380.

[74] M. C. C. Bampton and J. R. Craig. "Coupling of substructures for dynamic analyses." In: *AIAA Journal* 6.7 (1968), pp. 1313–1319.

[75] C. Droz, J.-P. Ichchou Lainé, M.N., and G. Inquiété. "A reduced formulation for the free-wave propagation analysis in composite structures." In: *Composite Structures* 113 (2014), pp. 134 –144.

[76] D. Krattiger and M. I. Hussein. "Bloch mode synthesis: Ultrafast methodology for elastic band-structure calculations." In: *Phys. Rev. E* 90 (6 2014), p. 063306.

[77] C. W. Zhou, J. P. Laine, M. N. Ichchou, and A. M. Zine. "Wave finite element method based on reduced model for one-dimensional periodic structures." In: *International Journal of Applied Mechanics* 7.02 (2015), p. 1550018.

[78] C.W. Zhou, J. P. Lainé, M. N. Ichchou, and A. M. Zine. "Multi-scale modelling for two-dimensional periodic structures using a combined mode/wave based approach." In: *Computers & Structures* 154 (2015), pp. 145–162.

[79] I. Bartoli, A. Marzani, F. Lanza di Scalea, and E. Viola. "Modeling wave propagation in damped waveguides of arbitrary cross-section." In: *Journal of Sound and Vibration* 295 (2006), pp. 685 –707.

[80] H. Khales, A. Hassein-Bey, and A. Khelif. "Evidence of ultrasonic band gap in aluminum phononic crystal beam." In: *Journal of Vibration and Acoustics* 135.4 (2013), p. 041007.

[81] P. Krysl. *fineale*. https://github.com/PetrKryslUCSD/FinEALE. 2012–2014.

[82] V. Romero-García, J. O. Vasseur, L. M. Garcia-Raffi, and A. C. Hladky-Hennion. "Theoretical and experimental evidence of level repulsion states and evanescent modes in sonic crystal stubbed waveguides." In: *New Journal of Physics* 14.2 (2012), p. 023049.

[83] R. S. Langley. "Some perspectives on wave-mode duality in SEA." In: *IUTAM symposium on statistical energy analysis*. Springer. 1999, pp. 1–12.

[84] J-M Mencik. "Model reduction and perturbation analysis of wave finite element formulations for computing the forced response of coupled elastic systems involving junctions with uncertain eigenfrequencies." In: *Computer Methods in Applied Mechanics and Engineering* 200.45 (2011), pp. 3051–3065.

[85] J-M Mencik. "A model reduction strategy for computing the forced response of elastic waveguides using the wave finite element method." In: *Computer Methods in Applied Mechanics and Engineering* 229 (2012), pp. 68–86.

[86] J-M Mencik and D. Duhamel. "A wave finite element-based approach for the modeling of periodic structures with local perturbations." In: *Finite Elements in Analysis and Design* 121 (2016), pp. 40–51.

[87] C. Droz, C. Zhou, M.N. Ichchou, and J. P. Lainé. "A hybrid wave-mode formulation for the vibro-acoustic analysis of 2D periodic structures." In: *Journal of Sound and Vibration* 363 (), pp. 285 –302.

[88] D.J. Thompson. "Wheel-rail Noise Generation, Part III: Rail Vibration." In: *Journal of Sound and Vibration* 161.3 (1993), pp. 421 –446.

[89] P. Wilcox, M. Evans, B. Pavlakovic, D. Alleyne, K. Vine, P. Cawley, and M. Lowe. "Guided wave testing of rail." In: *Insight-Non-Destructive Testing and Condition Monitoring* 45.6 (2003), pp. 413–420.

[90] I. Bartoli, F. Lanza di Scalea, M. Fateh, and E. Viola. "Modeling guided wave propagation with application to the long-range defect detection in railroad tracks." In: *Ndt & E International* 38.5 (2005), pp. 325–334.

[91] J. Ryue, D. J. Thompson, P. R. White, and D. R. Thompson. "Decay rates of propagating waves in railway tracks at high frequencies." In: *Journal of Sound and Vibration* 320.4 (2009), pp. 955–976.

[92] Y. Bozorgnia and V. V. Bertero. *Earthquake engineering: from engineering seismology to performance-based engineering*. CRC press, 2004.

[93] S. L. Kramer. *Geotechnical earthquake engineering*. Pearson Education India, 1996.

[94] K. F. Graff. *Wave motion in elastic solids*. Courier Corporation, 2012.

[95] R. D. Woods. "Screening of surface waves in soils." In: *Am Soc Civil Engr J Soil Mech* (1968).

[96] D. D. Barkan. *Dynamics of bases and foundations*. McGraw-Hill, 1960.

[97] J. Aboudi. “Elastic waves in half-space with thin barrier.” In: *Journal of the Engineering Mechanics Division* 99.1 (1973), pp. 69–83.

[98] W. A. Haupt. “Surface waves in nonhomogeneous half-space.” In: *Dynamical methods in soil and rock mechanics* (1978), pp. 335–367.

[99] G. Segol, J. F. Abel, and P. CY Lee. “Amplitude reduction of surface waves by trenches.” In: *Journal of the Engineering Mechanics Division* 104.3 (1978), pp. 621–641.

[100] M. Fuyuki and Y. Matsumoto. “Finite difference analysis of Rayleigh wave scattering at a trench.” In: *Bulletin of the Seismological Society of America* 70.6 (1980), pp. 2051–2069.

[101] DE Beskos, B. Dasgupta, and I.G. Vardoulakis. “Vibration isolation using open or filled trenches.” In: *Computational mechanics* 1.1 (1986), pp. 43–63.

[102] H. Takemiya. “Field vibration mitigation by honeycomb WIB for pile foundations of a high-speed train viaduct.” In: *Soil Dynamics and Earthquake Engineering* 24.1 (2004), pp. 69–87.

[103] L. Andersen and S. RK Nielsen. “Reduction of ground vibration by means of barriers or soil improvement along a railway track.” In: *Soil Dynamics and Earthquake Engineering* 25.7 (2005), pp. 701–716.

[104] M. Adam and O. Von Estorff. “Reduction of train-induced building vibrations by using open and filled trenches.” In: *Computers & structures* 83.1 (2005), pp. 11–24.

[105] J. Huang and Z. Shi. “Vibration Reduction of Plane Waves Using Periodic In-Filled Pile Barriers.” In: *Journal of Geotechnical and Geoenvironmental Engineering* 141.6 (2015), p. 04015018.

[106] M. Miniaci, F. Krushynska A.and Bosia, and N. M. Pugno. “Large scale mechanical metamaterials as seismic shields.” In: *New Journal of Physics* 18.8 (2016), p. 083041.

[107] J. Bao, Z. Shi, and H. Xiang. “Dynamic responses of a structure with periodic foundations.” In: *Journal of Engineering Mechanics* 138.7 (2011), pp. 761–769.

[108] H. J. Xiang, Z. F. Shi, S. J. Wang, and Y. L. Mo. “Periodic materials-based vibration attenuation in layered foundations: experimental validation.” In: *Smart Materials and Structures* 21.11 (2012), p. 112003.

[109] S. H. Kim and M. P. Das. “Artificial seismic shadow zone by acoustic metamaterials.” In: *Modern Physics Letters B* 27.20 (2013), p. 1350140.

[110] J. Zhu, Y. Chen, X. Zhu, F. J. Garcia-Vidal, X. Yin, W. Zhang, and X. Zhang. “Acoustic rainbow trapping.” In: *Scientific reports* 3 (2013).

[111] V. K. Dertimanis, I. A. Antoniadis, and E. N. Chatzi. "Feasibility analysis on the attenuation of strong ground motions using finite periodic lattices of mass-in-mass barriers." In: *Journal of Engineering Mechanics* 142.9 (2016), p. 04016060.

[112] Y. Achaoui, B. Ungureanu, S. Enoch, S. Brûlé, and S. Guenneau. "Seismic waves damping with arrays of inertial resonators." In: *Extreme Mechanics Letters* 8 (2016). Nanomechanics: Bridging Spatial and Temporal Scales, pp. 30 –37.

[113] P. Cacciola and A. Tombari. "Vibrating barrier: a novel device for the passive control of structures under ground motion." In: *Proc. R. Soc. A*. Vol. 471. 2179. The Royal Society. 2015, p. 20150075.

[114] A. Colombi, D.J. Colquitt, P. Roux, S. Guenneau, and R. V. Craster. "A seismic metamaterial: The resonant metawedge." In: *Scientific reports* 6 (2016).

[115] D.J. Colquitt, A. Colombi, R.V. Craster, P. Roux, and S.R.L. Guenneau. "Seismic metasurfaces: Sub-wavelength resonators and Rayleigh wave interaction." In: *Journal of the Mechanics and Physics of Solids* 99 (2017), pp. 379 – 393.

[116] Z. Cheng and Z. Shi. "Novel composite periodic structures with attenuation zones." In: *Engineering Structures* 56 (2013), pp. 1271–1282.

[117] Z. Cheng and Z. Shi. "Vibration attenuation properties of periodic rubber concrete panels." In: *Construction and Building Materials* 50 (2014), pp. 257–265.

[118] G. Finocchio, O. Casablanca, G. Ricciardi, U. Alibrandi, F. Garescì, M. Chiappini, and B. Azzerboni. "Seismic metamaterials based on isochronous mechanical oscillators." In: *Applied Physics Letters* 104.19 (2014), p. 191903.

[119] A. Climente, D. Torrent, and J. Sánchez-Dehesa. "Gradient index lenses for flexural waves based on thickness variations." In: *Applied Physics Letters* 105.6 (2014), p. 064101.

[120] A. Colombi, S. Guenneau, P. Roux, and R. V. Craster. "Transformation seismology: composite soil lenses for steering surface elastic Rayleigh waves." In: *Scientific reports* 6 (2016).

[121] M. Farhat, S. Guenneau, and S. Enoch. "Ultrabroadband elastic cloaking in thin plates." In: *Physical review letters* 103.2 (2009), p. 024301.

[122] A. Khlopotin, P. Olsson, and F. Larsson. "Transformational cloaking from seismic surface waves by micropolar metamaterials with finite couple stiffness." In: *Wave Motion* 58 (2015), pp. 53–67.

[123] Y. Achaoui, T. Antonakakis, S. Brule, R. V. Craster, S. Enoch, and S. Guenneau. "Clamped seismic metamaterials: Ultra-low broad frequency stopbands." In: *arXiv preprint arXiv:1701.08841* (2017).

[124] A. Palermo, S. Krödel, A. Marzani, and C. Daraio. “Engineered metabarrier as shield from seismic surface waves.” In: *Scientific Reports* 6 (2016).

[125] S. Benchabane, O. Gaiffe, R. Salut, G. Ulliac, V. Laude, and K. Kokkonen. “Guidance of surface waves in a micron-scale phononic crystal line-defect waveguide.” In: *Applied Physics Letters* 106.8 (2015), p. 081903.

[126] T-T Wu, L-C Wu, and Z-G Huang. “Frequency band-gap measurement of two-dimensional air/silicon phononic crystals using layered slanted finger interdigital transducers.” In: *Journal of Applied Physics* 97.9 (2005), p. 094916.

[127] S. Benchabane, A. Khelif, J-Y Rauch, L. Robert, and V. Laude. “Evidence for complete surface wave band gap in a piezoelectric phononic crystal.” In: *Physical Review E* 73.6 (2006), p. 065601.

[128] A. Khelif, Y. Achaoui, S. Benchabane, V. Laude, and B. Aoubiza. “Locally resonant surface acoustic wave band gaps in a two-dimensional phononic crystal of pillars on a surface.” In: *Physical Review B* 81.21 (2010), p. 214303.

[129] N. Boechler, J. K. Eliason, A. Kumar, K. A. Maznev A. A.and Nelson, and N. Fang. “Interaction of a contact resonance of microspheres with surface acoustic waves.” In: *Physical review letters* 111.3 (2013), p. 036103.

[130] M. Christensen, A. B. Abrahamsen, N. B. Christensen, F. Juranyi, N. H. Andersen, K. Lefmann, J. Andreasson, C. R.H. Bahl, and B. B. Iversen. “Avoided crossing of rattler modes in thermoelectric materials.” In: *Nature Materials* 7.10 (2008), pp. 811–815.

[131] F. Bretaudeau, D. Leparoux, O. Durand, and O. Abraham. “Small-scale modeling of onshore seismic experiment: A tool to validate numerical modeling and seismic imaging methods.” In: *Geophysics* 76.5 (2011), T101–T112.

[132] F. Bretaudeau, D. Brossier R.and Leparoux, O. Abraham, and J. Virieux. “2D elastic full-waveform imaging of the near-surface: Application to synthetic and physical modelling data sets.” In: *Near Surface Geophysics* 11.3 (2013), pp. 307–316.

[133] N. Ricker. “The form and laws of propagation of seismic wavelets.” In: *Geophysics* 18.1 (1953), pp. 10–40.

[134] C. Yilmaz, G. M. Hulbert, and N. Kikuchi. “Phononic band gaps induced by inertial amplification in periodic media.” In: *Physical Review B* 76.5 (2007), p. 054309.

[135] S. Taniker and C. Yilmaz. “Phononic gaps induced by inertial amplification in BCC and FCC lattices.” In: *Physics Letters A* 377.31 (2013), pp. 1930–1936.

[136] B. Yuan, V. F Humphrey, J. Wen, and X. Wen. “On the coupling of resonance and Bragg scattering effects in three-dimensional locally resonant sonic materials.” In: *Ultrasonics* 53.7 (2013), pp. 1332–1343.

[137] R. Zhu, X. N. Liu, G. K. Hu, C. T. Sun, and G. L. Huang. “A chiral elastic metamaterial beam for broadband vibration suppression.” In: *Journal of Sound and Vibration* 333.10 (2014), pp. 2759–2773.

[138] D. J. Colquitt, R. V Craster, T. Antonakakis, and S. Guenneau. “Rayleigh–Bloch waves along elastic diffraction gratings.” In: *Proc. R. Soc. A*. Vol. 471. 2173. The Royal Society. 2015, p. 20140465.

[139] D. E. Goldberg and J. H. Holland. “Genetic algorithms and machine learning.” In: *Machine learning* 3.2 (1988), pp. 95–99.

[140] S. Foti, C. G. Lai, G. J. Rix, and C. Strobbia. *Surface wave methods for near-surface site characterization*. CRC Press, 2014.

[141] M. Destrade. “Seismic Rayleigh waves on an exponentially graded, orthotropic half-space.” In: *Proceedings of the Royal Society of London A: Mathematical, Physical and Engineering Sciences*. Vol. 463. 2078. The Royal Society. 2007, pp. 495–502.

[142] O. Balogun and J. D. Achenbach. “Surface waves on a half space with depth-dependent properties.” In: *The Journal of the Acoustical Society of America* 132.3 (2012), pp. 1336–1345.

[143] A.G. Alenitsyn. “Raleigh waves in a nonhomogeneous elastic half-space.” In: *Journal of Applied Mathematics and Mechanics* 27.3 (1963), pp. 816–822.

[144] X. Jacob, V. Aleshin, V. Tournat, P. Leclaire, W. Lauriks, and VE Gusev. “Acoustic probing of the jamming transition in an unconsolidated granular medium.” In: *Physical Review Letters* 100.15 (2008), p. 158003.

[145] L. Bodet, A. Dhemaied, R. Martin, R. Mourgues, F. Rejiba, and V. Tournat. “Small-scale physical modeling of seismic-wave propagation using unconsolidated granular media.” In: *Geophysics* 79.6 (2014), T323–T339.

[146] H. Kawase. “The cause of the damage belt in Kobe:“The basin-edge effect,” constructive interference of the direct S-wave with the basin-induced diffracted/Rayleigh waves.” In: *Seismological Research Letters* 67.5 (1996), pp. 25–34.